

Federal University of Rio Grande do Sul
Engineering School
Civil Engineering Post-Graduation Program

**Bender Elements, Ultrasonic Pulse Velocity, and Local
Gauges for the Analysis of Stiffness Degradation of an
Artificially Cemented Soil**

Marina Schnaider Bortolotto

Porto Alegre
2017

MARINA SCHNAIDER BOLOTOLOTTO

**BENDER ELEMENTS, ULTRASONIC PULSE
VELOCITY, AND LOCAL GAUGES FOR THE
ANALYSIS OF STIFFNESS DEGRADATION OF AN
ARTIFICIALLY CEMENTED SOIL**

Dissertation presented to the Civil Engineering Post-Graduation
Program from the Federal University of Rio Grande do Sul, as part
of the requirements for the title of Master in Engineering

Porto Alegre
2017

MARINA SCHNAIDER BORTOLOTTO

**BENDER ELEMENTS, ULTRASONIC PULSE VELOCITY,
AND LOCAL GAUGES FOR THE ANALYSIS OF STIFFNESS
DEGRADATION OF AN ARTIFICIALLY CEMENTED SOIL**

This master dissertation was considered suitable for obtaining the title of MASTER IN ENGINEERING, in the field of Geotechnical Engineering, its final version was also approved by the supervisor and by the Civil Engineering Post-Graduation Program from the Federal University of Rio Grande do Sul.

Porto Alegre, September 29th 2017

Prof. Nilo Cesar Consoli
Ph.D. Concordia University, Canada,
Supervisor

Prof. J. Antonio H. Carraro
Ph.D. Purdue University, USA
Co-supervisor

Prof. Nilo Cesar Consoli
PPGEC/UFRGS Coordinator

BOARD OF EXAMINERS

Prof. Erdin Ibraim (University of Bristol)
Ph.D. INSA/ENTPE Lyon

Prof. Karla Salvagni Heineck (UFRGS)
D.Sc. Federal University of Rio Grande do
Sul

Prof. Lucas Festugato (UFRGS)
D.Sc. Federal University of Rio Grande do
Sul

Prof. Marcelo Maia Rocha (UFRGS)
Ph.D. Universität Innsbruck, Austria

To my Family, which offer me nothing but true love.

ACKNOWLEDGMENT

There are so many people that I am really grateful for their invaluable help and support along this hard journey, that is almost impossible to name them all. I do hope I can, at least, include those who have contributed the most in helping me to reach the finishing line. Those I have for some reason not included in this acknowledgement, remains the certainty that you will always remain in heart.

First of all, I would like to thank my family. Mom and dad, your example has been the basis for strength and determination I have today. Iara, you taught me to be resilient. Cesar, you have been like my true blood brother in so many ways. Fabio, thanks for the criticism, which has always kept my feet firmly on the ground. Gus and Dudu, for your unconditional love, which has always brighten my days.

My dearest Civil Engineering friends (Vévis, Claudio, André, and Miyazaki), I would like to thank you all for the conversations, whether they were related to Engineering or not. Your friendship, even at distance, has been fundamental to keep my focus on the work ahead.

My oldest friends (Alê, Tinho, Lu, and Lala), thanks! I have no words to express how nurturing your support has been. Cata and Caê, your presence has been also illuminating my days.

Gabreis, Guilherme, Marília, and Matheus, my dear friends, thanks for all the care and endless conversations, which have definitely helped me to keep in the right direction.

Antônio Carlos, I appreciate all the hours you have spent on reviewing the English grammar of my work and also for your timely criticism. Your assistance was essential to help me to deliver a consistent piece of work.

Fernanda, thanks for not letting me fall apart during difficult moments.

My dear Scout brothers (Marcel and Fernanda, Leo, Anê and Lucas), thanks for the support. Tati and Jonathan, thanks for making me feel so welcome to my new “family”, the Arno Friedrich Scout Group. My Venturer Scouts, spending time with you helped me to lighten the burden.

Mozara and Nati, your friendship has been essential in this journey; thanks for everything you have done for me. Marina and Thais, you made me feel welcome at my arrival at LEGG, and now I am thankful for your friendship. Carina, I appreciate all our conversations and the support (thank you so much!). Naloan and Helena, working together and embarking in such high level conversations with you was so enlightening. Eduardo and Gonçalo, I appreciate our long conversations and the endless sharing of ideas.

João and Pablo, your curiosity took us to long discussions and explanations, which I appreciated so much. I would also like to express my gratitude to Sr. João, who helped me so much in the daily hurdles of laboratory life.

Jorge, Alejandro, and Sérgio: thank you so, so much for all the time you dedicated helping and teaching me. I really appreciate your patience and support (and all our conversations!).

I would like to acknowledge the support in this journey, which started so many years ago, my dearest graduation professors: Cristhiane Okawa, Jeselay dos Reis, and Jesner Ildefonso.

Prof. Lucas Festugato, thank you for all the help and technical opinion. Your assistance was crucial to accomplish this project.

Prof. Marcelo Rocha, thanks for all the support from basic electronics to programming. Your help was fundamental to improve our BE system.

Prof. Antonio Carraro, thank you for introducing the Geotechnical world to me, and for always pushing me into producing research of the highest quality.

Prof. Nilo Consoli, above all, I would like to thank you for always believing in me from the beginning, when you entrusted such an important task to someone you hardly knew. I really appreciate all the support and guidance you have provided me along this arduous job.

Finally, I would also like to express my gratitude to CAPES and CNPq, whose financial support enabled the conduction of this study.

The important thing is not to stop questioning. Curiosity
has its own reason for existing
Albert Einstein

RESUMO

BORTOLOTTO, M. S. *Bender Elements, Ultrasonic Pulse Velocity, and Local Gauges for the Analysis of Stiffness Degradation of an Artificially Cemented Soil*. 2017. Dissertação (Mestre em Engenharia) – Programa de Pós-Graduação em Engenharia Civil, UFRGS, Porto Alegre.

A rigidez a pequenas deformações e sua respectiva degradação são informações cruciais para se determinar parâmetros de projeto mais precisos. Apesar de sua importância, estas propriedades não são usualmente investigadas. Assim, o objetivo do presente trabalho foi de estudar a degradação da rigidez da areia de Osório artificialmente cimentada por meio de diferentes métodos de laboratório. A escolha por um material cimentado ocorreu baseada em apelos ambientais, econômicos e técnicos. O presente estudo também objetiva desenvolver e validar um sistema de *Bender Elements* (BE), que forneça resultados confiáveis na avaliação da degradação do solo. Pares de BE foram construídos para serem utilizados em testes de bancada e ensaios triaxiais. Além disso, um amplificador de sinal, assim como *scripts* foram desenvolvidos especialmente para a interpretação dos dados no domínio do tempo. O aumento da rigidez durante o processo de cura foi avaliado por meio da velocidade de onda cisalhante, medida pelos BE e por um equipamento de ondas ultrassônicas (UPV), sob condições de pressão atmosférica. Ensaios de degradação da rigidez, por sua vez, foram conduzidos em uma câmara triaxial especialmente modificada para a instalação dos BE. Após sete dias de cura atmosférica, os corpos-de-prova foram cisalhados no equipamento triaxial modificado enquanto mudanças de rigidez eram obtidas por meio de testes de BE e instrumentação interna. Os resultados demonstraram que o sistema BE desenvolvido foi bem sucedido na avaliação da rigidez do solo estudado. A comparação entre os resultados do BE e UPV não foi conclusiva no que se refere à dependência do solo à frequência. A degradação do módulo obtida por ambas as metodologias apresentou uma adequada concordância para o corpo-de-prova com menor quantidade de cimento. Módulos obtidos por BE foram pouco maiores que os obtidos por medidas internas. Ainda, a interpretação no domínio do tempo dos resultados de BE para corpos-de-prova cimentados, especialmente durante ensaios triaxiais, foi difícil de ser executada, reforçando a necessidade de se combinar diferentes métodos de interpretação quando BE forem utilizados.

Palavras-chave: rigidez a pequeníssimas deformações; degradação da rigidez; bender elements; solos cimentados artificialmente

ABSTRACT

BORTOLOTTO, M. S. Bender Elements, Ultrasonic Pulse Velocity, and Local Gauges for the Analysis of Stiffness Degradation of an Artificially Cemented Soil. 2017. Master dissertation (Master in Engineering) – Civil Engineering Post-Graduation Program, UFRGS, Porto Alegre.

Stiffness at small strains and its respective degradation are crucial information to determine more precise design parameters. Despite their importance, these properties are not usually investigated. Thus, the objective of the present work was to study the stiffness degradation of artificially cemented Osorio sand by means of different laboratory methods. The choice for a cemented material was based on environmental, economic, and technical appeals. The present study also aimed to develop and validate a Bender Elements (BE) system that can provide reliable results in the evaluation of soil degradation. BE pairs were built for bench and triaxial tests. In addition, a signal amplifier, as well as scripts were specially developed for the interpretation of data in the time domain. Increase in stiffness during the curing process was evaluated by shear wave velocity measured by BE and an ultrasonic pulse wave velocity (UPV) equipment under atmospheric pressure conditions. Stiffness degradation tests were conducted in a specially modified triaxial chamber for BE installation. After seven days of atmospheric curing, specimens were sheared in the modified triaxial equipment, while stiffness changes were obtained by BE tests and internal instrumentation. The results showed that the developed BE system was capable of successfully evaluating the studied soil. The comparison between BE and UPV results was not conclusive regarding soil dependence on frequency. Shear module degradation obtained with the two methodologies presented an adequate agreement for the specimen with the smaller amount of cement. Shear moduli obtained with BE were slightly larger than those obtained with internal measurements. Also, BE results interpretation in the time domain for cemented specimens, especially in the triaxial tests, was difficult to perform, reinforcing the need to combine different interpretation methods when BE are used.

Key-words: Stiffness at very-small strain; stiffness degradation; bender elements; artificially cemented soils.

SUMMARY

LIST OF FIGURES	14
LIST OF TABLES	20
LIST OF CHARTS	21
LIST OF ACRONYMS AND ABBREVIATIONS	22
LIST OF SYMBOLS	23
1 INTRODUCTION	25
1.1 RELEVANCE AND RESEARCH JUSTIFICATION	26
1.2 OBJECTIVES	26
2 LITERATURE REVIEW	28
2.1 STRAIN	28
2.2 STRESS-STRAIN CURVE AND MODULUS	29
2.3 CEMENTATION BONDINGS	33
2.4 STIFFNESS DEGRADATION OF GEOMATERIALS	37
2.5 WAVES IN GEOMATERIALS	44
2.5.1 Bender elements	49
2.5.1.1 BE characterisation	57
2.5.1.2 Working frequency	60
2.5.1.3 Result interpretation	63
2.5.1.4 Bender elements on natural and cemented sand	66
2.6 ULTRASONIC WAVES	68
2.7 SOIL ANISOTROPY	68
3 EXPERIMENTAL DESIGN	69
3.1 INITIAL CONSIDERATIONS	69
3.2 VARIABLES	70
3.3 MATERIALS	73
3.3.1 Osorio sand	73
3.3.2 Cement	75
3.3.3 Calcined gypsum	76

3.3.4 Water	76
3.4 METHODS	76
3.4.1 Preparation of Osorio sand samples	76
3.4.1.1 Quartering process	76
3.4.2 Cement conditioning	77
3.4.3 Characterisation procedures	77
3.4.3.1 Particle size distribution	77
3.4.3.2 Specific gravity	78
3.4.3.3 Maximum and minimum void ratio	78
3.4.3.4 Water content	78
3.4.4 Specimen moulding and curing	78
3.4.5 Capping process	80
3.4.5.1 Capping mixture components and preparation	80
3.4.5.2 Specimen capping	81
3.4.5.3 Calibrations	84
3.4.6 Anisotropy assessment	85
3.4.7 Ultrasound pulse velocity (UPV) tests	87
3.4.7.1 UPV presentation	87
3.4.7.2 UPV Calibration	88
3.4.7.3 Wave measurements	90
3.4.8 Bender elements (BE) tests	93
3.4.8.1 BE Calibration	94
3.4.8.2 Work frequencies	101
3.4.8.3 BE system validation	101
3.4.8.4 BE coupling procedure	102
3.4.8.5 Bench BE operational procedure	104
3.4.9 Triaxial tests	106
3.4.9.1 Triaxial apparatus presentation	107
3.4.9.2 Equipment calibration	110
3.4.9.3 Initial procedures	112
3.4.9.4 Triaxial BE pair coupling	113
3.4.9.5 Triaxial procedures	114
3.4.9.6 Shearing and BE tests	116
4 RESULTS AND DISCUSSION	117

4.1 DATA PRESENTATION STANDARDISATION	117
4.2 QUALITY OF FABRICATED SPECIMENS	118
4.3 CAPPING CALIBRATION	122
4.3.1 Delays in wave travelling time due to capping	122
4.3.2 Changes in mass due to capping	125
4.4 BE COUPLANT CORRECTION	127
4.4.1 BE couplant time-effect	127
4.4.2 BE couplant effect on specimen mass	130
4.5 ANISOTROPY	131
4.6 ULTRASOUND TESTS	134
4.6.1 Cylindrical specimens	135
4.6.1.1 Cubical specimens comparison	136
4.6.1.2 Comparison with BE prediction equation	137
4.6.2 Specimen geometry	138
4.7 BE TRIAXIAL SYSTEM VALIDATION	139
4.8 BE BENCH TESTS	143
4.8.1 Time-domain – Peak-to-peak approach	144
4.8.2 BE bench system validation	149
4.8.3 BE bench pair damage	150
4.8.4 Resonance response	151
4.9 BE TRIAXIAL TEST	153
4.9.1 Initial shear modulus	154
4.9.2 Stiffness degradation	158
5 CONCLUSIONS	164
5.1 BE SYSTEM	164
5.1.1 BE fabrication	164
5.1.2 BE signal amplifier	166
5.1.3 Working frequency and noise	166
5.1.4 BE system validation	167
5.2 BE RESULTS	167
5.2.1 BE bench results	167

5.2.2 Stiffness at very-small strains	168
5.2.3 Stiffness degradation	168
5.3 FINAL REMARKS	168
5.4 SUGESTIONS FOR FUTURE WORKS	168
5.4.1 BE tests condition	169
5.4.2 BE received signal and data acquisition	169
5.4.3 BE behaviour and calibration	169
REFERENCES	171
APPENDICES	I
APPENDIX A - BE EQUIPMENT	II
INTRODUCTION	III
APPENDIX A.1 BE SYSTEM	IV
Appendix A.1.1 Wave generation - Function generator	VII
Appendix A.1.2 Wave transmission and reception – BE transducers	VIII
Appendix A.1.3 Wave amplification – Signal amplifier	IX
Appendix A.1.4 Signal acquisition – Oscilloscope	XI
Appendix A.1.5 Data processing	XIII
Appendix A.2 BE FABRICATION	XV
Appendix A.2.1 Piezoceramic	XV
Appendix A.2.2 Piezoceramic wiring	XVI
Appendix A.2.3 Piezoceramic encapsulating	XXII
Appendix A.2.4 Final assembling	XXVII
Appendix A.3 SIGNAL AMPLIFIER CIRCUIT DESIGN	XXIX
Appendix A.3.1 Amplifier power supply	XXX
Appendix A.3.2 Input and output amplifier connector	XXXII
Appendix A.3.3 First gain step	XXXIII
Appendix A.3.4 Second gain step	XXXV
Appendix A.4 MACHINED PARTS	XXXVII
Appendix A.4.1 BE mould	XXXVII
Appendix A.4.2 BE metal case	XXXVII
Appendix A.4.3 Metal BE templates	XXXVIII
Appendix A.4.4 Bench pedestal	XXXVIII
Appendix A.4.5 Triaxial top cap and pedestal	XXXIX

Appendix A.4.6 Porous disks	XL
Appendix A.4.7 Calibration rods	XLI
APPENDIX B - MATLAB® SCRIPT	XLII
APPENDIX C - MACHINED PARTS	LII
Appendix C.1 - BE mould	LIII
Appendix C.2 - BE metal sockets	LVIII
Appendix C.3 - Metal BE templates	LIX
Appendix C.4 - Bench pedestal	LX
Appendix C.5 - Triaxial top cap and pedestal	LXI
Appendix C.6 - Porous disks	LXVI
Appendix C.7 - Calibration rods	LXVII
APPENDIX D - TRX_0.00_15.4 AFTER CONSOLIDATION	LXIX
APPENDIX E - DAILY BE BENCH TESTS	LXXIII
Appendix E.1 - Specimen BEN_31.9_15.4	LXXIV
Appendix E.2 - Specimen BEN_8.64_15.4	LXXVII
APPENDIX F - TRIAXIAL TESTS	LXXXI
Appendix F.1 - Specimen BEN_31.9_15.4	LXXXII
Appendix F.2 - Specimen BEN_8.64_15.4	LXXXIII
APPENDIX G - BE TRIAXIAL TESTS	LXXXIV
Appendix G.1 - Specimen BEN_31.9_15.4	LXXXV
Appendix G.2 - Specimen BEN_8.64_15.4	LXXXIX

LIST OF FIGURES

Figure 2.1: Common stress-strain relation for – a) granular soil (fine-medium sand) in dense packing (curve above) and loose density ($\sigma_3= 207$ kPa); b) materials with different behaviours	30
Figure 2.2: Stress-strain relationship – a) typical soil behaviour; b) elastic perfectly plastic model; c) rigid perfectly plastic model; and d) elastic-strain hardening and softening plastic models	30
Figure 2.3: Different types of moduli	31
Figure 2.4: Distinction between the tangent and secant modulus of a non-linear material	33
Figure 2.5: Comparison of an uncemented soil (left) and a cemented soil (right). The soil particles are here represented by spheres for simplification purposes	34
Figure 2.6: Phases of the cementation process in a granular media	35
Figure 2.7: Scanning electron microscopy image of calcareous sand with the addition of 8% Portland cement (in relation to the dry mass of the soil)	36
Figure 2.8: Characteristic stiffness degradation curve including – a) strain levels typically observed in the field; b) laboratory tests for stiffness measurement at different strain levels....	38
Figure 2.9: Effect of cementation in G_0 – a) gain in initial shear modulus due to cementation (bold line); b) stress independence of a cemented soil (only cemented soil is presented)	40
Figure 2.10: Two different control regions for the behaviour of cemented and uncemented soils when loaded	41
Figure 2.11: Comparison of stiffness degradation between a fine-grained offshore cemented and uncemented calcareous soil ($\sigma'_3= 200$ kPa; $\gamma_d= 11.5$ kN/m ³) – a) secant shear modulus; b) normalization of the modulus by its initial shear modulus	42
Figure 2.12: Soil behaviour within the strain-range dependency, associated phenomena, theoretical models, and laboratory measurements	43
Figure 2.13: Body waves – a) compressional wave (V_p); b) vertical shear wave with horizontal propagation ($V_{s,hv}$); c) horizontal shear wave with horizontal propagation ($V_{s,hh}$)....	45
Figure 2.14: Velocity variation of p-waves (V_p) and s-waves (V_s) with increasing B-value for loose Toyoura sand ($D_r=30\%$) subjected to an effective isotropic pressure of 98 kPa	48
Figure 2.15: BE and UPV work frequency ranges	49
Figure 2.16: Piezoceramics polarisation – a) series connection, shear wave receiver; b) parallel configuration, shear-wave transmitter	50
Figure 2.17:BE schematic assembling into a cylindrical specimen; “ d_e ” is the tip-to-tip distance, while “H” represents total specimen height	51
Figure 2.18: BE placed inside a triaxial apparatus – (a) BE embedded in a soil, and BE movement during vibration (red arrows); (b) wave propagation from transmitter to receiver ...	52

Figure 2.19: Response of a BE pair embedded into a saturated silty soil ($\sigma'_1 = 40$ kPa) with deteriorated insulation – (a) excitation step; (b) short pulse excitation	52
Figure 2.20: Waves generated during BE transmitter vibration – (a) side view; (b) top view	53
Figure 2.21: Both shear and compression waves reaching a BE embedded in dry Ticino sand	54
Figure 2.22: Crosstalk effect – (a) BE pair using connection in series without grounding on both transducers; (b) parallel-to-series transducers configuration without shielding or grounding; (c) oscilloscope; (d) zooming oscilloscope crosstalk	55
Figure 2.23: Alternatives to mitigate near-field effects – (a) distorted input signal; (b) forced oscillation at resonant frequency	62
Figure 2.24: Input and output waves used in a parametric study, simulating dispersion effects, note the output wave is a composition of wave A and B	64
Figure 2.25: Interpretation possibilities for wave arrival time– (a) time-domain; (b) cross-correlation; (c) frequency-domain	65
Figure 2.26: Residual soil subjected to BE tests and time-domain analysis – (a) $\sigma'_3 = 100$ kPa; (b) $\sigma'_3 = 800$ kPa	65
Figure 2.27: Normalised shear modulus obtained through bender elements tests for fibre reinforced and non-reinforced Osorio sand subjected to different confining pressures	66
Figure 2.28: Data for initial shear modulus (G_0) measured by bender elements for two different soils, with the equations to predict G_0 using $\eta/(c_{iv})^{\text{exponent}}$	67
Figure 2.29: .. Initial shear modulus (G_0) measured by bender elements in respect to artificially Osorio sand subjected to different confining pressures	67
Figure 3.1: Location of the natural deposit of Osorio sand, situated in the city of Osorio, Brazil	74
Figure 3.2: Scanning electron microscopy images of Osorio sand – magnified at (a) 40 x; and (b) 500 x	74
Figure 3.3: Particle size distribution curve for Osorio sand obtained by manual sieving	74
Figure 3.4: Expected compressive strength gains over time of different types of Portland cement	75
Figure 3.5: Reducing samples of aggregate to testing size by manual quartering	77
Figure 3.6: Moulds used for fabricating specimens – (a) cylindrical; (b) cubical	79
Figure 3.7: Cured Osorio sand/cement specimens – (a) cylindrical specimen (b) cubical specimen	80
Figure 3.8: Capping mixture production – (a) dry solids are added together; (b) resulting mixture after adding distilled water; (c) capping mixture appearance 3 min after mixing	81
Figure 3.9: Capping of cubical specimens – (a) mould made with a plastic cup to delimit the application of the capping mixture; (b) mixture poured into the mould; (c) capping mixture homogeneously distributed; (d) capping mixture without the mould; (e) regularization of the capping mixture surface; and (f) aspect of the finished surface	82

Figure 3.10: Capping of cylindrical specimens – (a) adhesive tape wrapped around the specimen; (b) capping mixture being levelled up; (c) finished top surface; (d) bottom of the specimen with the capping mixture; (e) finished bottom surface; (f) specimen prepared with the capping mixture on the top and bottom surfaces	83
Figure 3.11: Scheme of cubical specimens indicating the direction of compaction (T-T’), and the faces retained by the mould during compaction (A-A’ and B-B’)	86
Figure 3.12: Ultrasound pulse velocity device – (a) compressional waves (p-waves) transducers; (b) shear-waves (s-waves) transducers	88
Figure 3.13: Trigger pulse and received waveform displayed on an oscilloscope	88
Figure 3.14: Calibration rod of the ultrasound pulse velocity equipment	89
Figure 3.15: Calibration rod positioned for p-waves transducer calibration	89
Figure 3.16: Step-by-step calibration procedure	90
Figure 3.17: Possible transducer arrangements	91
Figure 3.18: Scheme for positioning UPV transducers for p-waves (horizontally) and s-waves (vertically)	92
Figure 3.19: Procedure for p-waves measurement	92
Figure 3.20: Time travelling measurement for s-waves using the software Pundit Lab+®	93
Figure 3.21: Manually held BE in direct contact (tip-to-tip) for BE peak signal alignment (red arrows)	95
Figure 3.22: Amplitude frequency response of Bender elements in direct contact (tip-to-tip), with no confinement and all frequencies subjected to same sinusoidal input voltage ($\pm 1V$)	95
Figure 3.23: BE bench pair responses in direct contact – (a) before any bench tests; (b) after all bench tests	96
Figure 3.24: Calibration cylinders for BE tests – (a) cylinder with a cross sectional slot on both extremities for signal quality evaluation and time-delay correction of the entire system; (b) cylinder with circular holes on both extremities to assess couplant effect	97
Figure 3.25: Bench bender elements system during calibration using the slotted nylon cylinder	98
Figure 3.26: Waves captured by the pair of bench BE tested with the slotted nylon calibration cylinder	99
Figure 3.27: UPV test for shear wave propagating through the slotted nylon calibration cylinder	99
Figure 3.28: Metal mould design with a handle part used for excavating BE cavities in specimens	103
Figure 3.29: Bender Elements coupling – (a) perspective view of the excavated cavity; (b) view from the top of the excavated cavity; (c) bottom cavity filled with the coupling paste; (d) top cavity filled with the coupling paste with the bottom BE in place; (e) top and bottom pair of BE perfectly aligned; (f) specimen conditioned into a plastic bag before the first measurement (day 2 of cure)	104
Figure 3.30: Oscilloscope showing the input (upper line) and output (lower line) signals during BE bench test	105

Figure 3.31: Scheme of the Bishop-Wesley press type found at LEGG-UFRGS	107
Figure 3.32: Imperial College-type device for volume change measurement	108
Figure 3.33: Local deformation measurements by Hall effect sensors: 2 sensors to measure axial deformation (top and bottom thirds), and 1 to measure radial deformation (midline)	109
Figure 3.34: Axial (Hall effect) sensors calibration – (a) axial 01; (b) axial 02	111
Figure 3.35: Radial (Hall effect) sensor calibration	111
Figure 3.36: Calibration of the volume change measurement device – (a) downwards metal pin movement; (b) upwards metal pin movement	112
Figure 3.37: Drainage lines saturation and verification of lack of obstruction of permeable elements	113
Figure 4.1: Scheme for the identification of specimens subjected to UPV tests	117
Figure 4.2: Scheme for specimen nomenclature subjected to BE tests	118
Figure 4.3: Target η/c_{iv} ratio versus actual η/c_{iv} ratio for all tested specimens	120
Figure 4.4: Target dry unit weight ($\gamma_{d,d}$) versus real dry unit weight (γ_d) for all tested specimens	121
Figure 4.5: Target dry unit weight ($\gamma_{d,d}$) versus real dry unit weight (γ_d) for each kind of specimen separately – (a) cylindrical specimens subjected to UPV tests; (b) cubical specimens subjected to UPV tests; (c) cylindrical specimens subject to BE tests	121
Figure 4.6: Differences in velocities of identical capped and non-capped specimens– (a) p-wave velocity; (b) s-wave velocity	123
Figure 4.7: Fit-equations for s-wave and p-wave velocities over time	124
Figure 4.8: Calibrated velocities for capped specimens compared to the non-calibrated capped specimen and non-capped specimen – (a) p-waves velocity; (b) s-waves velocity	124
Figure 4.9: Change in moisture content over the curing period for – (a) cylindrical specimens; and (b) cubical specimens	125
Figure 4.10: Dry unit weight after mass correction due to capping for – (a) cylindrical specimens; and (b) cubical specimens	126
Figure 4.11: BE test frequency sweep response with the calibration cylinder filled with BE couplant on day 1 of cure	128
Figure 4.12: BE test frequency swept response with the calibration cylinder filled with BE couplant on day 2 of cure	128
Figure 4.13: BE test frequency swept response with the calibration cylinder filled with BE couplant on day 3 of cure	129
Figure 4.14: BE test frequency swept response with the calibration cylinder filled with BE couplant on day 4 of cure	129
Figure 4.15: Moisture content changes over time for the couplant filling the calibration cylinder with circular cavities, coupled to BE bench pair	130
Figure 4.16: Corrected natural unit weight over time for specimens subjected to BE bench tests	131

Figure 4.17: Anisotropy analysis based on p-wave velocity measurements on the three orthogonal planes (faces) for the following cemented Osorio sand specimens – (a) CUB_31.9_15.4_CAP; (b) CUB_8.64.15.4; (c) CUB_31.9_14.3_CAP; (d) CUB_8.64.14.3.....	132
Figure 4.18: Anisotropy analysis based on s-wave velocity measurements on the three orthogonal planes (faces) for the following cemented Osorio sand specimens – (a) CUB_31.9_15.4_CAP; (b) CUB_8.64.15.4; (c) CUB_31.9_14.3_CAP; (d) CUB_8.64.14.3.....	133
Figure 4.19: Examples of A-A'/VT-T' and B-B'/VT-T' ratio for p-waves and s-waves for specimens – (a) CUB_31.9_15.4_CAP; (b) CUB_8.64.15.4; (c) CUB_31.9_14.3_CAP; (d) CUB_8.64.14.3	134
Figure 4.20: Cylindrical specimens wave velocities obtained during UPV tests along the cure period – (a) p-wave velocities; (b) s-wave velocities	135
Figure 4.21: Cylindrical specimens moduli obtained from wave travelling times measured during UPV tests along the cure period – (a) constrained modulus (M); (b) shear modulus (G)	136
Figure 4.22: Comparison of different moduli obtained from cylindrical specimens and from the vertical direction of cubical specimens during UPV tests – (a) constrained modulus (M); (b) shear modulus (G)	137
Figure 4.23: Comparison between the shear modulus obtained from UPV tests and those calculated based on the prediction equation for BE tests on day 7 of cure	138
Figure 4.24: BE triaxial test frequency swept responses (5 to 40 kHz) of specimen TRX_0.00_15.4, right after consolidation ($\sigma'_3 = 200$ kPa)	140
Figure 4.25: BE triaxial test frequency swept responses (1 to 8 kHz) of specimen TRX_0.00_15.4, right after consolidation ($\sigma'_3 = 200$ kPa)	142
Figure 4.26: Triaxial BE pair validation using initial shear modulus of Osorio sand (not cemented), after consolidation ($\sigma'_3 = 200$ kPa), in comparison to previous study of Heineck, Coop, and Consoli (2005)	143
Figure 4.27: BE triaxial test frequency swept responses of specimen BEN_8.64_15.4 on day 2 of cure	145
Figure 4.28: BE triaxial test frequency sweep responses of specimen BEN_31.9_15.4 specimen on day 2 of cure	146
Figure 4.29: BE triaxial test frequency sweep responses of specimen BEN_31.9_15.4 specimen on day 14 of cure	147
Figure 4.30: Shear moduli evolution of tested specimens over time with the BE bench pair and UPV device	148
Figure 4.31: BE bench pair validation using the prediction equation as a reference for the shear moduli obtained on day 7 of cure	149
Figure 4.32: Damaged pair of BE – (a) cracked transmitter; (b) receiver with a small area not covered by the resin	151
Figure 4.33: Voltage response of the frequency sweep of the specimen BEN_8.64_15.4 subjected to single sine pulses over the time of cure	152

Figure 4.34: Resonance frequency response over time of cure of specimen BEN_8.64_15.4 subjected to single sine pulses	152
Figure 4.35: B-value evolution against the confining pressure during the saturation process with back pressure increments	154
Figure 4.36: BE tests frequency sweep responses of specimen TRX_31.9_15.4 on day 7 of cure, right after consolidation ($\sigma'_3 = 50$ kPa)	156
Figure 4.37: BE tests frequency sweep response of specimen TRX_8.64_15.4 on day 7 of cure right after consolidation ($\sigma'_3 = 50$ kPa)	157
Figure 4.38: Initial shear modulus of artificially Osorio sand specimens (BE tests subjected to $\sigma'_3 = 50$ kPa)	158
Figure 4.39: Changes in the saturated unit mass of specimens subject to shearing, the indicated points represent BE tests	159
Figure 4.40: BE measurements uncertainty after reaching the strength peak – regarding the measurement VII (TRX_31.9_15.4)	160
Figure 4.41: Comparison of Young and shear modulus in terms of respective strains, obtained through internal instrumentation – (a) Young modulus; (b) shear modulus	161
Figure 4.42: Shear modulus degradation measured by BE and internal instrumentation – (a) specimen TRX_31.9_15.4; (b) specimen TRX_8.64_15.4	162

LIST OF TABLES

Table 2.1: Frequencies free of near-field effect and minimum wave-length	61
Table 3.1: Reference B-values for typical soils as a function of saturation	115
Table 4.1: Summary of the target and real parameters of all tested specimens	119
Table 4.2: Differences between measured velocities for capped and non-capped specimens used for time calibration	123
Table 4.3: Effect of specimen dimensions on pulse transmission	139
Table 4.4: Natural unit weight (γ_n) right after specimen fabrication, and the hypothetical saturated unit mass (ρ_{sat})	153

LIST OF CHARTS

Chart 2.1: Relationship between elastic parameters for the analysis of homogeneous and isotropic materials	31
Chart 2.2: Input waves suggested by different authors	57
Chart 3.1: Bench testes performed on artificially cemented Osorio sand (shear-wave velocity over time)	71
Chart 3.2: Triaxial tests with bender elements performed on artificially cemented Osorio sand after 7 days of cure	72
Chart 3.3: Physical properties of Osorio sand	75
Chart 3.4: Summary of procedures associated to each day of cure for artificially cemented Osorio sand subjected to triaxial tests	106
Chart 3.5: Work range and sensitivity of each sensor used in triaxial instrumentation	110
Chart 3.6: Calibration constants for triaxial instrumentation	110
Chart 4.1: Summary of symbols and lines adopted for each kind of specimen subjected to BE and UPV tests	118

LIST OF ACRONYMS AND ABBREVIATIONS

AC: Alternate Current

ASTM: American Society for Testing and Materials

ABNT: Brazilian Association for Technical Norms

BE: Bender Elements

DC: Direct Current

DDS: Direct Digital Synthesizer

DIP: Dual In-line Packages

GND: Ground of circuits

IC: Integer Circuit

LEGG: Laboratory of Geotechnical and Geoenvironmental Engineering

LVDT: Linear variable differential transformers

PCB: Printed circuit board

PSD: Particle size distribution

Op-amp: Operational amplifier

UFRGS: Federal University of Rio Grande do Sul

UPV: Ultrasound pulse velocity

LIST OF SYMBOLS

- GREEK ALPHABET

Δ : Small changes

Δq : Deviatoric stress ($\sigma_1 - \sigma_3$)

γ : Bulk density; Shear strain

γ_d : Dry density

γ_s : Grain density

$\gamma_{w,0}$: Density of water at temperature of 20°C (0.99821 g/ml)

δ : Infinitesimal changes or increments

$\varepsilon_1, \varepsilon_3$: Strains in directions “1” and “3”

ε_a : Axial strain

ε_r : Radial strain

ε_v : Volumetric strain

φ' : Effective friction angle

n : Porosity

ν, ν' : Poisson's ratio

ρ : Bulk (natural) unit mass

σ : Total normal stress

σ' : Effective stress

$\sigma_1, \sigma_2, \text{ and } \sigma_3$: Principal, intermediate and minor stresses

τ : Shear stress

- ARABIC ALPHABET

B: Bulk modulus

C_c : Curvature coefficient

C_u : Uniformity coefficient

c' : Effective cohesion intercept

c_i : Cement content as a function of mass

c_{iv} : Volumetric cement content

D_{10} : Effective diameter

D_{50} : Mean diameter

d: Day of curing

d_e : BE tip-to-tip distance (effective distance)
 d_{31} : Piezoelectric constant that relates mechanical strains produced by an applied electric field
 E : Elastic or Young's modulus
 E_c : Piezoceramic polarising field
 E_p : Initial depolarising field (piezoceramic)
 e : Void ratio
 e_{max}, e_{min} : Maximum and minimum void ratio
 G : Shear modulus
 G_s : Specific gravity
 G_0 : initial shear modulus (at very-small strains)
 g_{31} : Piezoelectric constant that relates the electrical field produced by a mechanical stress
 L : Length
 M : Constrained modulus
 p' : Stress representation / $p'=(\sigma_1 + \sigma_3)/2$
 q : Stress representation / $q=(\sigma_1 - \sigma_3)/2$
 S_r : Degree of saturation
 t_p : Compressional-wave (or p-wave) travelling time
 t_s : Shear-wave (or s-wave) travelling time
 u : Pore pressure
 V : Total volume
 V_a : Air volume
 V_p : Compressional-wave (or p-wave) velocity
 V_s : Shear-wave (or s-wave) velocity
 V_{sol} : Solid volume
 V_v : Void volume
 V_w : Water volume
 W : Total weight
 w : Water content
 W_s : Weight of solids
 W_w : Weight of water
 Y^E_3 : Piezoceramic elastic modulus

1 INTRODUCTION

The development and globalisation experienced by contemporary societies has raised many questions for the engineering community, especially those concerning limited resources, financial analysis, and environmental issues. Frequently, geotechnical engineers have to deal with soils without adequate features, logistic difficulties (the transportation of high amounts of soil), the high costs involved, and where and how to dispose unwanted soil. As a result, improving local soil through its mechanical, physical, chemical, and biological stabilisation has become an effective option.

Improved soil characteristics can be remarkably influenced in the way they no longer behave like the original material. Consequently, it is the role of geotechnical engineers to understand how those newly created geomaterials will behave under different states of stress and how soil structures may affect their response. Geomaterial behaviour has been associated with the concept of soil non-linearity, a fact that is widely recognised and accepted by the scientific community nowadays. Soil non-linearity is actually a matter of strain ranges: while stiffness is constant at very-small strains ($10^{-3}\%$ for axial strains), it will reduce under larger strains, also known as stiffness degradation (ISHIHARA, 1996; ATKINSON, 2000; CLAYTON, 2011).

Shear strains that regular structures (retaining walls, foundations, and tunnels) impose to soils range between $10^{-2}\%$ and 1%, which represent medium to large strains. Therefore, the range in which stiffness degrades and non-linearity occurs need to be assessed. In order to assess these information, stiffness, strength and strain (at failure), as well as their relationship, need to be analysed. Moreover, the entire stiffness degradation curve, the initial stiffness modulus, which can be measured with bender elements, and the rate of stiffness degradation under different strains by imposing either a load or deformation also need to be measured (ATKINSON, 2000).

BE have been widely used in geotechnical engineering due to their operational simplicity and relative low cost. Moreover, because BE are a non-destructive test, they can be associated with different apparatuses (e.g., triaxial and oedometer cells), which makes them a versatile device (CLAYTON, 2011; YAMASHITA *et al.*, 2009; AIREY; MOHSIN, 2013). BE can

generate and receive shear waves through a soil specimen, allowing shear wave velocity (V_s) evaluation. Consequently, soil stiffness can be assessed through the shear modulus (G) as it is directly associated to the shear wave velocity (V_s). Although it is a simple test to be conducted, BE results interpretation is complex and has been the focus of recent studies (LEE; SANTAMARINA, 2005; ARROYO *et al.*, 2006; WANG *et al.*, 2007; DA FONSECA; FERREIRA; FAHEY, 2009; ALVARADO; COOP, 2012; CAMACHO-TAUTA *et al.*, 2015).

Stiffness obtained through BE tests can be associated or compared to other tests using the same material. Resonant column tests have been commonly compared to BE tests (DYVIK; MADSHUS, 1985; CAMACHO-TAUTA *et al.*, 2015). When installed in a triaxial chamber, BE can obtain shear modulus at very-small strains, which is generally associated to shear modulus degradation (at medium and large strains) obtained by local gauges measurements (e.g., JOVIČIĆ; COOP, 1997). In regard to bench tests, a few studies comparing BE with other equipment have been conducted. As a matter of fact, BE have been compared to ultrasound pulse velocity (UPV) in studies on cement paste and cement-stabilised soils (SILVA *et al.*, 2013; GRANJA *et al.*, 2014).

1.1 RELEVANCE AND RESEARCH JUSTIFICATION

New materials have been sought and developed due to the demand for durable, resistant, stiff, cheap, and environmentally friendly geomaterials. Therefore, the need for a more rigorous understanding of improved soil behaviour is one of the main challenges in the current scientific scenario. Therefore, stiffness degradation of artificially cemented soils has become a relevant research matter.

1.2 OBJECTIVES

The present study has two major objectives. First, it intends to fabricate an operational and user-friendly BE system to be used in bench and triaxial tests, and validate its performance based on the data found in the literature. This goal includes BE fabrication, the development of a signal amplifier, and a data interpretation script. Secondly, it aims to obtain the stiffness degradation curve for artificially cemented Osorio sand.

Besides, two secondary objectives are also investigated: i) stiffness gain over a specific period of cure is evaluated using both BE and UPV devices; and ii) the frequency-dependency of the studied artificially cemented soil is evaluated by comparing BE and UPV results.

2 LITERATURE REVIEW

Geotechnical engineering is primordially concerned with the assessment of two main topics: strength and strain. Strength analysis is usually represented by Mohr's circle (τ x σ) or p' x q diagram. Strain analysis, on the other hand, is dealt with in terms of stiffness. The present work will mainly focus on the latter.

2.1 STRAIN

Specimen deformations occur due to stress, which are usually presented by a normalised formula called strain. Strains can be presented in two different ways: normal (ε) and shear strains (γ). Normal strain leads to actual change in volume or length, while shear strain only distorts a specimen (changes the shape without changing the volume). Changes in length will take place in a direction parallel to load application; whereas, distortions take place in a direction initially perpendicular to load application (LAMBE; WHITMAN, 1979; BUDHU, 2011; SALGADO, 2013).

The application of an axial load will cause a deformation along the axial direction, and then its respective linear or axial strain is presented by Equation (2.1). Assuming the specimen is subject to normal forces on all planes, the specimen will suffer changes in length in all three directions, which will lead to volume strain (Equation (2.2)). The shear stress applied in any direction (" ij ") will generate shear strain, as described by Equation (2.3) (LAMBE; WHITMAN, 1979, p. 122; WHITLOW, 2001, p. 132; SALGADO, 2013, p. 125 and 128).

$$\varepsilon_a = \frac{\Delta L}{L} \quad (2.1)$$

$$\varepsilon_v = \frac{\Delta V}{V} = \varepsilon_a + 2 \cdot \varepsilon_r \quad (2.2)$$

$$\gamma_{ij} = \frac{\delta u_i}{\delta x_j} + \frac{\delta u_j}{\delta x_i} \quad (2.3)$$

Where: " ε_a " and " ε_v " are the normal axial and volumetric strains, respectively (both dimensionless); " Δ " indicates a small variance of the initial length component (L in meters) or volume (V in m^3); " ε_r " is the radial strain when the specimen is cylindrical; " γ_{ij} " is the shear

strain (dimensionless) in regards to directions “ i ” and “ j ”; “ δu_i ” and “ δu_j ” are infinitesimal distortions in the “ δx_j ” and “ δx_i ” directions, respectively.

2.2 STRESS-STRAIN CURVE AND MODULUS

Each material will respond differently to an applied load. That is the reason stress versus strain graphs can provide many insights about the tested material, such as soil composition, compaction, presence of natural or artificial cementation, fibre insertion, stress state, and drainage condition. Figure 2.1- (a) presents results for a medium-fine sand in two different porosity states (dense and loose); the upper curve represents the dense specimen, indicated by its peak, which is expected for low confining stress. On the other hand, the absence of a peak is an expected behaviour of loose granular materials also subjected to low confining stress. Cemented materials, for instance, will present a more brittle behaviour; whereas the insertion of fibres will provide a ductile behaviour. Brittle materials are characterised by a stress-strain linear relationship (at small strains range), followed by a sudden rupture; while ductile materials have also the same stress-strain linear relationship, but is followed by its continuous yielding strains under small increments of stress - Figure 2.1 – b) (LAMBE; WHITMAN, 1979; WHITLOW, 2001; CONSOLI *et al.*, 2007, 2009a).

Granular soils are stress-dependant materials. As such, their features are related to the level of stress applied. Higher confinement stresses provide higher stiffness to the soil (LAMBE; WHITMAN, 1979). On the other hand, cemented soils are not stress dependent at small strains range, as it will be discussed later (see 2.3, and 2.4). Isotropic compression is actually capable of breaking cementation (de-structuring), affecting stress-strain behaviour of cemented soils. Due to that phenomenon, soil behaviour may alter from brittle at low confining pressures, to ductile if under higher confinements (LADE; OVERTON, 1989).

As it can be observed (Figure 2.2), the stress-strain relationship is not always a straight line. In order to classify soil behaviour within a known model, simplifications are usually made. The figure presents a general curve for stress-strain of a soil (a), then two different models for initial strains are included: elastic and rigid; both followed by a perfectly plastic yielding (b and c). Finally, although the concepts of hardening and softening are introduced (d), they are not going to be further discussed, as they are beyond the scope of this study (CRAIG, 2004).

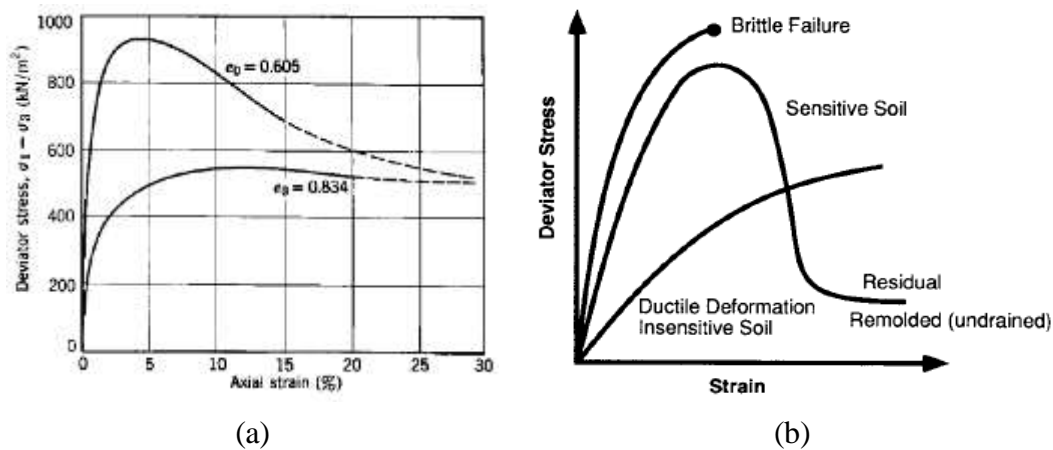


Figure 2.1: Common stress-strain relation for – a) granular soil (fine-medium sand) in dense packing (curve above) and loose density ($\sigma_3 = 207$ kPa); b) materials with different behaviours (LAMBE; WHITMAN, 1979; MITCHELL; SOGA, 2005)

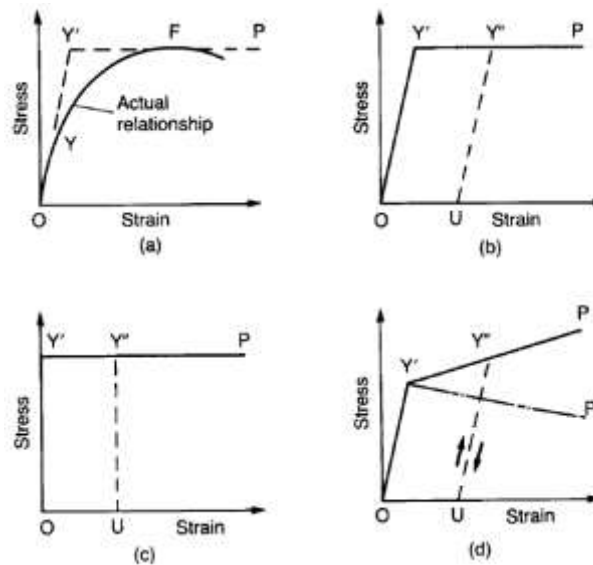


Figure 2.2: Stress-strain relationship – a) typical soil behaviour; b) elastic perfectly plastic model; c) rigid perfectly plastic model; and d) elastic-strain hardening and softening plastic models (CRAIG, 2004)

Soils are usually assumed to be elastic (linear stress-strain relationship) and isotropic (the same properties in any direction) materials. Despite the fact these assumptions are not always valid, at this point they will be accepted, as discussed in 2.4 and 2.7. This supposed linear relationship allows obtaining stiffness parameters called moduli. Stiffness is the ratio of stress to a related strain. For instance, normal stress divided by normal strain is the elastic modulus (Young's modulus, E), and the ratio of shear stress to shear strain is the shear modulus (G). Figure 2.3 presents a scheme for each modulus. It also includes the bulk modulus, which is used for isotropic compression (LAMBE; WHITMAN, 1979).

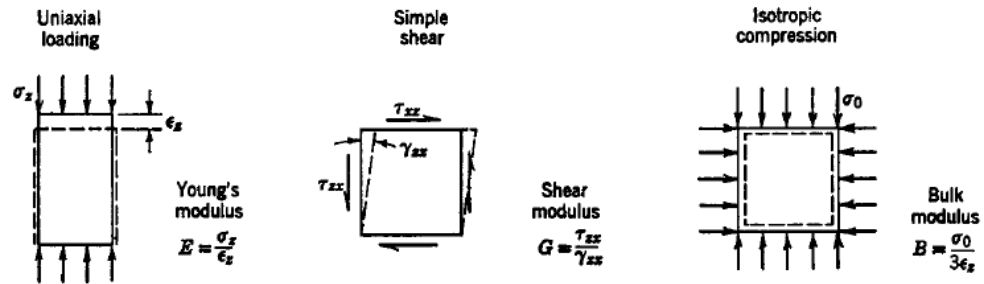


Figure 2.3: Different types of moduli
(based on: LAMBE; WHITMAN, 1979)

This linear behaviour of general materials was developed by Hooke in 1676. Although it was firstly observed for the tensile load applied to a metal bar, this concept was then expanded to other types of loads and geometries. This linear stress-strain relationship represents the pillar of elastic theory; in other words, it means that a certain amount of stress will cause the same level of strain independently of previous loading. In practice, this is only applicable for very-small strain levels (γ and $\varepsilon < 0.001\%$). Additionally, when the soil is assumed to be isotropic and homogeneous (uniform material within constant point to point properties), only two parameters are required in an elastic solution (TIMOSHENKO; GOODIER, 1970; LAMBE; WHITMAN, 1979; BUDHU, 2011; CLAYTON, 2011; SALGADO, 2013).

Usually, the elastic pair to be chosen for elastic analysis is the modulus and Poisson's ratio – taking into consideration that it is valid for isotropic and homogeneous materials. Those parameters are mathematically related to each other, as observed in Chart 2.1. The four most common elastic parameters are presented in the chart (WHITLOW, 2001; SALGADO, 2013).

Chart 2.1: Relationship between elastic parameters for the analysis of homogeneous and isotropic materials

Elastic constant	Elastic pair	
	E, ν	K, G
Young's modulus $E =$	E	$\frac{9KG}{3K + G}$
Poisson's ratio $\nu =$	ν	$\frac{3K - 2G}{6K + 2G}$
Shear modulus $G =$	$\frac{E}{2(1 + \nu)}$	G
Bulk modulus $K =$	$\frac{E}{3(1 - 2\nu)}$	K
Constrained modulus $M =$	$\frac{E(1 - \nu)}{(1 + \nu)(1 - 2\nu)}$	$\frac{3K + 4G}{3}$

(source: SALGADO, 2013)

The constrained modulus (M), which has not been introduced yet, refers to oedometer tests: when a soil is submitted to vertical compression while laterally confined. The elastic pair, including the shear and elastic moduli, or another combination, needs to be measured, and then back calculation can provide the other parameters that were not measured (LAMBE; WHITMAN, 1979; BARDET, 1997; WHITLOW, 2001; BUDHU, 2011; CLAYTON, 2011; SALGADO, 2013).

Poisson's ratio (ν) relates strains generated in a normal direction to strains on the normal plane where the stress is applied, as observed in Equation (2.4). This phenomenon is easily understood for a metal bar stretched in a longitudinal direction, in which case it will be an elongated in the longitudinal direction, while the radial direction will shrink. This parameter relates strain compensations (LAMBE; WHITMAN, 1979; BARDET, 1997; WHITLOW, 2001; BUDHU, 2011; SALGADO, 2013).

$$\nu' = -\frac{\Delta\varepsilon_3}{\Delta\varepsilon_1} = 0.5(1 - \delta\varepsilon_v/\delta\varepsilon_1) \quad (2.4)$$

Where: " ν' " is Poisson's ratio; " Δ " denotes a small variation. Assuming directions "1" and "3" are perpendicular to each other and a normal stress is applied in direction "1", it is possible to say that " ε_3 " is the strain generated in direction "3"; " ε_1 " is the strain in direction "1". Poisson's ratio can be also determined through volumetric strain " ε_v ", as it is " $\Delta\varepsilon_v = \Delta\varepsilon_1 + 2\Delta\varepsilon_3$ ". All parameters described are dimensionless.

Stiffness and Poisson's ratio are not immutable properties of soils. They are in fact state variables of soils that change due to different sets of stresses, densities, drainage conditions, and so on. Typical Poisson's ratio ranges between 0.2 and 0.4 for clean sand in loose and dense states, respectively. Nevertheless, in the present work, a cemented material was investigated and, as a result, the Poisson's ratio is different than that for uncemented materials (LAMBE; WHITMAN, 1979; BARDET, 1997; WHITLOW, 2001).

If an undrained analysis is considered for a saturated body, and water is assumed to be incompressible, Poisson's ratio assumes a value equal to 0.5. That means no volumetric strain exists as the water is incompressible, although an increment in pore pressure would be observed. On the other hand, values greater than 0.5 indicate an expansion, while values smaller than 0.5 would imply a reduction of material volume (LAMBE; WHITMAN, 1979; BARDET, 1997; CRAIG, 2004; BUDHU, 2011).

Due to the linearization of the non-linear (natural) behaviour of soils, their stiffness can be obtained in terms of tangent modulus or secant modulus. Both values are expected to be equal only at very-small strain ranges, when the tangent modulus is called initial tangent modulus. The tangent modulus is obtained by the slope of a line tangent to the real stress-strain curve, as indicated in Figure 2.4. On the other hand, the secant modulus is obtained by the slope of a line between two separated points on the curve (LAMBE; WHITMAN, 1979). Most authors consider the secant modulus between the origin of the axes and any other point on the curve (BARDET, 1997; WHITLOW, 2001; MITCHELL; SOGA, 2005; BUDHU, 2011).

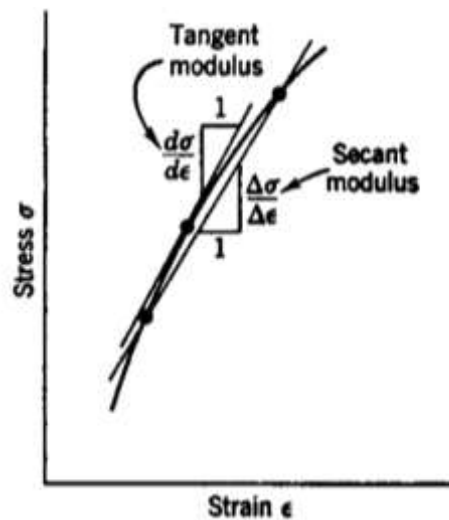


Figure 2.4: Distinction between the tangent and secant modulus of a non-linear material (LAMBE; WHITMAN, 1979)

2.3 CEMENTATION BONDING

Soils can be naturally cemented due to chemical reactions such as carbonates or oxides precipitation. When lightened cemented material remains at the same location under the influence of the weather, it is called residual soil. Soils can also be artificially cemented through the addition of cement or lime. The main result of both kinds of cementation is that the saturated soil can resist tensile and shear stress at zero confinement; besides, cemented soils are stiffer than non-cemented counterparts (MITCHELL; SOGA, 2005; BUDHU, 2011; SALGADO, 2013). Figure 2.5 presents a comparison between uncemented and cemented soil particles; based on this figure and related studies (e.g. CHANG; WOODS, 1992), it is clear that cementation also increases contact areas between soil particles.

Chang and Woods (1992) investigated cementation chemical bonds affecting shear modulus of granular soils. Their findings indicate a gain in shear modulus due to cementation, and also an increment in shear modulus as cement content increases (both results are endorsed by other authors, e.g.: LADE; OVERTON, 1989; AIREY, 1993; COOP; ATKINSON, 1993; HUANG; AIREY, 1998; SANTAMARINA, 2001; MITCHELL; SOGA, 2005). A significant factor affecting stiffness is the number of particle contacts, since those contacts might be bonded together by cementation. Therefore, particle distribution, and particle size and shape have great impact on particle packing and in their bonding. As the cementation reaction occurs, hydrate cement gradually starts filling the voids (CHANG; WOODS, 1992; COOP; ATKINSON, 1993; CLAYTON *et al.*, 2010).

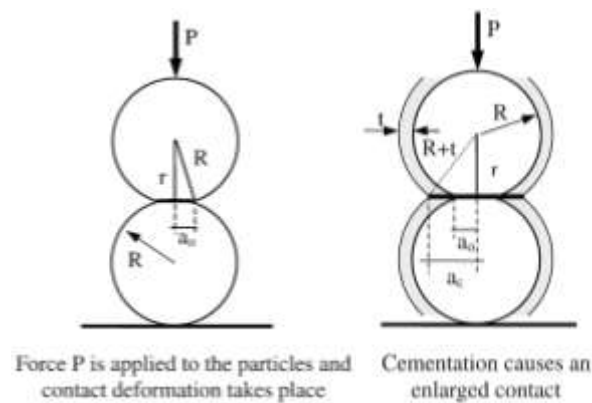


Figure 2.5: Comparison of an uncemented soil (left) and a cemented soil (right). The soil particles are here represented by spheres for simplification purposes (FERNANDEZ; SANTAMARINA, 2001)

From a microstructure point of view, the cementation process of granular media can be separated into three stages (CHANG; WOODS, 1992), as indicated in Figure 2.6. First, the cement partially covers the grain surface and some chemical bonding start to take place (zone I); the cement fills about 20-25% of the voids. Then, significant contact bonding entails (zone II), and 20-25% to 60-80% of the voids are filled by the cement. Finally, the cement fills 80-90% of the voids (zone III), chemical bonds are completed, and any remaining amount of cement will simply function as a filler. As the amount of cement was not mentioned, it is important to keep this process in mind as an exercise just for its comprehension. Hydrated cementation is usually followed by stiffness measurements, as observed in the work of Silva *et al.* (2013).

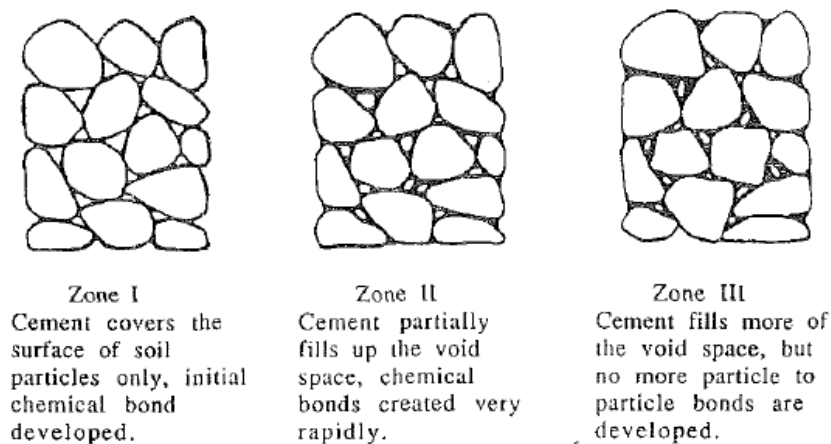


Figure 2.6: Phases of the cementation process in a granular media (CHANG; WOODS, 1992)

Particle-to-particle contact area bonding hold the particles together when tensile forces are applied. At zero effective stress, a cemented soil can resist shearing because it will have a real cohesive intercept (due to cementation) in Mohr's circle or $p' \times q$ diagram. Apart from such improvement, care must be exercised when considering cementation in a project, since bonds will break at certain levels of strain, returning to an uncemented soil behaviour (CRAIG, 2004; MITCHELL; SOGA, 2005; BUDHU, 2011; SALGADO, 2013).

This breakdown takes place due to both shear and volumetric strain. However, at small strain levels ($<0.001\%$), cementation starts being mobilized as cementation continuously degrades as the strain increases until most interparticle bonds are broken. By keeping the analysis in the small strains range, besides strength enhancement, cementation considerably improves stiffness. It may be concluded that cementation is more evident and effective at small strains, once at large strains it behaves like uncemented materials (CHANG; WOODS, 1992; MITCHELL; SOGA, 2005; BUDHU, 2011; SALGADO, 2013).

There are some specific factors that only affect the behaviour of cemented soils because of the addition of a cementitious agent. These include the degree of cementation, chemical bonding uniformity across contact areas, curing conditions (or the formation of naturally cemented soils), and the type of cementation (CONSOLI *et al.*, 2000, 2006, 2011; ROTTA *et al.*, 2003; BUDHU, 2011). There are studies on the type of cementitious agent (Ismail *et al.*, 2002), which investigated their effect on the response to shearing of calcareous soils. In the present study, cementation using Portland cement will be the only one to be addressed. A real example of hydrated Portland cement chemically bonding particles to calcareous sand (from the Western region of Australia) can be observed in Figure 2.7.

Historically, the term cement has been used for any bonding material. In fact, Portland cement is composed by a dry mixture of pulverized clinkers (crystalline hydraulic calcium silicate) and small amounts of calcium sulphate and limestone (up to 5%). Moreover, the addition of water is required to chemically trigger its bonding properties; a process called hydration. Fifty to sixty percent of the volume of Portland cement is composed by calcium silicates, which is mostly responsible for its adhesive characteristics when mixed to water. After hydration, the final components become stable in the aqueous environment and, as a result, Portland cement is classified as a hydraulic cement (MEHTA; MONTEIRO, 2014).

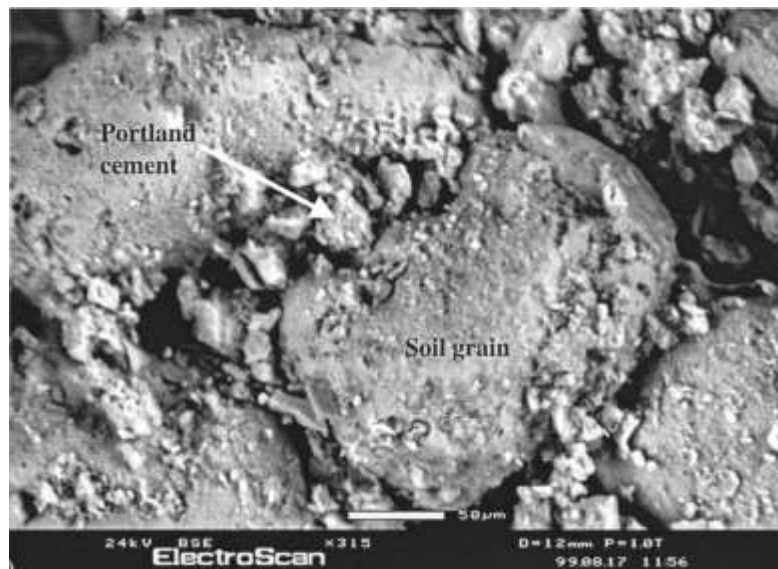


Figure 2.7: Scanning electron microscopy image of calcareous sand with the addition of 8% Portland cement (in relation to the dry mass of the soil) (ISMAIL *et al.*, 2002)

There are four main solid elements present in a hydrated cement paste: calcium silicate hydrate, calcium hydroxide ($\text{Ca}(\text{OH})_2$), calcium sulfoaluminate hydrates, and dehydrated clinker grains, all of which can be identified by scanning electron microscopy. As indicated before, the first element represents the major part of the solid volume formed during hydration, and is mostly responsible for the long-term strength and durability of the cement paste. Its structure is not completely known, and is usually referred as C-S-H crystals in a colloidal dimension. The second and third elements represent 20-25% and 15-20%, respectively, of the total volume of solids in a hydrated paste. Due to its small surface area, calcium hydroxide contributes very little to strength (MEHTA; MONTEIRO, 2014).

2.4 STIFFNESS DEGRADATION OF GEOMATERIALS

The understanding of soil non-linearity was one of the most important accomplishments of geotechnical engineering in the last 40 years. The concept of non-linearity has also brought to light the strain dependence (magnitude rather than rate) of soils (ATKINSON, 2000). According to Clayton and Heymann (2001), contemporary geomaterial models are quite sophisticated, due to the inclusion of recent concepts such non-linear elasticity and recent stress history effects.

Although natural soils are known as anisotropic materials, isotropy is usually assumed during regular analysis. Another simplification would be to consider a soil as an elastic body. As presented before, soils possess a unique linear relationship between stress and strain. However, from a quick look at Figure 2.1 – a) an insight that this assumption is not actually accurate can be gained. In fact, soils non-linearity is already known, and some more realistic models have been developed over the years to capture their behaviour. Experimentally based and non-linear attempts dating from the 19th century include the parabolic model by Hodgkinson, the hyperbolic model by Cox, and the non-linear exponential model by Bach (ATKINSON, 2000; CLAYTON, 2011).

Before continuing the discussion on soil non-linearity, it is important to define stiffness formally. Clayton (2011, p. 6) described stiffness as “the resistance of that body to deformation under applied force (*sic*),” which stems from the shape of the analysed body, the boundary conditions, and intrinsic characteristics of the material. Nevertheless, the author separates the analysis into two strain levels: very-small strains, where stiffness parameters can be assumed to be constant; and greater strains (small to large strains), where stiffness decreases with increasing strain.

At very-small strain levels, stiffness depends upon many factors, such as: void ratio; grain characteristics (mineralogy, particle size, angularity, and roughness); soil fabric and particle arrangement (interparticle contact for granular material); stress state (especially the effective stress for uncemented materials); stress history; discontinuities; and loading rate. The very-small strain levels are represented by the horizontal straight part of the line in the stiffness curve in Figure 2.8. As it can be observed, at larger strains, stiffness starts to degrade. Consequently, other factors different from those aforementioned should be considered in the

analysis: strain level; loading path, and all the changes happening in the loading path; effective stress, and loading rate; recent stress history; and de-structuring (CLAYTON, 2011).

The straight part of the curve in Figure 2.8 follows linear elasticity, from which soil parameters may be obtained through dynamic methods usually based on wave propagation through the soil. The velocity of waves associated to the bulk unit mass will result into the so-called small-strain stiffness (G_0 or E_0). This is the maximum value for the modulus, and it is constant at this range of strains, and are known as maximum shear or Young's modulus, G_{max} or E_{max} (LAMBE; WHITMAN, 1979; ATKINSON, 2000; CLAYTON, 2011).

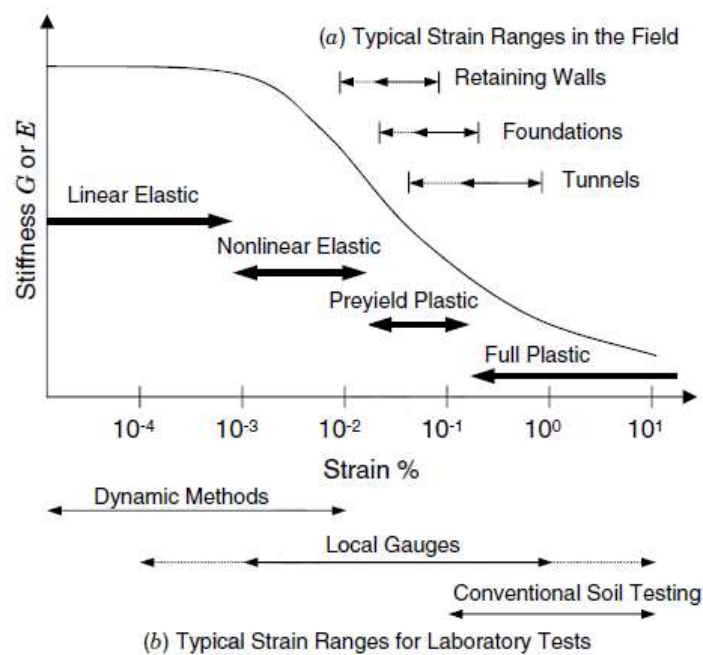


Figure 2.8: Characteristic stiffness degradation curve including – a) strain levels typically observed in the field; b) laboratory tests for stiffness measurement at different strain levels (MAIR, 1993 and ATKINSON, 2000 *apud* MITCHELL; SOGA, 2005)

Among the dynamic methods available for small-strain modulus procurement are bender elements and resonant column. Besides those, Clayton (2011) also presents a non-dynamic possibility: advanced triaxial tests. Progress in instrumentation resolution, and improvements both in equipment and practices, have taken regular triaxial tests to a new level with reliable results for small-strains currently being obtained. This improvement occurred mainly due to the insertion of local strain measurement devices, such as LVDTs (linear variable differential

transformers) and the Hall effect sensor (CLAYTON, 2011). This methodology has been employed for small-strain stiffness assessment over the years by many authors (e.g. CUCCOVILLO; COOP, 1997; CLAYTON; HEYMANN, 2001; GASPARRE *et al.*, 2014), using many types of materials.

In fact, in the eighties, local gauges came to solve problems associated to bedding (accommodation between platens, porous stones and soil), setting errors, and misalignments between pistons and the platen in triaxial chambers. Those errors contributed to the misguided perception that dynamic methods lead to an initial modulus different than those obtained through static loads (ISHIHARA, 1996; ATKINSON, 2000; CLAYTON, 2011). Another factor mentioned by Lambe and Whitman (1979) regard oedometer tests, whose initial loads increments were too large, generating strains that went beyond linear elastic limits. Nevertheless, comparisons between any larger strains and small-strain methods could never be established. In conclusion, Atkinson (2000) states that dynamic and static stiffness are reunited since the non-linearity of geomaterials has been acknowledge and better understood.

Bardet (1997) adds that elastic properties of soils (which include strains at very-small level) are also influenced by water content, temperature, and time. When analysing Young's modulus, water content interferes with the results, and the analysis should address either drained or undrained cases. For shear modulus, however, due to water non-resistance to shearing forces, the same value for both drained and undrained conditions is assumed (CLAYTON, 2011). According to Hardin and Richart (1963), the differences due to changes in mass density resulting from saturation would be small. Furthermore, Lambe and Whitman (1979) state that undrained Young's modulus at very-small strains is three times the corresponding shear modulus at same strain level. This can be easily understood through the relation between G and E in Chart 2.1 ($G = E/2(1 + \nu)$), where Poisson's ratio under undrained conditions is equal to 0.5 – for a linear-elastic and isotropic material.

Small stress increments at very-small strain ranges only results in the elastic deformation of particles, i.e., with no sliding among particles (LAMBE; WHITMAN, 1979; MITCHELL; SOGA, 2005; SALGADO, 2013). Particle arrangement, also known as interparticle contact stiffness, has great impact in the response of granular soil. In fact, interparticle stiffness is effective stress dependant, i.e., the higher the confinement stress, the stiffer the soil response (LAMBE; WHITMAN, 1979; CLAYTON, 2011).

Stiffness stress-dependant behaviour can be observed in Figure 2.9 – a), in which the dashed lines represent an uncemented granular soil under several levels of stress. However, the interparticle stiffness can be removed due to cementation, as observed in Figure 2.9 – b), in which G_0 does not present a significant increase with the increment of stress (FERNANDEZ; SANTAMARINA, 2001; SANTAMARINA, 2001; CLAYTON, 2011). Figure 2.9 – a) highlights the gain in G_0 due to cementation. It also indicates a unique relation between G_0 and the void ratio curves, which is stress independent. The cementation of this specific soil is actually obtained through methane hydrate depositions. For further details see Clayton *et al.* (2010).

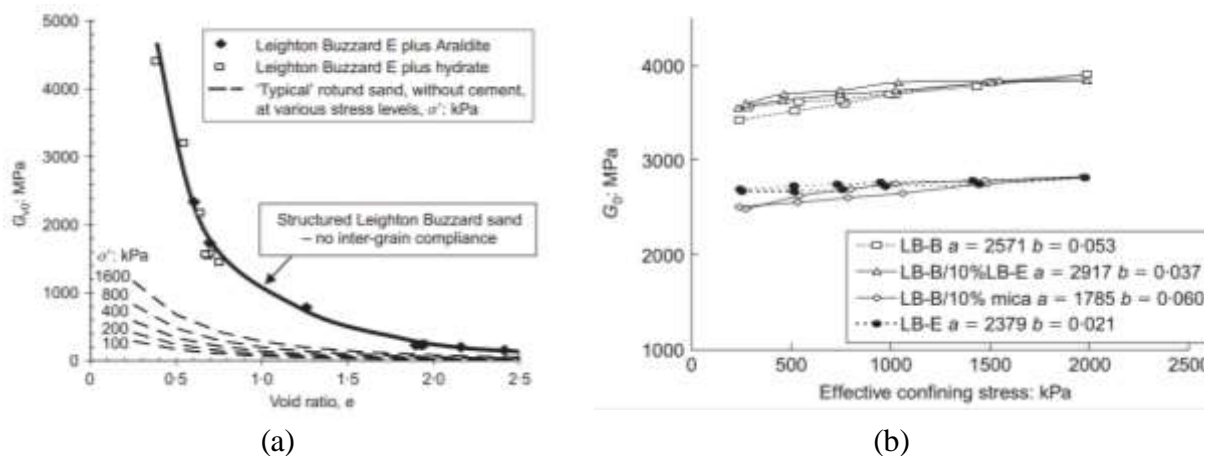


Figure 2.9: Effect of cementation in G_0 – a) gain in initial shear modulus due to cementation (bold line); b) stress independence of a cemented soil (only cemented soil is presented) (CLAYTON, 2011; CLAYTON *et al.*, 2010)

Cementation gradually degrades due to increments in stress or strain. Therefore, its contribution is assured as long as yielding is prevented. Bonding breakage directly affects stiffness; from the first yielding, the shear modulus starts to degrade, and its behaviour starts to converge towards the expected behaviour of an uncemented material, a fact observed for both monotonic and cyclic triaxial loadings. Likewise, yielding can occur even during isotropic compression at high confining stresses. At intermediate stress levels, however, yielding occurs in the initial stages of shearing (AIREY; FAHEY, 1991; COOP; ATKINSON, 1993; CUCCOVILLO; COOP, 1997; SHARMA; FAHEY, 2003).

Based on this transition from cemented to uncemented behaviour, Fernandez and Santamarina (2001) proposed two control regions presented in Figure 2.10. The upper left side of the figure

is the region controlled by cementation, while the bottom right is the uncemented region. A cemented material is initially situated in the cemented region, and its position depends on the cement content and initial modulus. In this region, stiffness is stress-independent, as the flat lines indicate; it means that no change occurs in the modulus due to stress increment. Then, as stress increases, bonding starts to break down and soil stiffness gradually becomes stress-dependent (lines start sloping). This behaviour will continue until the dividing line is reached, after which the soil will present an uncemented behaviour.

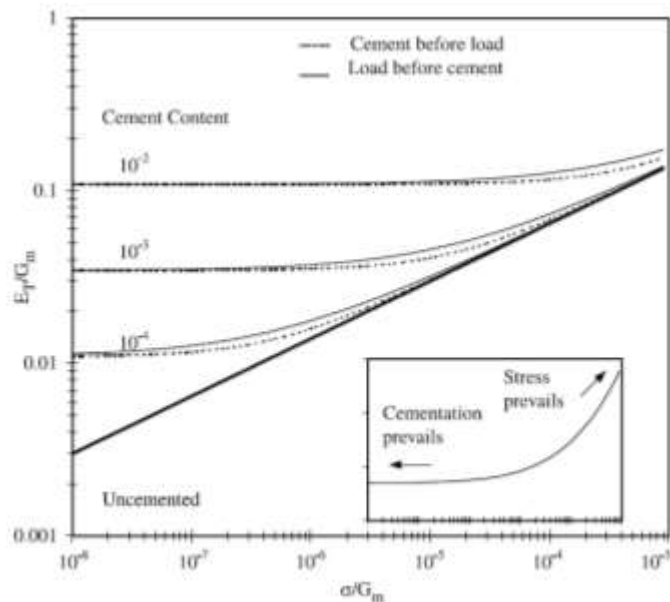


Figure 2.10: Two different control regions for the behaviour of cemented and uncemented soils when loaded (FERNANDEZ; SANTAMARINA, 2001)

Prior to yielding, a cemented material is considered as being elastic, and with no breakdowns. Therefore, cementation has been related to three main regions: no breakdown; stable breakdown; and rapid breakdown. These are associated to the following responses, respectively: elasticity without increment in pore pressure; pore pressure is generated, and stabilization occurs; and pore pressure increases until failure (SHARMA; FAHEY, 2003). These phenomena could be explained by internal deformation at different ranges of strain. At small strains, particles are still in contact and the soil structure is constant. On the other hand, large-strain usually implies major volume or pore pressure changes (for drained and undrained conditions), and soil structure modifications are expected as well (SANTAMARINA, 2001).

Figure 2.11 illustrates two stiffness degradation curves for the same material, with and without cementation, exemplifying what has been discussed previously. The cemented material is initially much stiffer, then it degrades until reaching the uncemented degradation curve. Hence, although the contributions of cementation are very expressive at small strains, they are almost negligible at large strains (SALGADO, 2013; ALVARADO *et al.*, 2012). At this point, it would be important to highlight that Coop and Atkinson (1993) stated that comparisons between cemented and uncemented soils are only possible if soils have the same particle size distribution and states.

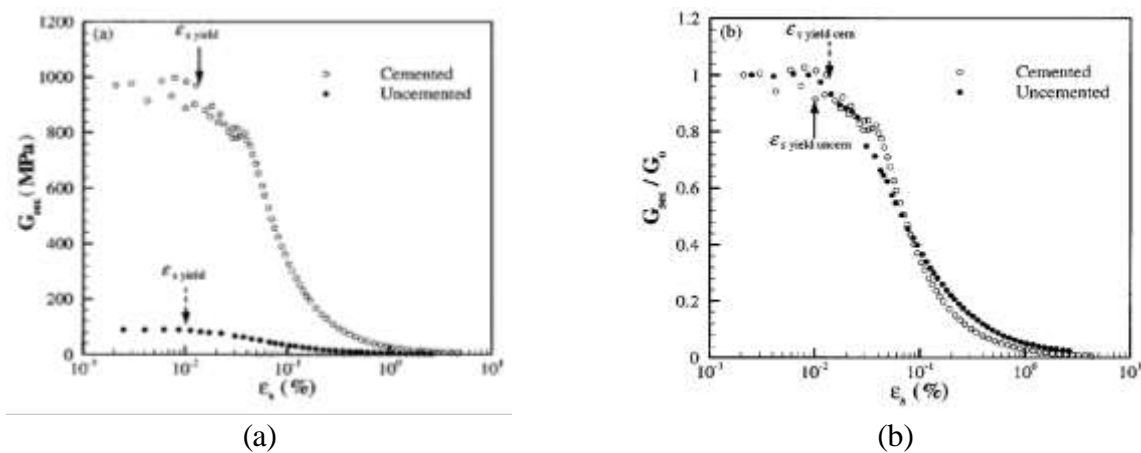


Figure 2.11: Comparison of stiffness degradation between a fine-grained offshore cemented and uncemented calcareous soil ($\sigma'_3 = 200$ kPa; $\gamma_d = 11.5$ kN/m³) – a) secant shear modulus; b) normalization of the modulus by its initial shear modulus (SHARMA; FAHEY, 2003)

Stiffness degradation occurs at certain levels of strain, and then its behaviour is no longer linear-elastic. At this point, soils start an elastoplastic path, requiring different analytical approaches. Figure 2.12 illustrates the associated phenomena, soil response, and interpretation method within strain ranges (options for cyclic conditions). At medium and large strains, the soil can be interpreted as a viscoelastic material. The main differences between elasticity and viscoelasticity are related to the fact that viscous elements are both time-dependant and capable of energy dissipation (KARASUDHI, 1991; ISHIHARA, 1996; BARDET, 1997).

As a matter of fact, linear elasticity and viscoelasticity are completely opposite theories, and the majority of materials behave in between these axioms. Elastic materials store energy with no dissipation; whereas viscoelasticity proposes the storage and dissipation of part of the input

energy. Therefore, viscoelastic analysis can be simplified to a linear relationship between stress and strain, superimposed by the measurement of its energy dissipation capability. The damping ratio comes to fill in this need to measure the dissipated energy. Moreover, viscoelastic materials are rate dependent, i.e., the soil behaviour is rate dependent (KARASUDHI, 1991; ISHIHARA, 1996; BARDET, 1997).

Shear strain	10 ⁻⁶	10 ⁻⁵	10 ⁻⁴	10 ⁻³	10 ⁻²	10 ⁻¹
	Small strain	Medium strain		Large strain	Failure strain	
Phenomena	Wave propagation, vibration		Cracks, differential settlement		Slide, compaction, liquefaction	
Elastic	[Graph: Linear increase in stress with strain]			[Graph: Non-linear increase in stress with strain]		
Elasto-plastic	[Graph: Linear increase in stress with strain up to a point, then non-linear increase]					
Failure	[Graph: Linear increase in stress with strain up to a point, then sharp drop]					[Graph: Non-linear increase in stress with strain]
Effect of load repetition	[Graph: Stress increases with strain, but lower for repeated loading]					
Effect of loading rate	[Graph: Stress increases with strain, but higher for faster loading rate]					
Constants	Shear modulus, Poisson's ratio, damping				Angle of internal friction,	
Model	Linear elastic model		Visco-elastic model		Load history tracing type model	
Method of response analysis	Linear method		Equivalent linear method		Step-by-step integration method	
Laboratory measurement	Wave propagation, precise test [Graph: Stress vs strain]					
	Resonant column, precise test [Graph: Stress vs strain]					
	Repeated loading test [Graph: Stress vs strain]					

Figure 2.12: Soil behaviour within the strain-range dependency, associated phenomena, theoretical models, and laboratory measurements (based on: ISHIHARA, 1996)

Viscoelasticity is an option to address stiffness degradation (at medium strains) through dynamic methods. However, the energy required to dynamically produce this level of strain is high and is usually associated with instability. On the other hand, repeated loading at low frequency is suitable for these measurements, and does not require any theory to interpret system response, as parameters are obtained directly (KARASUDHI, 1991; ISHIHARA, 1996; BARDET, 1997). Strain dependence is a controversial issue among authors. Some

researchers present soils as strain-magnitude dependant rather than strain-rate dependant. For instance, Atkinson (2000) generalized his claims for all kinds of soils, while the results obtained by Airey and Fahey (1991) for calcareous soil demonstrated the effect-rate independence. On the other hand, significant outcomes endorsing strain-rate dependence has also been obtained for stiff clays (Gasparre et al., 2014) and sandy soils (Lo Presti et al., 1997).

The non-linear stiffness degradation can also be described by the hyperbolic model, presented for the first time in the 19th century. As the name indicates, soil non-linearity is described by a hyperbole on a stress plane versus the corresponding strain (shear stress and strain). For further details, see Duncan and Chang (1970). Santamarina, Klein and Fam (2001) also present this methodology with a different approach, pointing out the difference between the tangent and secant moduli.

2.5 WAVES IN GEOMATERIALS

Waves are classified as dynamic events due to its velocity during loading application. When their amplitudes are small enough, they can also present an elastic relationship. However, equilibrium equations are replaced by motion equations when dealing with wave propagation. Waves can be understood as the irradiation of stress and strain with a finite propagation velocity. When travelling through an elastic medium, different wave formats and characteristic velocities may be present (TIMOSHENKO; GOODIER, 1970).

There are two types of elastic waves: surface waves and body waves. Surface waves are usually used in geotechnical site characterization, as they generally propagate along the interface between two different materials, or on their surface, as their name indicate. On the other hand, body waves travel through the material, and their features depend only upon the density and stiffness of the body. The latter is regularly used in laboratory tests and is subdivided into two different kinds of waves travelling at different velocities (RICHART; WOODS; HALL, 1970; BUDHU, 2011; CLAYTON 2011):

- a) P-wave (primary wave, compression wave, dilatational wave),
 - propagates at V_p velocity (Figure 2.13 – a));
 - first wave arriving;
 - particles move in the same direction of wave propagation;

- induces volumetric strains;
 - dependence on volumetric compressibility of both water and soil skeleton pore;
 - proportional to the constrained modulus (M);
 - its velocity is proportional to the undrained volumetric stiffness, as its dominant frequencies avoid drainage;
- b) S-wave (secondary wave, shear wave, distortional wave),
- propagates at $V_{s,hh}$ and $V_{s,vh}$ velocities (Figure 2.13 – b) and c));
 - second wave arriving, after compressional waves;
 - particles move transversally to wave propagation;
 - induces distortions, i.e., changes in shape with no changes in volume;
 - water presence independent;
 - proportional to shear modulus (G);
 - its velocity is only a function of soil density (bulk unit mass).

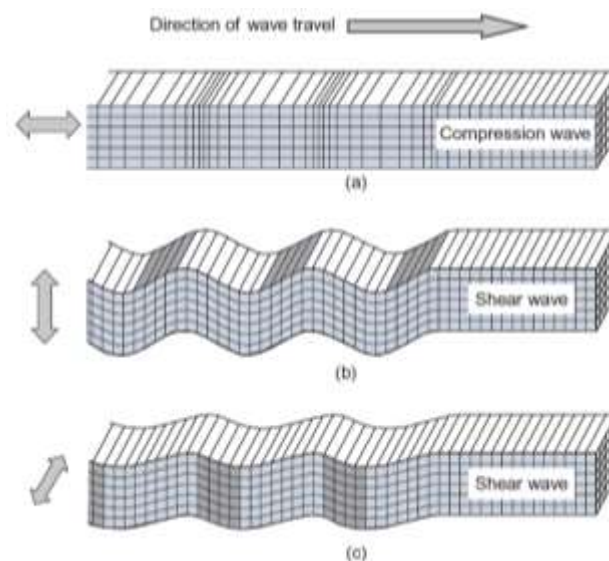


Figure 2.13: Body waves – a) compressional wave (V_p); b) vertical shear wave with horizontal propagation ($V_{s,hv}$); c) horizontal shear wave with horizontal propagation ($V_{s,hh}$) (CLAYTON, 2011)

There are some criticisms concerning p-waves obtained from *in situ* tests. Saturated soils close to the surface typically produce compressional wave velocities close to 1,500 m/s, which imply that the respective undrained bulk modulus (calculated from this velocity) is similar to the bulk modulus for water only. Therefore, the measurement of volumetric skeletal

stiffness cannot be obtained, making p-waves a poor option (MITCHELL; SOGA, 2005; CLAYTON 2011).

Likewise, s-waves also present some issues. Sometimes, its first arrival is masked by the primary wave, leading to travelling time overestimation. Other factor regarding shear wave measurements concerns the phenomenon known as near-field effect (see 2.5.1.2). The near-field effect is understood as the merge of both shear and compression waves inside a body mass, generating shear waves (particles moving transversally to wave propagation) travelling at p-wave velocity. Moreover, there is electromagnetic merging (also known as crosstalk), which can become a real issue if transducers are not adequately grounded (SÁNCHEZ-SALINERO; ROESSET; STOKOE, 1986; SANTAMARINA; KLIEN; FAM, 2001; LEE; SANTAMARINA, 2005; MITCHELL; SOGA, 2005; CLAYTON 2011).

P-waves and s-waves can be generated and measured with different types of equipment in the laboratory. In the present study, two devices were used: bender elements (BE) and ultrasonic pulse velocity (UPV). Assuming that wave velocities can be measured, they can be associated to bulk unit mass to obtain soil stiffness parameters. P-wave velocity is associated with the constrained modulus (M) with Equation (2.5); whereas s-wave velocity is associated to shear modulus (G) with Equation (2.6). It is important to mention that these equations are only valid for continuous, elastic, isotropic and homogeneous media (SANTAMARINA; KLIEN; FAM, 2001; MITCHELL; SOGA, 2005; CLAYTON, 2011).

$$M = \rho \cdot V_p^2 \quad (2.5)$$

$$G = \rho \cdot V_s^2 \quad (2.6)$$

Where “ ρ ” refers to the bulk (natural) unit mass of the specimen. Even though water presents no shear resistance, the total mass of the specimen should be used. S-wave can only travel through a medium that presents shear resistance and, therefore, it is filtered in fluids. On the other hand, p-wave propagates through fluids and solids, being filtered only in vacuum (RICHART; WOODS; HALL, 1970; LAMBE; WHITMAN, 1979; SANTAMARINA; KLIEN; FAM, 2001; MITCHELL; SOGA, 2005).

Both BE and UPV use specific transducers to measure the time that a specific wave takes to propagate through a soil, i.e., the difference in time between the sent and the received waves.

Therefore, by knowing the distance between transducers, it is possible to calculate wave velocities with Equations (2.7) and (2.8).

$$V_p = \frac{d}{t_p} \quad (2.7)$$

$$V_s = \frac{d}{t_s} = \frac{d_e}{t_s} \quad (2.8)$$

Where “ V_p ” and “ V_s ” are the p-wave and s-wave velocities, respectively; “ t_p ” and “ t_s ” are p-wave and s-wave travelling time through the soil; “ d ” is the distance between UPV transducers; “ d_e ” is the effective BE tip-to-tip distance.

The ratio between the two velocities (V_p/V_s) is affected whether the soil is dry, wet or fully saturated. As presented before, shear velocity is not affected by water content, because s-waves cannot travel through water. P-waves, on the other hand, can travel through water and its value is very susceptible to water content. In fact, even small additions of air into a saturated body can result in significant decreases in p-wave velocity. The reason for this is the fact that p-wave velocity is dependent on the saturation, porosity and elastic properties of the soil skeleton and water present in the soil (MITCHELL; SOGA, 2005).

Tsukamoto *et al.* (2002) compared p-waves and s-waves to B-value (saturation parametre) increments on loose Toyoura sand (Figure 2.14). While s-wave velocity was constant with different B-values, p-wave velocity, on the other hand, decreased from 1,700 m/s to 500 m/s with B-values ranging from 0.90 to 0.05, corresponding to a small change in the degree of saturation (S_r) from 100% to 90%. For a dry body, however, V_p/V_s ratio is considered constant as the water content is zero. Adapting M and G equations presented in Chart 2.1, and using Equations (2.5) and (2.6), V_p and V_s can be related to Poisson’s ratio through Equation (2.9). Considering a Poisson’s ratio equal to approximately 0.1, the V_p/V_s ratio assumes a value of 1.5 (LEE; SANTAMARINA, 2005).

$$\frac{V_p}{V_s} = \sqrt{\frac{2 \cdot (1 - \nu)}{1 - 2 \cdot \nu}} \quad (2.9)$$

It is important to mention that the points raised here are valid for elastic waves travelling through an ideal medium (continuous, elastic, isotropic and homogeneous). Otherwise, the

literature must be reviewed for a suitable solution. For instance, Santamarina, Klein and Fam (2001) present solutions for a particulate media, and also discuss anisotropy.

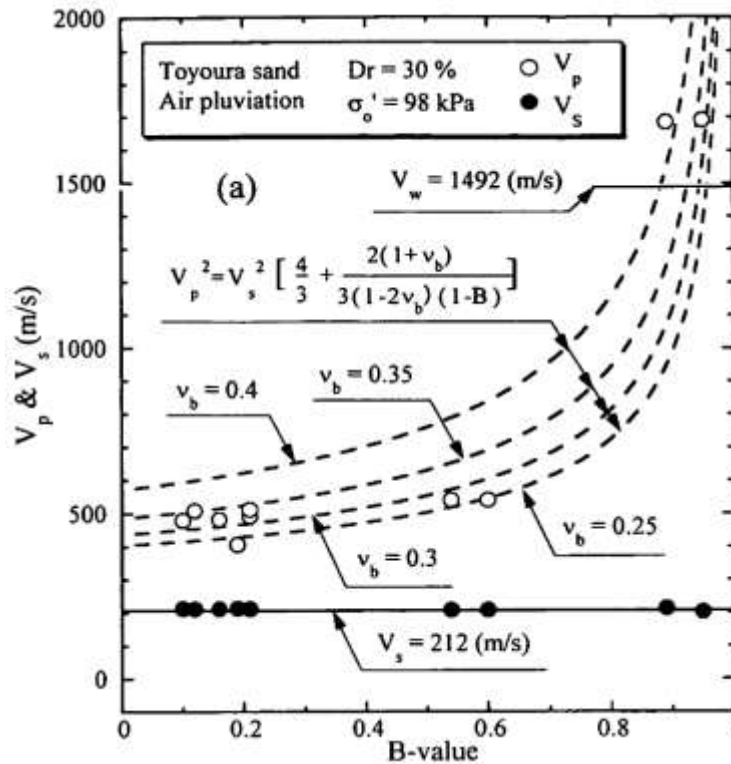


Figure 2.14: Velocity variation of p-waves (V_p) and s-waves (V_s) with increasing B-value for loose Toyoura sand ($D_r=30\%$) subjected to an effective isotropic pressure of 98 kPa (TSUKAMOTO *et al.*, 2002)

Moreover, because those moduli are obtained through wave propagation, which imposes strains within the elastic range, they are associated to the stiffness at very-small strains or, at least, to stiffness obtained by means of very-small strains. This second option can be illustrated by the propagation of a wave through a soil natural deposit, which provides “indirect information regarding the state and natural soil structure” (MITCHELL; SOGA, 2005, p. 447). Considering a natural deposit might be already loaded, and its range of strains no longer correspond to the elastic range, Equations (2.7) and (2.8) cannot be used directly because their application is based on the assumption of isotropic elasticity. As discussed before (2.4), strains beyond the linear range require a new model of interpretation (viscoelasticity model). However, waves propagating through viscoelastic materials are

frequency dependent (MITCHELL; SOGA, 2005) and new solutions have to be used – Santamarina, Klein and Fam (2001) also provide solutions for viscoelasticity models.

The following two sections (2.5.1 and 2.6) present the two devices (BE and UPV) used to assess soil stiffness through wave propagation in the present work. Although these devices are capable of transmitting and receiving waves, the main difference between them is the frequency range each one vibrates (Figure 2.15). While BE vibrates at the audible spectrum, UPV vibrates at higher frequencies, beyond human capability to detect sound.

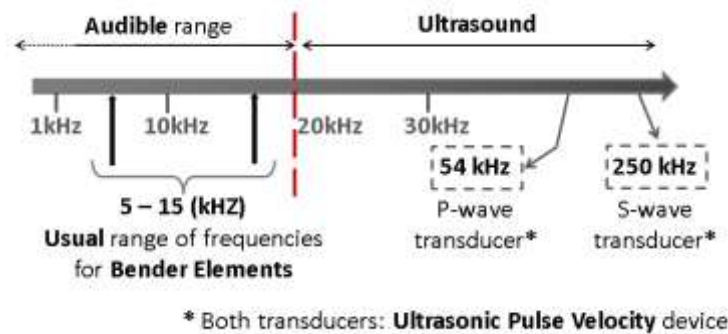


Figure 2.15: BE and UPV work frequency ranges

2.5.1 Bender elements (BE)

BE are capable of assessing shear wave velocity and, therefore, the initial shear modulus (G_0), by generating and receiving shear waves through a soil specimen in laboratory tests. It was initially used in marine sediments by Shirley and Hampton (SHIRLEY; HAMPTON, 1978; SHIRLEY, 1978). Since then, it has become increasingly popular and applied to many kinds of soils, from clays (VIGGIANI; ATKINSON, 1995a) to stiffer soils (CARRARO; PREZZI; SALGADO, 2009; GASPARRE et al., 2014, ALVARADO *et al.*, 2012). Despite their particularities, such as BE-soil coupling for cemented materials, BE is still suited the purpose in every case.

Other reasons for BE popularization are its operational simplicity, relatively low cost, capacity to determine soil mass anisotropy, and it is a non-destructive test with a wide range of applications with different apparatuses (CLAYTON, 2011; YAMASHITA *et al.*, 2009; AIREY; MOHSIN, 2013). Given the fact that BE can be placed inside triaxial chambers, it can track special phenomena such as curing under stress (SILVA *et al.*, 2013). On the other

hand, BE results interpretation has been an important concern in recent papers (VIGGIANE; ATKINSON, 1995; JOVIČIĆ; COOP; SIMIĆ, 1996; LEE; SANTAMARINA, 2005; ARROYO *et al.*, 2006; WANG *et al.*, 2007; DA FONSECA; FERREIRA; FAHEY, 2009; ALVARADO; COOP, 2012; CAMACHO-TAUTA *et al.*, 2015; O'DONOVAN *et al.*, 2015), which is dealt with in detail in 2.5.1.3.

The maximum estimated shear strain achieved by BE is 10^{-5} , giving support to the hypothesis that BE generate elastic waves, and validating the use of Equation (2.6). This is possible due to the fact that BE is made of piezoceramics, an electro-mechanical transducer capable of converting movement (mechanical energy) into electrical energy, and vice-versa. Depending on its wiring, it can become more sensitive to mechanical or electrical impulses (DYVIK; MADSHUS, 1985).

Piezoceramics are multilayered materials. Two very thin piezoceramic layers are rigidly bonded by a metallic shim, and their surfaces are covered by a conducting material. When wired in series (see Figure 2.16 – a), it is very effective in transforming mechanical movement into electrical excitation (generator), and should be used as a receiver. On the other hand, the parallel connection is more effective in converting electrical into mechanical energy (motor), being more indicated to transmit waves, as presented in Figure 2.16 – (b) (DYVIK; MADSHUS, PIEZ1985; PIEZO SYSTEMS, 2015).

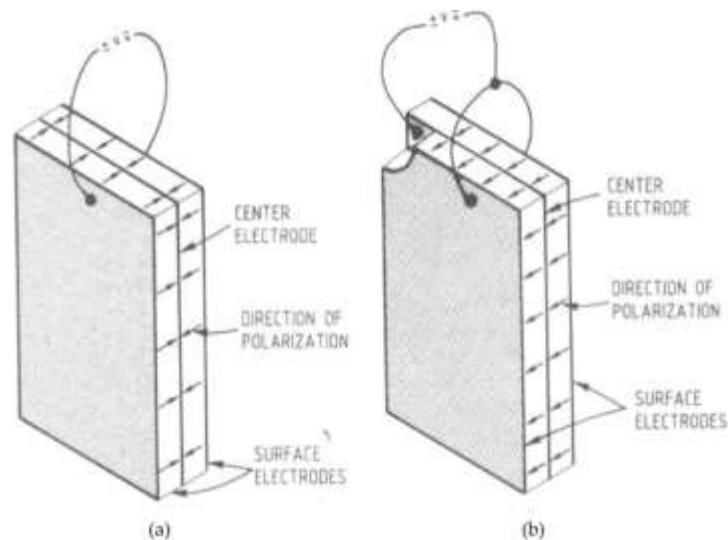


Figure 2.16: Piezoceramics polarisation – a) series connection, shear wave receiver; b) parallel configuration, shear-wave transmitter (DYVIK; MADSHUS, 1985)

The transmitter element is inserted into the top extremity of a soil specimen, making sure that the BE transmitter is completely in contact with the soil (Figure 2.17). Then, when BE is vibrated, it forces particles in contact to assume a perpendicular direction in relation to its axis (Figure 2.18 – a). When the system is continuously fed, BE keep vibrating back and forward generating waves, which are controlled by the input frequency and amplitude. Once generated, shear waves propagate perpendicularly to particle movement until reaching the other piezoceramic located at the opposite extremity of the specimen (Figure 2.18 – b). The wave travelling time through the studied specimen (tip-to-tip BE) is measured and the shear wave velocity can be calculated, as long as path length is also known. Initial studies used the tip-to-tip distance as the path length (e.g. DYVIK; MADSHUS, 1985), as indicated by “ d_e ” in Figure 2.17. Although there are some divergences, as reported by Yamashita *et al.* (2009), who compared wave measurements on Toyoura sand conducted in 23 different laboratories in 11 countries, the majority of the laboratories used the tip-to-tip distance (specimen height minus the upper and lower BE protrusion in the soil), as previously described by Viggiani and Atkinson (1995b).

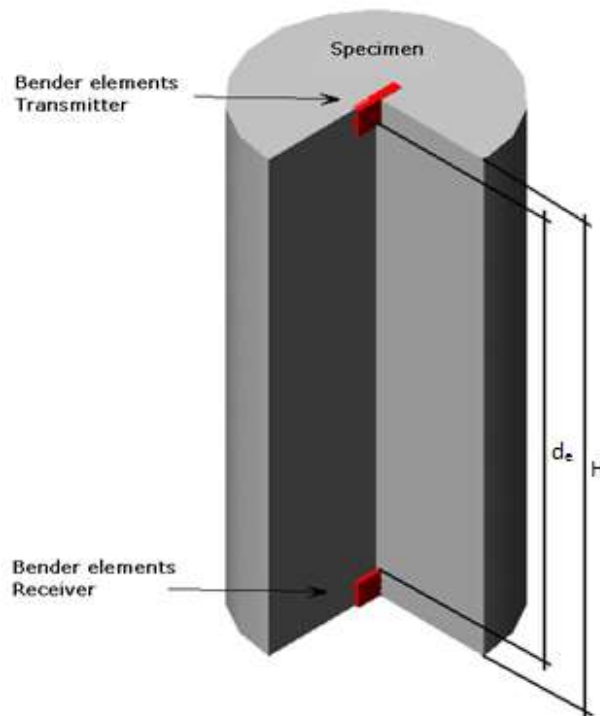


Figure 2.17: BE schematic assembling into a cylindrical specimen; “ d_e ” is the tip-to-tip distance, while “ H ” represents total specimen height

(based on: FESTUGATO, 2011)

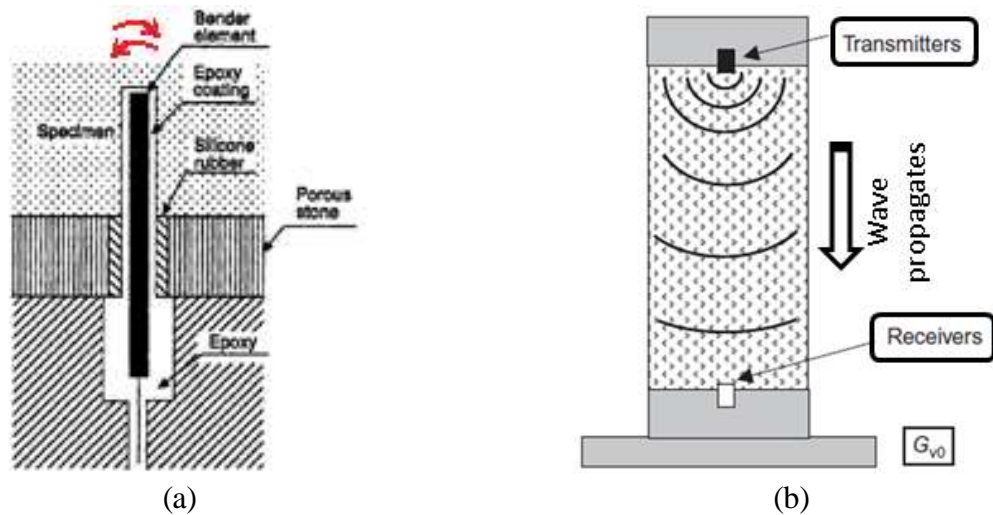


Figure 2.18: BE placed inside a triaxial apparatus – (a) BE embedded in a soil, and BE movement during vibration (red arrows); (b) wave propagation from transmitter to receiver (based on: MITCHELL; SOGA, 2005 and CLAYTON, 2011)

Figure 2.18 – (a) also illustrates BE insulation by an epoxy coating. Waterproofing piezoceramics is essential, once any water that penetrates into the piezoceramics can generate short circuit, compromising measurements. More information on BE coating is presented in Appendix A (A.2.3). Montoya *et al.* (2012) also provided some important information on waterproofing piezoceramics. Despite piezoceramic coating, it is expected that water will reach the piezoceramic over time by diffusion, as claimed by Santamarina and Fam (VIGGIANI; ATKINSON, 1997). Figure 2.19 presents a BE pair response without water-insulation.

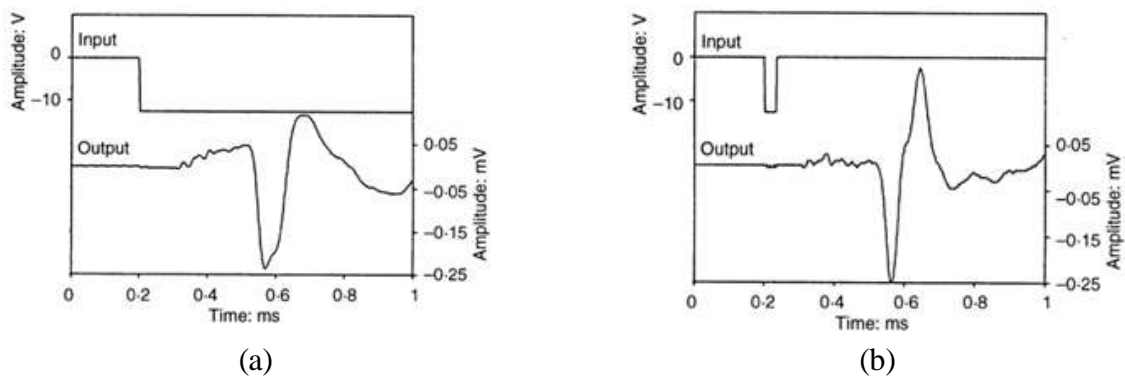


Figure 2.19: Response of a BE pair embedded into a saturated silty soil ($\sigma'_1 = 40$ kPa) with deteriorated insulation – (a) excitation step; (b) short pulse excitation (VIGGIANI; ATKINSON, 1997)

Although BE arrangement aims to transmit and receive only shear waves, transducer movement can in fact generate both compression and shear waves at the same time (RIO; GREENING; MEDINA, 2003; LEE; SANTAMARINA, 2005), as observed in Figure 2.20. Eventually, generated p-waves will reach the other side of the specimen, and when a compression transducer is installed in that side, it will vibrate as soon as the p-waves reach it. Figure 2.21 presents the example after p-waves had travelled through a dry specimen of Ticino sand. As described previously, the coupling of both shear and compressional waves is possible and, therefore, the received waves are subjected to near-field effect (see 2.5.1.2). The use of a compression transducer is especially interesting for this situation, because it can flag the arrival of p-waves, indicating near-field effect arrival in the shear transducer, which may facilitate wave interpretation.

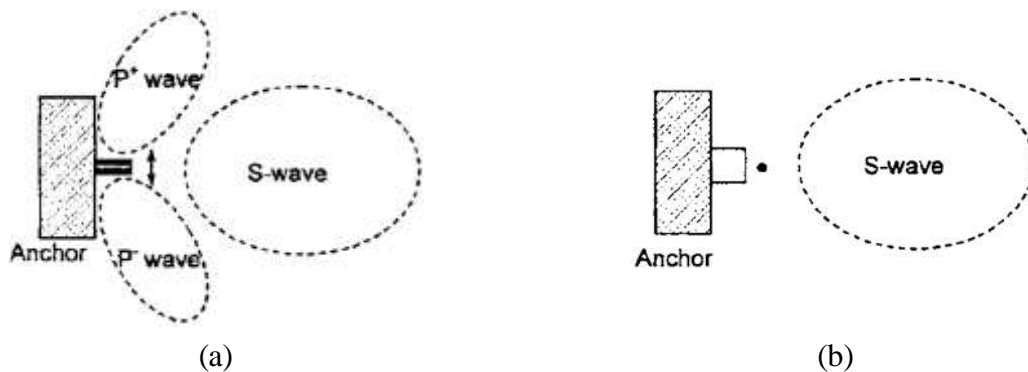


Figure 2.20: Waves generated during BE transmitter vibration – (a) side view; (b) top view
(LEE; SANTAMARINA, 2005)

The use of compression transducers in routine tests is also associated to the inference of saturation (BRIGNOLI; GOTTI; STOKOE II, 1996; GAJO; FEDEL; MONGIOVI, 1997; ARROYO *et al.*, 2006; AIREY; MOHSIN, 2013). For fully saturated soils, the expected result should be close to 1,450 and 1,550 m/s, which is the p-wave velocity of water. For unsaturated soils, on the other hand, p-waves travel slower, and can even obscure shear-wave arrival (CLAYTON, 2011). Fact that is corroborated by Yamashita *et al.* (2009) when reporting more “noise” for dry Toyoura sand when compared to the same saturated sand.

As it was briefly mentioned before, crosstalk is an electromagnetic effect that occurs due to the electromagnetic coupling between BE transmitter and receiver. Its manifestation is described as an “output signal with an early component that is quasisimultaneous with the Bender Elements, Ultrasonic Pulse Velocity, and Local Gauges for the Analysis of Stiffness Degradation of an Artificially Cemented Soil

input signal” (LEE, SANTAMARINA, 2005, p. 1063), as observed in Figure 2.22. Moreover, it is usually attributed to two main phenomena: capacitive or conductive coupling. The first mechanism is generated by an induced electric signal, which is directly associated to the conductivity and dielectric properties of the tested soils, which is in turn affected by the presence of water. The second mechanism happens when BE waterproofing is compromised, establishing a conductive path through the pore fluid from the transmitter to the receiver (MONTROYA *et al.*, 2010). Lee and Santamarina (2005) believe that crosstalk can be removed by properly grounding both the transducer or the receiver. Montoya *et al* (2010), on the other hand, believe that the addition of a drain line can sink most of the transmitted and induced electric signals before reaching the receiver. Nonetheless, Jovičić, Coop, and Simić (1996) claim that proper cable shielding is enough to increase signal quality. Additionally, Rio (2006) reported the presence of crosstalk originating in the oscilloscope, which could only be removed by digital filtering.

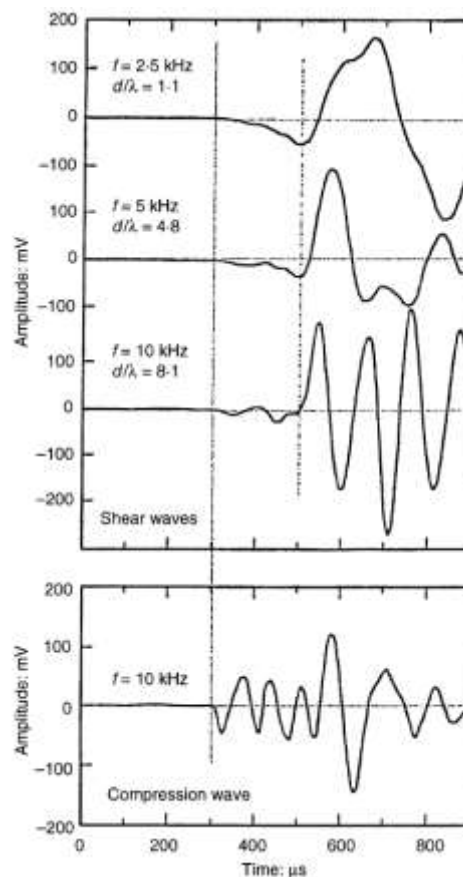


Figure 2.21: Both shear and compression waves reaching a BE embedded in dry Ticino sand (BRIGNOLI; GOTTI, 1992 *apud* VIGGIANE; ATKINSON, 1997)

Many different BE signal inputs have been tested over the years, including square and sine waves; continuous and pulse excitation; peak-to-peak amplitudes ranging from $\pm 10\text{V}$ to $\pm 50\text{V}$ (YAMASHITA, 2009); and frequencies ranging from 50 Hz (in early studies, DYVIK; MADSHUS, 1985) up to 20 kHz (CONSOLI *et al.* 2012a). A summary, with suggestions made by different authors, is presented in Chart 2.2. Although early studies usually used square pulses, sine pulses have become more popular over the years, as their results have been shown to be more reliable (JOVIČIĆ; COOP; SIMIĆ, 1996; BLEWETT; BLEWETT; WOODWARD, 2000; VIANA DA FONSECA; FERREIRA; FAHEY, 2009). However, there is no consensus among authors regarding the input signal. Some waveforms are, apparently, more suitable than others, but the lack of a conclusive agreement has opened the way to personal preferences.

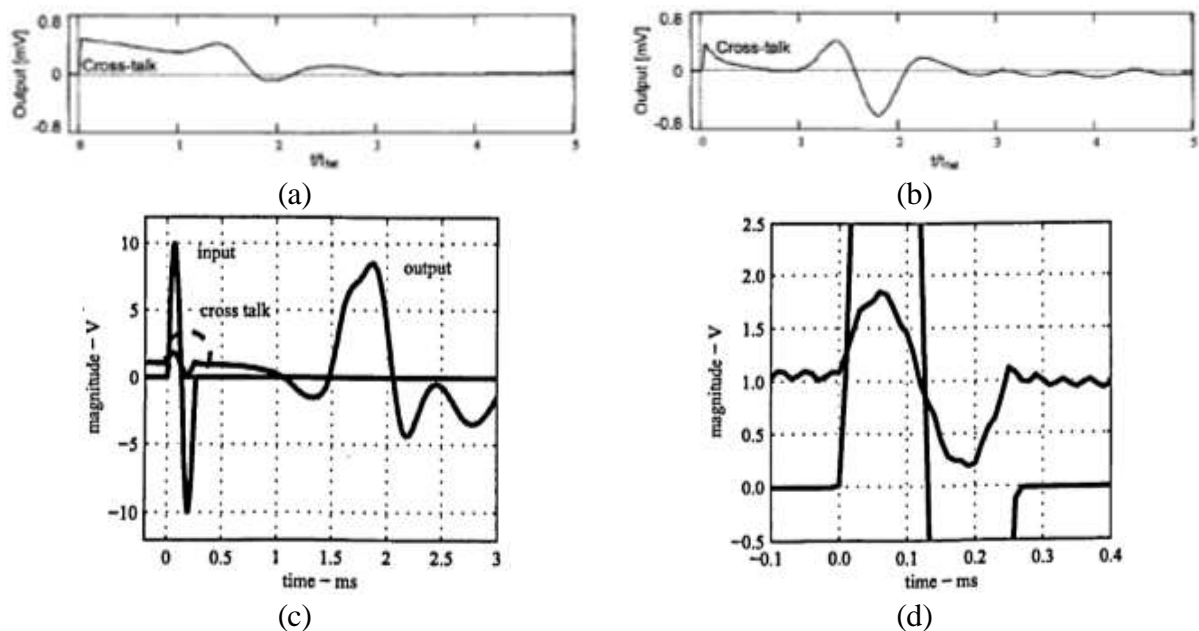


Figure 2.22: Crosstalk effect – (a) BE pair using connection in series without grounding on both transducers; (b) parallel-to-series transducers configuration without shielding or grounding; (c) oscilloscope; (d) zooming oscilloscope crosstalk (LEE; SANTAMARINA, 2005; RIO, 2006)





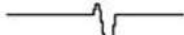

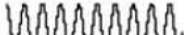

Although square waves are composed by a broader spectrum of frequencies, which may facilitate wave interpretation (JOVIČIĆ; COOP; SIMIĆ, 1996; LEE; SANTAMARINA, 2005), the received signal does not even likely resemble the input signal, which may be an issue (VIGGIANE; ATKINSON, 1995; JOVIČIĆ; COOP; SIMIĆ, 1996; WANG *et al.*,

2007). Moreover, it has been argued that the piezo-transducer is unable to perform a real step signal, which in practical terms means that the transducer should be able to instantaneously reach the applied voltage. Therefore, it is believed that the generated step signals are very different from the hypothetical input signal (RIO, 2006).

Once the shape of a signal is defined (e.g.: sine, or square), it is necessary to choose the hypothetical vibration (e.g.: single pulse, continuous waves, continuous frequency sweep, forced oscillation, distorted pulse waves) (Chart 2.2). Forced oscillation and distorted pulse waves were proposed by Jovičić, Coop, and Simić (1996) to minimise near-field effects, and are explored in more detail in 2.5.1.2. The continuous frequency sweep will be dealt with at this point as a kind of continuous wave. Therefore, the main difference between a single sine pulse and a sinusoidal input is the system response. Continuous waves, when applied long enough, reach a steady-state response in which the applied vibration and system vibration are in tune, i.e., the system is more likely to vibrate at the input vibration. Single pulses, on the other hand, cause transient effects, which means that the system vibration is strongly affected by its own dynamic properties. As a result, regardless of the different input frequencies, the system will vibrate at its resonance frequency (SASCHE; PAO, 1978; CLOUGH; PENZIEN, 1993; GREENING; NASH, 2004). Despite of all the possible transient effects caused by single pulses, Alvarado and Coop (2012) demonstrated that the BE system is a constant parameter system, i.e., that the output is independent of the input (see more details in 0) and, therefore, single-cycle sine pulses are appropriate as driving signals. The authors reached their conclusion after testing several kinds of soils subjected to different confining pressures in a triaxial chamber.

Regardless of the kind of input wave, some important procedures to calibrate and monitor the BE system quality are required. A simple alternative is to place the BE transmitter and receiver in physical contact, and send waves to determine the time-delay between the sent and received waves; which should be deducted from the time the wave took to travel thorough the soil. Moreover, the polarity of both input and output signals must be in phase to avoid signal misinterpretation (BRIGNOLI; GOTTI; STOKOE II, 1996; YAMASHITA *et al.*, 2009; CAMACHO-TAUTA *et al.*, 2015). Transducer alignment is also important, as demonstrated by an in-plane directivity study by Lee and Santamarina (2005). Although misalignments of up to 20° have been shown to cause amplitudes virtually the same as 0°, misalignments of 30° were shown to present a 20% decreased amplitude when compared to 0°.

Chart 2.2: Input waves suggested by different authors

Input wave shape		Reference
	Square or step signal	Dyvik and Madshus (1985); Fam and Santamarina (1995)
	Impulse signal	Lee and Santamarina (2005)
	Sine wave	Viggiani and Atkinson (1995); Brignoli et al. (1996)
	Sine pulse [90° phase shift]	Pennington et al. (2001)
	Distorted sine wave [typically 30° phase shift]	Jovicic et al. (1996)
	Forced oscillation [sine wave cycles at resonance frequency]	Jovicic et al. (1996)
	Continuous sine wave of constant frequency	Greening and Nash (2004)
	Sine sweep of frequencies [typically 100Hz to 20kHz]	Greening and Nash (2004); Ferreira et al. (2006)
random signal	Stochastic random noise	Roesler (1979); Santos et al. (2007)

(source: VIANA DA FONSECA *et al.*, 2008) BE characterisation)

2.5.1.1 BE characterisation

Despite the non-dispersive nature of soils, the BE-specimen system is considered as a dispersive system, i.e., it is frequency dependent (BLEWETT; BLEWETT; WOODWARD, 2000; GREENING; NASH, 2004; RIO, 2006; ALVARADO; COOP, 2012; OGINO *et al.*, 2015). According to Greening and Nash (2004), the dispersive behaviour can occur anywhere from wave generation signal reception. The authors also point out that dispersion is a well-documented physical phenomenon (e.g., HAVELOCK, 1914). Dispersion can be understood as the wave decomposing in different frequencies, whose components present characteristic propagation velocities (RIO, 2006). Some of the reasons for dispersion have been presented by Sachse and Pao (1978), which include: specimen boundaries, non-homogeneous materials, energy dissipating into heat, frequency dependence on the constitutive parameters of the investigated material, and amplitude dependence on wave speed. Alvarado and Coop (2012) also consider the excitation of resonant modes as a cause for dispersion. The propagation of waves in a dispersive medium directly affect the received signal as the transient waves (pulses) may suffer distortion, and continuous waves may suffer phase shifts (ALVARADO; COOP, 2012).

This frequency-dependent behaviour is corroborated by many authors reporting a ceiling input frequency, from which all received signals seemed to vibrate at frequencies smaller than the input signal (BRIGNOLI; GOTTI; STOKOE II, 1996; LEONG; CAHYADI; RAHARDJO, 2009; CLAYTON, 2011; O'DONOVAN *et al.*, 2016). Moreover, once this frequency is exceeded, the received signal frequency is reported to be constant and independent of the input frequency in the time domain. The reason for that is probably due to the transient response of the system subjected to single pulses (CLOUGH; PENZIEN, 1993), while the ceiling frequency might be one of the natural frequencies of the BE transducer. Moreover, Brignoli, Gotti, and Stokoe II (1996) claim that frequency responses are due to soil absorbing energy, and the dynamic response of the soil-BE transducer association. Nonetheless, Yamashita *et al.* (2009) observed a small, but consistent, influence of the input frequency on stiffness gains.

The response of an ideal physical system is characterised by its unit-impulse response function (time-domain) or transfer function (frequency-domain). Both alternatives can directly relate to input and output signals through specific equations. An ideal physical system will present the following features: capable of being executed; has constant parameters; and is linear and stable. A constant parameter system means that the output signal is not dependent on the nature and period of the input signal. Linear systems are characterised for being homogeneous and additive. In a homogeneous system, the magnitude of both the input and output signals are proportional to each other. In an additive system, on the other hand, the final output signal is considered as the sum of individual contributions of each output signal, which are proportional to each different input signal (principle of superposition). The transfer function is considered a powerful tool in characterising and monitoring the performance of a system (BENDAT; PIERSOL, 1993; ALVARADO; COOP, 2012).

Although not usually mentioned, the response obtained from BE transducers characterises the non-dispersive shear bulk plane wave travelling model, as indicated by its transfer function (Equation (2.10)). This is a simple model that does not take into account other effects apart from the transfer function phase. As a result, reflected and refracted waves are disregarded, and specimen-size effects are also not considered; even though these are considered the main reasons for signal distortion due to lateral boundary reflections. Specimen-geometry effects become more significant when second-order effects, such as anisotropy, are analysed and when different test configurations are compared (BRIGNOLI; GOTTI; STOKOE II, 1996; JOVIČIĆ, 1997; ARULNATHAN; BOULANGER; RIEMER, 1998; BLEWETT;

BLEWETT; WOODWARD, 2000; ARROYO; WOOD; GREENING, 2003; CLAYTON; THERON; BEST, 2004; GREENING; NASH, 2004; ARROYO *et al.*, 2006; MOHSIN, 2008; VIANA DA FONSECA; FERREIRA; FAHEY, 2009; ALVARADO; COOP, 2012; CAMACHO-TAUTA *et al.*, 2015).

$$S(\omega, x) = e^{ikx} \quad k = \frac{\omega}{V_s} \quad (2.10)$$

Where “ ω ” is the angular frequency, “ k ” is the wavenumber, “ x ” is the distance between the two transducers, and “ V_s ” is the phase wave velocity. Considering the non-dispersive isotropic elastic material mode, phase wave velocity can be understood as shear wave velocity and, therefore, can be related to shear modulus with Equation (2.7).

Another accepted model analogous to BE test responses is the damped single-degree of freedom (SDOF) system, whose mass is subjected to forced vibration. Santamarina and Fam (VIGGIANI; ATKINSON, 1997) sustain the idea that the entire BE system can be represented by this specific model. Later studies used this model only to describe the response of the BE receiver, instead of the global system (WANG *et al.*, 2007; OGINO *et al.*, 2015). Simulations of a SDOF mass-spring-damper system (which is constant parameter and linear), using values applied for real soils, presented less dependence on the system natural frequency as the number of input cycles increased, i.e., a tendency to vibrate at the same input frequency with increased number of cycles (ALVARADO; COOP, 2012). That probably reflects a transient system behaviour moving to a steady-state response as the “load” (pulses) are applied long enough until input and system response frequencies are in tune.

When performing BE tests, there are uncertainties whether BE transmitter movement actually matches the electrical input signal. Rio (2006, p. 202) claimed that “the transmitting bender element behaves as a dynamic multiple degree of freedom system with a certain degree of independence from the transient input pulse signals,” after laser monitoring BE movements. Other BE monitoring techniques, such as the self-monitoring element, which involves partly wiring the transmitter element as a receiver element (SCHULTEISS, 1982 *apud* JOVIČIĆ; COOP; SIMIĆ, 1996; WANG *et al.*, 2007); accelerometers (BROCANELLI; RINALDI, 1998; CAMACHO-TAUTA *et al.*, 2015); and strain gauges (GREENING; NASH, 2004), have been also used. Although some studies on BE self-monitoring transmitter showed a good match between the electrical and actual transmitted signal, Gordon and Clayton (1997) point

out that the mechanical BE-specimen coupling is yet unknown, which prevents direct comparisons between transmitted and received signals (cross-correlation). Although Rio (2006) described the BE transmitter as a more complex vibratory system, the description is broad and simply disregard the alternative of a cantilever bending in flexure movement, which theoretically underlies BE tests.

The use of a SDOF mass-spring-damper system is also inaccurate, as it assumes a single vibration mode. The BE-system has been shown to be inherent a multi-vibrational system that may include signal distortion, making signal interpretation a challenge. The multi-vibrational behaviour can be assessed by analysing the gain factor graph in the frequency-domain, which should present defined multiple-peaks along the frequencies. Another implication of a multi-vibrational system is that group wave velocity is not equal to shear-wave velocity and, therefore, Equation (2.7) cannot be associated to Equation (2.10) to obtain shear modulus. (RIO, 2006; ALVARADO; COOP, 2012; O'DONOVAN; O'SULLIVAN; MARKETOS, 2012; O'DONOVAN, 2014). Although a single vibration mode for the conventional range of BE frequencies would be ideal, in fact each part of the BE system (tested soil, specimen boundaries, and the transducers) may introduce different vibration modes into the system. Alvarado and Coop (2012), using transfer function, demonstrated that the BE system is both linear and constant parameter. Consequently, as a linear system, the contribution of each part of the system can be superimposed, resulting in the possibility of associating the simplified unimodal non-dispersive system with the more complex characteristics added by other components of the system.

However, nor individual contributions, neither real BE-soil interactions are fully understood, and BE interpretation remains a challenge (BLEWETT; BLEWETT; WOODWARD, 1999; BLEWETT; BLEWETT; WOODWARD, 2000; ARROYO *et al.*, 2006; RIO, 2006; ALVARADO; COOP, 2012).

2.5.1.2 Working frequency

The main limitation in regard to the working frequency is usually related to near-field effects or overshooting; the first typically associated to lower, while the latter to higher frequencies.

Near-field effects can be formally defined as being “caused by coupling between waves which exhibit the same particle motion but which propagate at different velocities and attenuate at different rates” (SÁNCHEZ-SALINERO; ROESSET; STOKOE, 1986, p. IV). In their study,

Sánchez-Salineró, Roesset, and Stokoe suggested that the distance of 2 wavelengths (λ) between transducers should always be respected to avoid near-field effects. Many authors have investigated distances free of near-field effects. Mancuso and Vinale (1988 *apud* VIGGIANI; ATKINSON, 1995b), using parametric studies, found that distances outside the interval between $1/4\lambda$ and 4λ would be suitable; Arroyo *et al.* (2006) suggested values higher than 3λ ; Leong *et al.* (2005) made their considerations using the ASTM D2845 (ASTM, 1995) for ultrasonic pulse velocity devices, which recommends values higher than 3.3λ . Although there are differences between the suggested values free of near-field effects, authors agree that the greater the distance between transducers, the smaller the near-field effects (e.g., BRIGNOLI; GOTTI; STOKOE II, 1996; YAMASHITA *et al.*, 2009; O'DONOVAN *et al.*, 2016).

Wavelength is inversely dependant on wave frequency, and directly proportional to wave velocity ($\lambda = V_s/f$). Therefore, the above-mentioned distances (in λ) can be re-calculated in terms of frequency, which facilitates the evaluation of near-field effects-free ranges (VIGGIANI; ATKINSON, 1995b). Table 2.1 present the corresponding frequencies for the λ values suggested by Mancuso and Vinale (1988 *apud* VIGGIANI; ATKINSON, 1995b), as they were the lowest and highest values, and Sánchez-Salineró, Roesset, and Stokoe (1986), as their findings were used general guidelines for many studies conducted later. The shear-wave velocities (V_s) presented in the table are those first presented by Consoli *et al.* (2012a), who studied artificially cemented Osorio sand subjected to bench tests.

Table 2.1: Frequencies free of near-field effect and minimum wavelength

Data from Consoli <i>et al.</i> (2012a)						Frequency (kHz)		
Material	Density	C_i (%)	ρ_d (kg/m ³)	G_0 (MPa)	V_s (m/s)	$f \geq 4.V_s/L_e$	$f \leq V_s/4.L_e$	$f \geq 2.V_s/L_e$
Artificially cemented Osorio sand	Loose	2	1,460	314	463.39	20.15	1.26	10.07
		7	1,460	1,031	840.44	36.54	2.28	18.27
	Dense	2	1,620	563	589.26	25.62	1.60	12.81
		7	1,620	1,609	996.72	43.34	2.71	21.67

As can be observed in the table above, the frequency range is dependent on the stiffness of the studied material (in terms of shear-wave velocity). Therefore, the near-field effects on stiffer materials, such as the cemented ones, affect a broad range of frequencies, requiring higher frequencies. The frequencies illustrated in the table possibly exceed BE capacity, resulting in overshooting (JOVIČIĆ; COOP; SIMIĆ, 1996), making the advice by Greening and Nash

(2004) to work with frequencies that are not potentially affected by near-field effects difficult to follow.

Signal attenuation can be understood as the amplitude decay over time and distance (FRATTA; SANTAMARINA, 1996). More severe attenuations are usually related to higher frequencies (VIANA DA FONSECA; FERREIRA; FAHEY, 2009; AIREY; MOHSIN, 2013). Therefore, stiffer soils measurements will always take place at frequencies affected by near-field effects. Because of that, Jovičić, Coop, and Simić (1996) proposed two alternatives: send a distorted signal in order to cancel near-field effects by reducing the amplitude of the upward signal portion (Figure 2.23 – a), and use forced oscillation at one of the natural resonant frequencies (Figure 2.23 – a) and the corresponding element at the output.

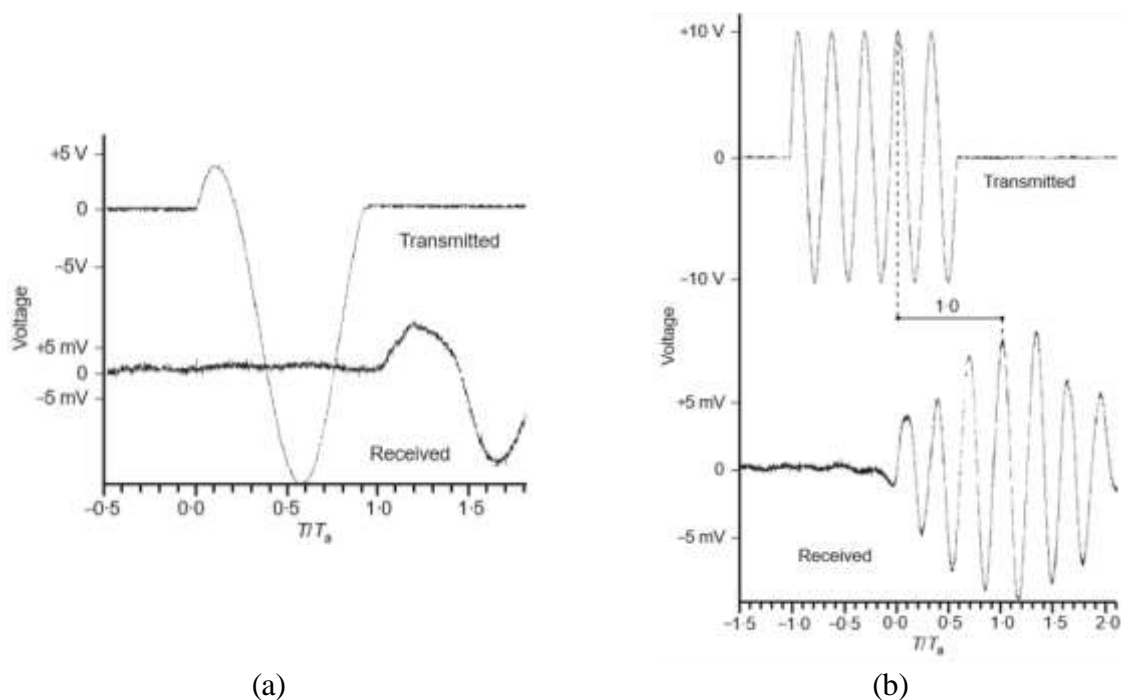


Figure 2.23: Alternatives to mitigate near-field effects – (a) distorted input signal; (b) forced oscillation at resonant frequency (JOVIČIĆ; COOP; SIMIĆ, 1996)

Another limitation that requires attention regards the inherent multi-vibrational nature of BE system. As previously discussed, input signals at any vibration mode can lead to signal distortion (BLEWETT; BLEWETT; WOODWARD, 2000). An alternative to avoid the effects that come with BE multimodal nature is to work at low frequencies away from resonance, where the system can be simplified, as a SDOF system (BROCANELLI;

RINALDI, 1998; WANG *et al.*, 2007). However, the modes of vibration are influenced by the confining stress (for non-cemented soils), and increments in effective confining pressure usually result in a movement of vibrational modes in the direction of the higher frequencies, which leads to a reduction of the region free of peaks. The movement of vibration peaks is also attributed to changes in lateral boundary and specimen stiffness, and specimen unit weight (BLEWETT; BLEWETT; WOODWARD, 2000; ARROYO, 2001; LEE; SANTAMARINA, 2005; OGINO *et al.*, 2008; OGINO *et al.*, 2010; ALVARADO; COOP, 2012; CAMACHO-TAUTA *et al.*, 2015). Therefore, it is difficult to follow the suggestion to avoid frequencies associated to distortion and attenuation. Because of that, it is important to understand the limitations involved in the test conditions, and choose the adequate alternative to interpret results, as discussed in the following section.

2.5.1.3 Result interpretation

In the previous sections, some of the main reasons for errors in BE interpretation were presented: near-field effects, wave interference at the specimen boundary, specimen geometry, resonance and overshooting transducers, and electrical noise associated to grounding (VIANA DA FONSECA; FERREIRA; FAHEY, 2009). Nonetheless, Viggiani and Atkinson (1995) estimated that wave travelling time is, perhaps, the main source of errors. Any chosen method for BE signal interpretation can bring errors (YAMASHITA *et al.*, 2009; OGINO *et al.*, 2015).

Moreover, BE transmitter movement generates uncertainties to data interpretation, as it produces waves that are also complex. These not-entirely known waveforms are captured and, when associated to the many causes of errors, result in a complex and complicated signal interpretation (VIANA DA FONSECA; FERREIRA; FAHEY, 2009; YAMASHITA *et al.*, 2009; O'DONOVAN; O'SULLIVAN; MARKETOS, 2012). Alvarado and Coop (2012) performed a parametric study, in which they used a sine waveform composed by two different sine waves (each one with own frequency, duration, and arrival time) to simulate what is usually found with BE received data (Figure 2.24) showed that dispersion typically causes wave fragmentation.

Mohsin (2008) has presented and discussed different alternatives for BE results interpretation, including: peaking directly first arrival at the output signal; corresponding characteristic points in both input and output signal; second arrival at the output; phase velocity analysis; and cross correlation. Generally speaking, the three main alternatives for BE data

interpretation are: time- and frequency-domain method, and cross-correlation method (Figure 2.26). One of the most relevant studies in this matter, performed by Alvarado and Coop (2012), strongly criticised group-wave velocity (cross-correlation) mainly because of the dispersive nature of the system.

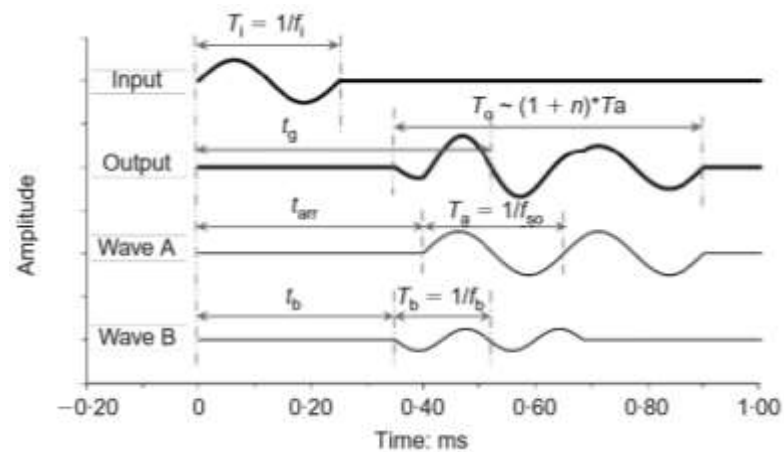


Figure 2.24: Input and output waves used in a parametric study, simulating dispersion effects, note the output wave is a composition of wave A and B (ALVARADO; COOP, 2012)

Therefore, the time- and frequency-domain methods are the only remaining alternatives for BE results interpretation. Time-domain is usually criticised as being a time-consuming and biased method. Frequency-domain, on the other hand, requires further corrections because of the dispersive nature of the system (ALVARADO; COOP, 2012). The best-case scenario would be an association of both methods, evaluated simultaneously, as recommended by Viana da Fonseca, Ferreira, and Fahey (2009).

Because frequency-domain requires a more complex analysis, it was considered beyond the scope of the present study. Therefore, time-domain was the alternative chosen for interpreting BE data as presented by Viana da Fonseca, Ferreira, and Fahey (2009). The procedure mainly involves stacking data from different frequencies in one graph, allowing to evaluate all frequency effects at once. The authors also recommended to use lower frequencies to roughly provide the region where the first wave arrival is, and sharpen its position using higher frequencies.

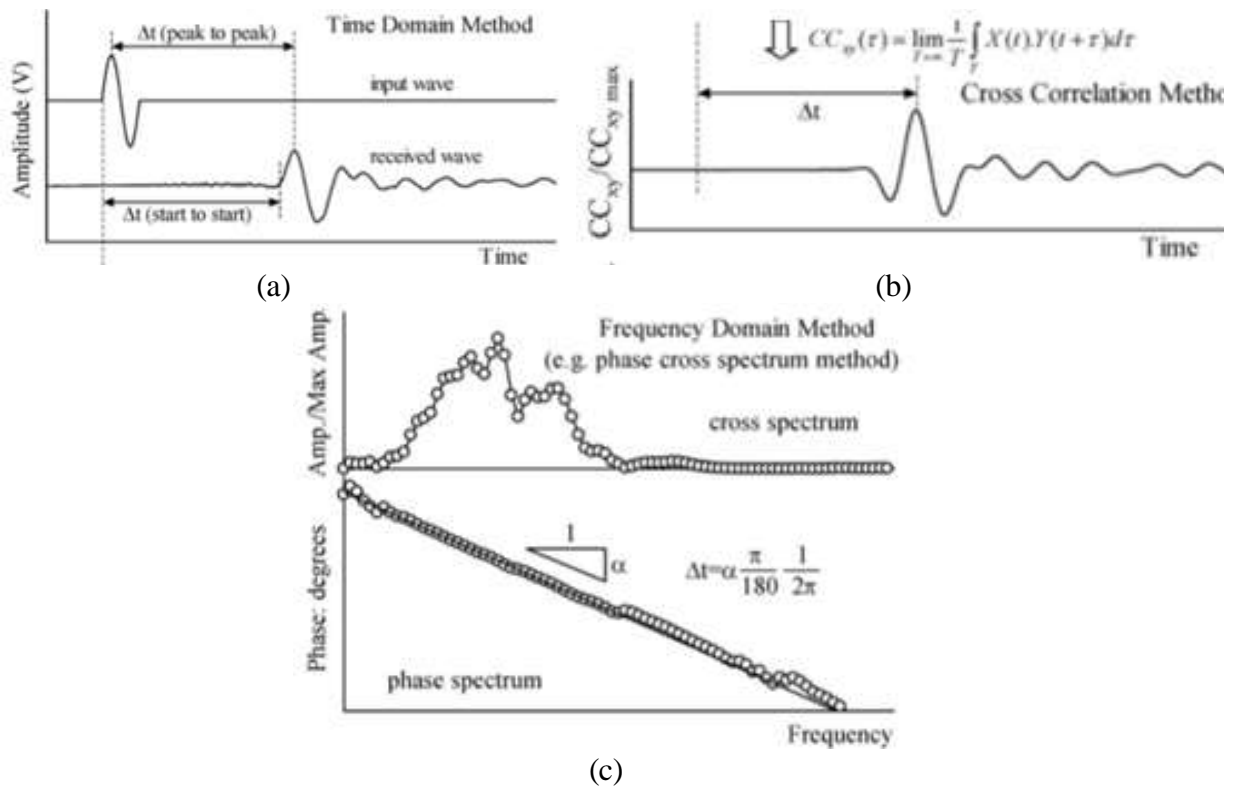


Figure 2.25: Interpretation possibilities for wave arrival time– (a) time-domain; (b) cross-correlation; (c) frequency-domain (YAMASHITA *et al.*, 2009)

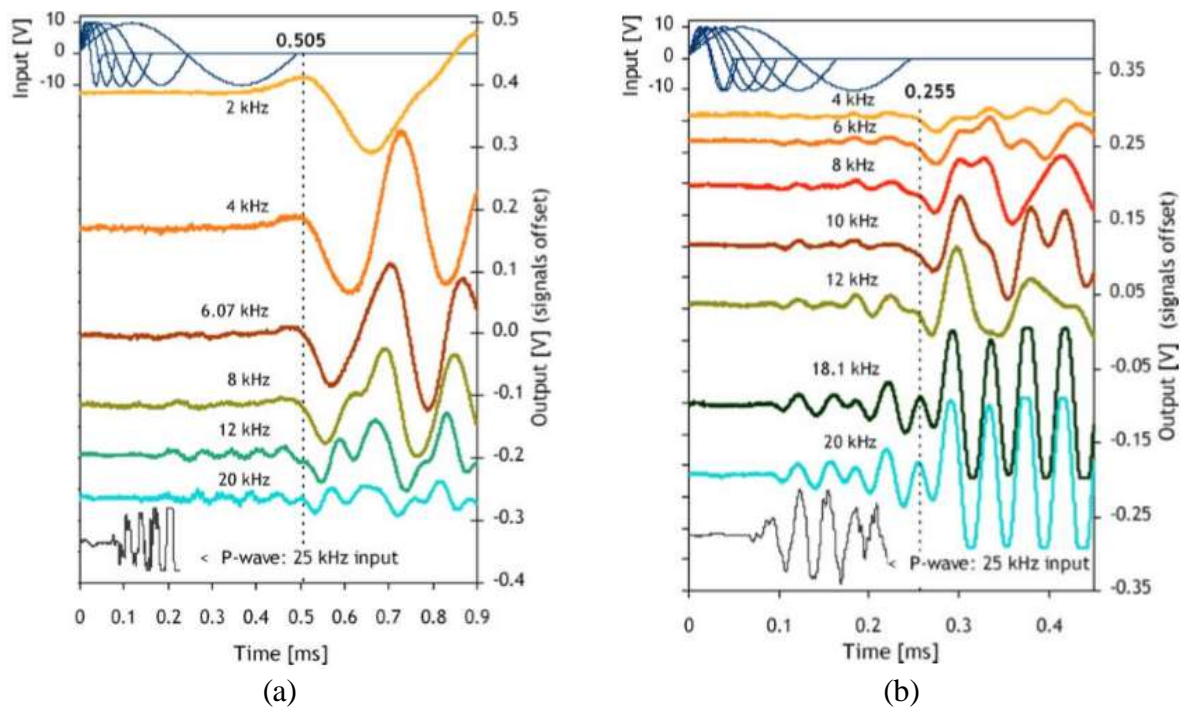


Figure 2.26: Residual soil subjected to BE tests and time-domain analysis – (a) $\sigma'_3 = 100$ kPa; (b) $\sigma'_3 = 800$ kPa (VIANA DA FONSECA; FERREIRA; FAHEY, 2009)

2.5.1.4 Bender elements on natural and cemented sand

Several investigations using BE have been conducted in the Laboratory of Geotechnical and Geoenvironmental Engineering (LEGG – UFRGS) over the years (e.g. SPINELLI, 1999; FESTUGATO, 2008; DALLA ROSA, 2009; MARQUES, 2016). BE have also been employed in researches conducted elsewhere (HEINECK, 2002; CABERLON, 2008; LOPES JUNIOR, 2011; FLOSS, 2012; FONINI, 2012).

Heineck (2002), in her doctoral thesis, studied uncemented Osorio sand with and without the addition of polypropylene fibres in a triaxial chamber (HEINECK; COOP; AND CONSOLI, 2005). The authors found a unique relationship for both the fibre reinforced and non-reinforced sand (Figure 2.27), in regard to the normalised parameter, making possible to obtain the shear modulus of Osorio sand with Equation (2.11). Where “ $R_0=1$ ” (normally consolidated soil), and “ p_r ” is equal to 1 kPa, therefore, G_0 is also in kPa.

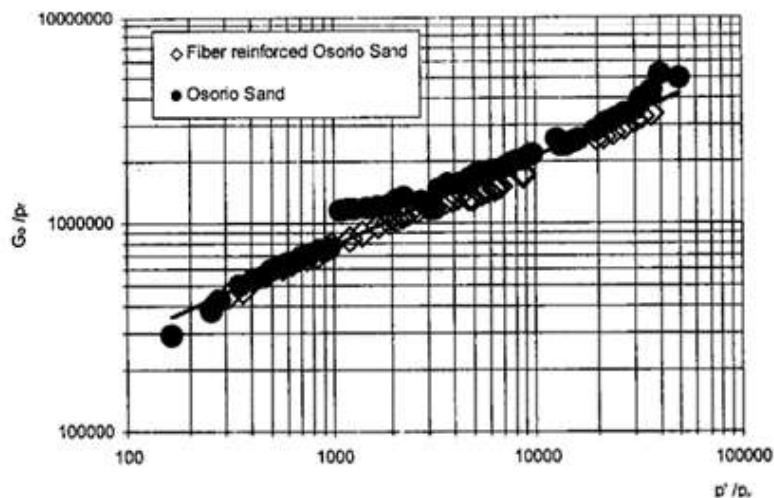


Figure 2.27: Normalised shear modulus obtained through bender elements tests for fibre reinforced and non-reinforced Osorio sand subjected to different confining pressures (HEINECK; COOP; AND CONSOLI, 2005)

$$\frac{G_0}{p_r} = A \cdot \left(\frac{p'}{p_r}\right)^n \cdot R_0^m \Rightarrow \frac{G_0}{p_r} = 39,500 \cdot \left(\frac{p'}{p_r}\right)^{0.43} \quad (2.11)$$

Fonini (2012) performed bench tests on artificially cemented Osorio sand. While Caberlon (2008) performed BE triaxial tests on cemented Osorio sand. Their findings are presented in Figure 2.28 and Figure 2.29. Consoli *et al.* (2012a) found a unique relationship between G_0

and η/c_{iv} ratio for BE bench tests, as presented in Equation (2.12). Consoli *et al.* (2009b) found another unique relationship between G_0 and η/c_{iv} ratio for different confining pressures, as presented in Equation (2.13). Where η/c_{iv} ratio is the ratio between porosity (η) and cement content in relation to volume (c_{iv}). Despite the differences between the two types of tests, the two relationships are similar to each other.

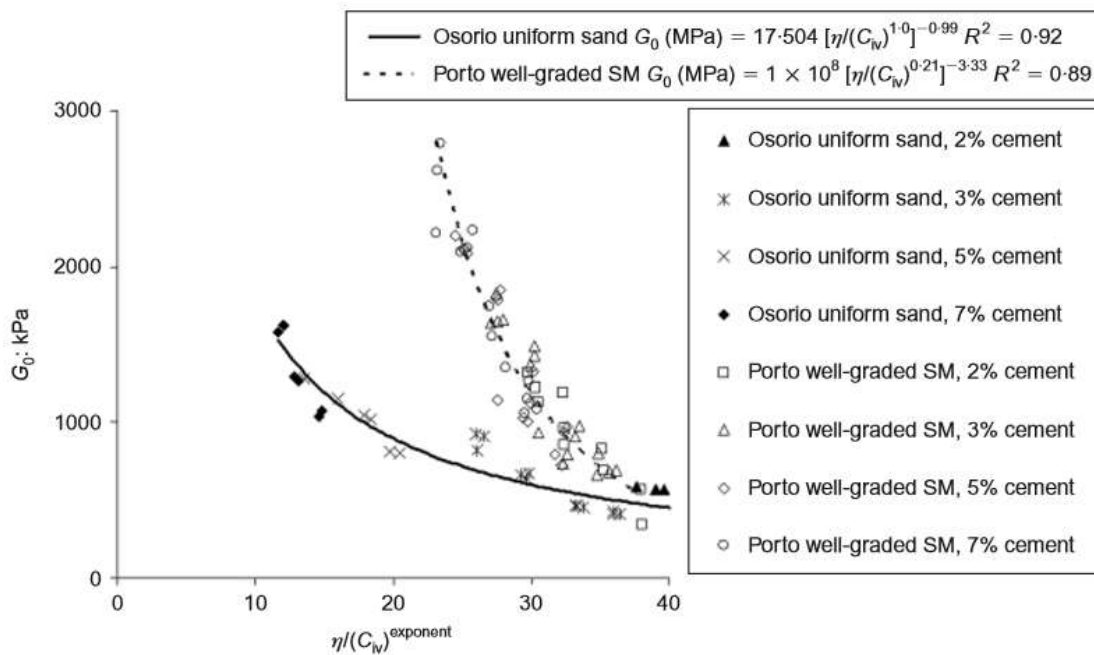


Figure 2.28: Data for initial shear modulus (G_0) measured by bender elements for two different soils (bench tests), with the equations to predict G_0 using $\eta/(c_{iv})^{\text{exponent}}$ (CONSOLI *et al.*, 2012a)

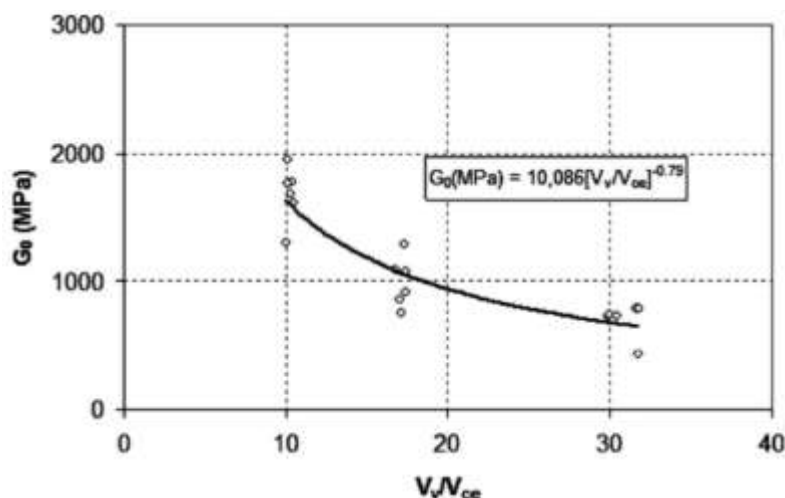


Figure 2.29: Initial shear modulus (G_0) measured by bender elements in respect to artificially Osorio sand subjected to different confining pressures (CONSOLI *et al.*, 2009b)

$$G_0 = 17,504 \left[\eta / (c_{iv})^{1.0} \right]^{-0.99} \quad (2.12)$$

$$G_0 = 10,086 \left[\eta / (c_{iv})^{1.0} \right]^{-0.79} \quad (2.13)$$

2.6 ULTRASONIC WAVES

Ultrasonic waves are elastic waves (stress) that propagate at frequencies higher than 20 kHz. This specific frequency separates spectra in two different ranges based on human hearing ability: audible, between 20 Hz and 20 kHz; and inaudible, frequencies higher than 20 kHz (ultrasound).

This method is applied to concrete and rocks, with few applications for soils (SENTHILMURUGAN; ILAMPARUTHI, 2005; CHRIST; PARK, 2011). However, it is a simple approach to measure wave velocity in different materials with no confinement. All the theoretical background provided in section “2.5 WAVES IN GEOMATERIALS” is applicable to this methodology. Moreover, an interesting paper comparing ultrasonic waves and BE results in cement pastes is available (GRANJA *et al.*, 2014).

2.7 SOIL ANISOTROPY

Natural soils, known as anisotropic materials, or at least, cross-anisotropic materials – are classified based on the symmetry or asymmetry between planes. The reasons for anisotropy can be divided into stress induced, and inherent structural (due to its mineralogy, for example). If a material is classified as anisotropic (at any degree), the assumption of symmetry between planes is no longer valid and, therefore, the three elastic parameters cannot be applied (FERNANDEZ; SANTAMARINA, 2001; CLAYTON, 2011).

In fact, a completely anisotropic material would require 21 independent elastic constants. On the other hand, a cross-anisotropic material will only require seven parameters: Young’s modulus in both directions (E_v and E_h); vertical and horizontal shear modulus (G_v and G_h); and Poisson’s ratio for each direction (ν_{vh} , ν_{hv} , and ν_{hh}). Thus, the same approach to obtain elastic parameters can be employed with independent measurements in each direction (FERNANDEZ; SANTAMARINA, 2001; CLAYTON, 2011).

3 EXPERIMENTAL DESIGN

In the present study, the experimental design has been divided into four main topics, all of which of extreme importance for the comprehension of the proposed work. In the topic entitled “Initial considerations”, an overview of the entire work is provided, and explanations about how the study was developed and their associations with the main goals are presented. In the next topic, “Variables”, η/c_{iv} ratio and reading times are introduced. Then, in the third topic “Materials”, all the materials employed (soil, water, cementitious agent, and capping agent) are presented. Finally, in the topic “Methods”, the characterisation of all materials, and a detailed description of processes, equipment, procedures, and analyses, required for the reproducibility of this experiment are provided.

3.1 INITIAL CONSIDERATIONS

This work has been designed with two main objectives in mind. First, the fabrication of two pairs of operational bender elements (BE) systems – one to be used as a bench system and the other inside a triaxial apparatus – and validate their performance. For the BE bench system validation process, two tests were conducted with artificially cemented Osorio sand, and the results of the seven-day cure samples compared to the calculated initial shear modulus obtained with the behaviour prediction equation described by Consoli (2012a). The BE triaxial system was validated by testing the uncemented Osorio sand under an effective confining pressure (200 kPa), enough to force sand particles to grip onto the BE pair, and the results obtained were confronted with those found in the literature for similar granular soils (HEINECK; COOP; CONSOLI, 2005).

The second main objective was to obtain the stiffness degradation curve for artificially cemented Osorio sand. Two specimens with different percentages of cement were tested in the triaxial apparatus. The initial very-small strains shear modulus of seven-day cure specimens was initially measured with the BE pair under an effective stress of 50 kPa. As the shearing process progressed, strains were imposed to the soil and stiffness degradation could be evaluated with the BE and local sensors.

Moreover, two additional secondary objectives also need to be addressed in this section. They concern the investigation of stiffness gain over time (due to cementation), and the frequency-dependency of the studied cemented soil. To this aim, BE and ultrasound pulse velocity (UPV) tests were used to measure stiffness. The BE system ordinarily works between 5 to 20 kHz, while the UPV apparatus vibrates at 50 kHz, when compressional waves are transmitted, and 250 kHz when shear waves are employed. With the combination of these two systems, the impact of the frequency on the tested soil could be assessed more comprehensively.

One of the primary hypotheses regarding wave propagation used in this study is based on the premise that any soil (or material that propagates waves) is isotropic. However, as presented previously on the Literature Review section, soils in general are cross-anisotropic materials (FERNANDEZ; SANTAMARINA, 2001; CLAYTON, 2011). Cemented Osorio sand isotropy was investigated and confirmed with UPV measurements applied to cubical specimens – all the three pairs of opposite faces of the cube were consecutively subjected to the propagation of compressional and shear waves.

Finally, unless otherwise stated, all specimens used were cylindrical, 5 cm in diameter and 10 cm high, fabricated with the same targeted dry unit weight (15.40 kN/m^3) to allow a direct comparison among all tests. Thus, to achieve a different η/c_{iv} ratio, only the amount of cement varied. Cubical specimens, on the other hand, were made with different targeted dry unit weights. It is also important to point out that the UPV tests were exclusively applied to bench tests, so that these tests were only relevant for zero confining pressure analysis.

3.2 VARIABLES

Artificially cemented soils are more dependant of some factors (void ratio and cement content) than others (confining stress at small strains), as previously discussed in the Literature Review (FERNANDEZ; SANTAMARINA, 2001; SANTAMARINA, 2001; CLAYTON *et al.*, 2010; CLAYTON, 2011). The approach adopted in the Laboratory of Geotechnical and Geoenvironmental Engineering (LEGG – UFRGS), using the η/c_{iv} ratio, has been demonstrated to be very effective in predicting the behaviour of improved soils, including cemented soils, under a variety of loading conditions and analyses (CONSOLI *et al.*, 2006, 2009, 2011, 2012a, 2012b; MARQUES *et al.*, 2012; FESTUGATO *et al.* 2017). Therefore, the effect of the η/c_{iv} ratio was used in the present work to analyse stiffness, as well as changes in stiffness over time.

Cubical specimens were used to determine the upper and lower limits of the η/c_{iv} ratio. Unit weight of these cubical specimens was limited by their increased mass, which restricted the action of the hydraulic jack during the compaction process. The target dry unit weight limited by the compaction process was 15.40 kN/m³, which approximately corresponded to the porosity (η) of 42%. This target dry unit weight was used in all specimens tested (cylindrical specimens) for initial stiffness and stiffness degradation. By using the same target dry unit weight, η/c_{iv} ratio was obtained by varying the cement content only. The two extreme η/c_{iv} ratio values (8.64 and 31.90) were selected for the assessments.

The variable “time” was based on the age of cemented specimens. UPV tests were conducted after 1, 3, 5, 7, and 14 days of cure in all specimens (cylindrical and cubical). Bench BE tests were performed after 2, 3, 4, 5, 6, 7, and 14 days of cure. The seven-day time interval between day 7 and 14 was established because the cementitious agent used in the tests was an early high-strength-type cement (Portland cement type III). Thus, strength and stiffness gains were expected to be more evident in the first 7 days of cure (for more details, see 3.3.2). The other test times were selected based on equipment or process limitations. In other words, UPV tests were limited by the high cost of the shear-wave couplant required for each measurement. When one pair of bender elements was cemented to a specimen, it could not be removed until the end of the test period (14 days). As result, BE measurements were performed daily, except on day 1 (for more details, see 3.4.8.4).

For specimens tested inside the triaxial apparatus, initial stiffness and stiffness degradation were only assessed on day 7. The two specimens tested in the triaxial apparatus were subjected to a confining effective stress of 50 kPa. Chart 3.1 and Chart 3.2 summarize the details and variables related triaxial and bench tests, respectively.

Chart 3.1: Triaxial tests with bender elements performed on artificially cemented Osorio sand after 7 days of cure

Specimen geometry	γ_d (kN/m ³)	η/c_{iv}	Initial stiffness	Stiffness degradation	
			Bender elements	Bender elements	Local sensors
Cylindrical	15.40	31.90	X	X	X
		8.64	X	X	X
X: Tests effectively performed;					
-: Tests not performed.					

Chart 3.2: Bench testes performed on artificially cemented Osorio sand
(shear-wave velocity over time)

Specimen geometry	γ_d (kN/m ³)	η/c_{iv}	Shear modulus at very-small strain	
			Ultrasound tests	Bender elements tests
			(at 1, 3, 5, 7, and 14 days)	(at 2, 3, 4, 5, 6, 7, and 14 days)
Cylindrical	15.40	31.90 ⁽¹⁾	X	X
		8.64 ⁽²⁾	X	X
	14.30	31.9 ⁽³⁾	X	-
		8.64 ⁽²⁾	X	-
Cubical	15.40	31.9 ⁽³⁾	X	-
		8.64 ⁽²⁾	X	-
	14.30	31.9 ⁽³⁾	X	-
		8.64 ⁽²⁾	X	-
⁽¹⁾ One specimen with, and one specimen without gypsum-cement capping;				
⁽²⁾ Specimens without gypsum-cement capping;				
⁽³⁾ Specimen with gypsum-cement capping;				
X: Tests effectively performed;				
-: Tests not performed.				

A summary of each type of variable is presented below:

a) investigated variables,

- porosity (η): will be also presented by indexes such as void ratio (e), and dry unit weight (γ_d);
- cement content (c_i): percentage of the cement mass in relation to dry soil mass. This variable was used to calculate the volumetric cement content (c_{iv}) and to compose the η/c_{iv} ratio; and
- time of cure (d): between 1 and 14 days for bench tests, and 7 days for triaxial tests (for further details, see Chart 3.1 and Chart 3.2);

b) control variables,

- type of soil: Osorio sand;
- cementitious bonding agent: Portland cement type III;
- water content used in the compaction process: 10% of the specimen dry mass; and
- axial deformation rate during triaxial tests: 2 mm/hour;

- c) response variable,
 - shear-wave time (t_s) travelling through the investigated soil for BE and UPV tests;
- d) noise variables,
 - operator bias;
 - ambient temperature;
 - digital scales accuracy; and
 - calliper precision.

3.3 MATERIALS

All materials used during the tests were physically characterised (for a detailed description of the characterisation procedures see 3.4.3). The two main materials used in the present study were Osorio sand and Portland cement type III. Calcined gypsum was used as a subsidiary material.

3.3.1 Osorio sand

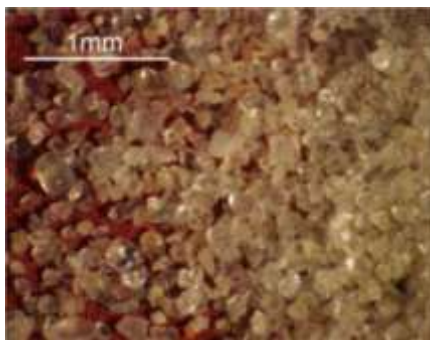
Osorio sand originates from a natural deposit located in the city of Osorio (Figure 3.1), in the state of Rio Grande do Sul (RS), Brazil. Because it is composed by 99% of quartz, Osorio sand has been described as quartz sand. The remaining of the material is composed by glauconite, limonite, tourmaline, and magnetite (SPINELLI, 1999). Magnified images (40 and 500 x) of Osorio sand were previously presented by Dalla Rosa (2009). On visual inspection, the author described Osorio sand as composed by lightly rounded grains with moderately rough surfaces (Figure 3.2).

Particle size distribution (PSD) curve for Osorio sand is presented in Figure 3.3. This curve was obtained by manually sieving the soil. According to ASTM D2487 (ASTM, 2011b), the soil is a poorly graded sand (SP), presenting no significant amount of fine grain particles.

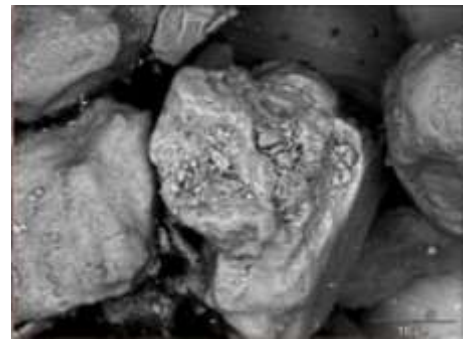


Figure 3.1: Location of the natural deposit of Osorio sand, situated in the city of Osorio, Brazil

(based on: GOOGLE MAPS, 2017)



(a)



(b)

Figure 3.2: Scanning electron microscopy images of Osorio sand – magnified at (a) 40 x; and (b) 500 x

(DALLA ROSA, 2009)

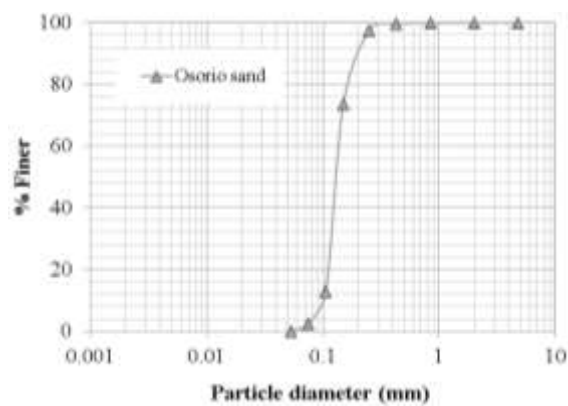


Figure 3.3: Particle size distribution curve for Osorio sand obtained by manual sieving

The PSD curve found in the present study (Figure 3.3) was not completely in accordance with previous data (FESTUGATO, 2008). The disagreement between PSD curves may be explained by the location where the samples were collected from, and the tests performed; the previous author used laser characterisation for the finer portion of the material, rather than manual sieving. Nonetheless, some of the indexes presented by the author will be used to complement Osorio sand characterisation in the present study: maximum and minimum void ratios (e_{\min} and e_{\max}), and specific gravity (G_s) (FESTUGATO, 2008). Those values are presented in Chart 3.3 together with the coefficients of uniformity (C_u) and curvature (C_c), and the effective and mean diameters (D_{10} and D_{50}).

Chart 3.3: Physical properties of Osorio sand

e_{\max}	e_{\min}	G_s	C_c	C_u	D_{10} (mm)	D_{50} (mm)
0.90	0.60	2.62	0.11	1.30	0.10	0.12

3.3.2 Cement

The cementitious bonding material chosen for the present work was Portland cement type III (ASTM C 150; ASTM, 2009). This type of cement is characterized by the early hydration, responsible for its early high compressive strength and stiffness. Figure 3.4 compares the expected strength gains of different types of Portland cement over time. It clearly illustrates the steep compressive strength gains of Portland cement type III very early in the hydration process. Specific gravity (G_s) of Portland cement type III is equal to 3.15 (FOPPA, 2005).

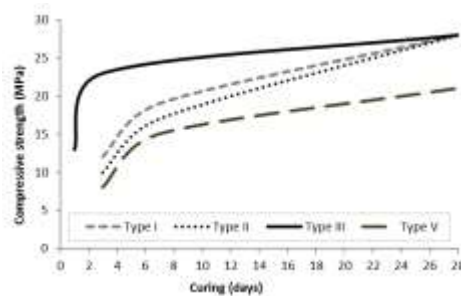


Figure 3.4: Expected compressive strength gains over time of different types of Portland cement

(based on: ASTM C150/C150M; ASTM, 2017a)

3.3.3 Calcined gypsum

According to ASTM C11 (ASTM, 2017b, p. 2), calcined gypsum ($\text{CaSO}_4 \cdot 2\text{H}_2\text{O}$ or calcium sulphate dehydrate) is defined as “a dry powder; primarily calcium sulphate hemihydrate, resulting from calcination of gypsum; cementitious base for production of most gypsum plasters.”

A 1 kg bag of dry powdered calcined gypsum was purchased from a local supplier. The material was kept inside the same plastic bag it was purchased during the entire testing period. The calcined gypsum was not physically characterised, as it was simply used to obtain the gypsum-cement mixture used for capping specimens and as a BE-specimen couplant. For further details on the application of calcined gypsum in the present study, see 3.4.5 and 3.4.8.4.

3.3.4 Water

To avoid variability, distilled water at room temperature was used in all experiments.

3.4 METHODS

This section includes all methods used in the present work, from basic procedures (Osorio sand preparation and characterisation), description of specimen fabrication and their curing conditions, and specimen capping, to a detailed description of more complex methods (anisotropy assessment, and UPV, BE, and triaxial tests).

3.4.1 Preparation of Osorio sand samples

A bag containing 20 kg of moist Osorio sand was purchased from a local supplier. The sand was gradually dried on a stove, and stored into a plastic container without a lid. At the end of the drying process, all the sand was homogenised, quartered (see 3.4.1.1), and stored into sealed plastic bags containing about 800 g of sand each. Because the drying process was conducted over a few days, the soil was exposed to the environment before being packed and, as result, was characterized as being air dried. Therefore, hygroscopic humidity was measured (3.4.3.4) to correct the water content during specimen moulding.

3.4.1.1 Quartering process

Reducing aggregate samples to testing size was conducted according to ASTM C702/C70M (ASTM, 2011a), Method B – manual quartering (Figure 3.5). After drying, the remaining soil

(about 15 kg) was progressively quartered until sub-samples with approximately 800g were obtained, which were stored into sealed plastic bags.

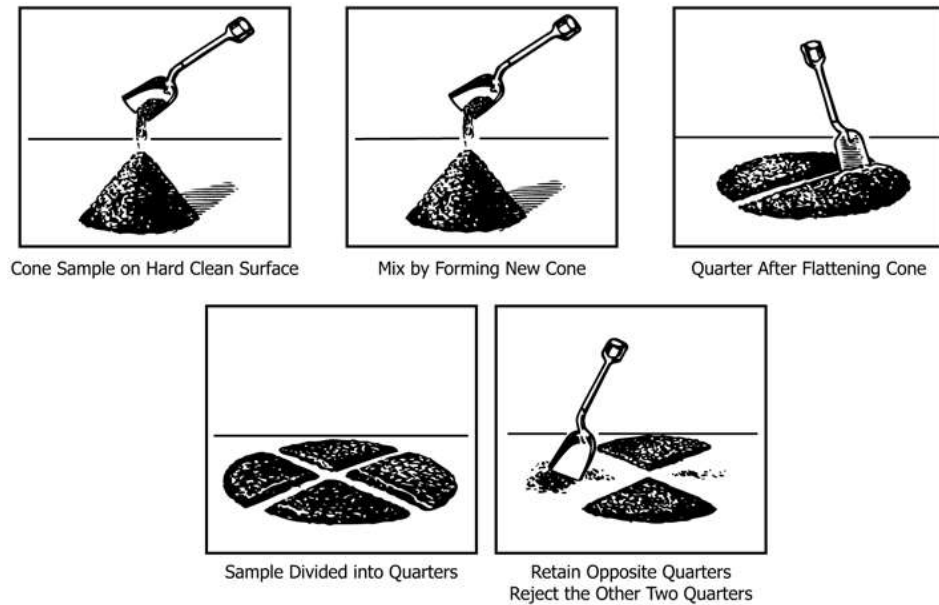


Figure 3.5: Reducing samples of aggregate to testing size by manual quartering (ASTM, 2011)

3.4.2 Cement conditioning

A sealed plastic container with approximately 2 kg of Portland cement type III from the same lot was separated for the tests in order to guarantee homogeneity. The container was only opened whenever necessary, and immediately closed again.

3.4.3 Characterisation procedures

Required laboratory physical index tests (specific gravity, maximum and minimum void ratio, and water content) are described below.

3.4.3.1 Particle size distribution

Particle size distribution (PSD) was conducted in accordance with ASTM D6913 (ASTM, 2004), with a single sieve-set. To reach the 100-g portion required for PSD determination, one 800-g bag of Osorio sand was reduced by quartering, as described above (3.4.1.1).

3.4.3.2 Specific gravity

The specific gravity (G_s) for the tested Osorio sand was obtained according to ASTM D854 (ASTM, 2014a), Method B – for oven dried specimens. Entrapped air was removed by simultaneous application of vacuum and heat (boiling). The nominal capacitance of the used pycnometer was 500 ml. De-aired water, as indicated in the norm, was not available, and distilled water was used instead.

The specific gravity test for Portland cement was that obtained by Foppa (2005) in accordance with the Brazilian norm NBR NM 23 for grain unit weight of cementitious bonding materials (ABNT, 2001).

3.4.3.3 Maximum and minimum void ratio

Maximum and minimum void ratios used in this study were those previously described by Festugato (2008). These values were obtained according to ASTM D4254 – Method A (ASTM, 2014b) and ASTM D4253 (ASTM, 2014c), with some adaptations due to differences in the equipment used.

3.4.3.4 Water content

Water content (w) was obtained according to ASTM D2216 (ASTM, 2010), Method B – with an accuracy of $\pm 0.1\%$. No desiccator was used, and samples were left overnight inside an oven at the temperature of $100 \pm 5^\circ\text{C}$.

3.4.4 Specimen moulding and curing

Both cylindrical and cubical specimens were moulded and cured in the same conditions. Cylindrical specimens were prepared in a tripartite mould 50 mm in diameter and 100 mm high, held together with a round clamp. On the other hand, cubical specimens were prepared in a specially designed mould with sides measuring 100 mm. The cubical mould was composed by a base, four individual vertical walls, a collar, and a square clamp to keep the walls in position. The cylindrical and cubical moulds are presented in Figure 3.6.

The contents of each individual 800-g bag of Osorio sand was once again mixed before being separated and weighed for specimen fabrication. The total amount of soil for each cylindrical specimen was approximately 300 g, and 1,600 g for cubical specimens. Portland cement type III was then weighed and mixed with the soil by placing both materials inside a plastic bag and

vigorously shaking it. After a uniform blend was obtained, the dry mixture was transferred to a metallic bowl, into which previously weighed distilled water was added and mixed until a homogeneous mixture was obtained. The optimal water content for compaction in relation to the dry mass of the specimen was 10%. Three small quantities of the mixture were separated and placed into small metal recipients and oven-dried ($100^{\circ}\text{C} \pm 5^{\circ}\text{C}$) until no change in mass occurred, and real water content was calculated according to proper equation ($w = W_w/W_s$).

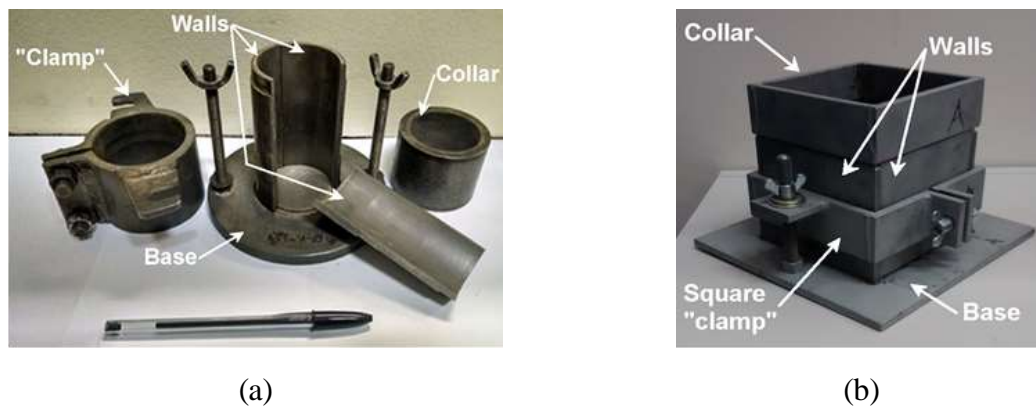


Figure 3.6: Moulds used for fabricating specimens – (a) cylindrical; (b) cubical

(based on: MARQUES, 2016 and SILVANI, 2017)

Cylindrical and cubical specimens were prepared with 3 and 6 layers each, respectively. The amount relative to each layer was weighed and placed into a sealed plastic container, to be opened only at the moment of moulding. Each layer was statically compacted using a hydraulic jack. The top of each layer was scarified using a knife before placing the next. When completed, specimens were then carefully de-moulded and its dimensions and mass immediately measured. Mass measurements were conducted on digital scales with an accuracy of 0.01 g. Linear measurements were performed with a calliper with an accuracy of 0.1 mm. Specimens were then placed inside plastic bags, to avoid significant changes in c content, and curing took place in ambient temperature. Cylindrical and cubical specimens can be seen in Figure 3.7.

Noteworthy, the amount of all materials (solids and water) was increased in about 15% to compensate for any eventual material loss and also to allow water content measurements. To ensure that the initial cementitious reactions were not disturbed, the time taken from cement-soil mixing to specimen de-moulding was always less than one hour.



Figure 3.7: Cured Osorio sand/cement specimens – (a) cylindrical specimen (b) cubical specimen.

3.4.5 Capping process

The decision to conduct specimen capping was based on the fact that during the pilot UPV tests conducted with cubical specimens with η/civ equal to 31.90, the area where the shear-wave couplant was applied started to deteriorate, creating increasingly deeper cavities after each measurement.

It may be argued that the capping process could affect UPV measurements. As a result, whether the capping process affected the shear-wave measurements or not needed to be verified. The most direct way to verify the effect of specimen capping was by measuring shear-waves travelling through cylindrical specimens with and without capping (see more details in 3.4.5.3). The same capping mixture was used on both cylindrical and cubical specimens, as described below (3.4.5.1).

3.4.5.1 Capping mixture components and preparation

Pilot tests were conducted to define the best proportion of the materials composing the capping mixture, taking into consideration the workability and consistency of the material. Initially, only calcined gypsum and water were mixed together. However, the very quick setting of the mixture made its application difficult. Then, with the intention of delaying the setting process, a small amount of Portland cement type III was added to the mixture. After a few attempts, the proportion of 10% of cement in relation to the mass of calcined gypsum was established. Likewise, to reach the adequate consistency, water addition had also to be fine balanced. The amount of water needed to achieve the desired fluidity to form an even smooth surface should also be enough to prevent capping mixture penetrating into the specimen, which could affect measurements. Therefore, the established water-solids (gypsum and cement) ratio was 1:1.

Nonetheless, despite the care dedicated to establishing the best capping mixture components ratio, penetration into the specimens was still observed. However, further reductions in water content would strongly affect material workability. Thus, considering the existing limitations, a more fluid mixture was considered as providing the best possible capping conditions.

Calcined gypsum and cement were individually weighed and then mixed together (Figure 3.8 – a) until a uniform colour was observed. After that, previously weighed distilled water was added to the dry components and mixed until a homogeneous paste was achieved (Figure 3.8 – b). Approximately 3 min after mixing, the paste became less fluid and more consistent (Figure 3.8 – c) and ready for capping.

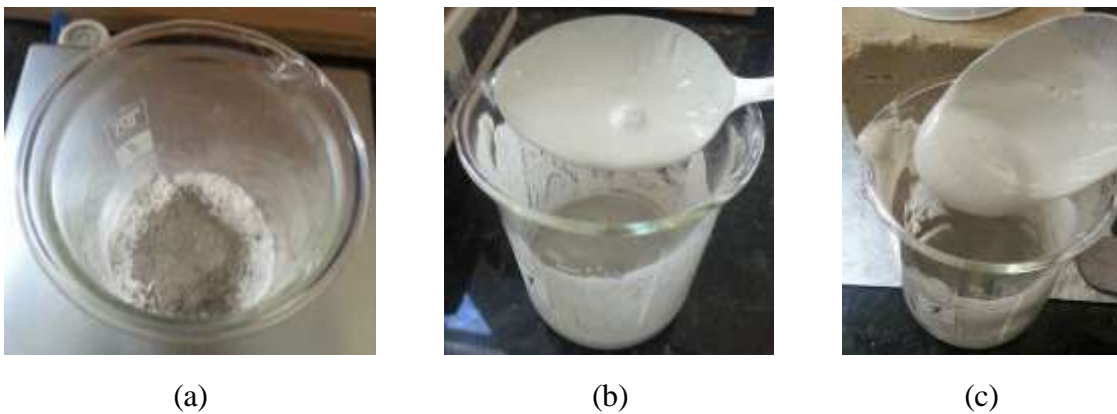


Figure 3.8: Capping mixture production – (a) dry solids are added together; (b) resulting mixture after adding distilled water; (c) capping mixture appearance 3 min after mixing

3.4.5.2 Specimen capping

Taking into consideration that the capping process in the present work was just conducted to prevent specimen surface deterioration, it was designed to be as simple as possible, using commonly found materials.

Cubical specimens: The mould used for pouring the capping mixture onto the cubical specimens was simply a plastic cup cut in the shape observed in Figure 3.9 – (a); the bottom of the cup was cut off to create a kind of a grip to facilitate handling. The capping mixture was poured inside the plastic mould positioned on the surface of the specimen (see Figure 3.9 – a, and Figure 3.9 – b). Then, the mixture was homogeneously distributed inside the plastic mould

using a spoon (Figure 3.9 – c), after which the mould was removed (Figure 3.9 – d), and the paste regularized and smoothed with a spatula (Figure 3.9 – e). The aspect of the finished capped surface is presented on Figure 3.9 – f. For cubical specimens, each batch of capping mixture was enough to cover two faces at a time. Therefore, three mixtures were consecutively prepared to cover all the six faces.

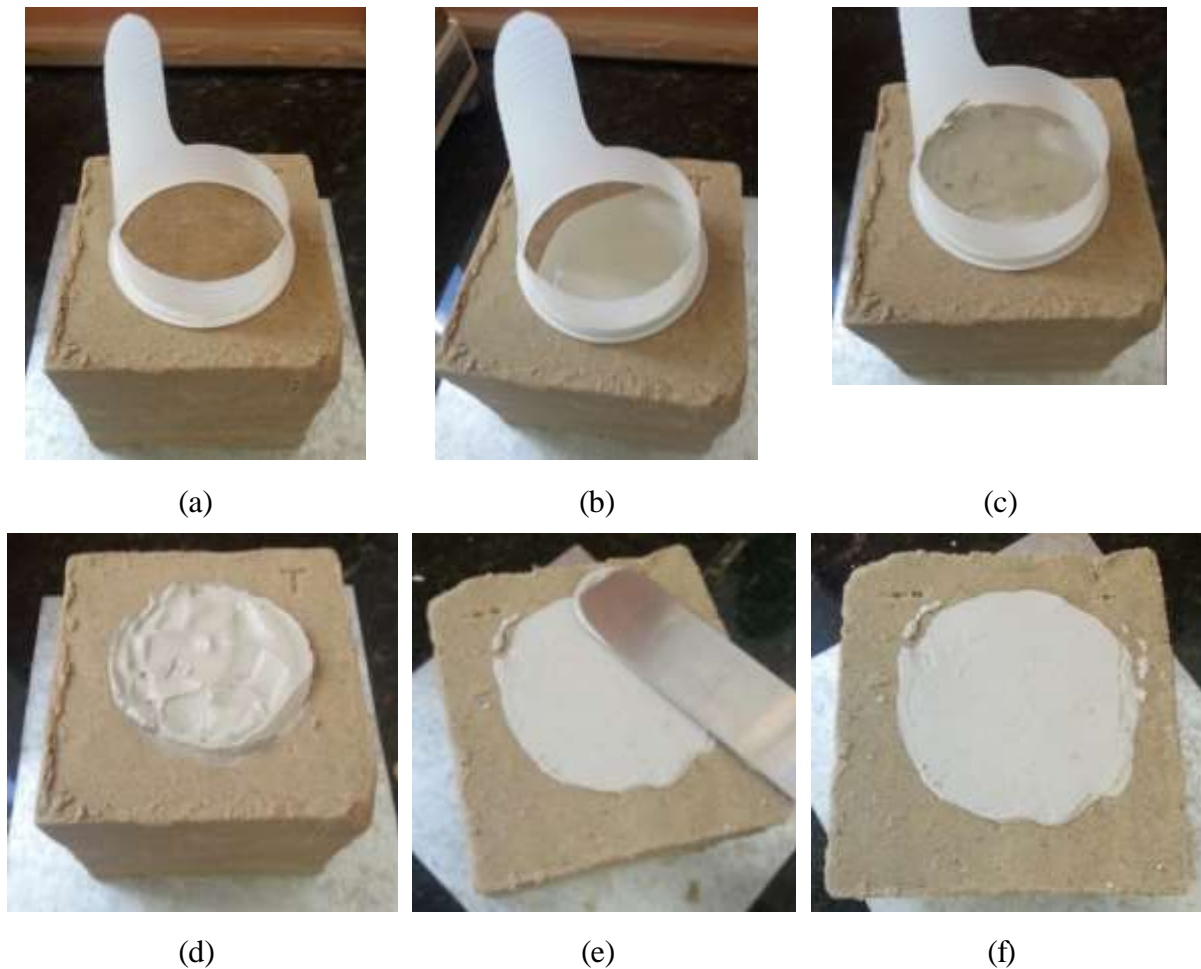


Figure 3.9: Capping of cubical specimens – (a) mould made with a plastic cup to delimit the application of the capping mixture; (b) mixture poured into the mould; (c) capping mixture homogeneously distributed; (d) capping mixture without the mould; (e) regularization of the capping mixture surface; and (f) aspect of the finished surface

Cylindrical specimens: in preparation to receive the capping mixture, cylindrical specimens were tightly wrapped with a large adhesive tape with the sticky side facing out. Then, the tape

was moved upwards to the edge of the specimen forming a kind of collar (Figure 3.10 – a). The capping mixture was then poured onto the surface of the specimen and levelled with a spatula (Figure 3.10 – b). After the top surface capping had sufficiently hardened (about 5 min), the tape was moved downwards so that the same process could be conducted on the opposite side of the specimen (Figure 3.10 – c to f). As a result, differently from the cubical specimens, each extremity of the cylindrical specimens required a single batch of capping mixture).

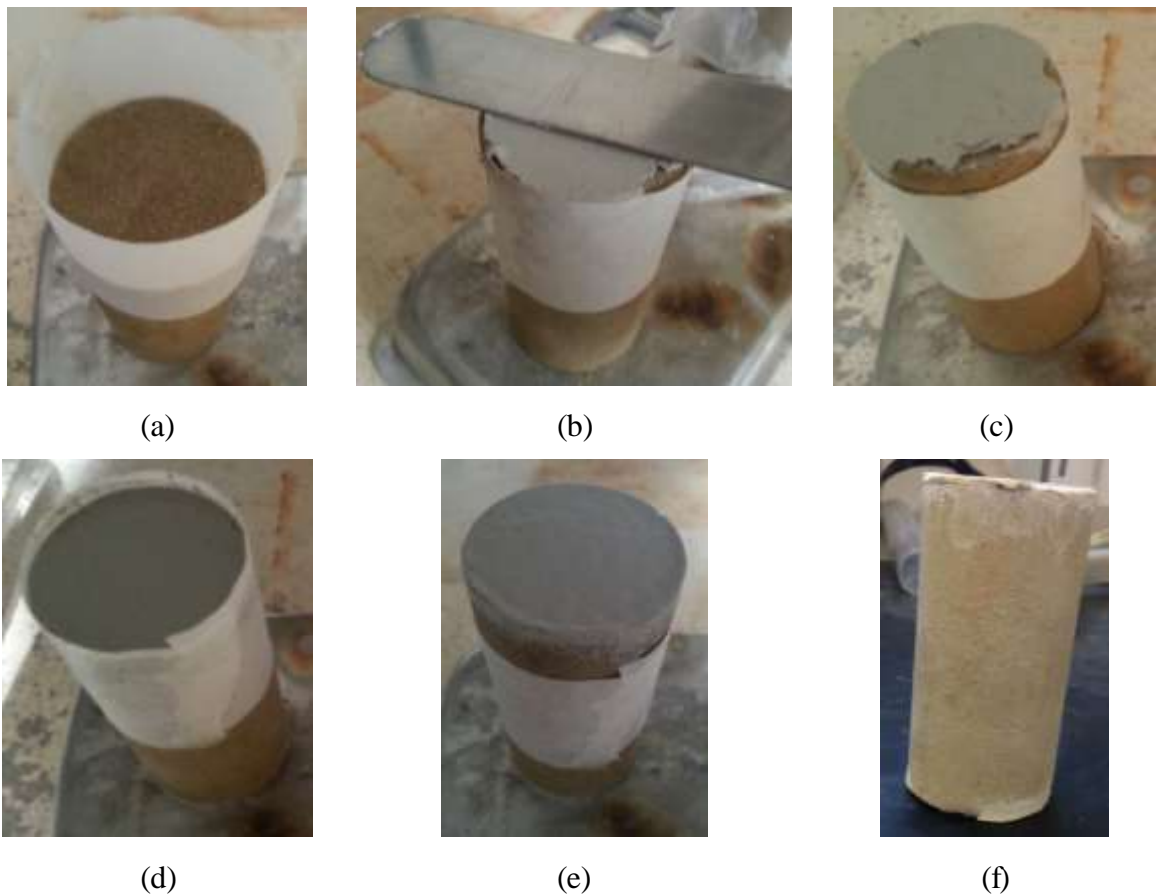


Figure 3.10: Capping of cylindrical specimens – (a) adhesive tape wrapped around the specimen; (b) capping mixture being levelled up; (c) finished top surface; (d) bottom of the specimen with the capping mixture; (e) finished bottom surface; (f) specimen prepared with the capping mixture on the top and bottom surfaces

Capping was always conducted 24 hours after specimen preparation (day 1 of cure). The first UPV test was performed about 3 hours after the capping procedure, as suggested by the norm

ASTM D1632 - “Making and Curing Soil-Cement Compression and Flexure Test Specimens in the Laboratory” (ASTM, 2007). Although this norm has been withdrawn, and not replaced by another norm, the section “Capping specimens” states that “The caps shall be as thin as practical and shall be aged sufficiently so that they will not flow or fracture when the specimen is tested (suggested time 3 h [...])”. Therefore, the adopted waiting time seemed to be adequate for a non-destructive test, such as the UPV test. Cap thickness ranged from 2 to 4 mm. After the cap had hardened, linear measurements between opposite sides were conducted to determine the correct distances between UPV transducers.

3.4.5.3 Calibrations

Because extra layers of capping mixture were added onto the surface of specimens, a question remained whether they would affect wave travelling measurements during UPV tests. Therefore, calibration was conducted to verify whether the time added by the cap layers was significant for the equipment sensitivity or not. Besides, as the initial specimen mass was altered, specimen shear modulus was also affected and had to be recalculated – see Equations (2.5) and (2.6).

The alternative to calibrate the added time due to layers of capping was to fabricate two identical cylindrical specimens (with the same target dry unit weight and η/c_{iv} ratio), and cap only one of the specimens. The waves travelling time through each one of the specimens were measured, their velocities calculated and then compared – the distance between transducers also had to be corrected for capped specimens, as transducers were slightly more distant from each other due to capping. The difference between measured velocities (ΔV) between the identical specimens (with and without capping) were obtained through Equations (3.1) and (3.2) for each test day. Then, each ΔV value was individually divided by total capping thickness (considering both the top and bottom layers), and this ratio ($\Delta V/d_{cap}$) was plotted over time. The best fit for each kind of wave velocity was obtained, and the fit equations were used to correct the time for all capped specimens. The fit equation used was: $y = f(x) \Rightarrow \Delta V/d_{cap} = f(t)$ / t: time of curing; / $\Delta V = [m/s]$ and $d_{cap} = [m]$.

$$\Delta V_s = V_{s_{k,not-cap.}} - V_{s_{k,cap.}} \quad (3.1)$$

$$\Delta V_p = V_{p_{k,not-cap.}} - V_{p_{k,cap.}} \quad (3.2)$$

Where: “ ΔV_s ” (s-waves) and “ ΔV_p ” (p-waves) are the difference between measured velocities obtained from capped and non-capped specimens; “ $V_{s_{k,not-cap}}$ ” and “ $V_{s_{k,cap}}$ ” are the s-wave velocities measured at “k” day of cure for non-capped and capped specimens; “ $V_{p_{k,not-cap}}$ ” and “ $V_{p_{k,cap}}$ ” are the p-wave velocities measured at “k” day of cure for non-capped and capped specimens.

First, each measured day was inserted into the fit equation, then the respective capping thickness was used to multiply the individual values calculated from the fit-equation, resulting in a velocity (m/s). This velocity was added to the velocity initially measured for capped specimens – as both shear and compressional wave velocities of capped specimens were consistently smaller than non-capped specimens. Finally, wave travelling time was back-calculated based on the new velocity (using the original specimen height, without the capping layers). The values found were considered the corrected time and velocity. This procedure was repeated for all capped specimens using the same fit equations regardless of the dry unit weight. Calibration process results are presented in 4.3.1.

Few attempts were made to correct changes in mass over time. As the water content of both specimens and capping paste varied with time, to separate their individual contribution was difficult. Therefore, it was decided to follow the simplest possible alternative, described as follows. The initial total amount of moist capping paste was subtracted from the combined measured specimen-capping total mass at each test day. The implications and limitations of this procedure are discussed in 5.3.2. The moist capping mass (M_{MP}) added to the specimen on day 1 of cure was calculated through Equation (3.3); where “ $M_{M(S+P),1}$ ” is the specimen moist mass of specimen and capping paste on day 1 of specimen cure, and “ $M_{MS,1}$ ” is the specimen water content right before the capping process. Then, water content was calculated through proper equation ($w = W_w/W_s$), and plotted over time for qualitative analysis. Moreover, natural unit weight was also calculated ($\gamma = W/V$).

$$M_{MP} = M_{M(S+P),1} - M_{MS,1} \quad (3.3)$$

3.4.6 Anisotropy assessment

Wave propagation analysis is based on the premise that the material is isotropic. However, soils are usually cross-anisotropic materials (FERNANDEZ; SANTAMARINA, 2001; CLAYTON,

2011). The assumption of cross-anisotropy is usually applied to natural soils. Because the geomaterial studied in the present work was not studied in its natural form, the anisotropy hypothesis had to be investigated in its cemented form. As UPV tests are based on the propagation of waves, only anisotropy at small strains was verified in the present work.

Cubical specimens are more suitable for this sort of assessment because its geometry allows investigating the influence of anisotropy on each of the three orthogonal planes. Moreover, their flat surfaces are more adequate for coupling transducers and measuring wave velocities between two opposite faces.

Anisotropy was assessed through the propagation of ultrasonic waves produced by a UPV apparatus (Pundit Lab, Proceq SA, Switzerland), available at LEGG-UFRGS. The velocity in the three directions was measured on day 1, 3, 5, 7, and 14 of cure. Figure 3.11 presents a scheme showing the different tested planes of the cube. UPV measurements were performed in the T-T' direction, which coincides with the compaction direction (axis z), while the planes relative to the A-A' and B-B' directions (axes x and y) were retained by the walls of the mould during the compaction process. See details of UPV procedures in 3.4.7.

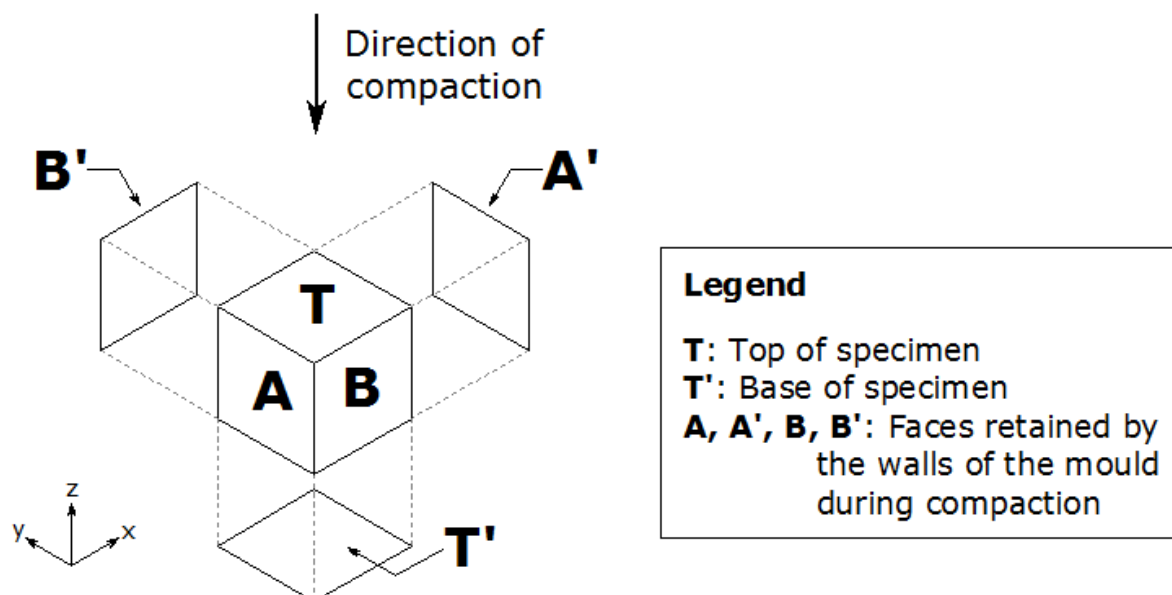


Figure 3.11: Scheme of cubical specimens indicating the direction of compaction (T-T'), and the faces retained by the mould during compaction (A-A' and B-B')

3.4.7 Ultrasound pulse velocity (UPV) tests

UPV measurements were conducted with the Pundit Lab[®] equipment. “Pundit” is the acronym for “Portable Ultrasonic Non-Destructive Digital Indicating Tester”. The expression UPV, used throughout the present work, always refers to the use of “Pundit”.

The UPV equipment sends and receives waves through materials, measuring wave travelling time. The time difference between sent and received waves are the times the compression waves (p-waves, “ t_p ”) and shearing waves (s-waves, “ t_s ”) take to propagate through the material. The distance between the transmitter and the receiver transducers divided by “ t_p ” and “ t_s ” results in the velocities (Equations (2.7) and (2.8)). These velocities are later associated to stiffness through Equations (2.5) and (2.6) – for constrained and shear moduli calculations, respectively.

Small strain-stiffness was accessed by UPV tests on both cubical and cylindrical specimens on days 1, 3, 5, 7 and 14 of curing (for further details, see Chart 3.1). No confining pressure was used during these tests as the UPV equipment is designed to be used exclusively for laboratorial bench tests. Cylindrical specimens were used to investigate stiffness gains over time. Cubical specimens, on the other hand, were used to verify the anisotropy hypothesis of artificially cemented Osorio sand (see 3.4.6).

The UPV equipment was originally designed for rock and concrete tests, and its standards (ASTM D2845, ASTM, 2008; BS1881: Part 203, BSI, 1986) do not cover tests on soils or cemented soils. Thus, all procedures were performed according to manufacturer recommendations in association with the relevant parts of the standards.

3.4.7.1 UPV presentation

The UPV equipment (Figure 3.12) can send both p-waves and s-waves by simply changing the probes. The probes have different shapes and they operate at different frequencies: p-waves are generated by standard 54 kHz transducers; whereas s-waves are propagated by special shear wave transducers that operate at 250 kHz. Each of these transducers uses a different couplant to ensure proper adherence to specimen surface and adequate wave propagation from the probe into the specimen (and vice versa).

The UPV equipment has a resolution of 0.1 μ s and time measurements can range from 0.1 to 9,999 μ s. The transmitters can send waves with 125, 250, 350, and 500V. The receivers have a

variable gain ranging from 1 to 100x for measurements taken directly by the equipment, and 1 to 1,000x when the software Pundit Lab[®], which comes with the equipment, is used.



Figure 3.12: Ultrasound pulse velocity device – (a) compressional waves (p-waves) transducers; (b) shear-waves (s-waves) transducers (PROCEQ, 2016)

The UPV equipment sends a single square pulse. After travelling through the material, this wave is received by the opposite probe, and its signal is amplified. An example of a trigger pulse and the received waveform plotted on an oscilloscope is presented in Figure 3.13.

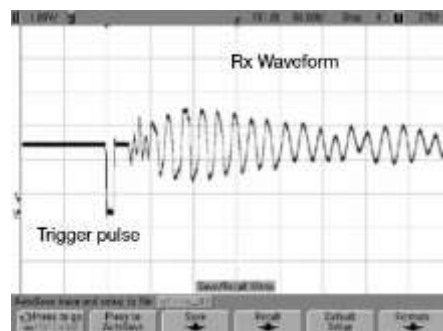


Figure 3.13: Trigger pulse and received waveform displayed on an oscilloscope (PROCEQ SA, 2013)

3.4.7.2 UPV Calibration

Cable-probe wave transmission and reception cause a time delay that affect the measured time. This time delay needs to be measured and then deducted from total wave travelling time. The zeroing procedure was based on the BS1881: Part 203 (BSI, 1986), which states: “Time delay

adjustment should be made while the transducers are coupled to the opposite end of a reference bar for which the transit time is accurately known". Therefore, a calibration rod, supplied by the UPV equipment manufacturer, with a known transit time of $25.4 \mu\text{s}$ was used (Figure 3.14).



Figure 3.14: Calibration rod of the ultrasound pulse velocity equipment

UPV calibration was conducted every time the equipment was turned on, and when probes or cables were changed before any measurement was taken. Calibration consisted of coupling the transmitter and receiver transducers to the calibration rod (Figure 3.15) and turning on the equipment.



Figure 3.15: Calibration rod positioned for p-waves transducer calibration

(PROCEQ SA, 2013)

Long (2000) suggested different materials to be used as couplants for the transducers, depending on whether the tested surface was smooth or rough. In the present work, p-waves

transducers were coupled using a common medical ultrasound gel. For s-waves transducer, on the other hand, a special gel described as “a non-toxic, water soluble organic substance of very high viscosity” (PROCEQ SA, 2013) was used. Regardless of the couplant, a layer as thin as possible was applied to the transducer to avoid any interferences with measurements. Special care was dispensed during couplant application to prevent the presence of entrapped air between the transducer and the specimen.

After the transducers were coupled to the calibration rod, calibration measurements were performed according to the scheme presented in Figure 3.16. Calibration of both kinds of transducers was conducted with the use of the equipment only, dispensing the use of the software.

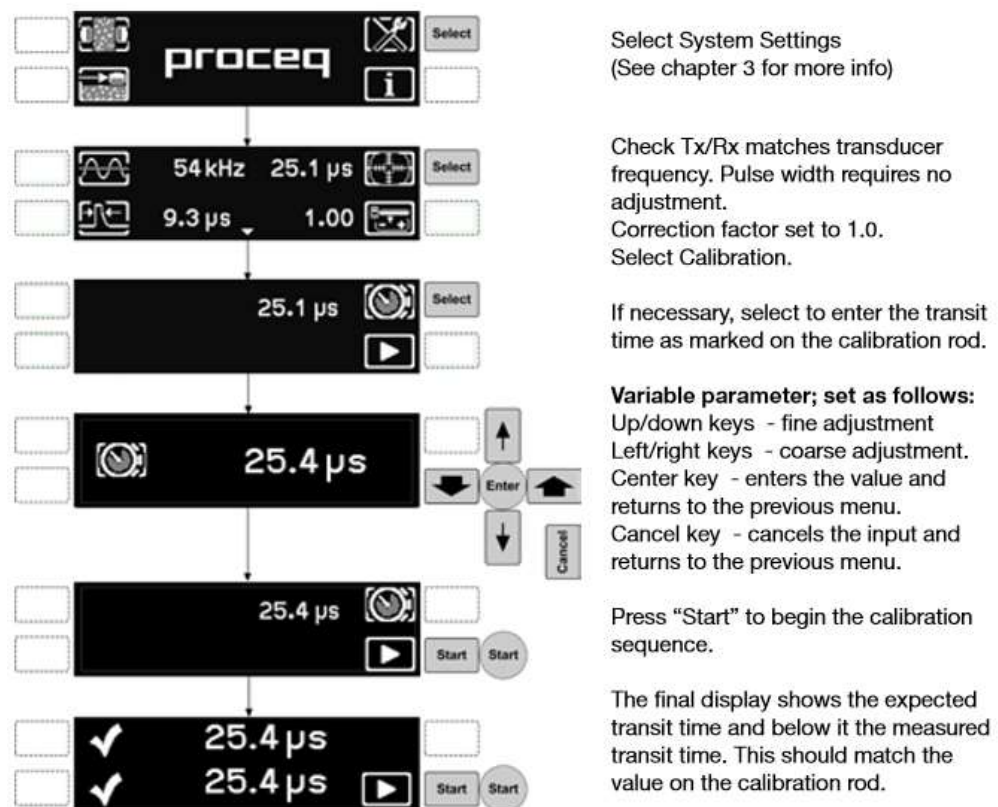


Figure 3.16: Step-by-step calibration procedure
(PROCEQ SA, 2013)

3.4.7.3 Wave measurements

Wave measurements were performed using the direct arrangement (Figure 3.17) in all specimens. With this kind of arrangement, the transferred energy is maximised, and the path

length is known. By knowing the exact distance between the transducers, wave velocity calculation could be accurately conducted (BSI, 1986).

A path length with a minimum distance of 100 mm was always used in this experiment, following the recommended value for concrete specimens – “100 mm for concrete with maximum aggregate size of 20 mm or less” (PROCEQ SA, 2013). The minimum permissible lateral dimension of a specimen is a matter of controversy, and it will be dealt with in 4.6.2. Moreover, no correction relative to ambient temperature was conducted, as it is not required for tests conducted between 10°C and 30°C, either with dry or wet concrete (PROCEQ SA, 2013).

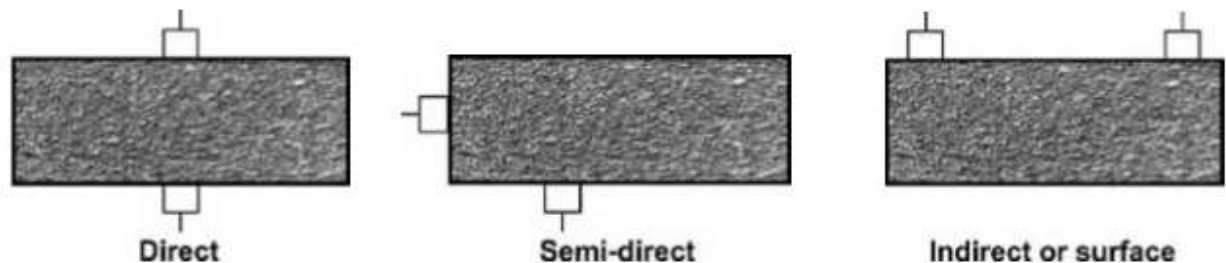


Figure 3.17: Possible transducer arrangements
(PROCEQ SA, 2013)

Before the first UPV test (day 1), specimen volume was calculated and path length, indicated by “d” in Figure 3.18, was measured with a calliper. Because the mass tends to vary as water content within the specimen changes as a result of the cementitious bonding reactions, it had to be measured prior to each UPV test (days 1 – 14). After calibration (3.4.7.2), additional couplant was applied onto the transducers (3.4.7.2), which were then positioned on the specimens according to the scheme presented on Figure 3.18, and tested.

Both transducers were firmly held in place until measurements were complete. P-waves were directly obtained from the equipment screen (Figure 3.19). Although the path length could be introduced (step III), and wave velocity automatically calculated, it was decided against it, and time was simply recorded to facilitate the process. Wave velocity was calculated with the assistance of a spreadsheet after all measurements had been taken. Furthermore, the “AUTO” configuration was selected for transmitter voltage and received gain – Rx gain – (indicated by the two red arrows in Figure 3.19). Although the suggested minimum received signal level is

75% (PROCEQ SA, 2013), accepted measurements were not inferior to 90%. Each measurement was conducted in triplicate, and a mean value of the three measurements was then calculated.

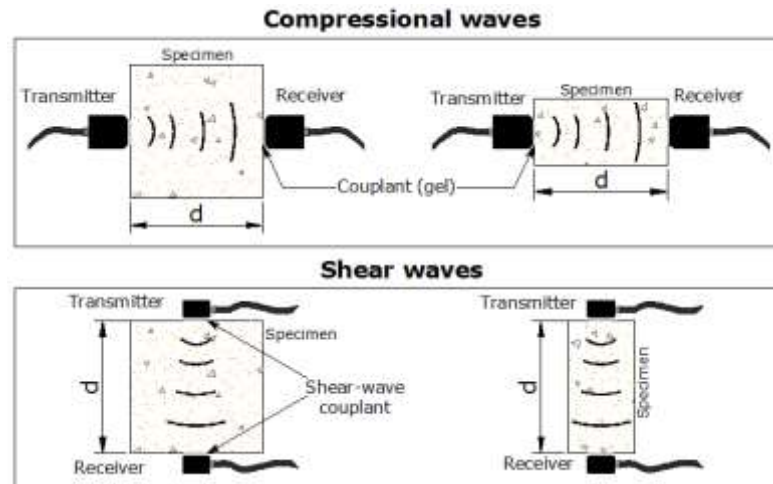


Figure 3.18: Scheme for positioning UPV transducers for p-waves (horizontally) and s-waves (vertically)

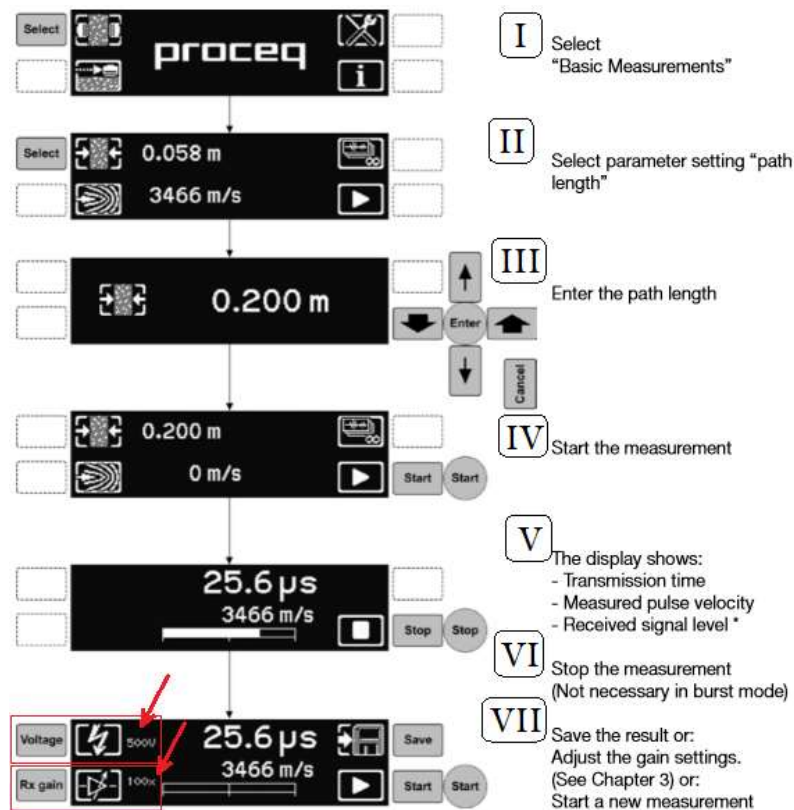


Figure 3.19: Procedure for p-waves measurement
(based on: PROCEQ SA, 2013)

S-wave measurements were slightly different from p-wave measurements, as it was always conducted using the Pundit Lab[®] software. Individual pulses were continuously emitted, and the transmitter voltage and Rx gain were manually adjusted until a stable and clear waveform was visualised (Figure 3.20), after which the file was saved. The same procedure was repeated three times, and the mean value was obtained from the three measurements.

Figure 3.20 illustrates the first small waves (p-waves) as indicated by the time 71.4 μ s. The time measured by the software roughly agreed with the time measured directly by the equipment. The s-wave, on the other hand, is characterised by the peak seen at around 130.8 μ s, after the p-wave.

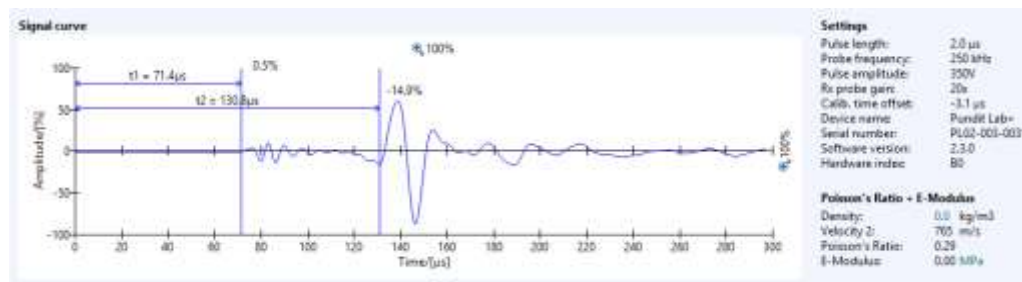


Figure 3.20: Time travelling measurement for s-waves using the software Pundit Lab[®]

After the p-waves and s-waves were measured, their corresponding moduli were calculated. As the s-wave arrival time is expected to take place after p-waves, p-waves were used to guide the interpretation of s-waves, which are the main objects of the present study.

3.4.8 Bender elements (BE) tests

Measurements were conducted using two specially manufactured pairs of BE (see Appendix A). Similarly to the UPV equipment, BE send and receive waves through materials and measure time. However, the BE fabricated for the present work was only capable of sending shear waves, not p-waves. Travelling time (t_s) was defined as the time taken by the waves to propagate through the material. The distance between the tips of BE (d_e , presented in Figure 2.17) divided by t_s was used to calculate velocity with Equation (2.8). Bulk unit mass was calculated by dividing the mass by the (total) volume of the specimen. The bulk unit mass was associated to the calculated velocity in order to obtain stiffness with Equation (2.6) – shear modulus calculation.

Only cylindrical specimens were used to obtain stiffness with BE under two different conditions: bench tests, which measured stiffness gain over time due to cementation (up to day 14 of cure); and triaxial tests, which measured stiffness degradation on day 7 of cure (for further details, see Chart 3.1 and Chart 3.2). Bench tests were conducted with no confining pressure, and small-strain stiffness was measured on days 2, 3, 4, 5, 6, 7, and 14 of cure. On the other hand, triaxial tests were performed with effective confining stress equal to 50 kPa, which permitted that both small-strain stiffness and intermediate stiffness (during shearing) measurements were performed with BE.

Regardless of type of test (bench and triaxial) and each pair of BE, the procedure was the same and, therefore, no distinction was made when describing the process. One of the main issues concerning the use of BE is the fact that no standard procedure is available. Therefore, the procedures presented in this study are a combination of information found on the literature, as well as suggestions supplied by partner universities in England and Australia.

3.4.8.1 BE Calibration

After the entire BE system was completed, including the amplifier, the system was calibrated. BE calibration included: time-delay calibration, conducted similarly to the UPV tests (3.4.7.2); and couplant effect calibration. These calibrations are described in detail in the following paragraphs. Signal quality was also evaluated.

With the entire system assembled and ready for measurements (see Appendix A.1), BE transmitter and receiver were put in direct contact (tip-to-tip). The pair of BE was held manually, without the use of clamps. With the pair of BE touching each other, a sine pulse was sent through the transmitter. Then, transmitted and received signals were verified on the oscilloscope screen. Whenever necessary one of the BE was rotated 180° until a suitable image showing the first deflections of the two peaks signals coinciding was obtained. Then, an arrow (red arrow) was drawn on the surface of each BE pedestal to indicate the correct alignment (Figure 3.21).

With the pair of BE still in direct contact, work frequencies were tested to verify if the fabricated BE was capable of vibrating within the same frequency range (50 Hz – 20 kHz) reported in the literature (2.5.1). Due to limitations imposed by the amplifier, the smallest frequency that could be tested was 1 kHz. Tests were conducted until 20 kHz, demonstrating BE adequate response. Moreover, the air-resonance produced by the bench BE pair could also be obtained (Figure

3.22). Although the resonance frequency is expected to alter once the BE pair is embedded into the tested soil, the graph provides an idea of BE behaviour.

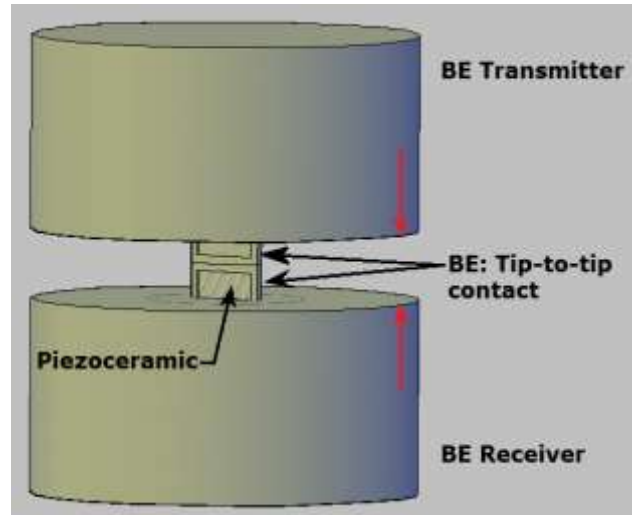


Figure 3.21: Manually held BE in direct contact (tip-to-tip) for BE peak signal alignment (red arrows)

Figure 3.22 was obtained by sending continuous sine waves with same voltage amplitude and increasing frequency. The voltage amplitude response of the signal captured by the receiver was then plotted against the input frequency.

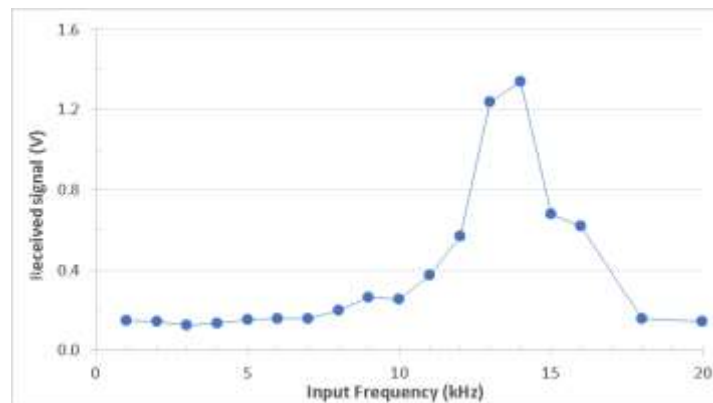
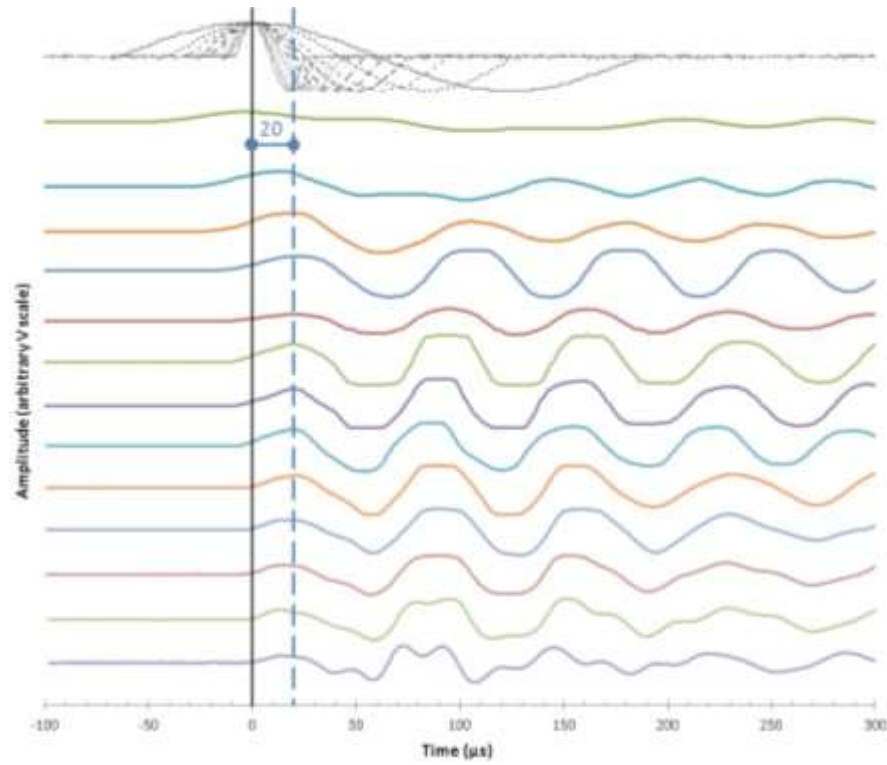
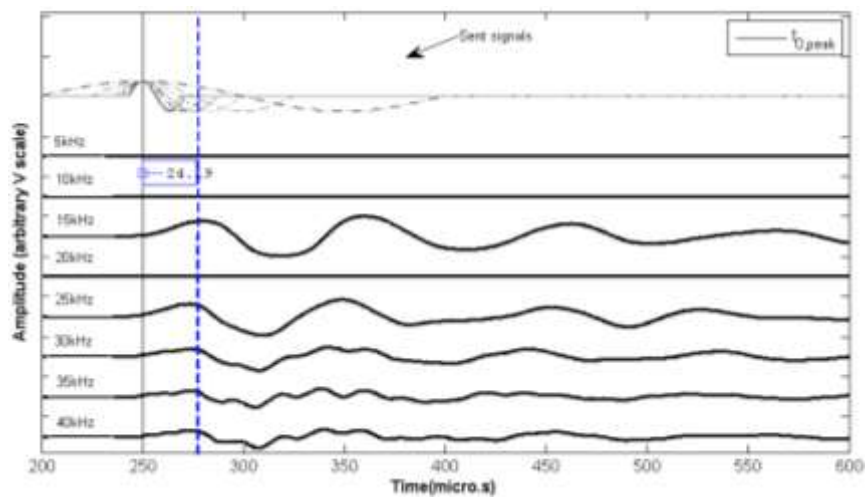


Figure 3.22: Amplitude frequency response of Bender elements in direct contact (tip-to-tip), with no confinement and all frequencies subjected to same sinusoidal input voltage ($\pm 1V$)

The time spent for the wave propagate through cables, transducers, and the amplification system is called time delay. This time delay was measured by manually holding the BE pair in contact, sending waves with different frequencies and, then, plotting sent and received signals for all frequencies in the same graph, such as Figure 3.23 – (a) and (b).



(a)



(b)

Figure 3.23: BE bench pair responses in direct contact – (a) before any bench tests; (b) after all bench tests

Figure 3.23 – (a) was obtained right after the entire system was assembled and before any tests on the cemented specimen was conducted, preventing any degradation to the BE pair; Figure 3.23 – (b), on the other hand, was obtained after all tests on cemented sand were performed, and the BE pair was visibly degraded. As the damage to the BE pair occurred continuously over the tests, it was difficult to establish the point at which the damage was enough to generate the difference observed between the two measured values (20.00 μs and 24.19 μs). As a consequence, the mean value of the two was used as the BE system time delay in the calculations (22.085 μs).

To assist the calibration process and the qualitative analysis of signal quality, two calibration nylon cylinders (Figure 3.24 – a and b) were manufactured (Appendix A.4.7). Signal quality assessment and time-delay correction of the entire system was performed using the slotted nylon cylinder (Figure 3.24 – a). The size of the slot was such that the BE could be tightly fitted in it. To assess couplant effect on BE measurements, a cylinder with circular cavities filled with the coupling material on both extremities was used (Figure 3.24 – b). Although the test cylinder material has a different stiffness in comparison to soil, it presents less discontinuity on a microscale, producing a clear signal without noise.



(a)



(b)

Figure 3.24: Calibration cylinders for BE tests – (a) cylinder with a cross sectional slot on both extremities for signal quality evaluation and time-delay correction of the entire system; (b) cylinder with circular holes on both extremities to assess couplant effect

Figure 3.25 illustrates the assembly of the system with the slotted calibration cylinder. BE cable arrangement was of utmost importance. Extreme care was taken to keep the cables as straight as possible to prevent noise generated by electromagnetic induction.

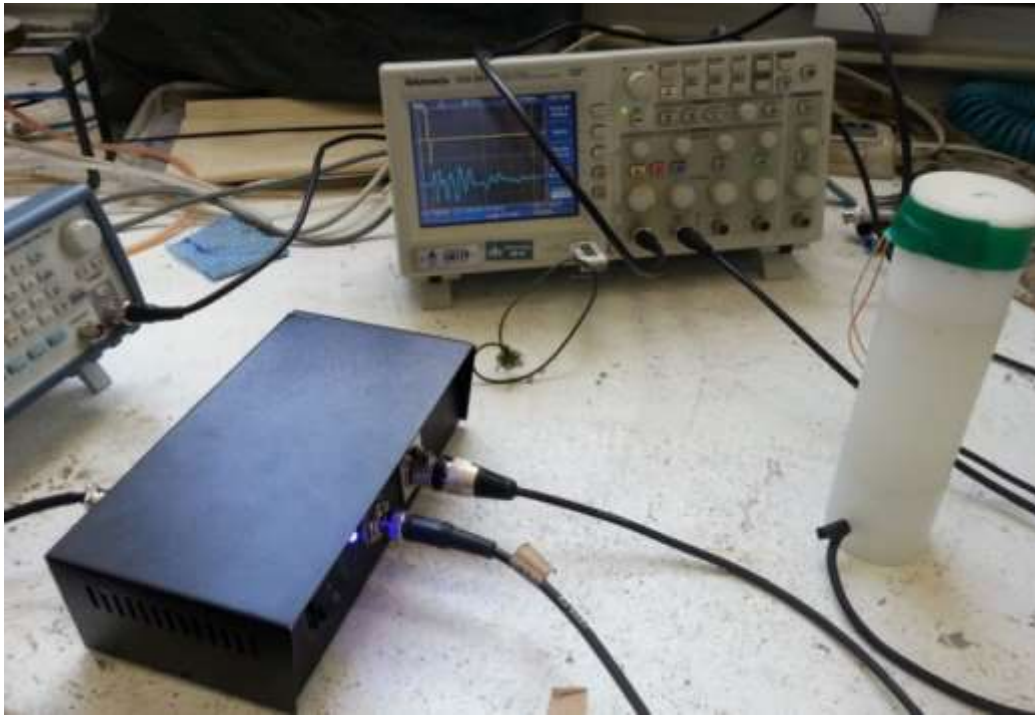


Figure 3.25: Bench bender elements system during calibration using the slotted nylon cylinder

A frequency sweep was performed, and the results can be observed in Figure 3.26. Based on the figure, it was possible to conclude that the fabricated pair of BE was actually capable of transmitting and receiving clear signals. Although peaks became more evident with increased frequencies, signal oscillation also became more apparent. Based on this observation, frequencies of 30 kHz or 35 kHz were chosen as the ceiling for BE excitation under the tested conditions.

The dashed red line (Δt_{ultras}) presented in Figure 3.26 is respective to the UPV measurement obtained with the slotted calibration cylinder. As matter of fact, the position of the line is the result of the UPV measurement plus the BE system time delay (22.085 μs). The shear-wave travelling time measured by the UPV equipment is presented in Figure 3.27, the value of 82.3 μs (indicated by the red arrow) is the measured time for s-wave.

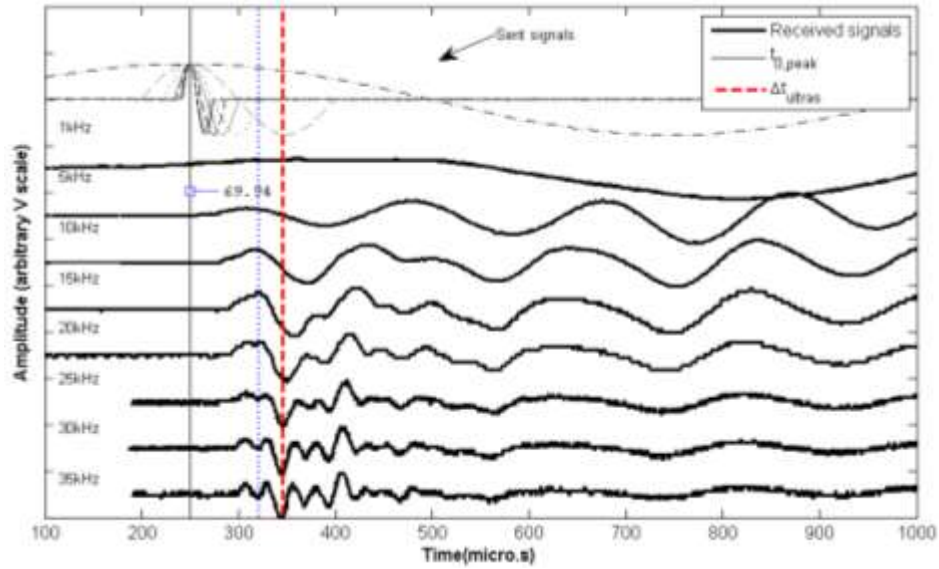


Figure 3.26: Waves captured by the pair of bench BE tested with the slotted nylon calibration cylinder

Returning to the Figure 3.26, the dotted blue line was interpreted as the first-peak arrival time; the value of $69.94 \mu\text{s}$ minus the time delay (which resulted in $47.855 \mu\text{s}$) is the s-wave travelling time measured by the BE bench pair, and interpreted using the time domain (peak-to-peak distance). Although the difference between the two methods (BE an UPV) are relevant, the discussion on the differences between the two methods was not the focus of the present chapter. Therefore, both methodologies will be properly compared in chapter 5. Although BE results interpretation is a source of disagreement in the literature, in the specific case of calibration rods, UPV signal interpretation was confusing as the shape of the received waves was different from that expected.

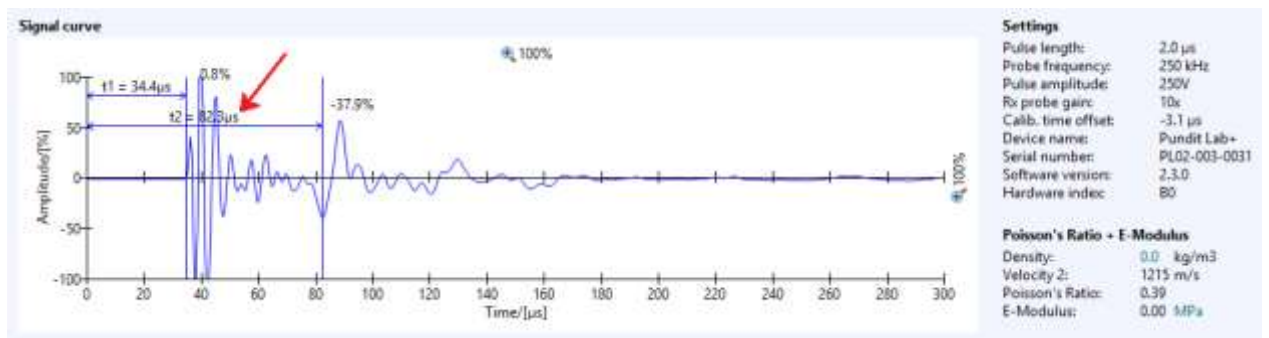


Figure 3.27: UPV test for shear wave propagating through the slotted nylon calibration cylinder

The effects of the couplant on BE measurements were evaluated relative to couplant mass change, and its impact on stiffness gain over time due to its hardening process. These assessments used the calibration cylinder with circular cavities (Figure 3.24 – b), which were filled with the same calcined gypsum-cement paste used for capping (for further details, see 3.4.5.1). These tests were conducted under ambient conditions only.

Couplant mass change correction was limited by the fact that the calibration cylinder possesses porosity different than that of the tested soil. Because of that, actual changes in couplant water content were probably different than that of the calibration cylinder. Nonetheless, this was as close as possible to test conditions. The calibration cylinder with circular cavities was filled with the couplant and the BE transducers were introduced. The entire calibration cylinder-BE set was daily weighed, and couplant water content was calculated on each test day using proper equation ($w = W_w/W_s$). Then, water content was plotted versus couplant curing time, and the best-fit to the curve was chosen. Using the best-fit equation, couplant water content was calculated for each BE test day, and couplant total mass was calculated and subtracted from the specimen-BE mass. The corrected unit weight was calculated by subtracting the couplant mass (with the corrected water content) from the specimen mass, and the specimen volume less the volume from the excavated cavities.

This mass correction was necessary only for bench tests. Triaxial tests did not require this calibration because all voids were filled with water to reach specimen total saturation ($S_r=100\%$). Further details regarding saturation of cemented soils using back pressure with the B-value is discussed in 3.4.9.5. Even though specimens had their water content changed before being inserted into the triaxial chamber, once the saturation point was reached and all voids were filled with water, water volume weight could be simply added to the initial dry mass of the specimen. However, the main issue regards the real amount of voids volume on the test day, once cementitious reactions tend to progressively occupy the voids initially present. Therefore, intending to simplify the analysis, and acknowledging the limitations of the present study, voids volume on day 7 of cure was considered as the voids volume before any cementitious reaction took place. As such, natural unit weight could be calculated using the saturated mass and the calculated volume of the specimen. The adopted unit weight for water, considering the temperature of 22°C, as defined by ASTM D854 (ASTM, 2014), was equal to 9.9978 kN/m³.

The possible hardening effect of the couplant was evaluated at the same time changes in couplant mass were assessed. After cylinder-BE weighing, BE tests were performed every day.

Then, wave travelling time results were plotted over time to evaluate whether travelling time was kept constant over time or not.

3.4.8.2 Work frequencies

The minimum work frequency was limited by the capacitor included in the amplification circuit to uncouple the mains constant current ($CC = 60$ Hz) from the signal (for further details see Appendix A.3). The maximum work frequency was limited by BE capacity to respond to the frequency. Bench tests on artificially cemented Osorio sand indicated a maximum frequency of 30 to 35 kHz, depending on whether a highly or poorly cemented soil was investigated, i.e., soil stiffness. For triaxial tests, although the response to the frequency was higher, it was also dependant on the degree of specimen cementation.

The primary concern about work frequencies was to obtain a clear signal. A detailed analysis of the range of work frequencies is presented in 5.4. It is important to highlight that a range of frequencies, not an individual frequency, should be always swept in order to obtain more reliable results.

Another concern regarding the range of frequencies is the near-field effect, which is dealt with in 2.5.1.2. Table 2.1 presents the range of frequencies (≤ 1.26 kHz and ≥ 43.34 kHz) free of near-field effect for specimens tested by Consoli *et al.* (2012a). As mentioned before, all tests were conducted within the likely near-field effect interval. Thus, further analysis of results considering this effect were required. Furthermore, as UPV tests were conducted with higher frequencies, the comparison between BE and UPV test results would provide further evidence for the discussion of the near-field effect.

3.4.8.3 BE system validation

The validation of the entire BE system was conducted according to each kind of test. For the bench BE pair, initial shear modulus results at 7 days of cure were compared to those previously presented by Consoli *et al.* (2012a). Figure 2.28 presents the equation predicting the expected behaviour of initial shear modulus (G_0) for a specific η/c_{iv} ratio. Therefore, the real η/c_{iv} ratio for each bench test specimen was introduced into the Equation (2.12), as described by Consoli (2012a). Then, using the respective G_0 and the real bulk unit mass of the tested specimen, Equations (2.6) and (2.8) were used to calculate shear wave travelling time. The resulting time was compared to that measured by the fabricated BE.

For the triaxial BE pair, uncemented Osorio sand was tested under an effective confining pressure of 200 kPa and, then, its G_0 was measured by the BE. The measured result was compared to the range of G_0 (Equation (2.11)) presented in the literature for clean and uniform sands (HEINECK; COOP; CONSOLI, 2005).

3.4.8.4 BE coupling procedure

Suitable BE coupling to the surrounding soil is a challenge for stiff soils. Opening BE slots by manually cutting the specimen may result in misalignment between the slots at the top and bottom of the specimen, or with inadequate formats. Hence, two alternatives were tested in the present work in an attempt to achieve reproducible BE slot preparation. In the first attempt, a BE template made of metal was fabricated (Appendix A.4.3). One of the templates was placed at the bottom of the cylindrical mould and followed by specimen moulding according to 3.4.4. The second template was then pushed into the top of the freshly moulded specimen. Usually, templates had to be left in place for three days to avoid distortions in the specimen while handling. Unfortunately, this alternative resulted in slots that were too short for the actual BE and, consequently, further work was required to deepen the slot. The manual operation resulted in irregularities; sometimes the slot was too deep, too wide, or too large. Moreover, the three-day waiting period would prevent measurements early in cementation bonding process, and the idea was abandoned. The positive aspect of using templates would be the precise alignment between the BE transmitter and receptor transducers.

The second alternative, which was adopted for all BE tests in the present work, consisted of opening a round cavity at the extremities of the specimen which was later filled with a material of adequate viscosity to allow wave propagation. This technique permitted that the BE was precisely introduced into this viscous material. The round cavity was selected because of its easy manufacturing and absence of edges – permitting perfect BE positioning into the specimens. Cavities were standardised always with same depth (7.5 mm) and diameter (15 mm).

To ensure proper cavity standardisation, a mould using a sheet of aluminium cut off from a drinking can was used (Figure 3.28). The taller part of the mould was used to facilitate handling during cavity excavating.

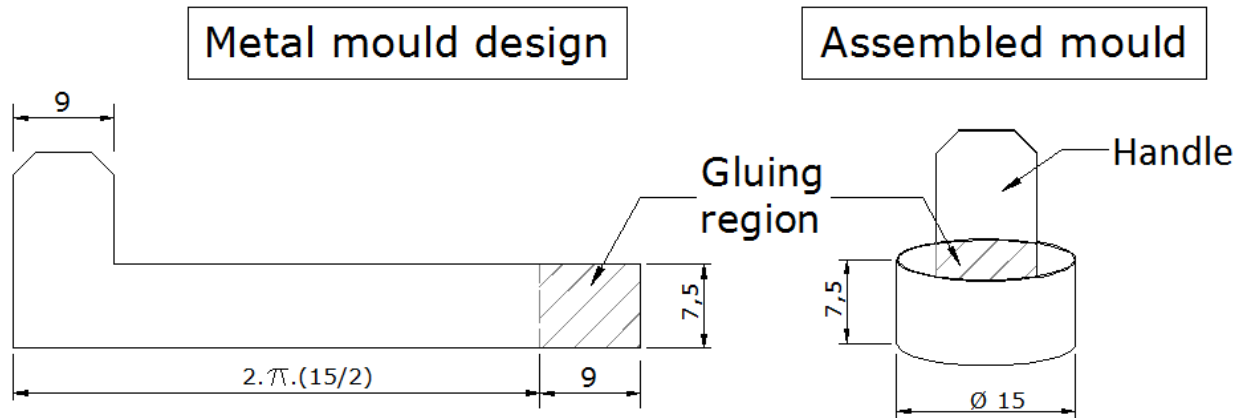


Figure 3.28: Metal mould design with a handle part used for excavating BE cavities in specimens

BE cavity excavating was performed 24 hours after specimen fabrication, when the specimen was considered soft enough to be excavated, and stiff enough to maintain the correct shape. Before starting excavating, the specimen was weighed to permit mass correction. The metal mould (Figure 3.28) was positioned on the centre of one of the extremities of the specimen, and lightly pushed into the soil, just enough to make a mark on the surface. Pressing the mould too hard could result in shearing the specimen. The cavity was carefully excavated with a sharp dental device. As the excavation progressed the mould was gently introduced until the metal mould was fully accommodated inside the cavity, leaving only the handle out. The same procedure was performed on the opposite side of the specimen. After carefully removing the mould out of the second cavity, the specimen was again weighed. The final appearance of the manufactured holes can be seen in Figure 3.29 – a and b. Finally, the diameter and depth of both cavities were measured in three different places using a calliper, and the mean value of the measurements was calculated.

Once finished, the cavities were filled with the coupling paste; the same calcined gypsum-cement mixture used for capping (for further details, see 3.4.5.1). The cavity at base of the specimen was filled first (Figure 3.29 – c), after which the BE receiver transducer was placed into the paste, making sure that it was aligned with one of the three vertical marks made by the metal triparted mould (Figure 3.6 – a). The specimen was then very carefully and tightly turned up-side down onto the bench to prevent any BE movement. The same procedure was then conducted on the top cavity (Figure 3.29 – d) and the BE transmitter was positioned in place, making sure that the BE pair was perfectly aligned by using the arrows previously marked on the pedestals of the BE pair (Figure 3.29 – e).

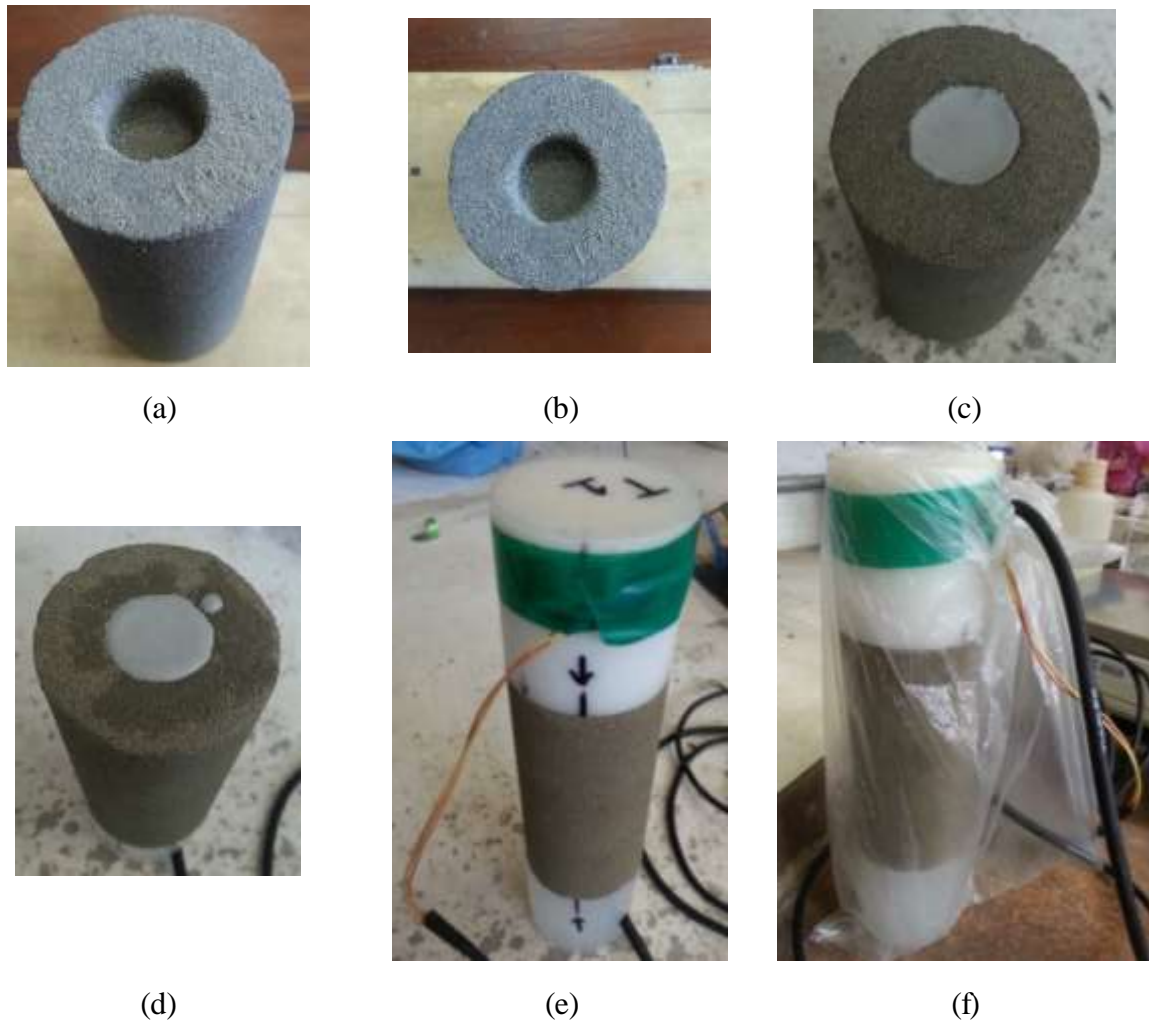


Figure 3.29: Bender Elements coupling – (a) perspective view of the excavated cavity; (b) view from the top of the excavated cavity; (c) bottom cavity filled with the coupling paste; (d) top cavity filled with the coupling paste with the bottom BE in place; (e) Top and bottom pair of BE perfectly aligned; (f) specimen conditioned into a plastic bag before the first measurement (day 2 of cure)

After BE alignment, the entire set containing the pair of BE (with cables and connectors) and specimen was carefully weighed and conditioned inside a plastic bag (Figure 3.29 – f) until the following day for the first BE test (day 2 of cure), when the couplant was considered stiff enough to initiate tests.

3.4.8.5 Bench BE operational procedure

On the test day, the BE-specimen set was removed from the plastic bag, weighed, and connected to the equipment. Before any actual measurements were taken, a quick frequency sweep was conducted in order to establish the most suitable frequency range (for further details, see 3.4.8.2).

For the actual test, the triggered voltage and time scale were also adjusted at this point in the oscilloscope. Then, the lower frequency was set on the function generator and the hypothetical sent wave was observed on the screen of the oscilloscope (Figure 3.30 - upper line). After being transmitted through the soil and amplified, the received signal was also observed on the oscilloscope screen (Figure 3.30, bottom line). Scales were adjusted until suitable wave signals were observed, and the screen was saved in a memory stick by pressing the button “Save” on the oscilloscope panel. The same procedure was conducted for all increasing frequencies until reaching BE upper frequency capacity.

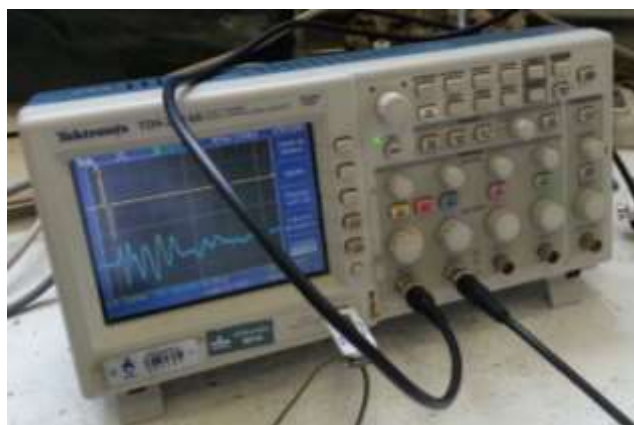


Figure 3.30: Oscilloscope showing the input (upper line) and output (lower line) signals during BE bench test

The interval between consecutive frequencies depended on whether a quick or a complete test was performed. For a quick test, measurements were made at each 5 kHz; for intermediated tests, only even or odd frequencies were tested; and for a complete test, measurements were conducted at each 1 kHz.

Files were automatically saved in the “.csv” format and organized numerically starting from zero. Because of that, a separate list was created so that each file could be matched to its corresponding wave frequency and shape.

After all sets of waves with different frequencies were saved, the input wave was changed. In a regular test, sine pulse waves were sent first, followed by sine continuous waves. Sometimes, squares pulses waves were also systematically sent. All wave inputs were conducted with voltage amplitude of ± 10 V.

After the end of each bench test, the BE-specimen set was returned to its plastic bag, closed and stored until the next test day. Each test, for a specific kind of input, provided data that generated images similar to Figure 3.26, which were used for BE signal interpretation.

3.4.9 Triaxial tests

BE were installed into a Bishop-Wesley triaxial apparatus developed by Dalla Rosa for his doctoral work (DALLA ROSA, 2009). Triaxial tests associated to BE measurements were conducted in order to assess stiffness at very-small strains and stiffness degradation of artificially cemented Osorio sand subjected to an effective confining pressure of 50 kPa. Internal instrumentation (Hall effect sensors) allowed comparing changes in shear modulus values to those obtained by BE. The confining pressure of 50 kPa was chosen to prevent the breakage of the cementation bonding due to isotropic compression.

As all the shearing processes intended to be performed on day 7 of cure, the earlier days were used for specimen preparation. Chart 4.4 summarises the entire period of cure and procedures associated to each day.

Chart 3.4: Summary of procedures associated to each day of cure for artificially cemented Osorio sand subjected to triaxial tests

Days of cure	Procedures	Item
0	Specimen fabrication	3.4.4
1	BE cavity excavating	3.4.8.4
2	Curing process	3.4.4
3	Curing process	3.4.4
4	BE operational check	3.4.9.4
	BE coupling procedure	3.4.9.4
	Couplant	3.4.5.1
	Internal sensor positioning	3.4.9.5
5	Chamber filling	3.4.9.5
	Water flushing	3.4.9.5
6	Saturation	3.4.9.5
7	Isotropic consolidation	3.4.9.5
	BE tests (stiffness at very-small strains)	3.4.8.5
	Conventional shearing	3.4.9.6
	BE tests (stiffness degradation)	3.4.9.6

3.4.9.1 Triaxial apparatus presentation

A scheme of the Bishop-Wesley press is presented in Figure 4.32. Differently from a conventional triaxial press, the Bishop-Wesley press applies deviatoric pressure at the bottom of the specimen (“Load piston”, Figure 4.31), while the weight of the entire apparatus works as counter-reaction. The apparatus inferior chamber, which is connected to a hydraulic pump, is filled with vegetal oil; as oil is considered incompressible, once pressurized the load piston moves towards the specimen compressing it. Just an overview of the equipment is provided in the present work. For further details, see Dalla Rosa (2009).

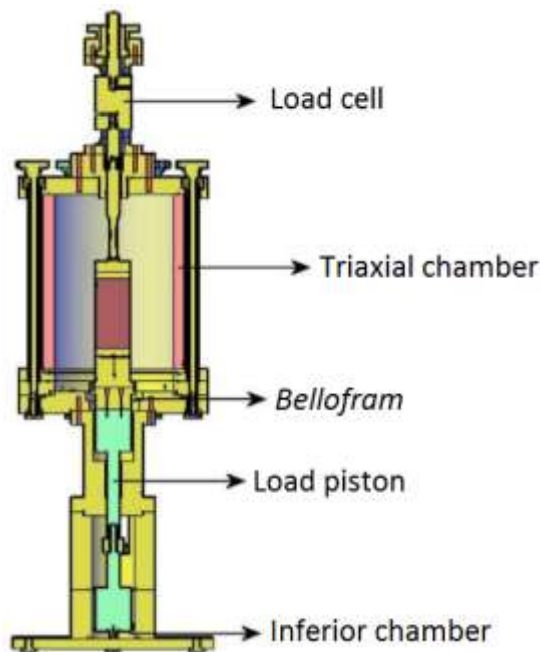


Figure 3.31: Scheme of the Bishop-Wesley press type found at LEGG-UFRGS

(DALLA ROSA, 2009)

A hydraulic pump is directly connected to the inferior chamber with its hydraulic cylinder, which is also filled with vegetable oil. The fluid inside the cylinder is pressurised by the actuation of a piston moved by a stepper motor associated to a gearbox and a ball screw. Once moving, the displacement rate is verified by external LVDT readings. The applied load is measured by a load cell (10kN) located outside, at the top of the chamber (Figure 3.31).

The triaxial chamber is made of a clear acrylic material, which can resist the maximum water-pressure imposed by the laboratory pressure system. LEGG-UFRGS has an air compressor with

the capacity of approximately 1 MPa. The triaxial air pressure is controlled by two digital proportional servo-controlled valves; one used to control back pressure, and the other cell (chamber) pressure. After each pressure is individually defined, the servo-controlled valves allow air into the triaxial lines and an air-water interface is established through bladders. Finally, when the drainage lines are closed, compressed water is available in the back pressure and cell pressure lines. These pressures are measured by two pore pressure transducers located right before the chamber (cell pressure), and at the bottom of the specimen (back pressure) – which means that specimen pore water pressure is exclusively measured at the bottom.

The device used for volume change measurement is similar to that used by the Imperial College (Figure 3.32). Basically, it is composed by an external cylinder connected to the specimen drainage lines – drainage is allowed either through the top or the bottom of the specimen, depending on the position of the valves. The device cylinder is internally divided into two chambers, each connected to one of the drainage lines. The chambers are separated by two *belloram* membranes, and when drainage is allowed in only one of the sides, the *belloram* membrane of one chamber is expanded and pushed against the other *belloram* membrane. A metal pin is positioned between the two *belloram* membranes, and as the membranes are pushed against each other, the metal pin moves either downwards or upwards. This linear movement is measured by a LVDT, and the change in water volume calibrated by the measured linear movement.

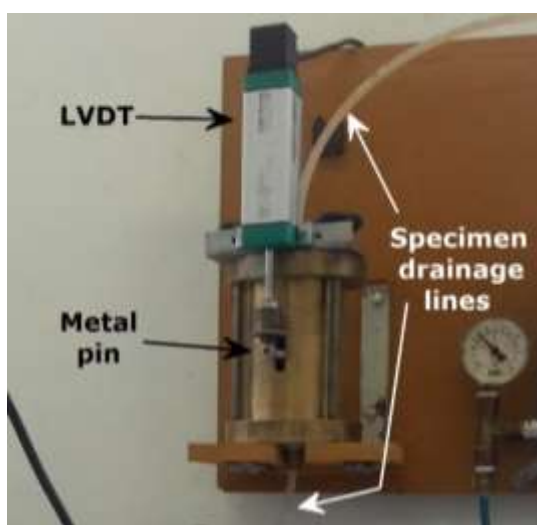


Figure 3.32: Imperial College-type device for volume change measurement

Deformations were measured inside the triaxial chamber by Hall effect sensors: 2 measuring axial deformations and 1 measuring radial deformations (Figure 3.33). The 2 axial sensors were positioned diametrically opposed to each other and fixed on the upper third of the top-half of the specimen, and on the lower third of the bottom-half of the specimen. The radial sensor is positioned exactly at the middle of the specimen. Porous disks, and specimen top cap and pedestal were specially manufactured, and are described in detail in Appendix A.4.6 and A.4.5.

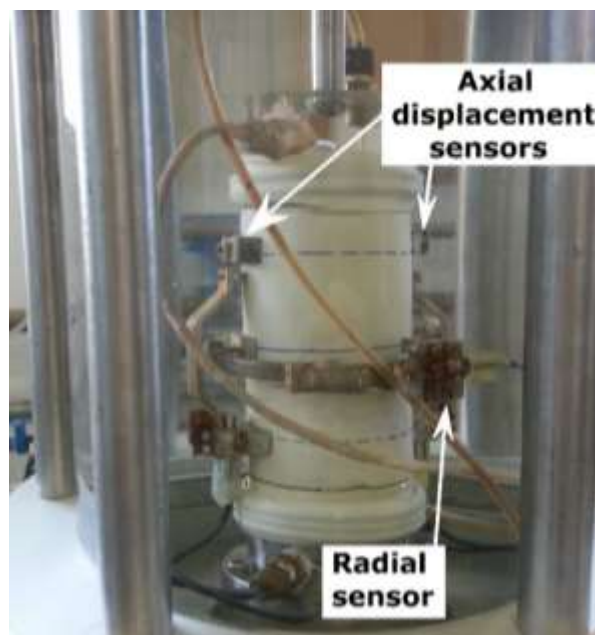


Figure 3.33: Local deformation measurements by Hall effect sensors: 2 sensors to measure axial deformation (top and bottom thirds), and 1 to measure radial deformation (midline)

Data acquisition was performed with an 8-channel analogical-digital differential acquisition board with a sample rate of 200 kHz. All the 8 channels were on use and connected to the following devices: internal axial sensors, radial sensor, pore pressure transducers (back and cell pressure), external axial LVDT sensor, load cell, and external volume change. The work range and sensitivity of each device is presented in Chart 3.5. The acquisition board also have 2 digital-analogical differential channels (16 bits) used to automate the servo-controlled pressure valves.

Chart 3.5: Work range and sensitivity of each sensor used in triaxial instrumentation

Feature	Device				
	Internal deformation measurements	Pressure transducers	Load cell	External volume change measurements	External axial deformation measurements
Work range	0 – 6 mm	0 – 1,000 kPa	0 – 10 kN	± 35 cm ³	0 – 50 mm
Sensitivity	1x10 ⁻³ mm	0.2 kPa	1 N	0.1 cm ³	0.1 mm

(based on: DALLA ROSA, 2009)

3.4.9.2 Equipment calibration

All calibrations presented in this item regard those that were actually performed for this study. Although some of the calibrations are not going to be presented or described, their respective calibration constants are presented in Chart 3.6, including: pore pressure transducers, load cell, and LVDT, which measures the external axial deformation.

Chart 3.6: Calibration constants for triaxial instrumentation

Device	Calibration constant
Cell pressure transducer	145.74440775
Back pressure transducer	146.78906831
External axial LVDT	5.34474996
External volume change measurement device	12.9141781273
Load cell	0.8773939008
Axial sensor 01	4.638363495097
Axial sensor 02	2.456935895325
Radial sensor	-1.1752025560

All Hall effect sensors were calibrated on their brackets, using their respective magnets. Starting from the beginning of the sensor course, the magnet was moved towards the sensor by increments of 0.1 to 0.5 mm, and the response in volts for each increment was recorded. The displacement (mm) and response voltage (V) results were plotted, and only the linear portion of the curve was used; the slope of this linear portion was then defined as the calibration

constant. Figure 3.34 – (a) and (b) presents the plots for both axial sensors; Figure 3.35 presents the plots for radial sensor calibration.

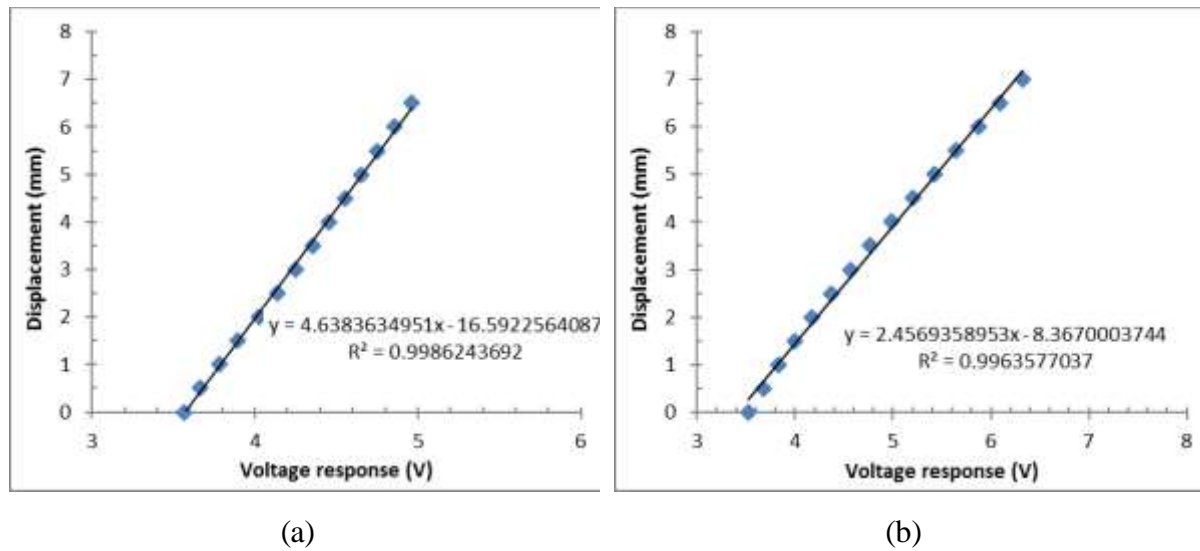


Figure 3.34: Axial (Hall effect) sensors calibration – (a) axial 01; (b) axial 02

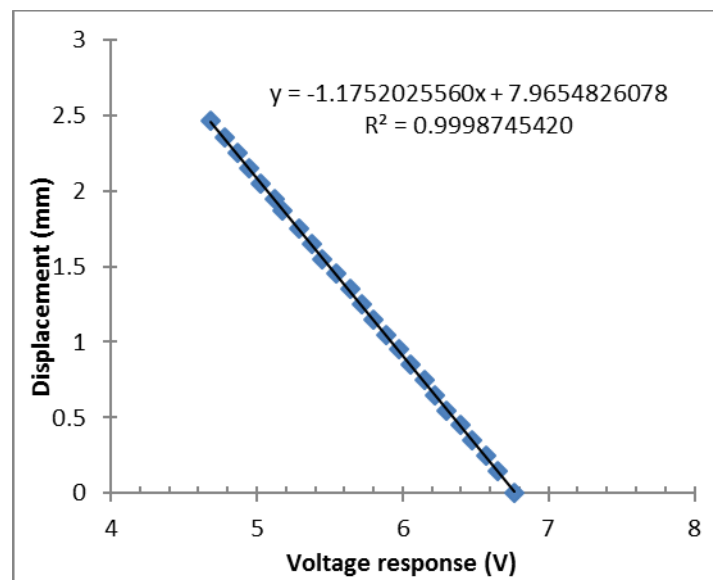


Figure 3.35: Radial (Hall effect) sensor calibration

The volume change measurement device was calibrated by allowing water to drain through the upper line, weighing the water mass in a high-precision digital scale with an accuracy of 0.0001 g, and measuring (in volts) the LVDT response to the linear movement of the metal pin (see

3.4.9.1). Then, the same procedure was repeated by allowing drainage through the bottom line. At the end, the values for both upper and bottom drainage lines were plotted against mass (g) and voltage response (V), as observed in Figure 3.36 – (a) and (b). The mean value of the slope of both lines (downwards and upwards metal pin movement) was defined as the calibration constant.

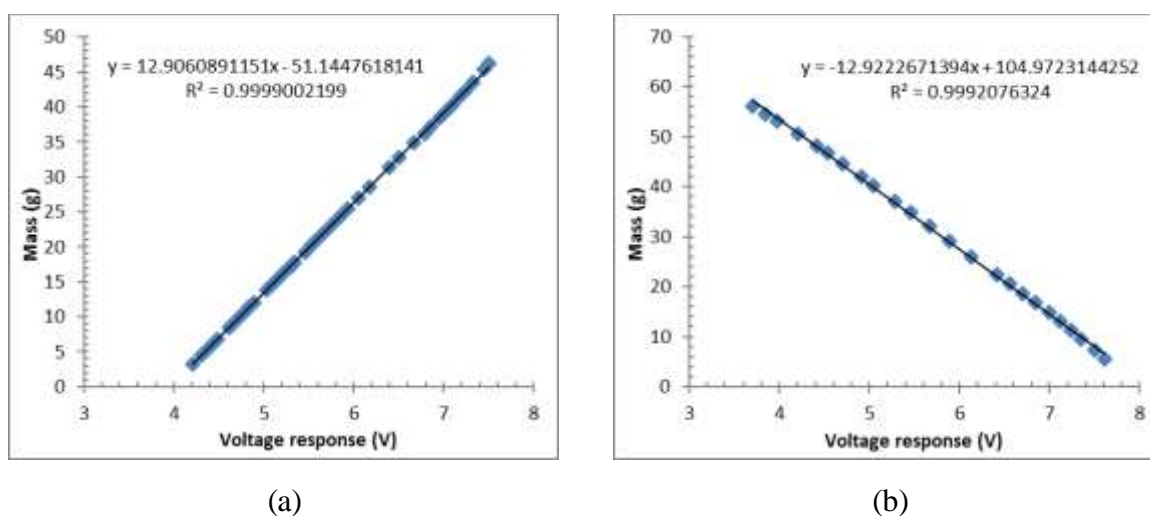


Figure 3.36: Calibration of the volume change measurement device –
(a) downwards metal pin movement; (b) upwards metal pin movement

3.4.9.3 Initial procedures

Before any triaxial test was conducted, BE operation was verified by simply connecting the transmitter BE to the function generator, varying the frequencies, and “listening” to BE vibrations. Then, the transmitter was put in direct physical contact with the receiver, and both were connected to the oscilloscope. Both signals were visually inspected to provide a signal free of excessive noise and instabilities, which approximately matched each other as the frequency varied. Once adequate triaxial BE operation was verified, the following procedures were performed:

Initially, all drainage lines and permeable parts were verified to ensure no water flow obstructions existed and the elements were free of air bubbles, according to the guidelines by Head (1998) and ASTM D7181 (ASTM, 2011c). Water was allowed to pass through the lines until only clear water was observed. The lines were then purged until water freely flowed out

from the top cap and pedestal. The porous disks, kept immersed in distilled water before the test, were placed on the pedestal and top cap. The top cap was positioned upside-down, and a piece of rubber membrane was positioned around it; another piece of rubber membrane was also placed around the pedestal and both drainage lines were opened to verify whether water could pass through the porous disks with no difficulties. A layer of a few millimetres of water was left (Figure 3.37) until the specimen was ready to be positioned; this layer of water prevented any dirt from clogging the permeable materials. Filter paper was also dipped in the layer of water and appropriately placed at the top of both porous disks.

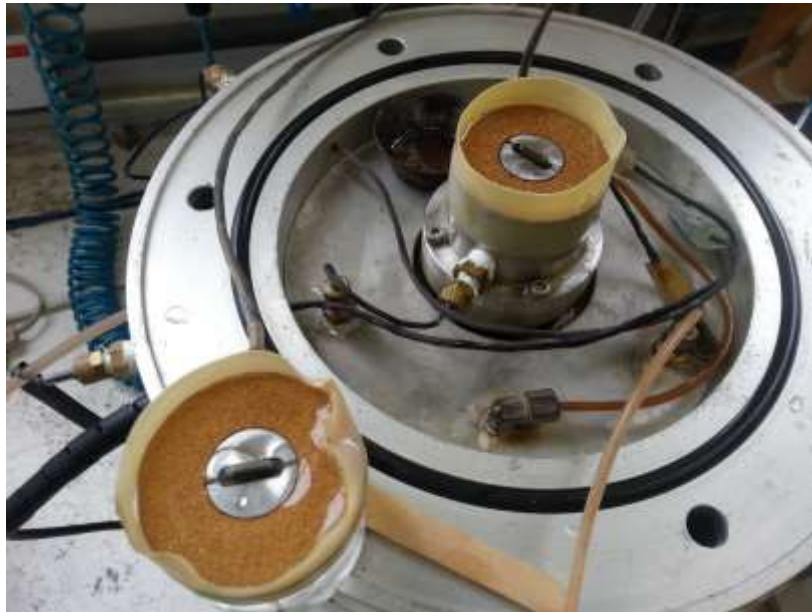


Figure 3.37: Drainage lines saturation and verification of lack of obstruction of permeable elements

3.4.9.4 Triaxial BE pair coupling

Specimens were fabricated according to 3.4.4. On the first day of cure, BE cavities were excavated (3.4.8.4) and the specimen returned to its plastic bag. On the fourth day of cure, the BE pair was coupled to the specimen. The coupling procedure was similar to that performed for bench specimens (3.4.8.4), and the couplant was the same paste used for the capping process (3.4.5.1). See the entire schedule for artificially cemented soil subjected to triaxial and BE tests in Chart 3.4.

First, the bottom of the specimen was cemented to the pedestal. To do so, the cavity at the bottom of the specimen was filled with the couplant. However, differently from the bench pair, the pedestal with the BE could not be removed from the triaxial chamber, requiring an extra viscous couplant so it would not slide during positioning. Therefore, the alternative was to wait for 3 to 5 minutes after filling the cavity until the couplant turned less fluid, and quickly turn the specimen upside-down to position it onto the pedestal. A piece of adhesive tape was aligned to the BE direction at the bottom of the pedestal, below the region the rubber membrane was positioned. Then, a rubber membrane was placed around the specimen, and two o-rings were placed around the bottom of the rubber membrane. Another piece of tape was aligned to the previously positioned tape, but this time on the surface of the rubber membrane along the height of the specimen. Two o-rings for the top cap were positioned around the specimen, close to the top. The upper part of the rubber membrane was carefully folded around the specimen, and the top BE cavity was filled with couplant. The top cap (with the porous disk and filter paper) was finally positioned on the top of the specimen and aligned to the adhesive tape in an attempt to keep both BE aligned. The rubber membrane was carefully positioned around the top cap and the two o-rings were carefully placed around the rubber membrane on the top cap.

Before positioning the rubber membrane, its thickness was measured and the absence of any small holes verified. Then, once the rubber membrane, o-rings and the top-cap were in place, Hall effect sensors were positioned as presented in Figure 3.33. The cell was closed and no further procedures were performed until the next day to allow the couplant to develop strength and stiffness.

3.4.9.5 Triaxial procedures

Triaxial procedures, according to the guidelines by Head (1998) and ASTM D7181 (ASTM, 2011c), started on day 5 of cure. First, the chamber was filled with tap water and a pressure of 35 kPa was applied to the cell. Before water-flushing, the specimen was subjected to carbon dioxide gas (CO₂) percolation (BRIGNOLI; GOTTI; STOKOE II, 1996). As the molecules of CO₂ can more easily dissolve in water than O₂, CO₂ flushing aimed to improve B-values during the saturation process. CO₂ was flushed during 30 min from the bottom of the specimen under a constant pressure of 15 to 20kPa.

Then, the water-flushing process started, which could last up to 24 hours. As the tank connected to specimen line was positioned 1.5 m high, a gravitational pressure of about 15 kPa was applied during flushing. Specimens were always flushed from the base, while its top was left open.

Flushing was visually inspected for the exit of air bubbles, and was considered complete when about 500 ml of water had percolated the specimen. To reach the percolation volume, flushing was left to occur overnight.

On day 6 of cure, the saturation procedure was performed. Saturation was accomplished by successive increments of back-pressure. As saturation is dependant of both pressure and time (HEAD, 1998; ASTM, 2011c), the time for each stage varied between 30 to 60 minutes. Usually, 8 stages with 50 kPa increments each were applied, and then the specimen was left under saturation overnight. Whenever necessary, one or two more stages were implemented in the following day to achieve the desired B-value. The difference between cell pressure and back pressure of 10 kPa was respected for all saturation stages. Regarding the B-value, Head (1998) presented the findings by Black and Lee (1973), who claimed that cemented soils (very stiff) with a B-value equal to 0.20 could represent a saturation of 99.5% - as observed in Table 3.1. Therefore, different from ASTM D7181 (ASTM, 2011c), which suggests a minimum B-value equal to 0.95, B-values lower than that can be admissible for cemented soils.

Table 3.1: Reference B-values for typical soils as a function of saturation

Soil category	Degree of saturation		
	100%	99.5%	99.0%
soft	0.9998	0.992	0.986
medium	0.9988	0.963	0.930
stiff	0.9877	0.69	0.51
very stiff	0.913	0.20	0.10

(BLACK & LEE, 1973 *apud* HEAD, 1998)

It is important to point out that de-aired water was not used, and distilled water was always used instead. Also, both the saturation and consolidation processes were conducted through the two drainage lines (top and bottom).

The last B-value measurement occurred during cell pressure increment for consolidation. After opening the valves, consolidation usually took a few seconds to dissipate pore pressure

increment. Pore pressure was monitored during more than 10 minutes before BE tests were conducted, as presented in the following item.

3.4.9.6 Shearing and BE tests

After the specimen was isotropically consolidated, BE tests were performed to identify stiffness at small-strains for the artificially cemented soil under isotropic pressure. BE tests followed the same procedures described in 3.4.8.5. After the complete set of wave frequencies and shapes were recorded, drained shearing was conducted.

All specimens were subjected to shearing at a rate of 2 mm/h. Because each set of BE tests took around 30 minutes to be completed, the press motor imposing shearing had to be fully stopped during BE measurements. The stops for BE measurements were established for each specimen individually, and varied from 15 to 30 minutes between pauses. Because all these stops resulted in a delay of the shearing process, a higher shearing rate was chosen to accelerate the entire process. BE tests were also conducted in accordance with 3.4.8.5, and each test resulted in a calculated shear modulus respective to a specific strain; both pairs of calculated shear modulus and their respective strains associated to the initial shear modulus (before shearing) provided the complete stiffness degradation curve.

4 RESULTS AND DISCUSSION

The first section of this chapter brings the standardisation used for presenting the data. Then, the following sections (4.2 to 4.4) discuss the quality of the fabricated specimens, and proceed with initial data treatment, such as capping and BE-specimen coupling mass and time-corrections. After that, anisotropy is analysed (4.5), as the studied η/c_{iv} ratios seemed to indicate isotropy (with a slight degree of cross-anisotropy for some specific specimens). It is followed by the UPV tests data in cylindrical specimens (4.6), whose results are compared to the stiffness obtained in the T-T' direction of cubical specimens. The analysis then focus on BE triaxial tests validation (4.7), demonstrating that the BE system used was capable of generating and receiving clear signals. Finally, BE data for bench tests (5.8), and the triaxial tests (4.9) are presented and discussed.

4.1 DATA PRESENTATION STANDARDISATION

Intending to facilitate identification, all results presented in this chapter were standardised in terms of symbols, colours and acronyms. The code used to refer to specimens subjected to UPV tests is presented in Figure 4.1, which includes the geometry of the specimen (cubical or cylindrical), the η/c_{iv} ratios and dry unit weights, and whether the specimen was capped or not. For specimens subjected to BE tests a different code (Figure 4.2) was used. The first three letters refer to bench (BEN) or triaxial (TRX) BE pair, followed by the η/c_{iv} ratio and the dry unit weight.

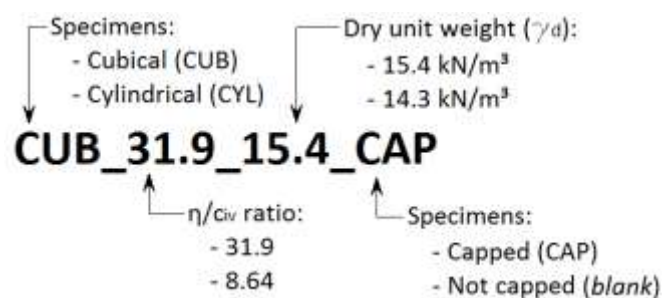


Figure 4.1: Scheme for the identification of specimens subjected to UPV tests

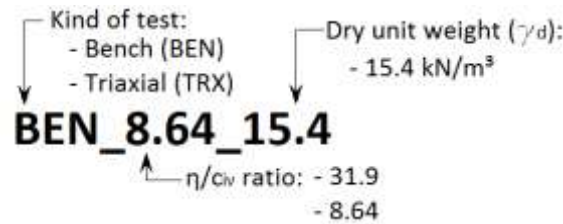


Figure 4.2: Scheme for specimen nomenclature subjected to BE tests

Regarding the graphical presentation of data, Chart 4.1 summarizes the adopted symbols, colours and types of lines for each specimen subjected to UPV and BE tests. Capped specimens subjected to UPV tests have their symbols filled with the same colour of their contours and lines (light shade of grey); while non-capped specimens use open symbols (dark colour). Specimens subjected to BE tests have distinct colours for filling and contouring each symbol. Finally, BE tests always present a solid line, while UPV tests use dashed (for cylindrical specimens) and dotted (for cubical specimens) lines. This pattern was used throughout the section, except for anisotropy (4.5), where specific symbols and lines were used for each face of cubical specimens.

Chart 4.1: Summary of symbols and lines adopted for each kind of specimen subjected to BE and UPV tests

Kind of test	Specimen geometry	γ_d (kN/m ³)	Symbols				Lines
			$\eta/civ=8.64$		$\eta/civ=31.9$		
			No capping	Capping	No capping	Capping	
BE - BEN	CYL	15.4	■	-	▲	-	—
BE - TRX		15.4	✱	-	▲	-	—
UPV	CYL	15.4	✕	-	▲	▲	- - - - or - - - -
		14.3	✕	-	-	●	- - - -
	CUB	15.4	+	-	-	◆ or
		14.3	✕	-	-	■ or

- : Tests not performed

4.2 QUALITY OF FABRICATED SPECIMENS

All fabricated specimens are presented in Table 4.1, along with the target and reached values for each variable; the “d” index refers to target values and the “0” index refers to initial values

obtained at moulding day. Cubical specimens presented more variation in terms of dry unit weight and water content in comparison to cylindrical specimens. That was mainly due to the amount of material required to fabricate each specimen. Because of its increased mass, extra water was added to cubical specimens in order to prevent water loss during the longer mixing time required. Even though only 0.5 g of extra water was added to each layer, water content of cubical specimens was consistently higher than the target water content ($w=10\%$), except for specimen CUB_8.64_14.3.

Table 4.1: Summary of the target and real parameters of all tested specimens

Specimen	Test	Design parameters				Real parameters			
		$(\eta/C_{iv})_d$	$\gamma_{d,d}$ (kN/m ³)	C_i (%)	$w_{0,d}$ (%)	η/C_{iv}	γ_d (kN/m ³)	w_0 (%)	S_r (%)
BEN_31.9_15.4	BE	31.90	15.40	2.78	10	31.36	15.30	9.97	36.06
BEN_8.64_15.4		8.64	15.40	11.28		7.66	15.47	9.94	36.24
TRX_31.9_15.4		31.90	15.40	2.78		31.55	15.26	9.99	35.93
TRX_8.64_15.4		8.64	15.40	11.28		7.58	15.54	10.17	37.42
TRX_0.00_15.4		0.00	15.40	0.00		-	21.46	10.02	114.33
CYL_31.9_15.4	UPV	31.90	15.40	2.78	10	31.32	15.34	9.14	33.18
CYL_31.9_15.4_CAP		31.90	15.40	2.78		31.27	15.35	9.68	35.20
CYL_8.64_15.4		8.64	15.40	11.28		7.94	15.27	9.90	34.91
CYL_31.9_14.3_CAP		31.90	14.30	3.30		29.80	14.54	9.55	30.63
CYL_8.64_14.3		8.64	14.30	13.64		7.32	14.57	9.61	30.40
CUB_31.9_15.4_CAP	UPV	31.90	15.40	2.78	10	30.08	15.19	10.20	36.19
CUB_8.64_15.4		8.64	15.40	11.28		8.43	15.93	10.54	41.25
CUB_31.9_14.3_CAP		31.90	14.30	3.30		27.97	14.54	10.46	33.52
CUB_8.64_14.3		8.64	14.30	13.64		8.47	14.70	8.51	27.52

It was fundamental that two specific specimens (CYL_31.9_15.4 and CYL_31.9_15.4_CAP) reached similar η/c_{iv} ratios and γ_d values to allow a direct comparison between specimens, which were later used to calibrate mass and wave travelling time of capped specimens. Although statistical analysis to establish whether specimens could be compared was not performed, such comparison seemed reasonable as their dry unit weights showed a variation of only 0.06%, and the η/c_{iv} ratios of only 0.15% in relation to the target value results.

Specimen TRX_0.00_15.4 refers to the non-cemented specimen ($\eta/c_{iv} = 0$) tested inside the triaxial apparatus to validate the triaxial BE pair. As observed in Table 4.1, its γ_d was much higher than the target value. This can be accounted by the fact that the specimen was moulded directly onto the top of the triaxial pedestal, compromising its fabrication. For instance, the

real amount of soil used to fabricate the specimen is unknown. Although it was possible to observe some material loss during moulding, the actual amount could not be determined. Therefore, the mass used to calculate the dry unit weight was only an approximation. Moreover, the final dimensions of the specimen used in the calculations, especially the diameter, were considerably smaller than expected, mainly due to the rubber membrane not being able to totally stretch and adhere to the mould walls during specimen compaction. Moreover, uncertainties related to the actual dry unit weight led to voids volume results out of the expected range for Osorio sand. Therefore, the dry unit weight was not corrected and the target value was adopted for future calculations.

Because it could directly affect the ratio and provide some insight about its behaviour, the degree of saturation (S_r) was also presented – see more details in 2.5. Although S_r was known at the moment of moulding, changes could not be measured during the following days due to cementitious reactions occupying the original voids.

The η/c_{iv} ratio can be better discussed based on Figure 4.3. The “Guideline 1:1” has a slope of 45° ; any point falling on the line achieved the exact desired η/c_{iv} ratio, while any point above or below the line reached higher or lower ratios, respectively. All tested specimens reached values that were lower than expected. However, specimens with $(\eta/c_{iv})_d = 8.64$ presented less dispersion than specimens with $(\eta/c_{iv})_d = 31.90$.

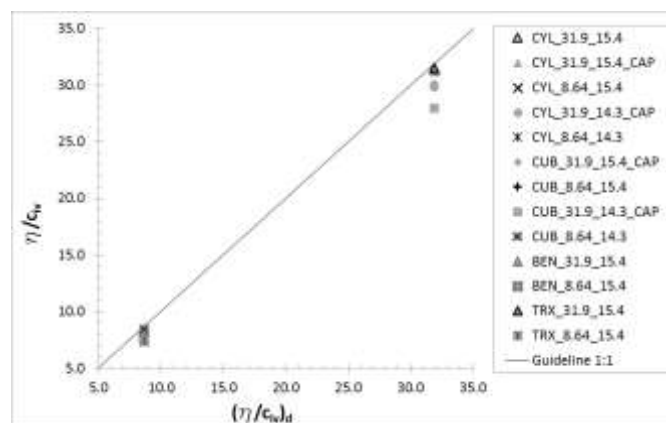


Figure 4.3: Target η/c_{iv} ratio versus actual η/c_{iv} ratio for all tested specimens

Likewise, the dry unit weight was also presented in terms of its target values and real values (Figure 4.4). Lower γ_d values (14.3 kN/m^3), above the line, means that the target γ_d for the

loosest specimens (which tend to reach a more dense state) was difficult to achieve. The higher γ_d values (15.4 kN/m³) presented more dispersion, requiring further individual analysis of each test. Therefore, Figure 4.5 – (a) to (c) presents target and real dry unit weights for each kind of specimen separately.

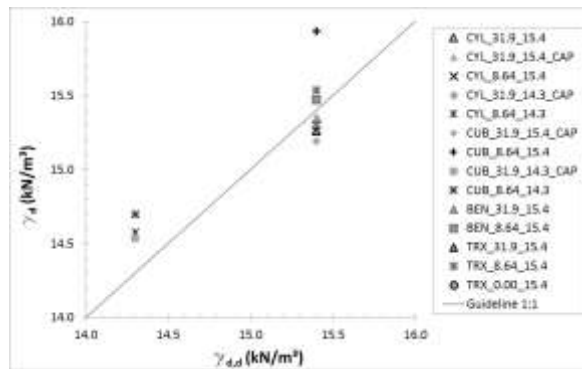


Figure 4.4: Target dry unit weight ($\gamma_{d,d}$) versus real dry unit weight (γ_d) for all tested specimens

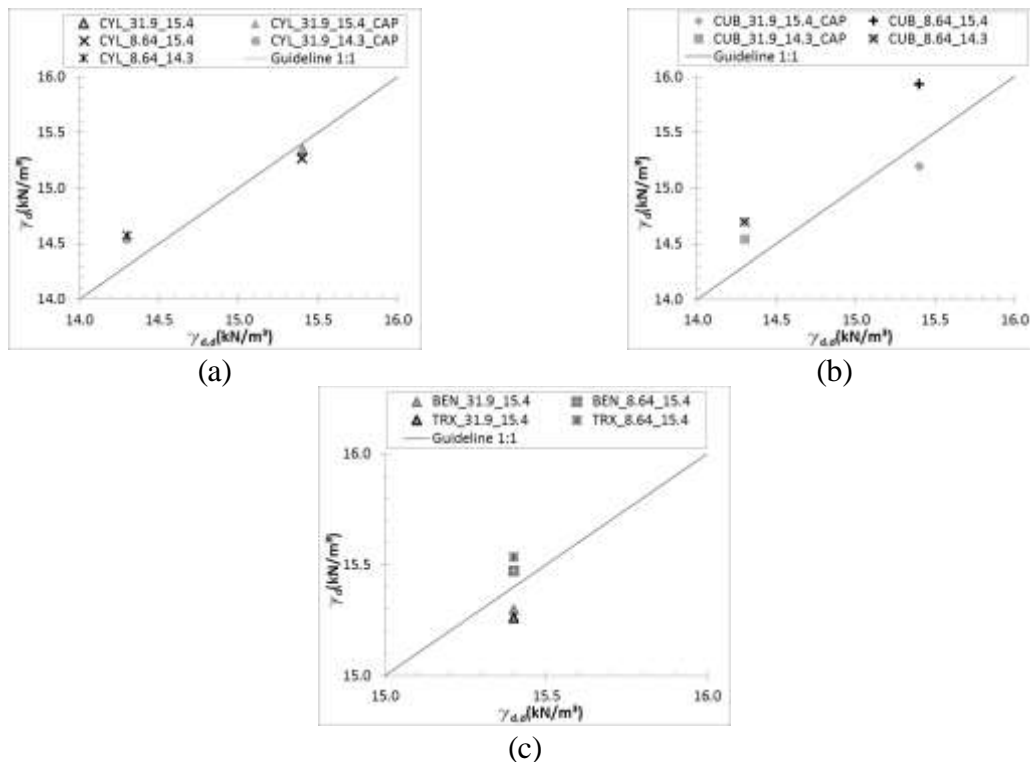


Figure 4.5: Target dry unit weight ($\gamma_{d,d}$) versus real dry unit weight (γ_d) for each kind of specimen separately – (a) cylindrical specimens subjected to UPV tests; (b) cubical specimens subjected to UPV tests; (c) cylindrical specimens subject to BE tests

Cylindrical specimens subjected to UPV tests with $\gamma_{d,d}=15.4$ kN/m³ were consistently looser than expected (Figure 4.5 – (a)). However, this pattern was not followed by the cylindrical specimens subjected to BE tests (Figure 4.5 – (c)). In fact, these specimens presented a new behaviour: those with $\eta/c_{iv}=8.64$ presented dry unit weights slightly higher than the target, while specimens with $\eta/c_{iv}=31.9$ presented dry unit weights lower than the target.

Moreover, generally, cubical specimens presented the highest dry unit weights dispersion. Although cubical specimens with $\gamma_{d,d}=14.3$ kN/m³ reached higher values, the two types of specimens were much closer to each other than specimens with $\gamma_{d,d}=15.4$ kN/m³, which presented a high dispersion. Specimen CUB_8.64_14.3 was below the target value, while CUB_8.64_15.4 was much above the target value – this great variation is more evident in the natural unit weight. Although problems regarding the water content of cubical specimens were already present, another fact also prevented it from reaching the target dry unit weight. The denser the specimens, the more suction was created between the top layer and the compaction piston; a situation which was mitigated by adding a sheet of butter paper. As the looser specimens were manually compacted, it was sometimes difficult to apply the same force during compaction, resulting in some dispersion.

4.3 CAPPING CALIBRATION

Capping was successfully applied to protect the surface of specimens, with no crumbling or degradation of the capping surface being observed during the entire test period. However, its likely interference on wave velocity travelling time (4.3.1) and specimen mass (4.3.2) required careful analysis.

4.3.1 Delays in wave travelling time due to capping

Time-calibration was described in 4.4.5.3. Initially, it was necessary to verify if the extra few millimetres of capping added onto specimens would result in significant wave travelling time changes detected by the UPV equipment. The specimens CYL_31.9_15.4 and CYL_31.9_15.4_CAP fabricated with very similar unit weights were used to allow direct comparisons. Figure 4.6 – (a) and Figure 4.6 – (b) present p-wave and s-wave velocities of the capped and non-capped specimen; the differences between specimens were more evident for the s-wave velocity. Despite similarities in the curves, V_p and V_s velocities seem to have the opposite behaviour: while V_p velocities found for capped a non-capped specimens tended to

approximate each other over time; V_s velocities tended to distance from each other over time. As the main difference between specimens was the presence of capping, the observed behaviour was probably due to stiffness and strength gains over time, change in water content, or even a combination of both factors, although clear conclusion could not be established. Nonetheless, the velocities found for the capped specimen were consistently slower than the velocities of the non-capped specimen, indicating that capping resulted in elongated wave travelling times and, consequently, slower velocities.

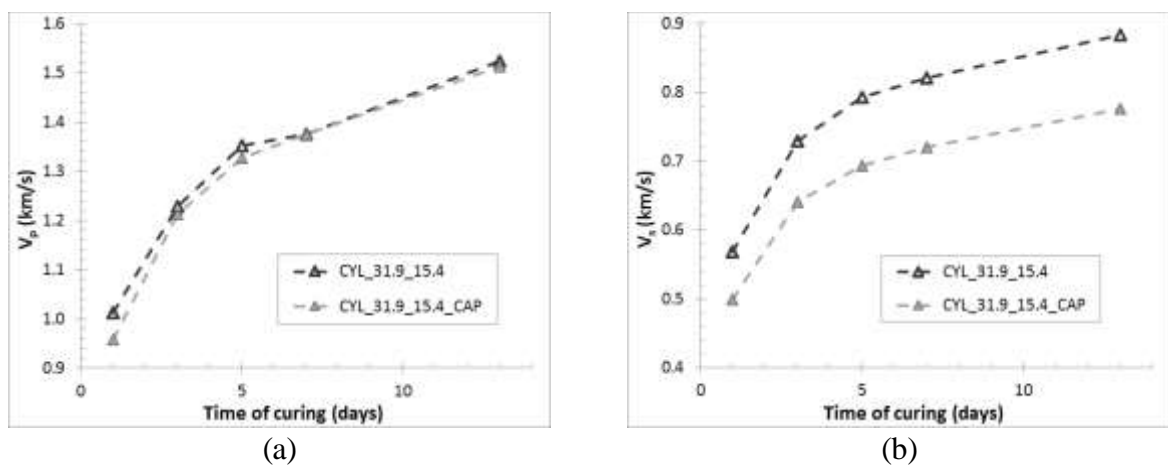


Figure 4.6: Differences in velocities of identical capped and non-capped specimens– (a) p-wave velocity; (b) s-wave velocity

From data in Figure 4.6 – (a) and Figure 4.6 – (b), it is possible to obtain Table 4.2. As the vertical axes of Figure 4.6 have different scales, a direct comparison between V_s and V_p is difficult; an issue that was circumvented by calculating the differences in velocities for capped and non-capped specimens (ΔV_s and ΔV_p), as presented in Table 4.2.

Table 4.2: Differences between measured velocities for capped and non-capped specimens used for time calibration

Age (days)	CYL_31.9_15.4		CYL_31.9_15.4_CAP		ΔV_s (m/s)	$\Delta V_s/d_{cap}$ (s^{-1})	ΔV_p (m/s)	$\Delta V_p/d_{cap}$ (s^{-1})
	V_s (m/s)	V_p (m/s)	V_s (m/s)	V_p (m/s)				
1	568.20	1,013.25	498.83	957.13	69.37	1.87E+04	56.12	1.52E+04
3	728.76	1,228.14	640.41	1,212.81	88.35	2.39E+04	15.33	4.14E+03
5	793.07	1,352.44	693.56	1,327.42	99.51	2.69E+04	25.02	6.76E+03
7	821.10	1,374.60	719.75	1,375.00	101.35	2.74E+04	-0.40	-1.08E+02
13	883.56	1,524.48	760.56	1,513.40	123.00	3.32E+04	11.08	2.99E+03

d_{cap} (total capping thickness) = 3.7 mm

Data from Table 4.2 reinforced what was described previously: ΔV_s and ΔV_p have the opposite behaviour over time, and ΔV_p is smaller than ΔV_s . Moreover, each ΔV_s and ΔV_p value was divided by the total cap thickness (3.7 mm), also observed in the table.

Based on Table 4.2, Figure 4.7 was plotted. The best-fit equation was used to calibrate the capped specimen CYL_31.9_15.4_CAP, as observed in Figure 4.8. The calibrated data were plotted as “CYL_31.9_15.4_CAP–Time correct.,” which practically superposed the CYL_31.9_15.4 data for both V_s and V_p , indicating that velocity calibration was achieved.

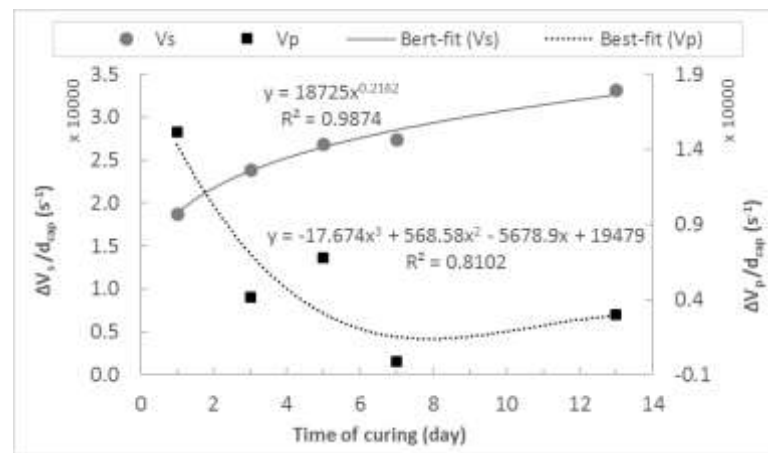


Figure 4.7: Fit-equations for s-wave and p-wave velocities over time

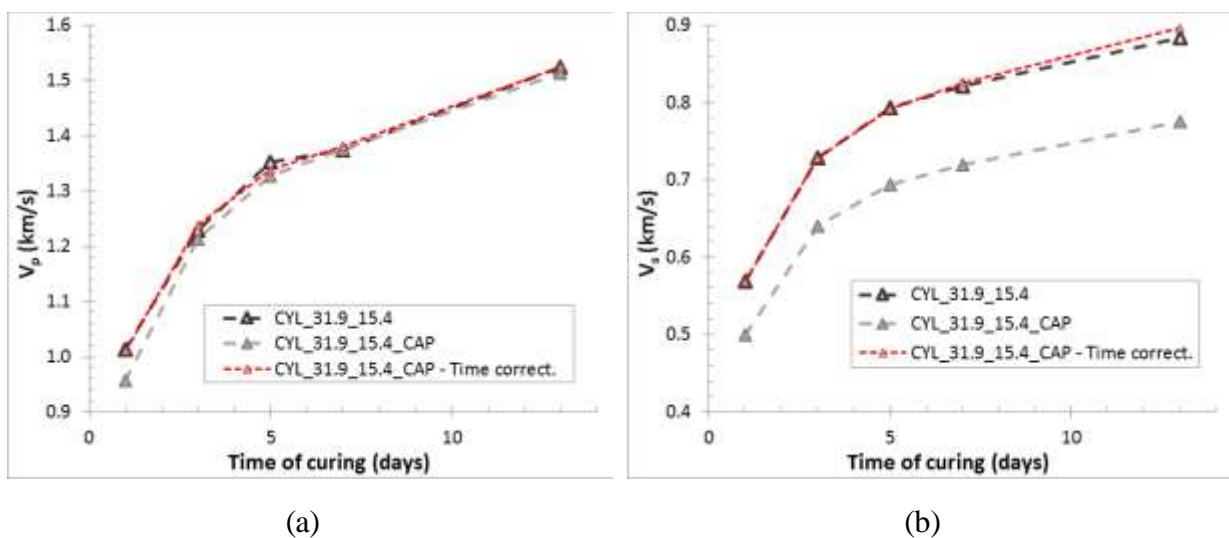


Figure 4.8: Calibrated velocities for capped specimens compared to the non-calibrated capped specimen and non-capped specimen – (a) p-waves velocity; (b) s-waves velocity

The same time correction procedure was performed for specimen CYL_31.9_14.3_CAP, but it was not plotted on the graph to avoid pollution. The non-capped specimen identical to the specimen CYL_31.9_14.3_CAP was accidentally damaged before calibration and could not be fabricated again due to time constraints. Thus, this capped specimen was calibrated using the best-fit of another η/c_{iv} ratio specimen (CYL_31.9_15.4). As capping on this specimen was thinner (1.57 mm) than in CYL_31.9_15.4_CAP, changes in velocity (and, consequently, in time) were considerably smaller than other calibrated cylindrical capped specimens. The two capped cubical specimens were also subjected to the same calibration procedure.

4.3.2 Changes in mass due to capping

The mass of capped specimens also had to be calibrated in order to obtain the correct dry unit mass and, consequently, the correct modulus. The calibration process was described in 4.4.5.3. Changes in water content over the curing time are presented in Figure 4.9 – (a) and (b), for cylindrical and cubical specimens, respectively. It can be observed in the figures that all the results for capped specimens presented behaviour similar to non-capped specimens. Therefore, based on the visual analysis of the graph, calibration was considered adequate.

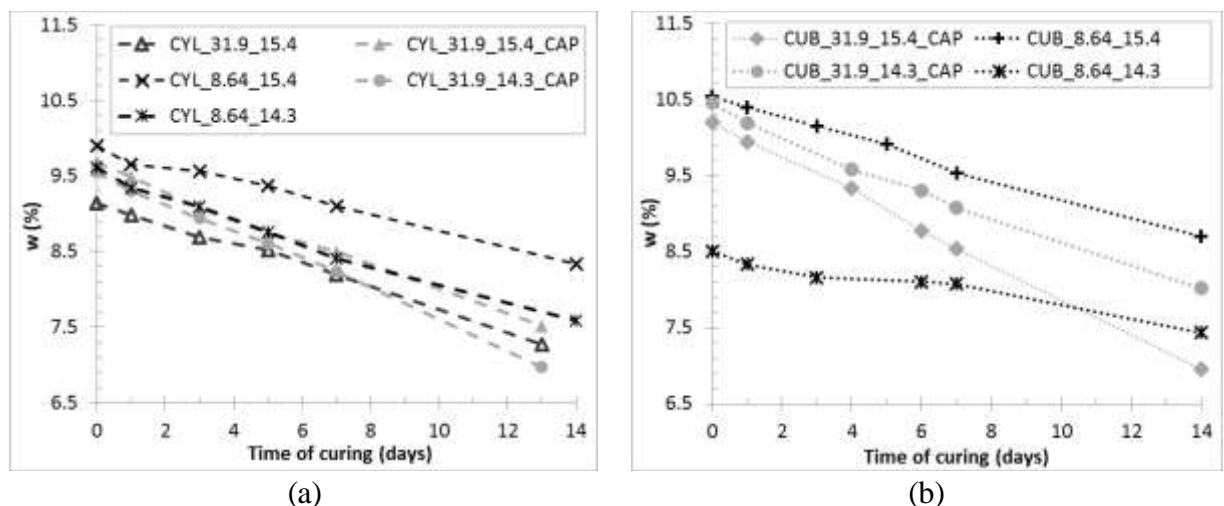


Figure 4.9: Change in water content over the curing period for – (a) cylindrical specimens; and (b) cubical specimens

Both the specimen and capping presented changes in mass over time due to changes in water content. However, for calculation purposes, the total amount of water mass of the paste

applied at the moment of capping was subtracted from the total mass measured at each test day. Although this did not correspond to reality, the impact on the calculations was minor. In the worst scenario, a specimen with a moist mass about 300 g and 333 g would be reduced by 5 g to 7 g, which represents 1.65% to 2.33% of the specimen moist mass; or a dry unit weight or a modulus 2.33% smaller – a value in favour of safety and slightly more conservative.

Although changes in water content for corrected capped specimens seemed to be quite dramatic when changes in natural unit weight (Figure 4.10 – a and b) were analysed, mass correction seemed much more adequate. The behaviour of the capped cylindrical specimen CYL_31.9_15.4_CAP matched its identical non-capped specimen. Although the capped CYL_31.9_14.3_CAP had no identical non-capped specimen to allow a direct comparison, the behaviour of the non-capped specimen CYL_8.64_14.3 was similar to CYL_31.9_14.3_CAP, with a slight change in natural unit weight over time.

Figure 4.10 – (a) and Figure 4.10 – (b) illustrate the natural unit weight, which means that water weight was considered in the calculations and, therefore, the values presented on the figures are higher than the dry unit weight. The corresponding value to $\gamma_d=15.4 \text{ kN/m}^3$ is $\gamma_n=17.13 \text{ kN/m}^3$, and the corresponding value to $\gamma_d=14.3 \text{ kN/m}^3$ is $\gamma_n=15.9 \text{ kN/m}^3$.

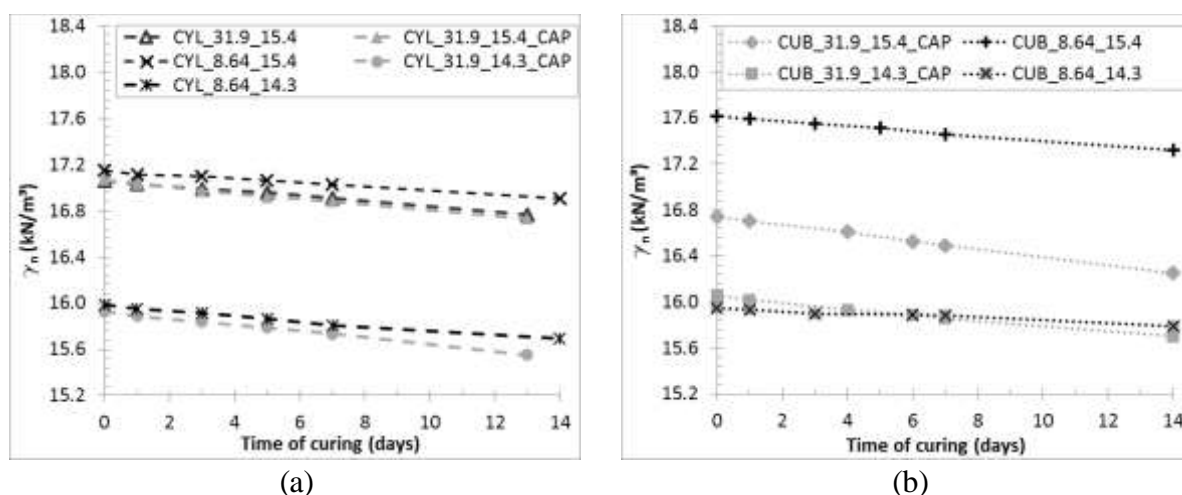


Figure 4.10: Dry unit weight after mass correction due to capping for
– (a) cylindrical specimens; and (b) cubical specimens

The specimen CUB_31.9_14.3_CAP presented a quite similar behaviour to specimen CUB_8.64_14.3, once again validating the adopted approach for mass correction. Lastly,

specimens CUB_8.64_14.3 and CUB_8.64_15.4 presented lower and higher natural unit weights than their target values (as discussed in 5.2), respectively. However, they presented a similar slope and behaviour to the other specimens. Therefore, despite some limitations, the adopted procedure for correcting specimen changes in mass due to capping was considered adequate.

4.4 BE COUPLANT CORRECTION

BE devices were coupled to specimens using the same calcined gypsum-cement paste used for capping. The procedure to calibrate the effects of this couplant on wave travelling time and mass of the specimen was described in 3.4.8.1, and the respective results are presented in the following sections.

4.4.1 BE couplant time-effect

The possible effect on time measurements due to stiffness gains in BE couplant was analysed after all tests on cemented sand were finished. As a result, the BE pair was a little damaged and the virtual working frequency range changed from 15 kHz to 60 kHz. Figure 4.11 to Figure 4.14 present the BE tests data obtained with the calibration cylinder with circular cavities filled with BE couplant for days 1, 2, 3 and 4 of couplant cure. Each day corresponds to one extra day in relation to specimen cure, i.e., day 2 of couplant cure corresponded to day 3 of specimen cure. All the figures mentioned above were plotted in terms of BE couplant cure, and all analysis in this section are also related to BE couplant cure as well.

Despite changes in frequency range, the smallest frequency (15 kHz) did not present a stable response, producing the highest level of noise and differences in relation to the input signal for all days of cure. As such, this frequency was ignored when choosing the wave peak corresponding to the first peak arrival. The vertical dotted blue line in the graph represents the points chosen for the first peak arrival.

Frequency behaviour on days 2, 3, and 4 of BE couplant cure was very similar, with a difference of around 1 μ s between the first peak arrival time along consecutive days. Therefore, between these days, the effect on time due to BE couplant was negligible.

The time difference between measurements obtained from day 1 and 2 was 14.28 μ s, which represents a difference in the calculated shear modulus of about 5 MPa, i.e., shear modulus on

day 1 was equal to 90% of shear modulus in the following day. Although the difference is not small, there are some attenuating factors to be considered. First of all, the presence of a line indicating the UPV measurements (red line) may influence the decision concerning the first peak arrival time. For instance, every cure day presented a small but consistent oscillation around 325 μs (for almost all frequencies), and that could represent the arrival of the first wave. However, as the UPV measurements (red line) were presented on the graph after these oscillations, it was decided to place BE measurements (blue line) nearby, as both methods corroborated with each other. It is important to be aware that this decision could implicate in masking the possible BE-specimen system dispersive response.

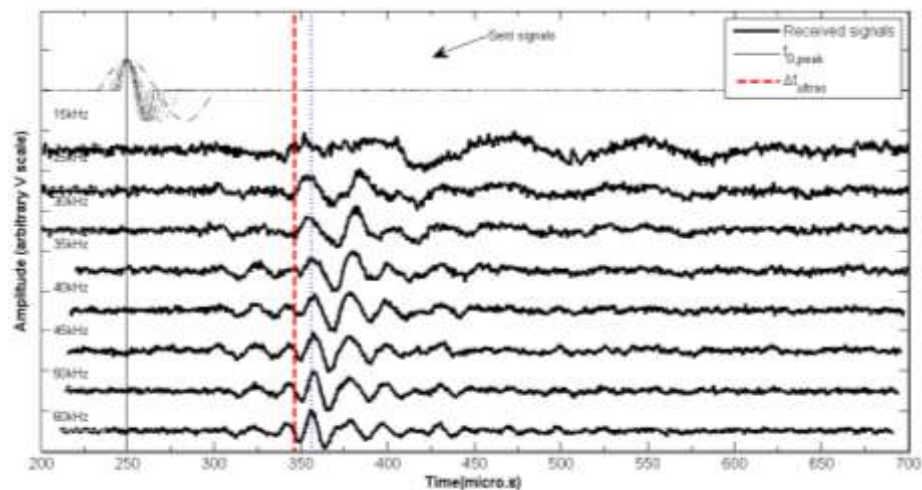


Figure 4.11: BE test frequency sweep response with the calibration cylinder filled with BE couplant on day 1 of cure

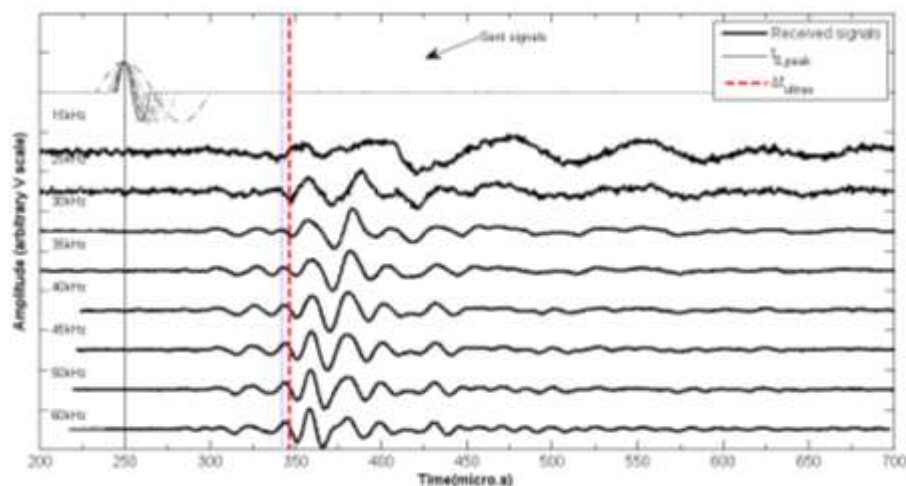


Figure 4.12: BE test frequency swept response with the calibration cylinder filled with BE couplant on day 2 of cure

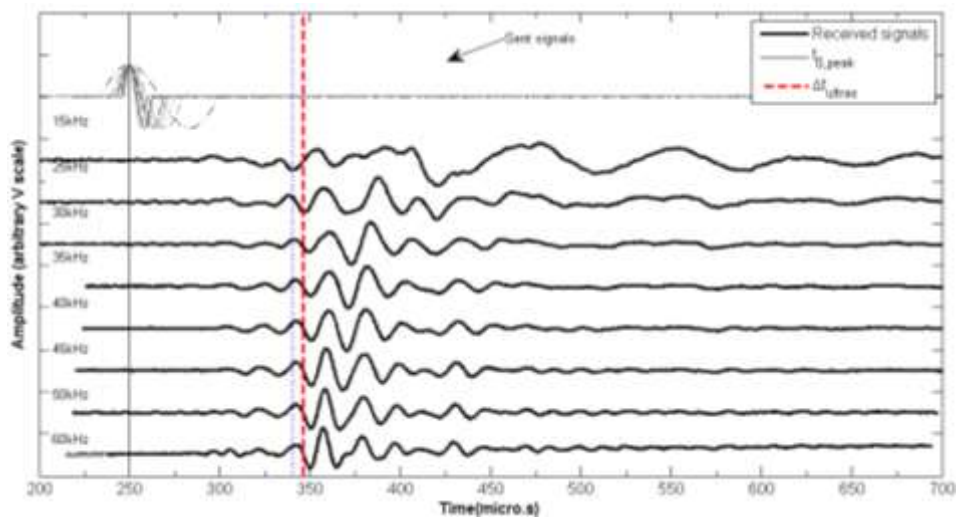


Figure 4.13: BE test frequency swept response with the calibration cylinder filled with BE couplant on day 3 of cure

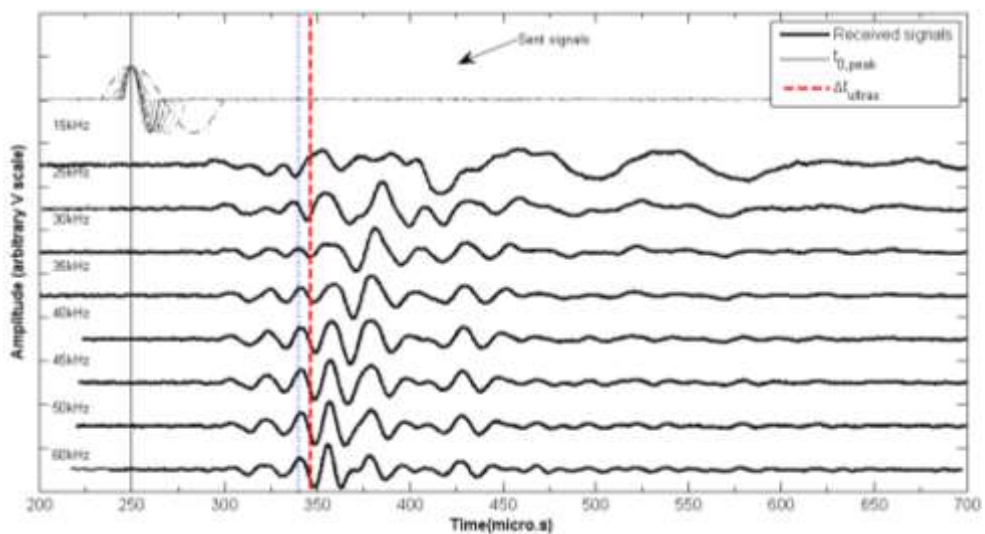


Figure 4.14: BE test frequency swept response with the calibration cylinder filled with BE couplant on day 4 of cure

The second factor to affect the first-peak arrival judgement was the near-field effect, as discussed in 2.5.1.2. The oscillation observed at 325 μs was more difficult to be identified at smaller frequencies (15-25 kHz), which could indicate the presence of near-field effect cancelling the arrival of earlier waves. This oscillation became more evident with time, probably due to stiffness gains (measured but ignored), indicating changes in the near-field effect range as specimen stiffness changed.

The last effect regards the frequency range. The 50 kHz and 60 kHz signal responses appeared to be the same, possibly indicating a “new” BE device ceiling. Therefore, although a different input was applied, the same response was reached for both frequencies. As a result, the frequency of 60 kHz was removed from in the BE peak arrival analysis.

Therefore, although the difference in time between day 1 and day 2 appeared to be significant, this difference was not considered due to the other factors that possibly affected measurements and decision making.

4.4.2 BE couplant effect on specimen mass

Due to time constraints, mass calibration using the calibration cylinder with the circular cavities was performed during 4 days, which corresponded to 5 days of specimen cure. The water content over time was plotted in Figure 4.15; the best-fit was adjusted to the plotted data from day 1 of couplant cure. As the best-fit is a second-degree polynomial, after its minimum point, the values would stop reducing and would start increasing. Thus, its minimum point was obtained by deriving the best-fit equation (which resulted in 4.5, approximately) and, after that, the variation in the water content was considered zero. In other words, from day 5 of the couplant cure, the water content in the couplant was considered the same for the rest of the test period.

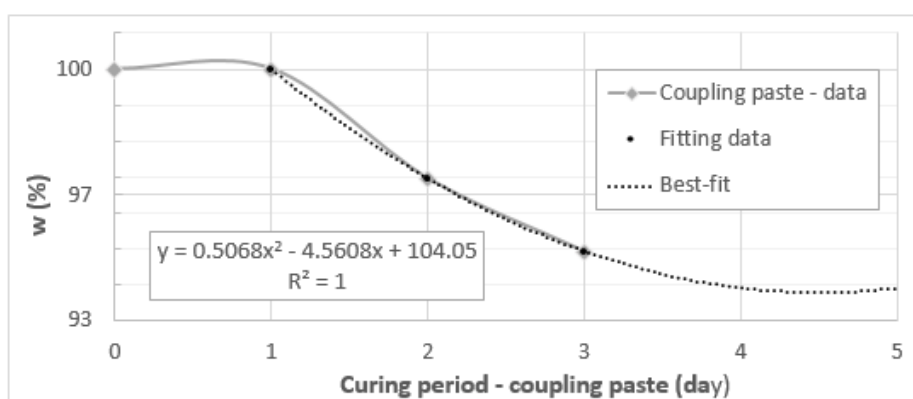


Figure 4.15: Water content changes over time for the couplant filling the calibration cylinder with circular cavities, coupled to BE bench pair

Figure 4.16 was obtained from the changes in couplant water content. The dashed line indicates when the calibration started. For the specimen BEN_8.64_15.4, changes in natural

unit weight were steeper than for the specimen BEN_31.9_15.4, but both corrections seemed to be adequate.

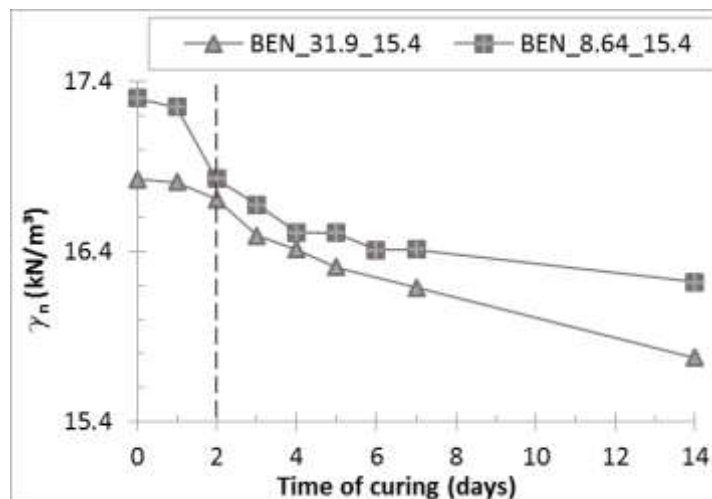


Figure 4.16: Corrected natural unit weight over time for specimens subjected to BE bench tests

4.5 ANISOTROPY

As the investigated soil was artificially cemented, the hypothesis of cross-anisotropy (applied for natural soils) had to be investigated. Prior to any test, it was considered that the compaction process would impose a degree of vertical anisotropy, as load application occurred only vertically, while the two horizontal directions in the cubical specimens only reacted to the load (lateral stress ratio, K_0). The associated expectation was that cement hydration would gradually mask anisotropy by occupying voids homogeneously. Nonetheless, despite the apparent dispersion (Figure 4.17 and Figure 4.18), the data suggested that the cemented Osorio sand was isotropic from day 1 of cure – indicating that no conclusions on anisotropy could be reached between the moment of specimen fabrication and test day 1. Furthermore, although a small degree of anisotropy was observed in some tests, they were not consistent among specimens neither among tests conducted in the same specimen, when p-waves and s-waves were compared.

Figure 4.17 (a) to (d) show p-wave velocities for cubical specimens. Specimens CUB_8.64.15.4 and CUB_8.64.14.3 presented an unexpected behaviour between day 1 and 3 of specimen cure. As this happened for two independent specimens, no further conclusions

could be reached regarding those test days, even though these seemed to be spurious data – but each measurement was performed on different days, excluding problems in equipment behaviour, raising some questions about this very similar behaviour for two different specimens. In fact, the 1st measurement (for both specimens) seemed to be out of the specimen behaviour, which might be related to some sort of water content effect, as this behaviour did not occur for s-wave velocities. On the other hand, the change in water content was not significant between these days, as presented in Figure 4.9. Thus, any conclusions about this unexpected behaviour would be merely speculative.

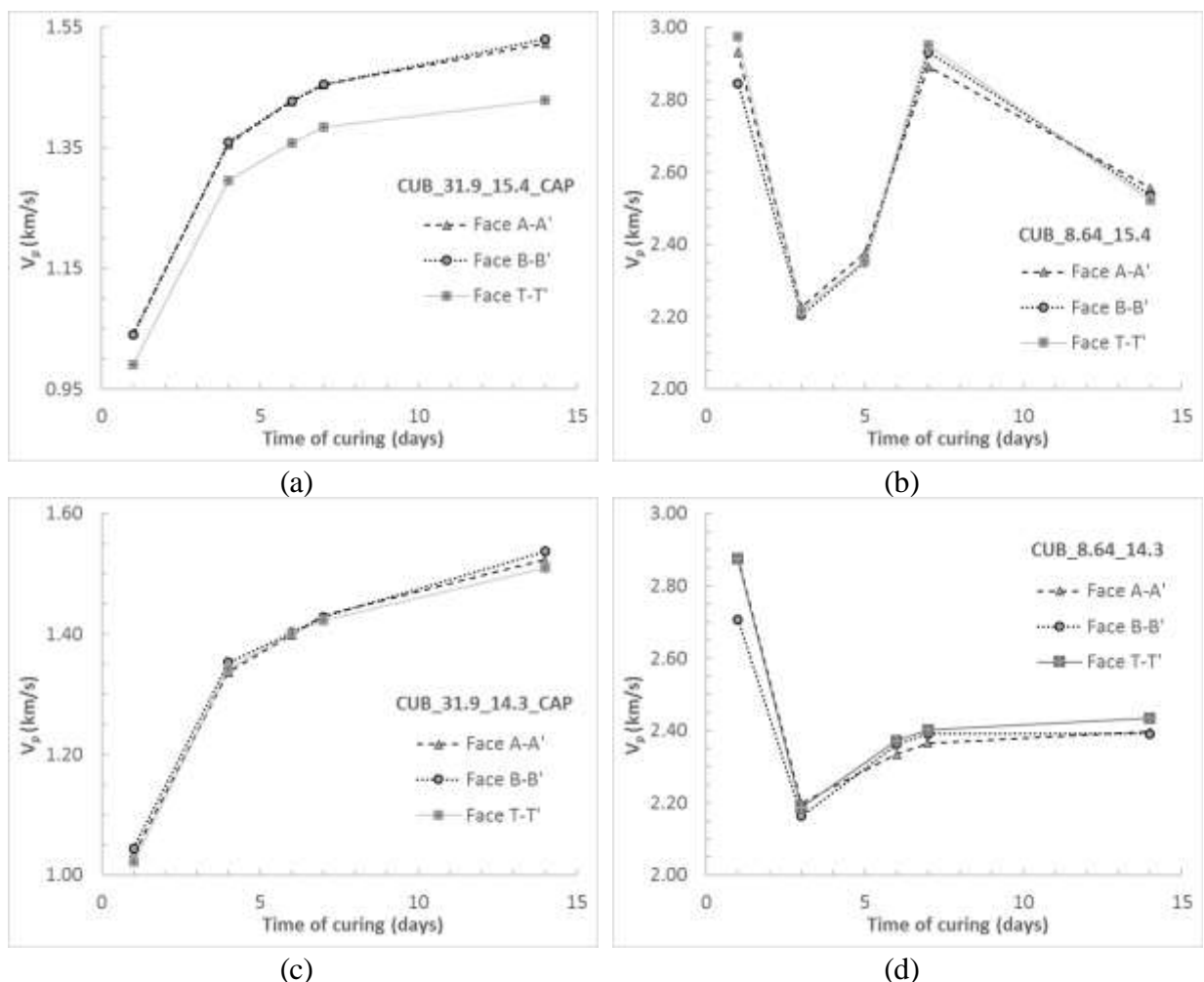


Figure 4.17: Anisotropy analysis based on p-wave velocity measurements on the three orthogonal planes (faces) for the following cemented Osorio sand specimens – (a) CUB_31.9_15.4_CAP; (b) CUB_8.64.15.4; (c) CUB_31.9_14.3_CAP; (d) CUB_8.64.14.3

Despite that, Figure 4.17 (b) to (d) seem to present isotropic specimens for the entire test period, as well as some random behaviour between faces of the same specimen, with lines crossing each other, supporting the non-prevalence of one velocity over of the others or, in other words, supporting the conclusion of isotropy. Only Figure 4.17 (a) presents cross-anisotropy. However, as this was not observed for the s-wave velocity (Figure 4.18 – a), it was considered an abnormality, and the conclusion of isotropy was kept.

Aiming to add to the anisotropy discussion, Figure 4.19 (a to d) present some examples of the ratio of each horizontal velocity (faces A-A' and B-B') to the T-T' direction velocity, for p-waves and s-waves velocities.

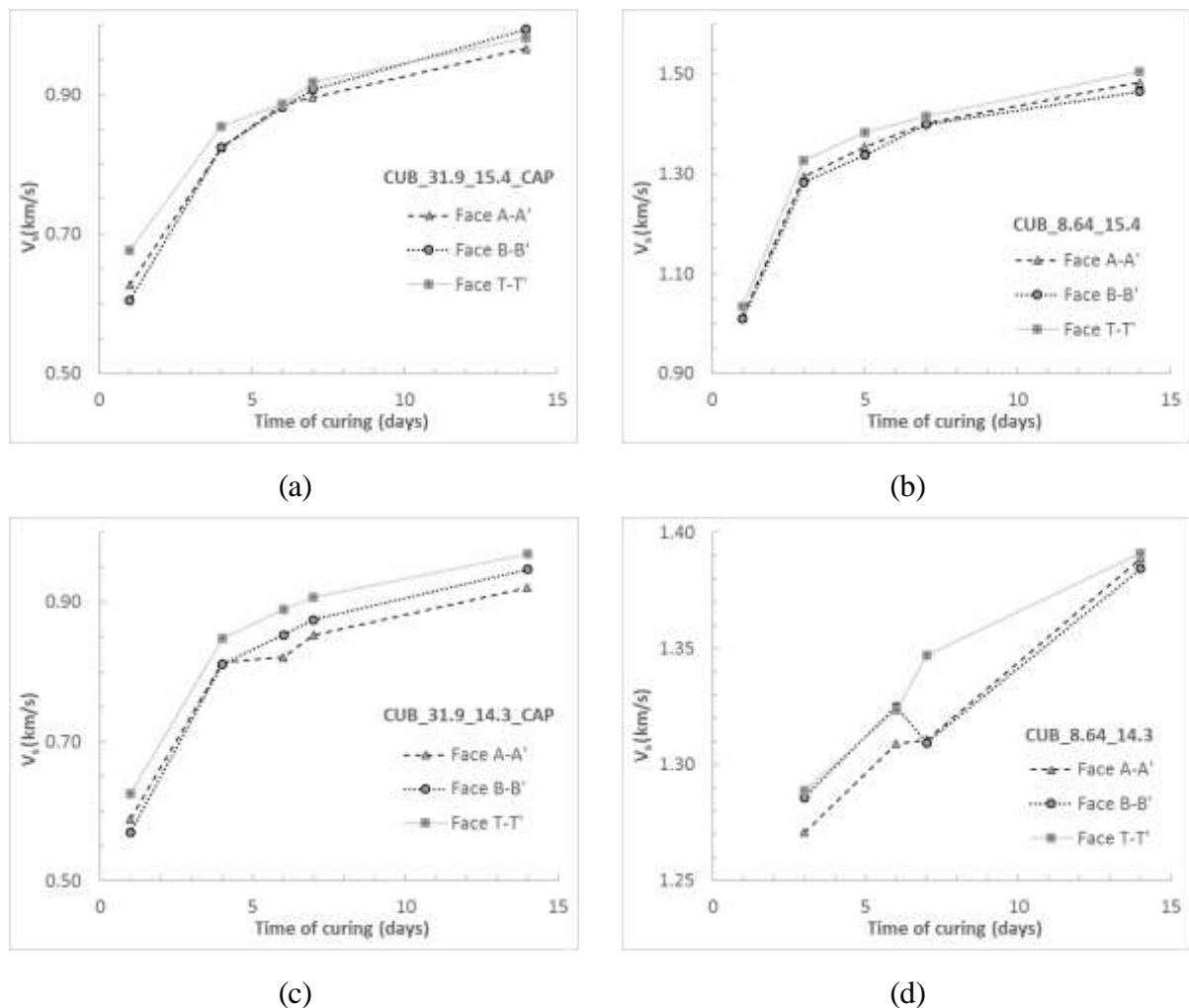


Figure 4.18: Anisotropy analysis based on s-wave velocity measurements on the three orthogonal planes (faces) for the following cemented Osorio sand specimens – (a) CUB_31.9_15.4_CAP; (b) CUB_8.64.15.4; (c) CUB_31.9_14.3_CAP; (d) CUB_8.64.14.3

A general analysis of Figure 4.18 indicates isotropy for the majority of specimens and cure periods. However, two specimens (Figure 4.18 – b, and Figure 4.18 – c) seemed to be slightly cross-anisotropic. When analysing these two specimens (CUB_8.64.15.4 and CUB_31.9_14.3_CAP), the ratio of each horizontal velocity (faces A-A' and B-B') to the T-T' direction velocity (Figure 4.19 – b and Figure 4.19 – c) ranged between 2.28% and 4.36% for V_p , and between 3.33% and 8.85% for V_s .

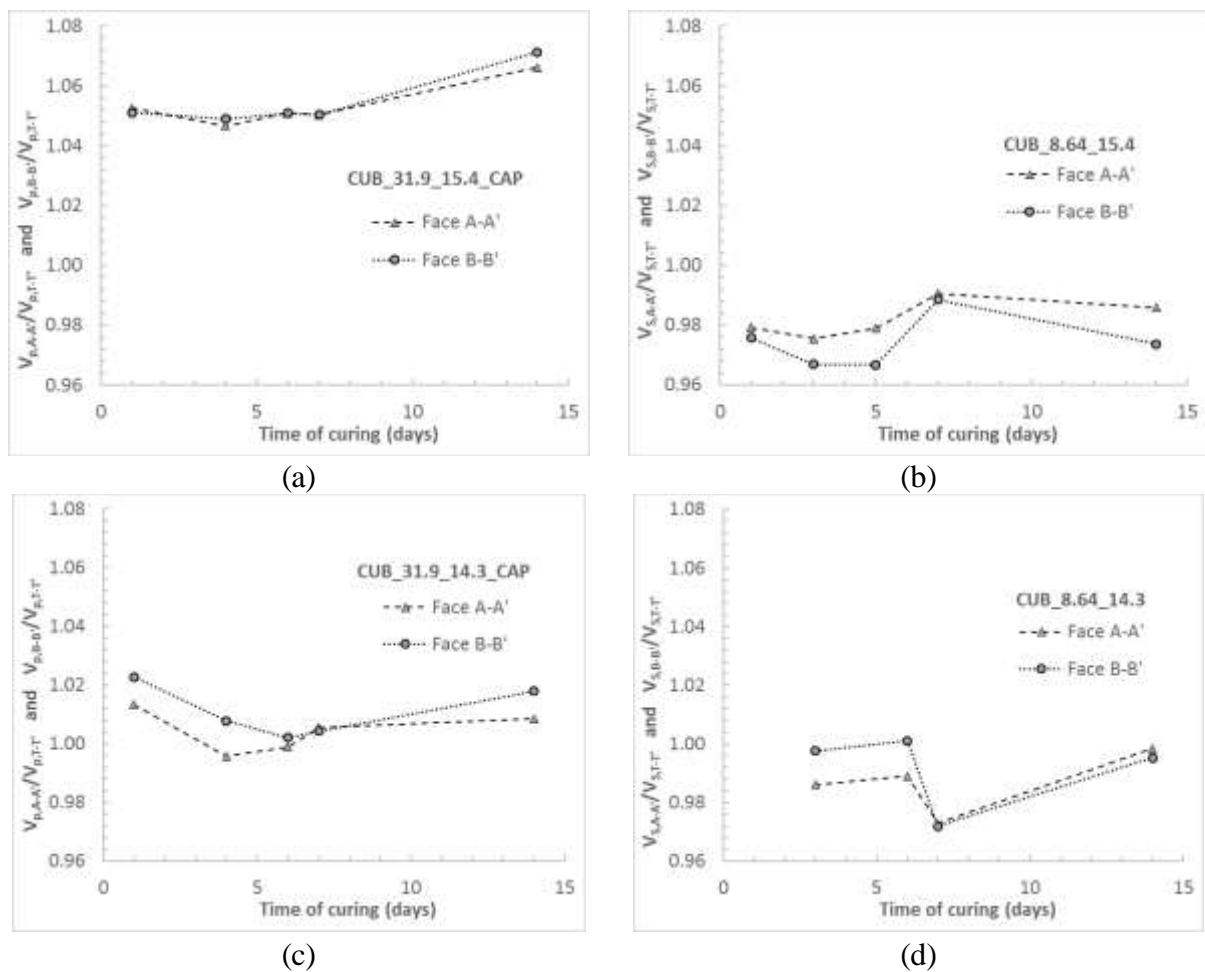


Figure 4.19: Examples of $V_{A-A'}/V_{T-T'}$ and $V_{B-B'}/V_{T-T'}$ ratio for p-waves and s-waves for specimens – (a) CUB_31.9_15.4_CAP; (b) CUB_8.64.15.4; (c) CUB_31.9_14.3_CAP; (d) CUB_8.64.14.3

4.6 ULTRASOUND TESTS

UPV tests were performed on both cylindrical and cubical specimens. Results for the cylindrical specimens are presented in 4.6.1, while the results for cubical specimens tested for

the investigation of anisotropy were previously presented in 4.5. Cylindrical specimens moduli were compared to the vertical moduli calculated from cubical specimens and their differences are presented in 4.6.1.1. Likewise, shear moduli calculated from the prediction equation presented in the literature for BE tests (2.5.1.4) were also compared to the cylindrical specimens shear moduli (4.6.1.2). Lastly, the effect of specimen geometry on UPV tests are discussed in 4.6.2.

4.6.1 Cylindrical specimens

The results for cylindrical specimens tested with the UPV device were very consistent regarding stiffness gains over time and behaviour among different specimens. Figure 4.20 – (a) and Figure 4.20 – (b) present the changes in p-wave and s-wave velocities over time. Generally, all specimens followed the same pattern of steeper velocity gains in the early days of cure, followed by slightly flatter gains in the last days – a behaviour that was expected due to the cementitious agent (Portland cement type III) used in the experiment. The same behaviour was observed for the constrained and shear moduli (Figure 4.21 – a and b). Returning to Figure 4.20, the vertical distance of specimens with the same η/c_{iv} ratio were very similar when p-waves and s-waves velocities were compared – despite the different offsets, both plots have the same vertical scale, allowing visual comparison. P-waves and s-waves velocities belonging to specimens with $\eta/c_{iv}=8.64$ were also consistently faster than specimens with $\eta/c_{iv}=31.9$ – a pattern that was also observed for modulus values.

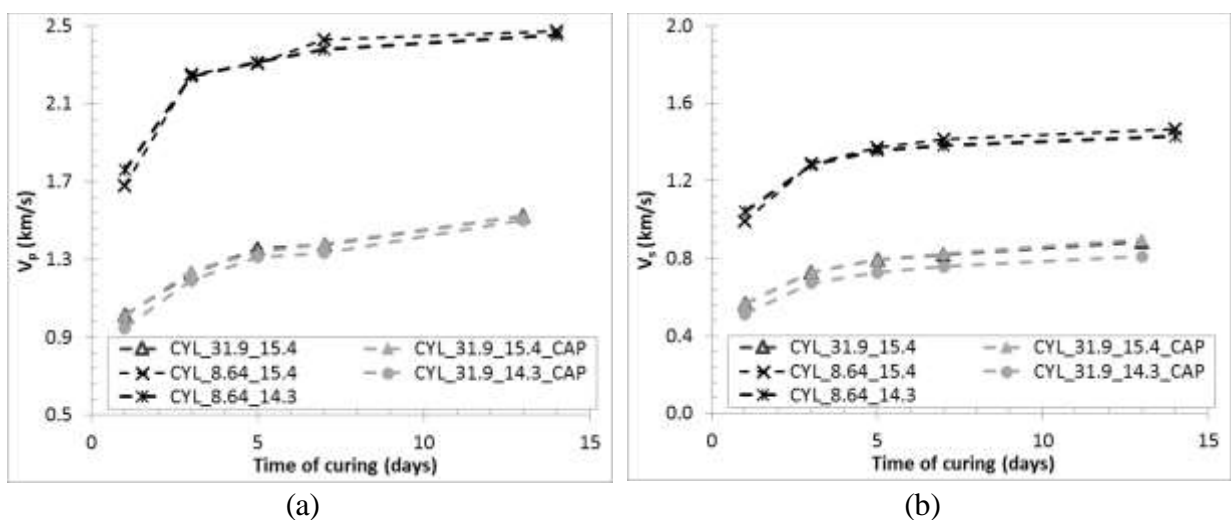


Figure 4.20: Cylindrical specimens wave velocities obtained during UPV tests along the cure period – (a) p-wave velocities; (b) s-wave velocities

Constrained modulus values were on average 3 times greater than shear modulus values for any specimen, representing a V_p/V_s ratio ranging between 1.64 and 1.85. No further conjectures will be conducted regarding the V_p/V_s ratio because this direct comparison was judged inadequate, as specimens were only partly saturated. This assessment is only considered admissible and correct when either a totally dry or totally saturated specimen is investigated, or when the degree of saturation is known and the possible effects of the suction matrix can be evaluated and corrected. P-wave velocity has been shown to be very sensitive to the degree of saturation – as presented by Tsukamoto *et al.* (2002), in which a 70% reduction in p-wave velocity was caused by only 10% change in saturation of an initially fully saturated body. In other words, this analysis could not be conducted unless the voids volume could be measured along the days of cure when the cementitious reactions were filling the voids. Moreover, the interpretation of compressional waves and their correlation to shear waves were not within the scope of the present work.

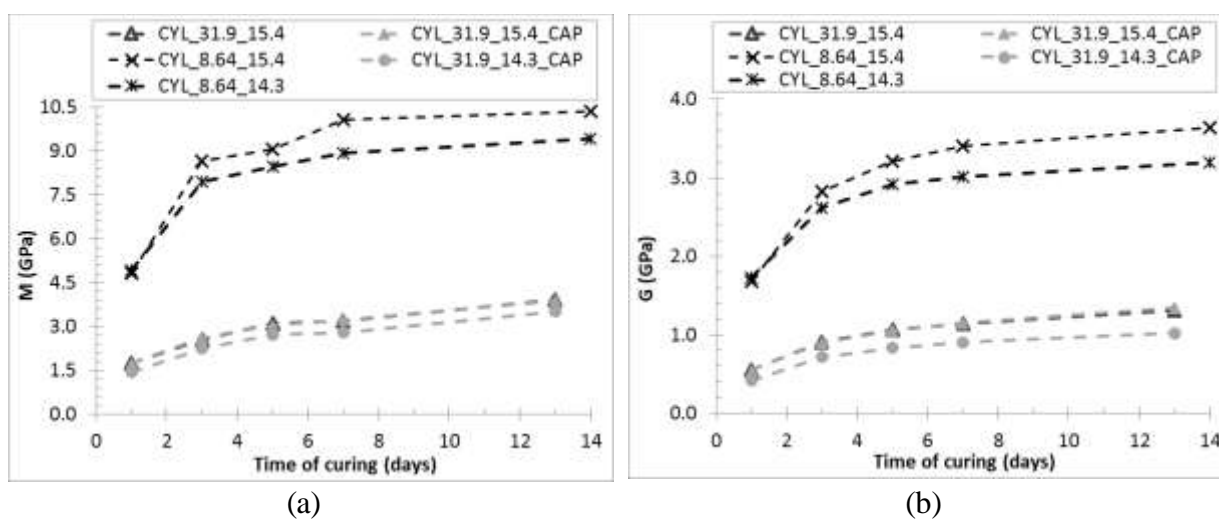


Figure 4.21: Cylindrical specimens moduli obtained from wave travelling times measured during UPV tests along the cure period – (a) constrained modulus (M); (b) shear modulus (G)

4.6.1.1 Cubical specimens comparison

The abnormal behaviour of p-wave velocities at the earlier stages of the cubical specimens CUB_8.64_15.4 and CUB_8.64_14.3, presented in Figure 4.17 – (b) and (d), was not observed in the cylindrical specimens (Figure 4.20 and Figure 4.21). As the argumentation previously presented in 4.5 is merely speculative and valid only for cubical specimens, the

findings led to the belief that specimen geometry can strongly affect wave measurements, which will be discussed in more detail in 4.6.2. The abnormal behaviour could be justified by water content distribution along the mass of the specimen, which could also involve specimen geometry, but not the nature of wave travelling. The constrained and shear moduli of cylindrical and cubical specimens are plotted in Figure 4.22 – (a) and (b).

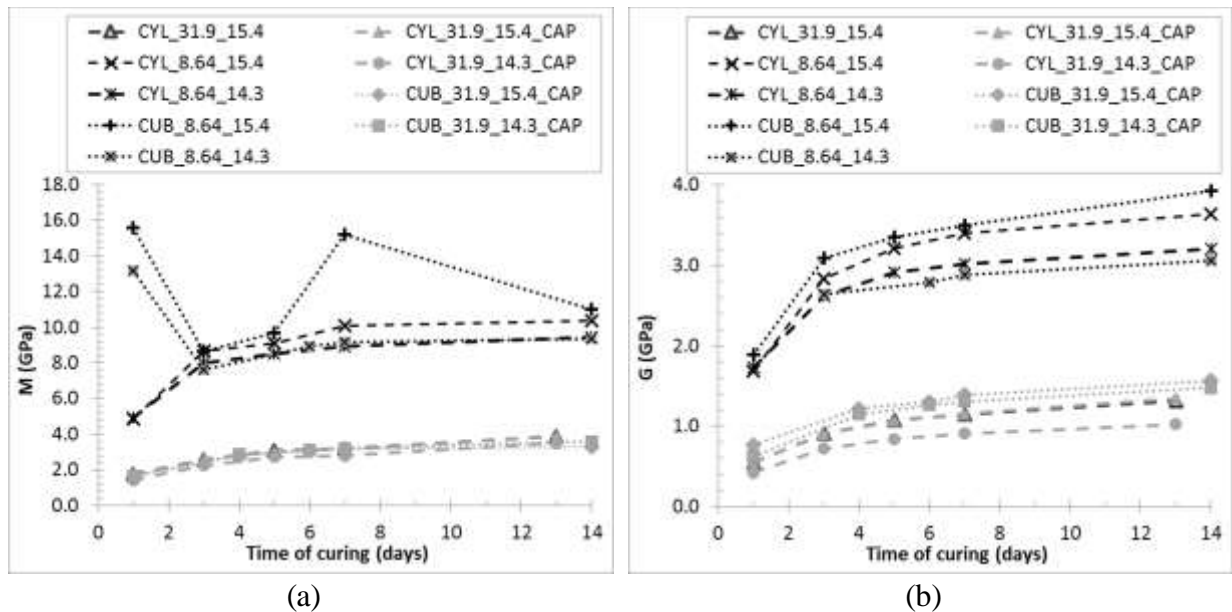


Figure 4.22: Comparison of different moduli obtained from cylindrical specimens and from the vertical direction of cubical specimens during UPV tests – (a) constrained modulus (M); (b) shear modulus (G)

Despite the abnormal behaviour of the two cubical specimens, all the other specimens moduli seem to follow the same pattern. Only the constrained moduli of specimens with $\eta/c_{iv}=31.9$ were superposed regardless of specimen geometry. All the other possible comparisons did not result in precisely the same values, although the results for each η/c_{iv} ratio respected the same order of magnitude. It is also important to point out that specimens did not have the same dry unit weight values or the same η/c_{iv} ratios, which had an impact on the calculated moduli.

4.6.1.2 Comparison with BE prediction equation

As the present work intended to compare UPV and BE methods, Figure 4.23 presents a preview of such comparison. However, the results regarding BE tests are just a prediction calculated with Equation (2.21), using the real η/c_{iv} ratio of each specimen. The presented shear moduli for day 7 of cure, and the results for UPV and BE tests were plotted together for

each specimen (labelled at the bottom). UPV results were 1.24 and 1.98 times higher than BE results for all specimens. Even though the prediction equation presented some intrinsic errors (because it was an approximation to the set of data), UPV values were almost twice as high as BE predicted values. This appeared to extrapolate the intrinsic best-fit error and, therefore, tended to reinforce the dispersive nature of the BE-specimen system as discussed in 2.5.1.1. These two outcomes are presented again with the measured results for BE bench tests in 5.8, using the proper correction.

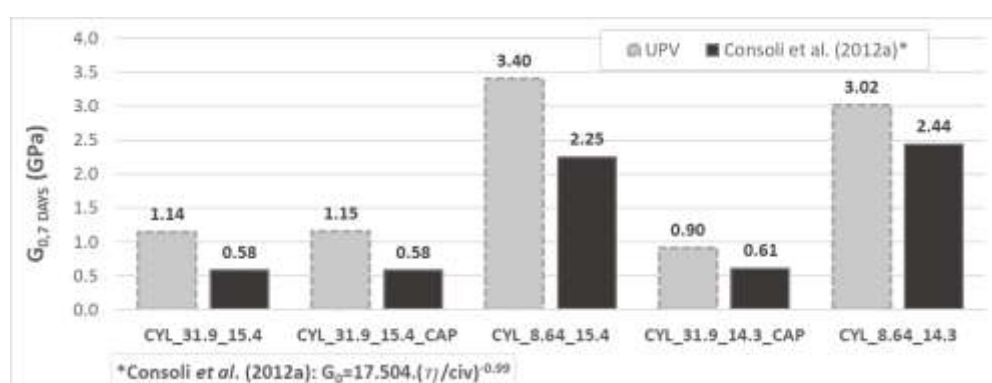


Figure 4.23: Comparison between the shear modulus obtained from UPV tests and those calculated based on the prediction equation for BE tests on day 7 of cure

4.6.2 Specimen geometry

The use of the UPV device has some limitations regarding the geometry of the specimen tested, according to the standard BS1881: Part 203 (BSI, 1986). As the standard guidelines for UPV tests are for concrete, and no standard for soil or improved soil is available, its recommendations had to be interpreted and approximated to the reality of soils. Although specimen length was not an issue, as presented in 4.4.7.2, it is important to mention that specimens were usually 100 mm high, sometimes slightly shorter. Nonetheless, the 100-mm reference regards concrete specimens, and slightly shorter heights was considered admissible, as an improved soil was being tested.

The lateral dimension, whether the diameter of cylindrical specimens or the distance between two opposite faces of cubical specimens, is a matter of debate as well. BS1881: Part 203 (BSI, 1986) establishes a minimum lateral dimension (Table 4.3) for wave velocity propagating

through concrete for a specific transducer and specific sent wave frequencies. Wave velocity values for concrete are higher than the maximum value obtained for the cemented Osorio sand (2.5 km/s). However, a linear regression involving velocities and the minimum lateral dimension (in respect to the 54 kHz transducer) resulted in a dimension equal to 47 mm for a velocity of 2.5 km/s. Therefore, considering the regression is valid, the dimensions of the specimens were considered adequate.

Table 4.3: Effect of specimen dimensions on pulse transmission

Transducer frequency (kHz)	Pulse velocity in concrete (in km/s)		
	vc = 3.5	vc = 4.0	vc = 4.5
	Minimum permissible lateral specimen dimension (mm)		
24	146	167	188
54	65	74	83
82	43	49	55
150	23	27	30

(source: BSI, 1986)

4.7 BE TRIAXIAL SYSTEM VALIDATION

As the validation of the triaxial BE pair used non-cemented Osorio sand, and consequently the signal should be clearer and easier to be interpreted, it was decided to present this item in advance. Moreover, signal quality evaluation of BE system outcomes would be more adequate without the uncertainties and “noise” that cementitious reactions impose to the system.

As presented before (3.1), the system does not include signal filtering (by frequency), neither analogical nor digital. Thus, all data presented in this work is basically the raw data obtained without further processing. Data were just subjected to time offset adjustment to align all the input peaks, and received signal increasing (arbitrary vertical scales) to permit peak identification more easily.

All data were collected as raw as possible, i.e., with the minimum number of points for each data acquisition. As the minimum acquisition sampling rate was 4 points, this value was used whenever possible. For the studied non-cemented Osorio sand, all tests were performed using an average of 4 points.

Figure 4.24 summarizes BE tests on the saturated specimen TRX_0.00_15.4 subjected to an effective confining pressure of 200 kPa. This figure presents single sine pulses of 5 kHz interval starting from 5 kHz until 40 kHz for all tests, see Appendix C. Some of the frequencies seem to have had their signal cut off in the beginning of the acquisition. As the oscilloscope exclusively acquires data presented on the screen, time limits would depend on the time scale used at the moment of acquisition. As a consequence, higher frequencies would require signal zooming to be seen.

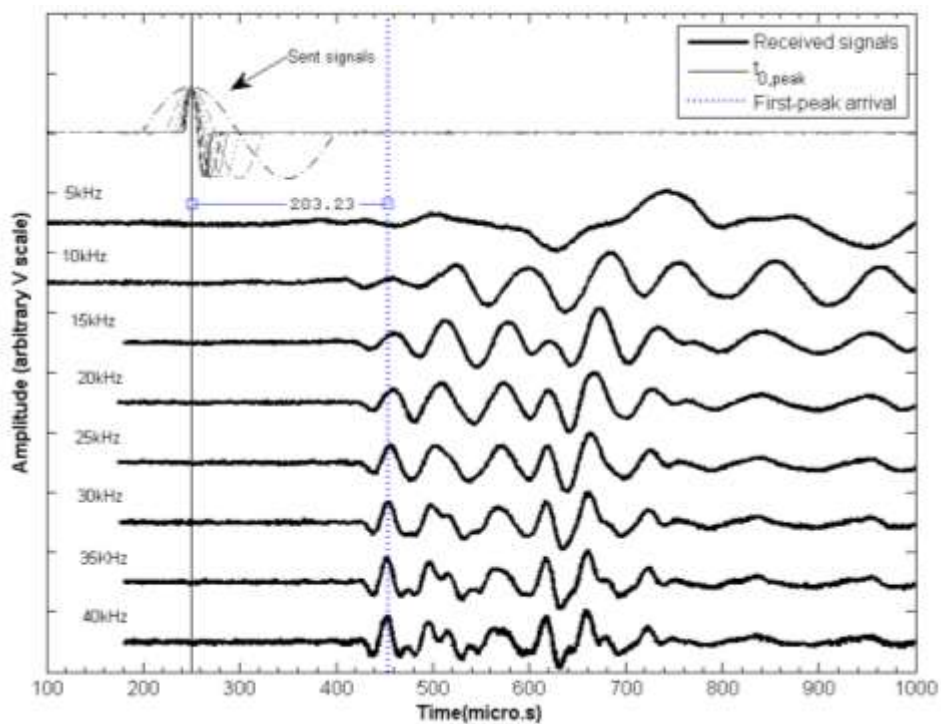


Figure 4.24: BE triaxial test frequency swept responses (5 to 40 kHz) of specimen TRX_0.00_15.4, right after isotropic consolidation ($\sigma'_3 = 200$ kPa)

The top horizontal line represents all the targeted input signals (for all frequencies) aligned to the peaks. Depending on their frequency (e.g. 1 kHz), input signals may not fit into the horizontal limits. The following lines represent all the received signals in an increasing order of frequencies. The black vertical solid line determines the alignment of input peaks, which was considered as point zero for wave travelling time measurements.

Lastly, the blue vertical dotted line indicates the peak-to-peak wave travelling time measurement, as indicated by the value “203.23” (μs). This value still contains the time-delay

caused by the whole system; therefore, the actual wave travelling time value was obtained by subtracting the previously found time-delay from this value (e.g.: $203.23 \mu\text{s} - 22.085 \mu\text{s} = 181.145 \mu\text{s}$). There is still one interesting element to be addressed. It refers to the consistent presence of troughs right before the majority of the identified first peak arrival time. Those troughs have no preceding peaks, becoming more accentuated with increasing frequencies. Moreover, as the pair was aligned in order to send and receive peaks (as the first deflection), these troughs are not explained by shear-waves propagating in the perpendicularity to BE movement. Although they may be explained by wave reflection or boundary conditions, its real nature remains unclear (ARULNATHAN *et al.*, 1998; BLEWETT; BLEWETT; WOODWARD, 2000; ARROYO *et al.*, 2006; VIANA DA FONSECA; FERREIRA; FAHEY, 2009; ALVARADO; COOP, 2012; CAMACHO-TAUTA *et al.*, 2015).

Figure 4.24 presents clear signals, without any relevant noise or oscillation, representing the quality of signal acquired by the system and, indirectly, the quality of the generated signal. However, as the observed generated signal was only a theoretical representation, it was not possible to directly assess the real generated signal. The different wave lengths of the received signals are a good indication that different frequencies were sent by the generator transmitter. This figure also illustrates the adequate gain obtained through the amplifier, and the good job performed by grounding the system and filtering external noise with the use of a drain line. These can be evidenced by the lack of crosstalk. Nonetheless, the piezoceramics waterproof coating seemed to be adequately achieved, considering the specimen and the BE pair were subjected to a back pressure of 590 kPa, and no interferences or signal noises were noticed. Taking into consideration the intrinsic limitations in regards to BE systems, the present results clearly demonstrate that a high quality system was developed, and that reliable BE measurements were conducted.

Regarding BE triaxial system validation, which would define BE system quality beyond any doubts, Figure 4.24 presents a good agreement between frequencies. Frequencies higher than 30 kHz seem to have a slight offset of the received signals to the left side, while frequencies smaller than 25 kHz seem to have an offset to the right side of the figure. This behaviour could suggest a dispersive behaviour of the BE-specimen system, establishing a frequency dependency. Nonetheless, the received signal of 5 kHz did not present a real peak at all, and even the following frequency responses did not present much similarity to the ideal 5 kHz sent waveform. That might be explained by interferences caused by near-field effect (as it is more evident for smaller frequencies in the kHz range). It is worth mentioning that near-field

effects is an issue intrinsic to wave propagation, and not to the BE system proper. Following the same procedure presented in Table 2.1, the two lowest options ($L_e > 2.\lambda$ and $L_e > 4.\lambda$) of a range of frequencies free of near-field effects are 10.6 kHz and 21.2 kHz. That reinforces the poor signal acquired at 5 kHz, which was probably affected by near-field effects.

Analysing the plots of each 1 kHz (Appendix C), there was only one disagreement between time measurements (Figure 4.25). The range of frequencies between 1 kHz and 8 kHz has the first evident peak after 239.205 μs (261.29 μs minus the system time-delay of 22.085 μs), which is higher than measurements for any of the higher frequencies. The frequencies at 7 kHz and 8 kHz show a light movement around the peak position shown in Figure 4.24, which might indicate the presence of a wave arriving earlier. Peaks at earlier times did not appear with lower frequencies, strongly indicating the presence of near-field effects, which might cause the delay observed for lower frequencies (between 1 and 8 kHz). However, any conclusions regarding the frequency range in which near-field effects are evident is only applicable for non-cemented specimens subjected to specific conditions. In other words, it is only possible to claim that near-field effects manifest with frequencies up to 8 kHz on non-cemented saturated Osorio sand, compacted at medium to dense state, and subjected to a confining pressure of 200 kPa.

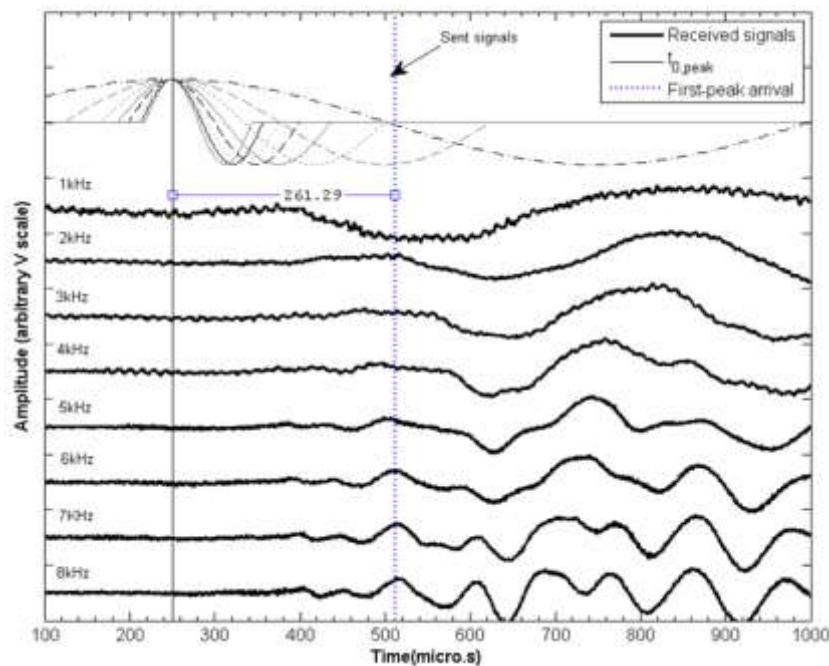


Figure 4.25: BE triaxial test frequency swept responses (1 to 8 kHz) of specimen TRX_0.00_15.4, right after consolidation ($\sigma'_3 = 200$ kPa)

Figure 4.26 presents the shear moduli calculated based on BE measurements and those presented by Heineck, Coop, and Consoli (2005), in which Osorio sand was also subjected to BE tests. The moduli previously found in the literature is 80% of the moduli found in the present study. Two relevant points should be discussed. First, the real dry unit weight of the specimen TRX_0.00_15.4 remained unknown, which could lead to inaccurate values and incorrect comparisons regarding the shear modulus. Although the specimens probably did not have the same unit weight, which limits the comparison from a more qualitative point of view, the analysis can be reduced to shear wave velocity to exclude the effects of the unknown dry unit mass. The shear wave velocity in the literature (441.15 m/s) was about 89% of that of the specimen TRX_0.00_15.4 (496.67 m/s).

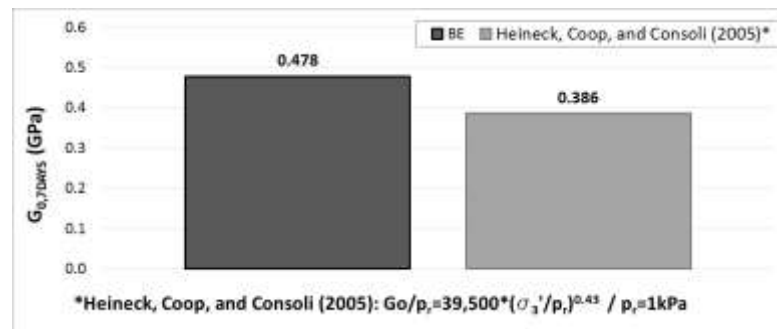


Figure 4.26: Triaxial BE pair validation using initial shear modulus of Osorio sand (not cemented), after consolidation ($\sigma'_3 = 200 \text{ kPa}$), in comparison to previous study of Heineck, Coop, and Consoli (2005).

These seem to be reasonable results, which leads to the second relevant point. Viggiani and Atkinson (1995) highlight that shear-wave travelling time is the main source of error in shear modulus calculation when using BE. They found errors $\pm 30\%$ in time estimation, leading to errors up to $\pm 60\%$ in shear modulus. Therefore, the difference between shear modulus found in the present study and that found in the literature seems to be in the expected BE accuracy interval. Therefore, the BE system developed for the present study was considered successfully validated, with reliable results.

4.8 BE BENCH TESTS

Results regarding BE bench test are presented only in relation to time-domain; more specifically, with the peak-to-peak approach. Data interpretation using this methodology is

presented in the next item. After that, bench system validation based on comparisons with data previously published in the literature is discussed. The following item discusses the damages caused to the BE pairs after piezoceramic exposure to water, and the consequent impairments to signal results. In the last item, resonance response over time is presented.

4.8.1 Time-domain – Peak-to-peak approach

In contrast with the usual order presented in this specimen, specimen BEN_8.64_15.4 is going to be presented first. This decision was made based on the fact that tests with this specimen were conducted before any damage was observed in the BE bench pair, which resulted in clearer signals, easier to be interpreted.

Figure 4.27 presents the stacked BE bench test signal responses of specimen BEN_8.64_15.4 on day 2 of cure. Notice that the smallest input frequency (1 kHz) extrapolates the plotting limits, and is barely visible. The red vertical dashed line refers to the UPV measurements adjusted for the dry unit mass and distance between transducers of specimens tested with BE. The black vertical dashed line refers to the BE predicted values (CONSOLI *et al.*, 2012), using the η/c_{iv} ratio of the investigated specimen, on day 7 of cure. Those two dashed lines are merely indicative, and should not interfere on the decision about the first peak arrival time.

As mentioned before, the blue vertical dotted line indicates peak-to-peak wave travelling time measurement. The calibrated time-delay (22.085 μ s) had to be subtracted from the illustrated value of “73.79” μ s, resulting in the actual wave travelling time of 51.705 μ s. UPV measurements and the values predicted by Consoli *et al.* (2012) had the time-delay added before being plotted, which allowed the correct graphical comparison among all vertical lines plotted in the graph.

All the graphs illustrating the stacked response frequencies over time are presented in Appendix D.2. Except for day 7 of cure, all the other measurements were consistent among themselves, and the behaviour of the received signals was very similar. UPV measurements, and the values predicted by Consoli *et al.* (2012) got increasingly apart from each other over time, and peak-to-peak measurements were consistently the smallest values – representing higher velocity and, consequently, higher shear modulus. Despite this difference, signal interpretation was considered suitable. In all cases, both UPV measurements and BE predicted values crossed the troughs of waves. The peak right after UPV measurements and BE predicted values did not present a good agreement among frequencies, resulting in peak

misalignment. As a result, the peaks right before UPV and BE predicted values, which were well established and aligned, could be recognised for almost all frequencies and, therefore, were chosen as the position of the first peak arrival.

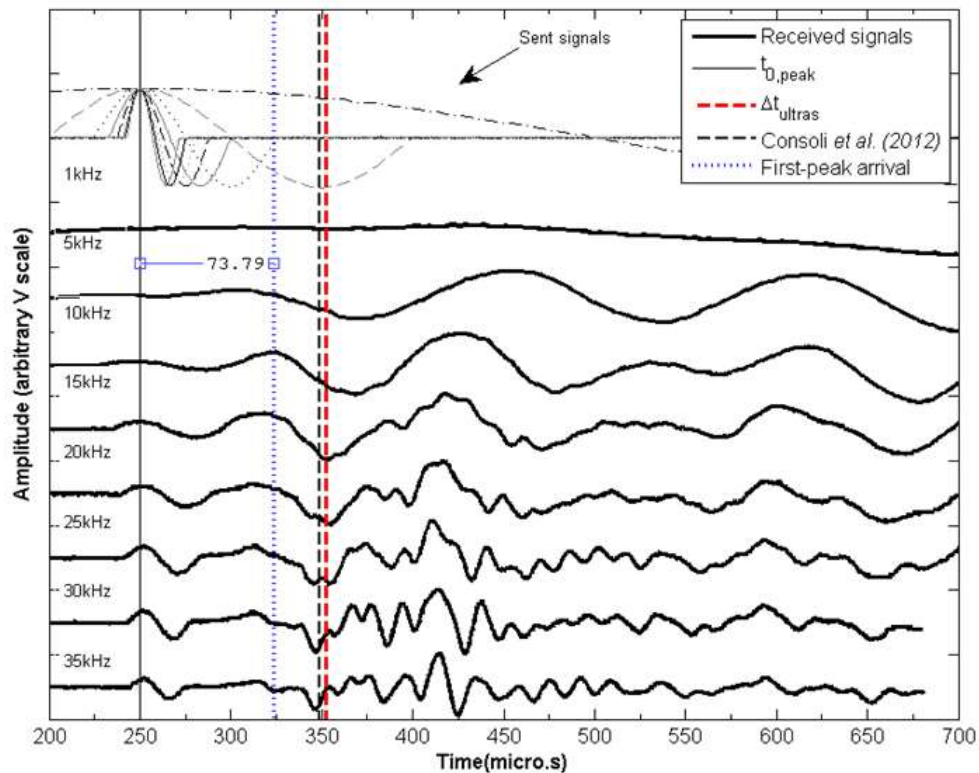


Figure 4.27: BE triaxial test frequency swept responses of specimen BEN_8.64_15.4 on day 2 of cure

The received signals mimicking the shape of input signals, almost aligned to the sent peaks especially in higher frequencies, could be related to electromagnetic crosstalk. The literature (JOVIČIĆ, COOP, AND SIMIĆ 1996; LEE, SANTAMARINA, 2005; MONTOYA *et al.*, 2010) usually indicates that crosstalk is caused by piezoceramics poor shielding, or perhaps due to the lack of drain lines in direct contact with the specimen. However, in the beginning of the study BE insulation was in perfect condition (BE were fully covered by epoxy resin). Thus, as the resin was new and the BE pair was subjected to no pressure, waterproofing should be adequate. Moreover, a drain line connecting the BE cables shield to the guard ports of the amplifier grounded to the energy source was used. As a result, the likely crosstalk observed in this specimen was somehow unexpected.

Moving to specimen BEN_31.9_15.4, Figure 4.28 presents the stacked frequency responses on day 2 of cure. Again, all data regarding this specimen is presented in Appendix D.1. These results were obtained after visible damages to the BE bench pair were observed and signal interpretation was more difficult than the previous specimen. The presence of noise and oscillation associated with the evident crosstalk are some issues related to BE damage, as Santamarina and Fam discussed (VIGGIANI; ATKINSON, 1997). Despite that, peak-to-peak measurements presented good agreement with UPV measurements and BE predicted values.

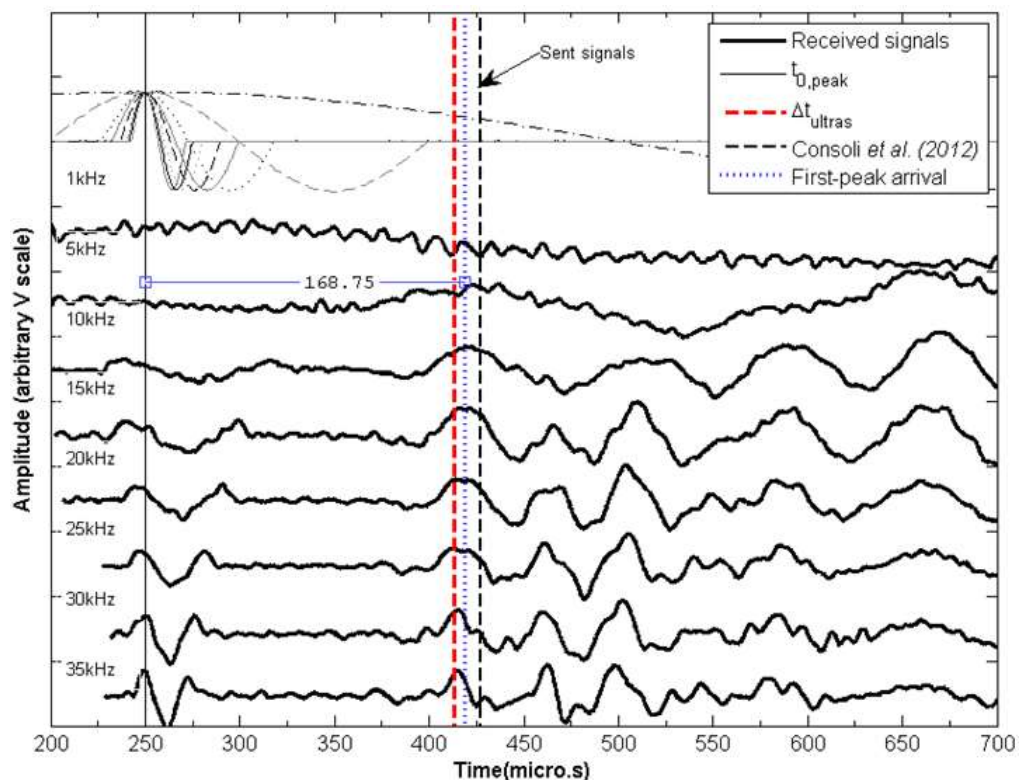


Figure 4.28: BE triaxial test frequency sweep responses of specimen BEN_31.9_15.4 specimen on day 2 of cure

Not all the sampling rates of specimen BEN_31.9_15.4 were obtained from the average of 4 points (as for specimen BEN_8.64_15.4). As a matter of fact, some measurements needed the average of 64 points in order to obtain a readable signal. The issue regarding sampling rate change, which probably resulted in different time-delays, is acknowledged, but its effects were not evaluated in the present work.

Crosstalk became even more evident in Figure 4.29 for two reasons: firstly, the vertical scale was bigger than that used with other specimens; and, secondly, as stiffness gains took place

over time, crosstalk became more evident, even at small frequencies – a fact not observed in the early days of cure. Although, a good agreement between peak-to-peak time and UPV measurements was observed, they became increasingly more distant from BE predicted values over time.

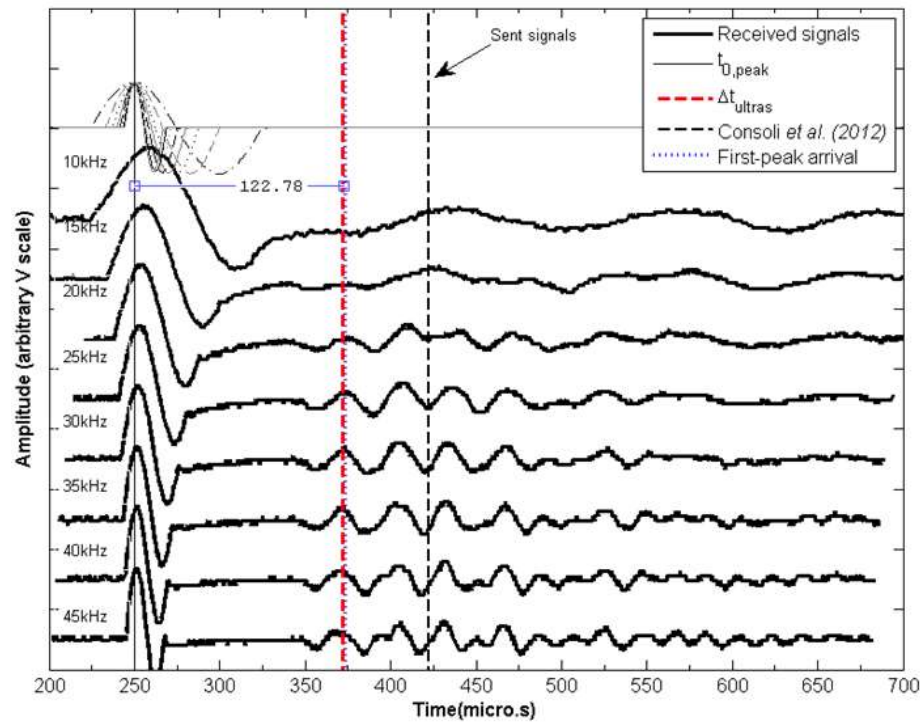


Figure 4.29: BE triaxial test frequency sweep responses of specimen BEN_31.9_15.4 specimen on day 14 of cure

Although the peak-to-peak and UPV measurements on day 14 of cure almost matched each other, an important point requires clarification. Figure 4.29 presents the consistent occurrence of troughs at about 355 μ s between 20 kHz and 45 kHz. These troughs were also observed in specimen TRX_0.00_15.4, indicating that it was not an isolated finding for the tested cemented material. The intriguing part concerns the lack of a preceding peak for any of these troughs. Hence, questions regarding the origin of these single troughs remain unanswered. It may be speculated that troughs could be generated by any sort of noise, near-field effects annulling only the presence of peaks, wave reflection, or boundary conditions (as mentioned before). Future studies will be required before a definite conclusion may be reached.

Using the evolution of wave travelling time measurements over the period of cure, Figure 4.30 was generated to present the final BE bench tests results, as well as the data obtained

from the UPV tests. A good agreement between methods was obtained with specimens with $\eta/c_{iv}=31.9$. However, BE bench tests results were about twice as high as the UPV measurements for specimens with $\eta/c_{iv}=8.64$. This difference was discussed in the beginning of this section, when the decision to select the first peak arrival was detailed. As UPV tests were not conducted every day, a linear regression between the two closest days to the day of interest was performed in order to obtain shear modulus (or wave travelling time) in respect to that specific day.

Despite difficulties choosing the first arrival peak, and some biases associated with signal interpretation, the time-domain approach was shown not to be a bad choice; although it is a time consuming method, it can be easily executed. The use of the frequency-domain approach, on the other hand, could accelerate data processing and also eliminate examiner-related bias on interpretation. However, it is not free of limitations regarding the BE-system dispersive nature either.

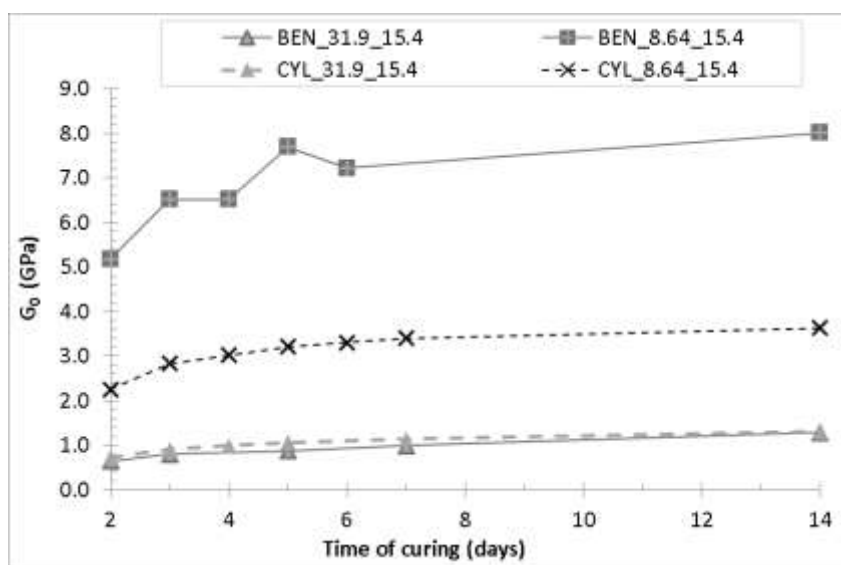


Figure 4.30: Shear moduli evolution of tested specimens over time with the BE bench pair and UPV device

In any case, regardless of the kind of data interpretation approach used, some factors are usually connected to the use of BE systems. For instance, the near-field effect is an intrinsic phenomenon associated with wave propagating at a certain range of frequencies; BE pairs with inadequate grounding will result in crosstalk, making the frequency-domain interpretation even more difficult; and noises and wave refractions are hard to avoid.

Moreover, test operators may not notice some of these factors without analysing a graph with plotted stacked frequencies, usually associated to time-domain.

In summary, while time-domain is a simple alternative, frequency-domain would be quicker and less prone to biases, but would require more elaborate corrections because of the dispersive nature of BE systems. Therefore, it seems to us that the best scenario would be an association of both techniques, using time-domain as a tool to confirm the findings obtained with frequency-domain, which would permit a more critical analysis concerning the acquired signal and its quality – following the recommendations by Viana da Fonseca, Ferreira, and Fahey (2009).

4.8.2 BE bench system validation

BE bench pair validation was conducted by comparing the shear moduli calculated based on BE test results and the shear moduli calculated with the prediction equation (CONSOLI *et al.*, 2012) using the η/c_{iv} ratio of tested specimens on day 7 of cure. Figure 4.31 presents the BE test and predicted data, as well as UPV results. Although the results are different, they roughly have the same order of magnitude, in respect to each η/c_{iv} ratio.

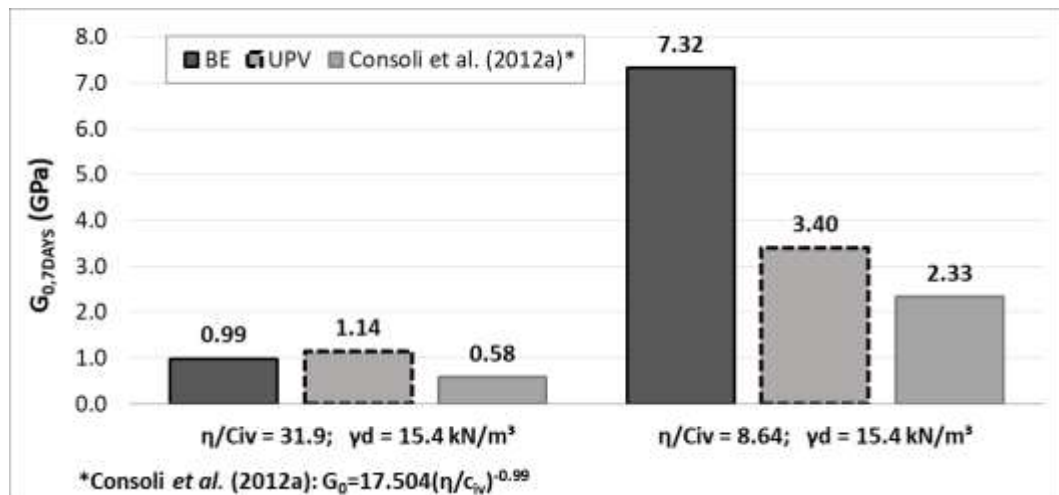


Figure 4.31: BE bench pair validation using the prediction equation as a reference for the shear moduli obtained on day 7 of cure

It is important to mention that the data used to construct the prediction equation (CONSOLI *et al.*, 2012) were also obtained using the time-domain approach, which is susceptible to operator biases. Thus, biases in predicted values associated to biases in the present work may

explain the difference obtained between the two results. As the shear modulus is proportional to the square of the velocity, any difference regarding the measured time had a real impact on the modulus, equal to the inverse of the square time. This may lead to larger errors associated to the shear modulus, as discussed in previously (VIGGIANI; ATKINSON, 1995). Errors that are probably magnified because of the signal interpretation complexity of stiffer soils (JOVIČIĆ, COOP, AND SIMIĆ 1996), as in the present case.

Moreover, as the prediction equation is, in fact, an approximation, real data do not necessarily match predicted data. As a matter of fact, real data around $\eta/c_{iv}=30$ and $\eta/c_{iv}=10$ are slightly higher than those predicted by the best-fit curve, i.e., the equation might underestimate shear moduli respective to $\eta/c_{iv}=30$ and $\eta/c_{iv}=10$. This could explain the significant differences between BE measurements and the data obtained with the prediction equation.

Another factor that might explain the distance between BE measurements and predicted data is how BE-specimen coupling was conducted in the present work. Although, the circular cavities were a good solution to standardise BE assembling, allowing proper coupling and pair alignment, they may have interfered with the results. Nonetheless, the main factor to influence the differences found in the results are probably related to data interpretation. Clayton (2011) estimated a difference of up to 15.4% on shear modulus obtained by different examiners with a clay specimen, whose signal is supposedly much simpler and easier to interpret when compared to cemented specimens.

Regarding UPV measurements, the difference between measured values and BE bench results can be an indication of the dispersive nature of the BE-specimen system, and frequency dependency. As a result, corrections when using the frequency-domain approach are required – as mentioned before.

4.8.3 BE bench pair damage

As mentioned before, the BE bench pair suffered physical damage, which resulted in signal noise and decreased signal quality. This section aims only to present the different types of damage caused to the BE bench pair, and the reasons for those, so that they may be avoided as much as possible in future studies.

At the end of the tests, BE transducers and receptors were damaged (Figure 4.32). The epoxy layer of the transmitter was cracked while being removed from the slotted calibration cylinder

(slightly twisted). Thus, care is recommended when removing BE from stiff slots, using gentle seesaw movements along the slot before pulling the BE transmitter out. Although the resulting crack was covered with cyanoacrylate glue (Superbonder[®]), the bond was inadequate and water got through and in contact with the piezoceramic over time.

Concerning the BE receptor, faulty BE manufacturing was responsible for BE damage. During BE epoxy encapsulating, the edge of the needle used to add the resin probably touched and moved the piezoceramic from its central position. Consequently, the piezoceramic was misaligned, and a small area was not covered with epoxy. Superbonder[®] was used in an attempt to cover the exposed area, but again, water was able to penetrate and reach the piezoceramic with time.

However, it is also important to mention that BE were in direct contact with the couplant, which is in itself a quite aggressive environment. Thus, regardless of the physical damage, BE coating would become more porous and more susceptible to water penetration under the same conditions (MONTROYA *et al.*, 2012).

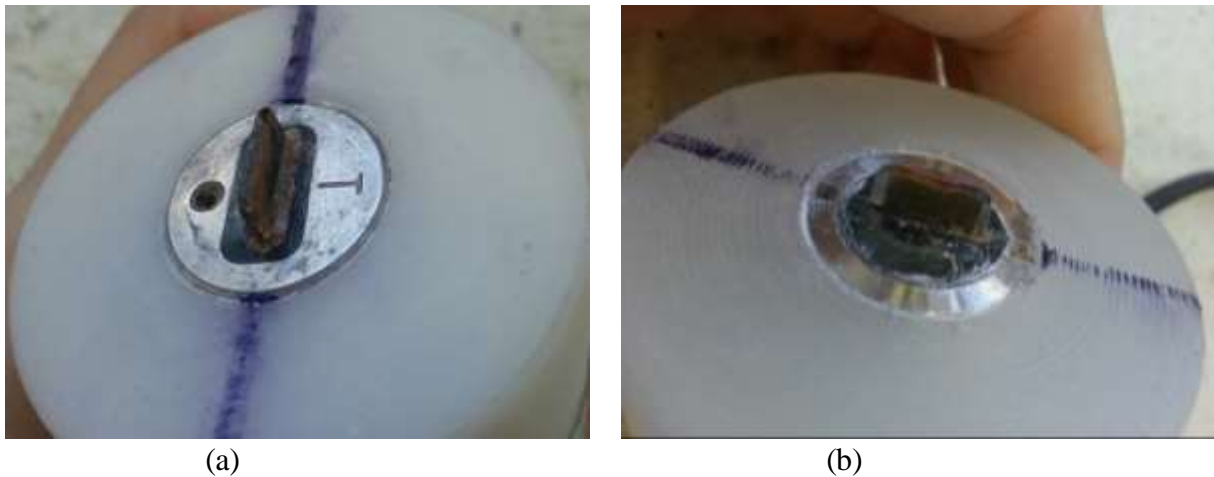


Figure 4.32: Damaged pair of BE – (a) cracked transmitter; (b) receiver with a small area not covered by the resin

4.8.4 Resonance response

The resonance response over the curing period was analysed with specimen BEN_8.64_15.4. Granja *et al.* (2014) observed noticeable change in resonance frequency over time for cement pastes. However, the response observed for the highly cemented Osorio sand did not seem to be so evident. Figure 4.33 was obtained by sending single sine pulses at different frequencies

with the same input voltage (± 10 V), then the received amplitude was plotted against the input frequency on each test day.

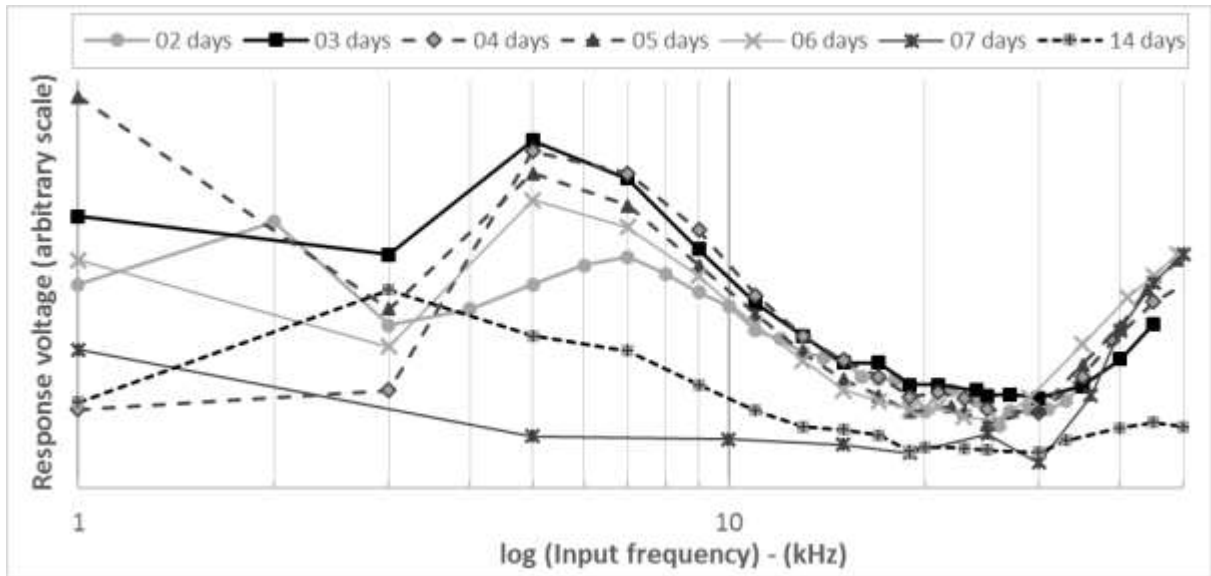


Figure 4.33: Voltage response of the frequency sweep of the specimen BEN_8.64_15.4 subjected to single sine pulses over the time of cure

The well-shaped peak at 7 kHz for day 2 of cure, moved to 5 kHz in the following day; days 4 to 6 of cure maintained the same peak at 5 kHz. The day 7 of cure has no evident peak in the studied range of frequencies. Day 14 of cure presented a peak at 3 kHz, indicating a decrease in the resonant frequency after stabilisation in the previous days. The resonant frequency over the days of cure is plotted in Figure 4.34.

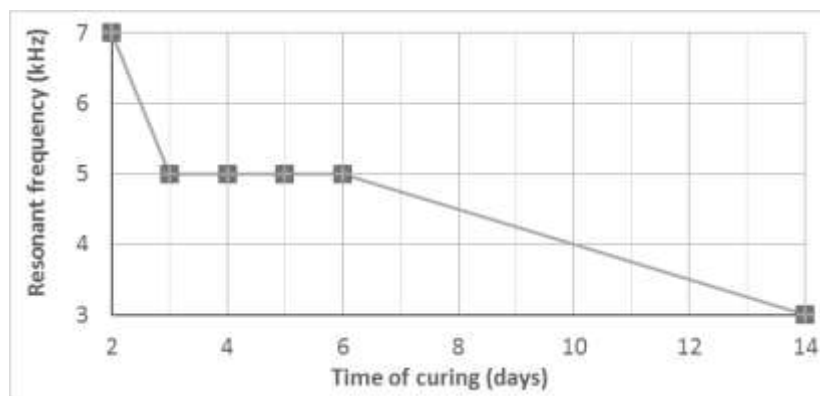


Figure 4.34: Resonance frequency response over time of cure of specimen BEN_8.64_15.4 subjected to single sine pulses

Although the peaks could be clearly observed within the range tested frequencies, frequencies higher than 12 kHz demonstrated a new increasing trend, which might suggest the presence of a new peak at higher frequencies. This might be an indication of BE-specimen multimodal vibration. However, more conclusive claims will require a spectral analysis in the frequency domain. Although response voltage behaviour at frequencies smaller than 3 kHz demonstrated an apparent increasing trend, this trend under 3 kHz cannot be considered reliable, because received signals at 1 kHz presented random behaviour.

4.9 BE TRIAXIAL TESTS

Due to the lack of a quantitative analysis of cementitious reactions filling voids over time for Osorio sand, a simplified hypothesis had to be established in order to calculate specimens saturated unit mass. Specimens subjected to triaxial tests were considered as presenting no changes in void volumes over the test period. As such, the amount of water after saturation was equal to the initial voids volume of the specimen; the mass of water was then calculated by using the unit mass of water at 22°C, as established by the ASTM D854 (ASTM, 2014), which is equal to 0.99777 g/cm³. The saturated unit mass values are presented in Table 4.4. The decision to use the saturated mass, rather than the dry mass, was based on the fact the unit mass in the shear modulus equation represents the inertia of studied body and, therefore, even though water does not resist shearing, water contributes to the inertia of the specimen.

Table 4.4: Natural unit weight (γ_n) right after specimen fabrication, and the hypothetical saturated unit mass (ρ_{sat})

Specimen	γ_n (kN/m ³) ⁽¹⁾	ρ_{sat} (kg/m ³) ⁽²⁾
TRX_31.9_15.4	16.79	1,950.56
TRX_8.64_15.4	17.12	1,975.60
TRX_0.00_15.4	16.99	1,959.23

⁽¹⁾ Natural unit weight at the end of moulding process

⁽²⁾ Natural unit mass considering full saturation

Specimen saturation was limited by time-constraints and the use of the available maximum back pressure. Figure 4.35 presents B-value evolution against the confining pressure, obtained with back pressure increments. It is clear that none of the specimens reached the maximum

possible value, which may represent full saturation. However, as discussed previously, and presented Table 3.1, very stiff materials, which include lightly cemented materials, require a B-value equal to 0.20 to reach saturation of 99.5%. Stiff materials, on the other hand, require a B-value of 0.69 to reach the same degree of saturation. The two cemented specimens reached saturations around 99.5% - 100%. For simplification purposes, full saturation (100%) was considered for cement specimens. The same rationale was employed for the specimen fabricated with non-cemented Osorio sand, and was considered as a fully saturated stiff material.

After the saturation stage, specimens were subjected to consolidation. The consolidation usually took place in few seconds, after opening the back pressure valve. The two artificially cemented specimens (TRX_31.9_15.4 and TRX_8.64_15.4) tested inside the triaxial chamber were subjected to an effective confining pressure of 50 kPa for all BE tests – which included BE tests before shearing to obtain initial shear modulus, and BE tests conducted during shearing to obtain stiffness degradation concomitantly with triaxial internal gauge measurements. The following two items present the initial shear modulus (4.9.1), before any modulus degradation, and then stiffness degradation (4.9.2) for the two cemented specimens subjected to shearing inside the triaxial cell.

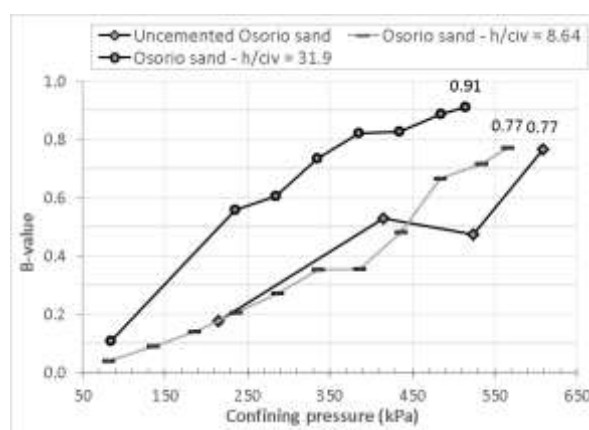


Figure 4.35: B-value evolution against the confining pressure during the saturation process with back pressure increments

4.9.1 Initial shear modulus

Graphs plotted with BE triaxial test results present one extra vertical line (dash-pointed pink line), representing the results calculated by Consoli *et al.* (2009), who tested artificially

cemented Osorio sand specimens on day 7 of cure subjected to triaxial tests using three different confining pressures (20, 200, and 400 kPa). For a full description of the plotted stacked frequencies, see 4.7. The vertical dashed black line represents the results of test performed under ambient pressure (CONSOLI *et al.*, 2012). It was decided to keep this line in the graph, because the literature indicates that cementation removes the interparticle stiffness of the material and, therefore, G_0 changes should be virtually inexistent under confining pressure increments (FERNANDEZ; SANTAMARINA, 2001; SANTAMARINA, 2001; 2011).

Figure 4.36 and Figure 4.37 illustrate the artificially cemented specimens TRX_31.9_15.4 and TRX_8.64_15.4. These two figures show much more noise in the received signals, when compared to Figure 4.27 (non-cemented specimen TRX_0.00_15.4), even though cemented specimens used data acquisition rate up to 64 points for each registered sample was used, which should minimise noises when compared to the average of 4 points used for the non-cemented specimen. When comparing the figures, difficulties associated to interpreting signals belonging to cemented specimens become clear.

The signal of specimen TRX_31.9_15.4 (Figure 4.36) presented much noise and irregular shaped waves. Frequencies higher than 7 kHz did not present a waveform signal at all – only noise could be recognised. Frequencies between 1.5 kHz and 3 kHz presented a peak at around the first peak arrival time ($87.1 \mu\text{s} - 22.085 \mu\text{s} = 65.015 \mu\text{s}$). Received signals of 5 kHz and 7 kHz presented a small movement that might be indicative of the first peak arrival. The first peak arrival time was defined in order to achieve good agreement between received signal peaks at frequencies between 1.5 kHz and 3 kHz, as their peaks presented a small offset to the left with increasing frequencies. Although this time ($65.015 \mu\text{s}$) presented good agreement with UPV measurements, the predicted values by Consoli *et al.* (2009) and Consoli *et al.* (2012) were far from UPV and first peak arrival measurements obtained in the present study.

The signal (Figure 4.36) was hard to interpret. In a range of 8 different frequencies only 3 (1.5 kHz, 2 kHz, and 3 kHz) presented a signal that nearly resembled the input signal or a sine waveform. Moreover, due to the low range of frequencies, these “pulses” could be merely near-field effects. Despite all that, and the fact that the distance of the first peak arrival time to the BE prediction equations (CONSOLI *et al.*, 2009, 2012) was considerable, the measurement was considered correct based on signal interpretation and the agreement with

the UPV measurement. The smaller measured time meant that a higher velocity was calculated when comparing to the BE predictions, and, therefore, a higher shear modulus was found.

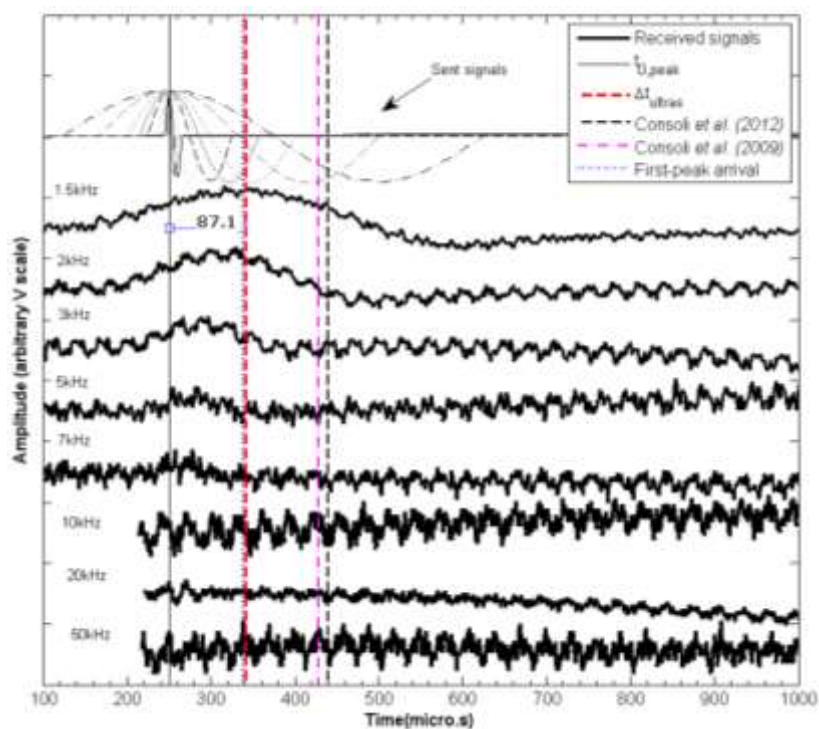


Figure 4.36: BE tests frequency sweep responses of specimen TRX_31.9_15.4 on day 7 of cure, right after consolidation ($\sigma'_3 = 50$ kPa)

The signal of specimen TRX_8.64_15.4 (Figure 4.37) was also difficult to interpret. Oscillations occurred right after 300 μs , which did not seem to be the first peak arrival. It could be noise, near-field effects (although not very plausible), or wave refraction. Whatever the case, it definitely did not seem to be the first wave arrival. Oscillations at around 335-340 μs (matching UPV measurements) seemed to be the first consistent and well-defined peak for frequencies higher than 15 kHz. However, when analysing stiffness degradation signals (Appendix F.2), these first oscillations tended to decrease over time as the shearing process advanced, which was the opposite expected behaviour of a degraded modulus. Therefore, these oscillations were discarded when choosing the first peak arrival time.

After the oscillations previously mentioned, more evident peaks could be observed at around 380-400 μs , with frequencies higher than 10 kHz, and at around 410-420 μs with frequencies

higher than 20 kHz. Although those two consecutive peaks could represent the first arrival peak, at closer analysis they all seemed to have the same input frequency. Differences between peaks with received signals from 15 kHz to 35 kHz are minimal and are very different when compared to target input frequencies (top horizontal line). The behaviour described matches that found in the literature in regards to the independent response of the received signal in relation to the target signal, again a probable effect caused by dispersion (BLEWETT; BLEWETT; WOODWARD, 2000; GREENING; NASH, 2004; RIO, 2006; ALVARADO; COOP, 2012; OGINO *et al.*, 2015). Moreover, this behaviour seems to represent a transient BE system response (CLOUGH; PENZIEN, 1993) due to the single sine pulse used in the tests. Although continuous pulses were tested, the actual script was unable to process those results. Therefore, those signals should be processed in future studies in order to achieve a steady-state response, more consistent with the input signal rather than its resonance frequencies.

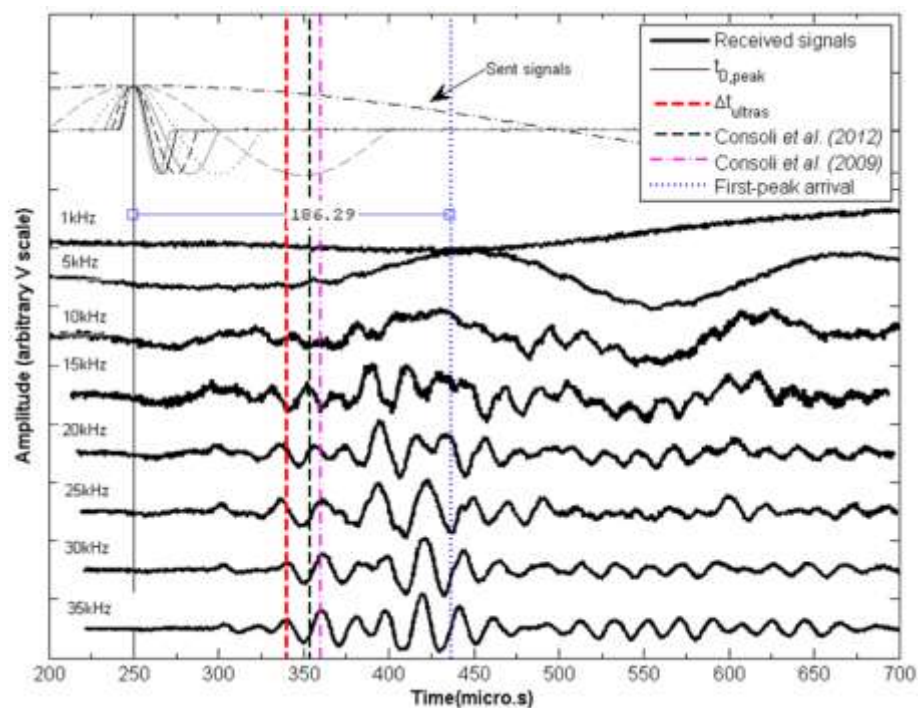


Figure 4.37: BE tests frequency sweep response of specimen TRX_8.64_15.4 on day 7 of cure right after consolidation ($\sigma'_3 = 50$ kPa)

Finally, although the received signal at 5 kHz could be subjected to near-field effects, it clearly presented consecutive peaks, whose waveforms were very similar to the target input

signal, reinforcing its s-wave reliability. Therefore, the decision to place the first peak arrival time was based on the first clear peak observed at 5 kHz, and some oscillations at 10 kHz, whose received signal vaguely resembled its input signal, despite a peak with an offset to the left side in relation to the peak at 5 kHz. The corrected time for first peak arrival time was $164.205 \mu\text{s}$ ($186.29 \mu\text{s} - 22.085 \mu\text{s}$).

Figure 4.38 illustrates the initial shear modulus (before shearing) for BE tests conducted under an effective confining stress of 50 kPa, and the two values found in the literature with bench tests (CONSOLI *et al.* 2012) and triaxial tests (CONSOLI *et al.* 2009) – which demonstrated a unique relationship between η/c_{iv} ratio and $G_{0,7\text{DAY}}$ regardless of the confining pressure. All the results are in respect to the day 7 of cure. There is a good agreement between values found in the literature, endorsing the phenomenon of interparticle stiffness removal due to cementation. Results found in the present study, however, are very different from the literature, with no clear tendency. Nonetheless, the differences are probably due to difficulties in time arrival interpretation, as the cementation in the triaxial environment produced a lot of noise and related issues (e.g., wave reflections). Therefore, the combination of time- and frequency-domain analysis would be especially helpful in achieving reliable results for this specific condition.

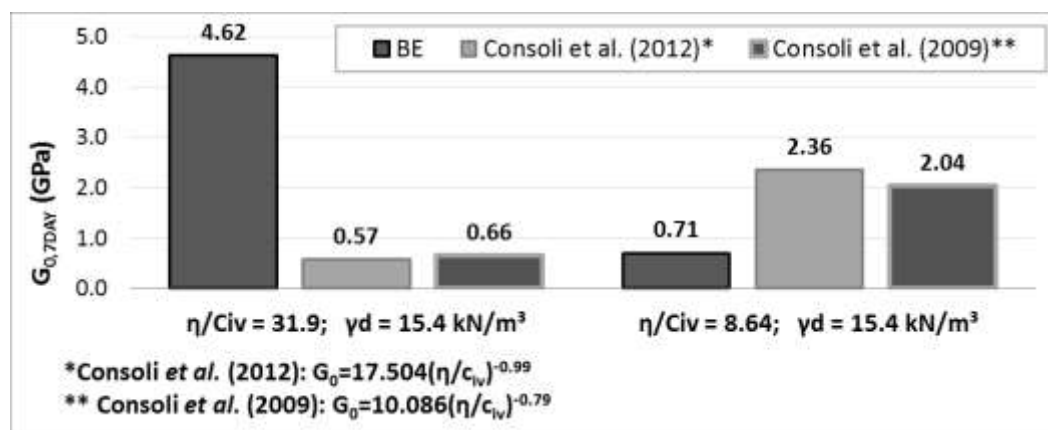


Figure 4.38: Initial shear modulus of artificially Osorio sand specimens (BE tests subjected to $\sigma'_3 = 50 \text{ kPa}$)

4.9.2 Stiffness degradation

Appendix E presents the triaxial results for the two tested specimen under shearing, where the red dots indicate those moments when the jack was turned off and BE measurements were

conducted. Figure 4.39 presents the different saturated unit masses at different stages of strains or, in other words, at different stages of shearing. As expected, TRX_8.64_15.4 presented a more dramatic change in unit mass after reaching the peak (the 6th and 7th BE measurements), because of its higher cement content and a more brittle behaviour.

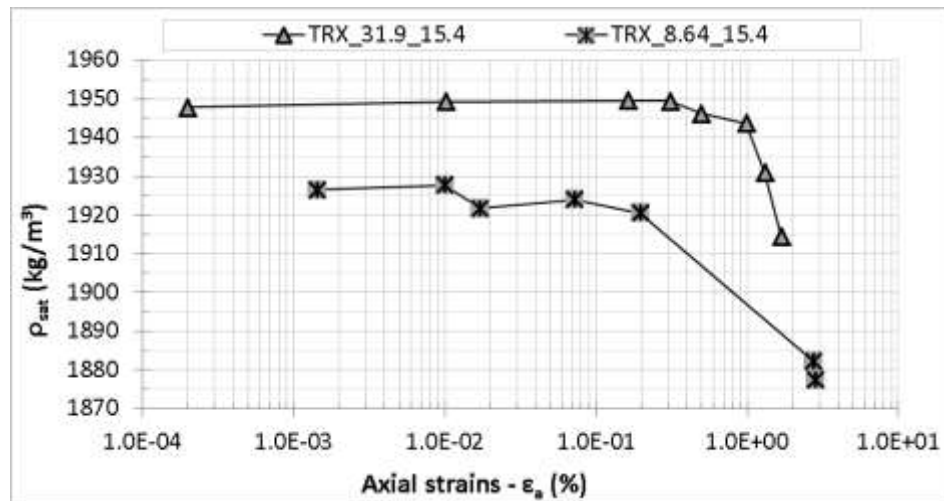


Figure 4.39: Changes in the saturated unit mass of specimens subject to shearing, the indicated points represent BE tests

Appendix F brings all the graphs illustrating the stacked response frequencies over the shearing process for both specimen tested. Although specimen TRX_31.9_15.4 presented a good agreement between measurements along the shearing process, measurement VII is an exception, as can be observed in Figure 4.40. Because it mostly shows noise, an agreement between frequencies is almost impossible to be established visually. Due to difficulties interpreting this test, it was excluded from further analysis.

As described by the literature, confinement pressures make BE data interpretation even more difficult. One possible cause is the range of frequencies (or fundamental frequencies) that, in theory, change to higher frequencies as the confining pressure rises (OGINO *et al.*, 2010; ALVARADO; COOP, 2012; CAMACHO-TAUTA *et al.*, 2015). However, these higher frequencies usually extrapolate BE capacity, resulting in overshooting. Despite that, the literature does not mention the extent the work frequency range is affected when cemented specimens are tested. With that in mind, higher frequencies were tried but results were poor, probably because overshooting.

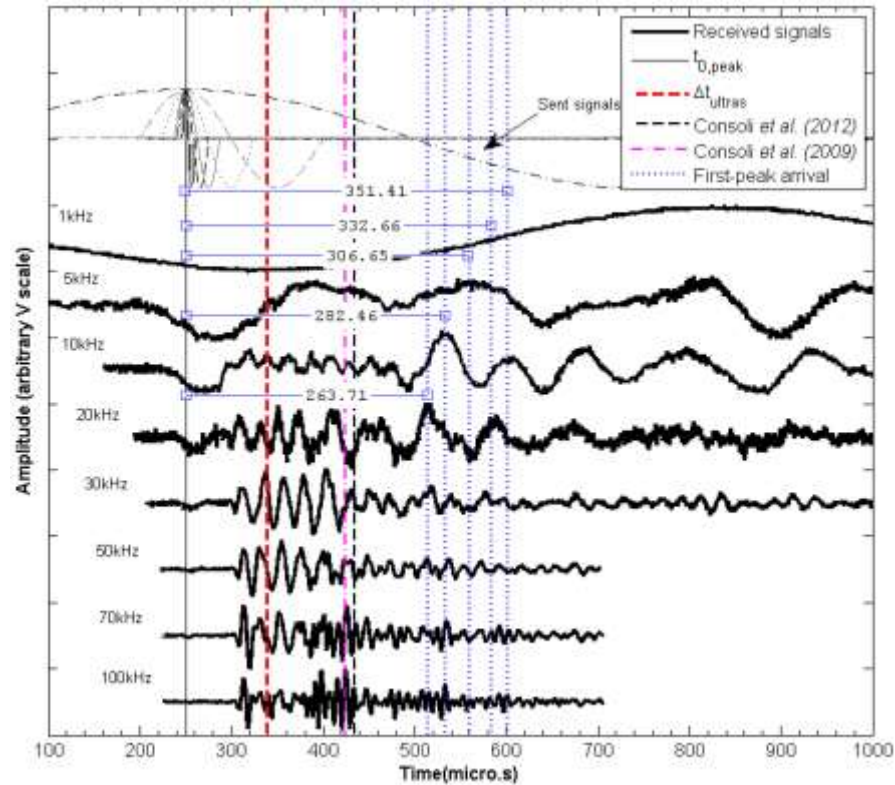


Figure 4.40: BE measurements uncertainty after reaching the strength peak – regarding the measurement VII (TRX_31.9_15.4)

Axial strains captured by Hall effect sensors (local gages) were directly related to Young’s secant modulus (Figure 4.41 – a), which was obtained from the “ $q \times \varepsilon_a$ ” diagram, where q is half of the deviatoric stress ($q = \Delta\sigma/2$). Shear modulus (from local gauges) was obtained through the equation “ $G = E/(2 \cdot (1 + \nu))$ ” presented in Chart 2.1. Poisson’s ratios were equal to 0.2 (nearly concrete) for specimens whose η/c_{iv} ratio is about 10, and equal to 0.265 for η/c_{iv} ratio about 32 (FONINI, 2012). Then, shear modulus was presented against shear strains “ γ ” (Figure 4.41 – b). Shear strains were obtained by, first, calculating the shear stress imposed to the specimen with Mohr-Coulomb envelop equation “ $\tau' = c' + \sigma' \cdot \tan(\phi')$ ” – using c' and ϕ' in Consoli *et al.* (2009). Then shear stains were obtained by simply dividing shear stress by the shear modulus.

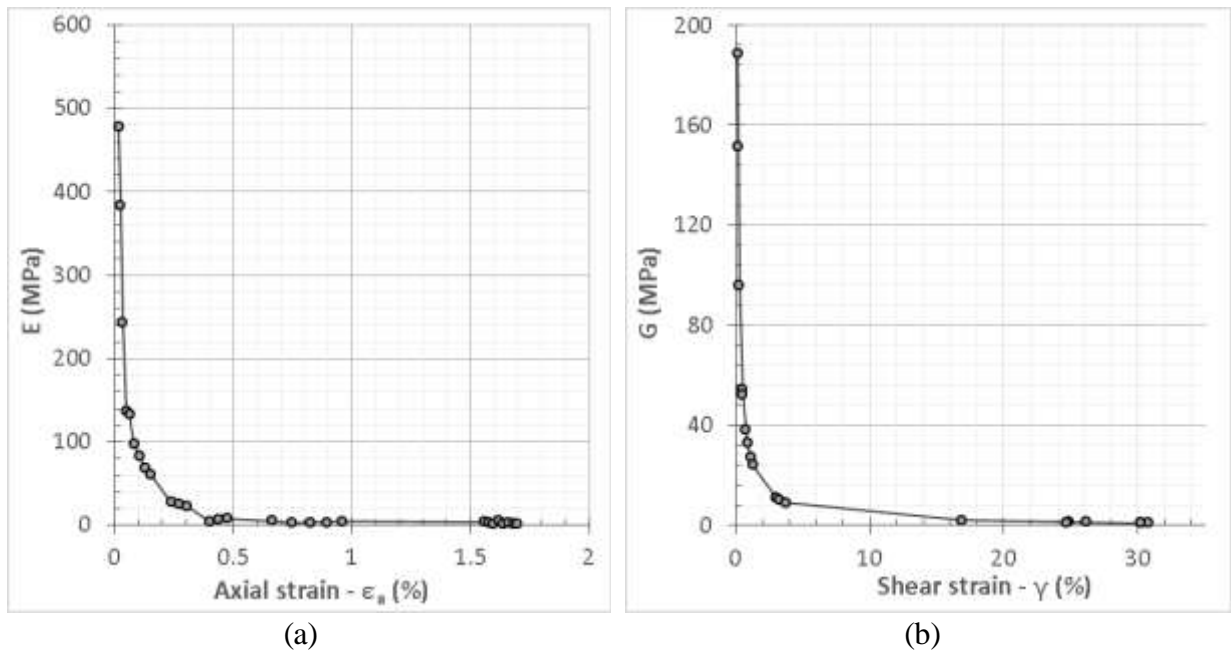


Figure 4.41: Comparison of Young and shear modulus in terms of respective strains, obtained through internal instrumentation – (a) Young modulus; (b) shear modulus

Based on BE time arrivals (time-domain and peak-to-peak), shear moduli were calculated for different shear strains. The shear moduli from specimens TRX_31.9_15.4 and TRX_8.64_15.4 were then plotted (Figure 4.42) in the same graphs with the moduli obtained from local gauges (“Int. instrumentation”). Measurements from specimen TRX_31.9_15.4 presented very good agreement (Figure 4.42 – a). Apart from the first BE measurement, all the following measurements presented the same trend shown by local gauges data. Only a small offset was observed, which could be justified by the initial simplification used in saturated unit mass calculations. Probably, after cementation, there were much less voids to be filled with water when compared to the initial quantity of voids. Therefore, the actual saturated unit mass was increased, reflecting in the shear modulus offset observed. Regarding the first BE measurement, and assuming that BE data interpretation was correctly performed, it was clear that the Hall effect sensors used were unable to measure the initial shear modulus. That means that, although BE capacity to measure the initial shear modulus can represent an improvement to triaxial tests, BE results cannot be corroborated by internal measurements at the very-small strains.

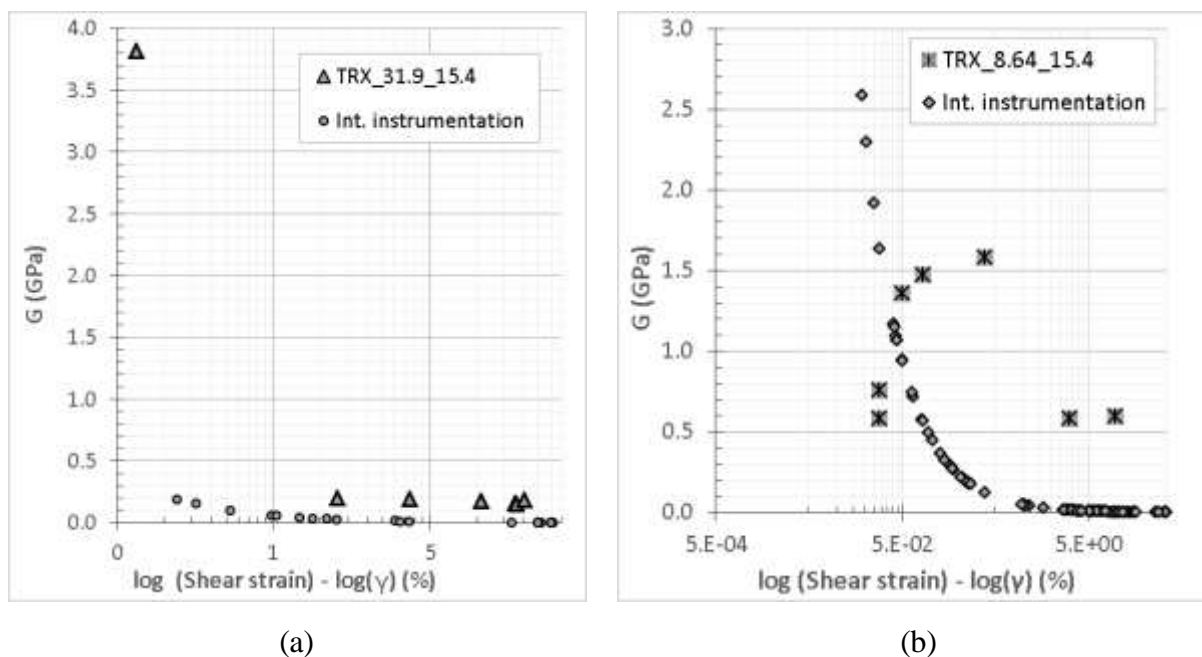


Figure 4.42: Shear modulus degradation measured by BE and internal instrumentation – (a) specimen TRX_31.9_15.4; (b) specimen TRX_8.64_15.4

Regarding specimen TRX_8.64_15.4 (Figure 4.42 – b), results were much less conclusive, and even harder to interpret, probably because of the high cement content. Although four BE measurements (bottom) seem to roughly follow the local gages tendency, the three points on the superior region of the graph seem to be only spurious data. Moreover, measurements regarding initial shear modulus were not achieved, as the first BE value is smaller than the moduli calculated from the local gauges. Another perspective can give rise to the hypothesis that the two first measurements were not adequately interpreted and, if so, they should correspond to higher shear moduli values and, therefore, only the higher point would be a spurious data. Although this alternative seems to be very interesting, all first movements observed under the strains were apparently at the same position (at around 305 and 310 μ s), regardless the strain range. That could mean that stiffness did not change with the medium and at large strains. Since this is an impossibility, BE data (of specimen TRX_8.64_15.4) needs to be further analysed to be appropriately interpreted. Again, frequency-domain in parallel to the time-domain analysis would be very helpful.

Regardless of the uncertainties and difficulties in BE data interpretation, the stiffness degradation curve was correctly obtained for, at least, one specimen (TRX_31.9_15.4). This curve highlighted the already well-known non-linearity of the soil, and contributed with the

understanding of artificially cemented soil behaviour subjected to stiffness degradation. Although not recommended, BE tests performed at large strains seemed to provide satisfactory results. However, as the triaxial chamber had internal instrumentation, it would be more interesting to focus on BE tests at very-small and small strains ranges, helping to build a stiffness degradation curve with smaller gaps.

Wave tests are not usually applied to medium and large strains because these strains contradict some fundamental tenets. The material is no longer in the elastic range, which means that soils can be understood much more alike visco-elastic materials; which would require specific analysis, and perhaps the addition of damping measurements. Continuity is not granted anymore, and micro-cracks can happen. Finally, if stress anisotropy is imposed to the specimen (i.e. during shearing), the soil will not be isotropic.

However, all the mentioned limitations are theoretical and, in many *in situ* tests, those tenets cannot be entirely withheld. Wave or seismic methods are daily applied in the field, and continue to use simplifying concepts. Therefore, as field conditions cannot be usually controlled, it is important to improve our understanding of all limitations, and flexibility, in order to apply better models, or to enable more detailed modelling.

5 CONCLUSIONS

The present study was designed with two main objectives in mind. The first was to develop a Bender Elements system with good signal quality, reliable outcomes, simple and user friendly that could have practical use in the soil laboratory. The second objective was to analyse stiffness degradation of artificially cemented Osorio sand with Bender Elements and compare results with measurements conducted with local gauges inside a triaxial chamber.

5.1 BE SYSTEM

Two pairs of bender elements were developed to be used in bench and triaxial tests. The main challenge in regards to developing a practical BE system was the lack of information in the literature. The system presented was the result of consults with partner universities in England and Australia. Based on the information received, BE system design had to be developed and validated from scratch. Every detail had to be discussed, designed and tested along the several attempts to achieve a reproducible high quality device.

In the present work, we incorporate all the plans and detailed instructions to effectively produce a new device, including BE fabrication and the analogical signal amplifier. New designs for all metal and plastic pieces fabricated are presented for future reference.

Despite the limitations and setbacks along the BE system development, the results of the present study demonstrated that the final arrangement was actually capable of sending and receiving noise free signals. In the items below, fabrication of BE system, amplifier, validation, and work frequencies are critically analysed.

5.1.1 BE fabrication

Issues that emerged during the fabrication of the BE themselves deserve to be highlighted. Among them, polishing with sandpaper (3.2.2) was conducted in order to expose the piezoceramic metal shim for parallel-connections. Only for the triaxial transmitter this procedure was successful. Even though polishing with sandpaper was carefully conducted, the piezoceramics did not work as expected. To mitigate this problem, two suggestions are made.

The first would be to use series-connections, rather than parallel-connections, for the transmitter. However, depending on the system, series-connection might require higher amplification. In the case of the bench pair, grounded series-to-series connection transducers were used with good results. The other alternative would be to use a very small drill (e.g., dental drill) in an attempt to remove the superficial layers of the piezoceramic more effectively without damaging the transducer.

Another issue concerns piezoceramics wiring. It is advisable to read the description in 3.2 carefully and thoroughly in order to ensure quality soldering, with good contact and without excessive dirt. It is easy to not achieve good soldering in the first attempt, but before a second attempt is made, it is important to verify whether some of the piezoceramic surface is available for a new attempt, if so, move the wire a few millimetres away from the first attempt, and try again. A person with soldering skills would be helpful. Nonetheless, it is not unusual for the dielectric insulation (plastic) covering the wires to melt. In such a case, a new insulation is essential to cover the exposed metal shim. The alternative presented in this work was to spread Superbonder[®] carefully along the melted region. Then, cable continuity and proper insulation needs to be verified using a multimeter.

Of fundamental importance, the piezoceramic integrity and connections needs to be systematically verified with the multimeter along all BE fabrication process. Moreover, whether a wired piezoceramic is vibrating or not before encapsulating is one of the most important steps in BE fabrication. No doubts concerning piezoceramic functionality should exist before encapsulating, according to the procedure described in 3.2.

Based on the experience gained with BE fabrication in the present study, some modifications to the BE bench pair are suggested. In order to avoid cable soldering, such as the piezoceramic wire to the shielded cable, the shielded cable could be directly soldered onto the piezoceramics, helping to mitigate noise in the system. However, the access hole in the metal case would need to be enlarged to fit the external diameter of the shielded cable.

Finally, BE-specimen coupling deserves some attention. Although the use of cavities filled with calcined gypsum-cement paste permitted adequate coupling with aligned transducers, the impact of this coupling mode on the results cannot be entirely understood. An attempt has been made to ascertain this impact through wave travelling time and specimen mass

corrections. Further studies with alternative coupling systems are required to assess their possible limitations and advantages.

5.1.2 BE signal amplifier

The use of an analogical amplifier was of fundamental importance for received signal recognition. To achieve the final amplifier arrangement, several trials had to be conducted. In the end, what deserves some highlight is the use of the integrated circuit INA116, which permitted that the first amplification step could be overcome. Moreover, the use of INA116 also permitted the use of a less sensitive chip in the second amplification step, helping to reduce costs without affecting final signal gains. The guard ports created around INA116 also helped to ensure a noise-free system. Apart from being an electromagnetic shielding of the received signal, the guard ports also functioned as groundings to the drain lines in direct contact with the specimens. Finally, this configuration permits gain changes by simply exchanging the resistor connected to the INA116 (R_G).

5.1.3 Working frequency and noise

One of the most significant aspects of the BE system refers to the working frequencies used in the tests. During trials, it was observed that very low frequencies (below 10 kHz) possibly resulted in near-field effects, which interfered with signal interpretation. The literature suggests that two wavelengths between the transducer and receiver should be maintained in order to avoid the near-field effects. However, in case of very stiff soils, such as in the case of cemented specimens, very high frequencies would be required to that effect, which would be much beyond the BE system capacity. Therefore, this is an inherent limitation of the BE system when applied to cemented specimens, which could lead to underestimated shear modulus results.

Crosstalk was not observed with the non-cemented specimen. However, with cemented specimens, crosstalk became increasingly evident over the cure period, especially with smaller frequencies. Apparently, this crosstalk is associated with the cementation of specimens. Electromagnetic induction was observed in bench tests, which behaved in a very similar fashion as crosstalk, which in fact was caused by cables being tangled. When cables were stretched, this effect disappeared completely. Thus, the way cables are positioned during tests is an important issue to avoid misinterpretations.

The transient response was clearly observed as a result of the frequency ceiling, above which the received signals vibrated at a constant frequency different from the input frequency. As a result, received frequencies interpretation in the time-domain was compromised, as a smaller number of reliable signals were available for analysis. This problem can be mitigated by sending continuous input waves long enough until reaching a steady-state system response.

5.1.4 BE system validation

The validation results obtained for bench tests, in the present work, were significantly different from that found in the literature for the same cemented material (Osorio sand) with the use of the time-domain. This difference is probably due to the several intrinsic factors to affect BE readings interpretation, such as specimen geometry and boundary reflection. As such, it is not possible to state that the results obtained with the validation process were actually inadequate. The literature shows that data dispersion among different laboratories is high. Therefore, based on the whole process, which was developed with extreme care and attention to detail along the present study, it is more likely that differences between results were due to uncertainties associated to BE system and their interpretation.

5.2 BE RESULTS

In general, the fabricated BE system demonstrated clear signals which permitted the assessment of shear wave velocity in cemented specimens, and calculate shear modulus.

5.2.1 BE bench results

BE bench results clearly demonstrated stiffness gains over the time of cure. As expected specimens with $\eta/c_{iv}=8.64$ presented higher stiffness when compared with specimens with $\eta/c_{iv}=30.9$. UPV results for specimens with $\eta/c_{iv}=30.9$ were slightly higher than BE results, which is in agreement with Yamashita *et al.*, (2009), who demonstrated that the higher the BE frequency, the higher the shear modulus. Thus, tests that make use of higher frequencies, such as UPV, reach higher shear modulus results. However, results for specimens with $\eta/c_{iv}=8.64$ were the opposite than that expected when UPV results were compared with BE results. Be results in the present study were higher than UPV results. BE specimens real η/c_{iv} ratio (7.66) was smaller than that for UPV specimens (7.94), which would result in higher shear modulus

for BE specimens, as observed. Nonetheless, differences in dry unit weight of UPV and BE specimens of around 1.29% may impede direct comparisons.

5.2.2 Stiffness at very-small strains

Apart from the high quality fabricated triaxial BE pair, stiffness at very-small strains did not present good agreement with data from the literature. Cementation associated with the confining pressure resulted in very noise signals, making the time-domain interpretation sometimes difficult to execute. When compared to shear modulus data obtained for higher strains, only one specimen (TRX_31.9_15.4) seemed to provide an adequate initial shear modulus.

5.2.3 Stiffness degradation

Only one specimen provided an adequate stiffness degradation curve (TRX_31.9_15.4), data from the other specimen requires further investigation for a more conclusive analysis, perhaps using the time-domain with adequate corrections. The full degradation curve clearly demonstrated that Hall effect sensors, used as local gauges in the Bishop-Wesley triaxial, does not have enough sensitivity to measure shear modulus at very-small strains. Therefore, the combined used of BE and local sensors seemed to be the best alternative for characterising stiffness degradation. Nonetheless, although BE was applied to large strains in the present study, it is recommended to focus BE tests on small-strains.

5.3 FINAL REMARKS

The strength of the present work resides on the careful development of a working BE system for the assessment of shear modulus. Although some of the results bring some inconsistencies, they do not detract from the importance of the work performed. Based on the information available in this study, improvements may be conducted with reference to the experience obtained here. Therefore, it is our expectation that this study may represent an important contribution to an area that requires further enlightenment.

5.4 SUGESTIONS FOR FUTURE WORKS

Suggestions have been divided into separated items in order to facilitate the examination of each suggestion.

5.4.1 BE tests conditions

- Investigate new BE couplants, preferably alternatives that do not require further corrections and that allow precise geometries and reproducibility;
- Further investigate artificially cemented soil behaviour between specimen fabrication day and day 2 of cure, especially in regard to soil isotropy; and
- Test other soils with different granulometry, with the addition of finer particles and fibres.

5.4.2 BE received signal and data acquisition

- Analyse how sampling rate (4, 16, 64, and 128 points) and mode (peak detection, sampling, averaging) influence BE results; whether they generate real time-delays, and how sensitive the system is in regard to these parameters;
- Add an electronic filter to the data interpretation script;
- Re-write the script in order to analyse signal input different than single sine pulse;
- Improve script feeding, by further automating scripts during data acquisition, directly from a spreadsheet;
- Associate frequency-domain analysis to the current time-domain analysis, applying the required corrections in order to mitigate dispersive effects; and
- Build an acquisition interface that may allow real time data analysis, optimising the quantity of tests performed.

5.4.3 BE behaviour and calibration

- Perform a broad BE calibration using dummy specimens with different geometries (heights and diameter), as recommended for the ultrasonic pulse velocity device, in order to enlighten the boundary conditions regarding wave reflection and dispersion;

- Perform BE tests in conjunction to other device (e.g. accelerometers), which can help in the understanding of specific BE behaviours; and
- Perform a deep and detailed analysis of BE behaviour when embedded (similar to RIO, 2006) into artificially cemented specimens, to improve our understanding of BE response to input voltage and real vibration when excited by a mechanical input (receiver behaviour).

REFERENCES

- AIREY, D. W., Triaxial Testing of Naturally Cemented Carbonate Soil. **Journal of Geotechnical Engineering**, v. 119, n.9, p. 1379-1398, 1993.
- AIREY, D. W.; FAHEY, M. Cyclic response of calcareous soil from the North-West Shelf of Australia. **Géotechnique**, v. 41, n. 1, p. 101-121, 1991.
- AIREY, D.; MOHSIN, A. K. M. Evaluation of shear wave velocity from bender elements using cross-correlation. **Geotechnical Testing Journal**, v. 36, n. 4, p. 506-514, 2013.
- ALVARADO, G.; COOP, M. R. On the performance of bender elements in triaxial tests. **Géotechnique**, v. 62, n. 1, p 1-17, 2012.
- ALVARADO, G.; COOP, M. R.; WILLSON, S. On the role of bond breakage due to unloading in the behaviour of weak sandstones. **Géotechnique** v 62, n. 4, p 303-316, 2012.
- AMERICAN SOCIETY FOR TESTING AND MATERIALS. **ASTM D2845**: Standard Test Method for Laboratory Determination of Pulse Velocities and Ultrasonic Elastic Constants of Rock. 1995.
- _____. **ASTM D6913**: Standard Test Methods for Particle-Size Distribution (Gradation) of Soils Using sieve Analysis. 2004.
- _____. **ASTM D1632**: Making and Curing Soil-Cement Compression and Flexure Test Specimens in the Laboratory. 2007.
- _____. **ASTM D2845**: Standard Test Method for Laboratory Determination of Pulse Velocities and Ultrasonic Elastic Constants of Rock. 2008.
- _____. **ASTM C 150**: Standard specification for Portland cement. 2009.
- _____. **ASTM D2216**: Standard Test Methods for Laboratory Determination of Water (Moisture) Content of Soil and Rock by Mass. 2010.
- AMERICAN SOCIETY FOR TESTING AND MATERIALS. **ASTM C702/C70M**: Standard Practice for Reducing Samples of Aggregate to Testing Size. 2011a.
- _____. **ASTM D2487**: Standard Practice for Classification of Soils for Engineering Purposes (Unified Soil Classification System). 2011b.
- _____. **ASTM D7181**: Standard Test Methods for Consolidated Drained Triaxial Compression Test for Soils. 2011c.
- _____. **ASTM D854**: Standard Test Methods for Specific Gravity of Soil Solids by Water Pycnometer. 2014a.
- _____. **ASTM D4254**: Standard Test Methods for Minimum Index Density and Unit Weight of Soils and Calculation of Relative Density. 2014b.

_____. **ASTM D4253**: Standard Test Methods for Maximum Index Density and Unit Weight of Soils Using a Vibratory Table. 2014c.

_____. **ASTM C597**: Standard Test Method for Pulse Velocity Through Concrete. 2016.

_____. **ASTM C150/C150M**: Standard Specification for Portland Cement. 2017a.

_____. **ASTM C11**: Standard Terminology Relating to Gypsum and Related Building Materials and Systems. 2017b.

ARROYO, M. **Pulse tests in soil samples**. 2001. Thesis (PhD) – Department of Civil Engineering, Faculty of Engineering, University of Bristol, Bristol, UK, 2001.

ARROYO, M.; MUIR WOOD, D.; GREENING, P.D. Source near-field effects and pulse tests in soil samples. **Géotechnique**, v. 53, n. 3, p 337-3452, 2003.

ARROYO, M.; MUIR WOOD, D.; GREENING, P. D.; MEDINA, L.; RIO, J. Effects of sample size on bender-based axial G_0 measurements. **Géotechnique**, v. 56, n. 1, p 39-52, 2006.

ARULNATHAN, R.; BOULANGER, R. W.; RIEMER, M. F. Analysis of Bender Element Tests. **Geotechnical Testing Journal**, v. 19, n. 4, p. 384-397, 1998.

ATKINSON, J. H. Non-linear soil stiffness in routine design. **Géotechnique**, v. 50, n. 5, p. 487–508, 2000.

BARDET, J.-P. **Experimental soil mechanics**. [s.l.] Prentice Hall, 1997.

BENDAT, J. S.; PIERSOL, A. G. **Engineering application of correlation and spectral analysis**. 2nd e.d, New York, John Wiley & Sons, 1993.

BK PRECISION. **Model 4045**: 20MHz DDS Sweep Function Generator with Arb Function. [s.l.s.n.], 2014. Operating manual.

BLEWETT, J.; BLEWETT, I. J.; WOODWARD, P. K. Measurement of shear-wave velocity using hase-sensitive detection techniques. **Canadian Geotechnical Journal**, v. 36, p. 934-939, 1999.

BLEWETT, J.; BLEWETT, I. J.; WOODWARD, P. K. Phase and amplitude responses associated with the measurement of shear-wave velocity in sand by bender elements. **Canadian Geotechnical Journal**, v. 37, p. 1348-1357, 2000.

BUDHU, M. **Soil mechanics and foundations**. 3rd. ed. [s.l.] John Wiley & Sons, Inc., 2011.

BURR-BROWN. **INA116**: Ultra Low Input Bias Current INSTRUMENTATION AMPLIFIER. [s.l.s.n.], 1994. Datasheet.

BRAZILIAN ASSOCIATION FOR TECHNICAL NORMS. **NBR NM 23**: Portland Cement and others Powered Materials - Determination of unit weighth. 2001. In Portuguese.

BRIGNOLI, E. G. M.; GOTTI, M.; STOKOE II, K. H. Measurement of shear waves in laboratory specimens by means of piezoelectric transducers. **Geotechnical Testing Journal**, v. 19, n. 4, p. 384-397, 1996.

BRITISH STANDARD. **BS 1881-Part 203**: Recommendations for measurement of velocity of ultrasonic pulses in concrete. 1986.

BROCANELLI, D.; RINALDI, V. Measurement of low-strain material damping and wave velocity with bender elements in the frequency domain. **Canadian Geotechnical Journal**, v. 35, p. 1032-1040, 1998.

CABERLON, R. C. **Influência de parâmetros fundamentais na rigidez, resistência e dilatância de uma areia artificialmente cimentada**. 2008. 194 p. – Thesis (D.Sc.) – Civil Engineering Post-Graduation Program, Department of Civil Engineering, Federal University of Rio Grande do Sul, Porto Alegre, BR-RS, 2008. In Portuguese.

CAMACHO-TAUTA, J. F.; CASCANTE, G.; VIANA DA FONSECA, A.; SANTOS, J. A. Time and frequency domain evaluation of bender element systems. **Géotechnique**, v. 65, n. 7, p. 548-562, 2015.

CARRARO, J. A. H.; PREZZI, M.; SALGADO, R. Shear Strength and Stiffness of Sands Containing Plastic or Nonplastic Fines. **Journal of Geotechnical and Geoenvironmental Engineering**, v. 135, n. 9, p. 1167–1178, 2009.

CHANG, T.-S.; WOODS, R. D. Effect of Particle Contact Bond on Shear Modulus. **Journal of Geotechnical Engineering**, v. 118, n. 8, p. 1216–1233, 1992.

CHRIST, M.; PARK, J. B. Determination of Elastic Constants of Frozen Rubber-Sand Mixes by Ultrasonic Testing. **Journal of Cold Regions Engineering**, v. 25, n. 4, p.196-207, 2011.

CLAYTON, C. R. I. Stiffness at small strain: research and practice. **Géotechnique**, v. 61, n. 1, p. 5–37, 2011. doi:10.1680/geot.2011.61.1.5.

CLAYTON, C. R. I.; HEYMANN, G. Stiffness of geomaterials at very small strains. **Géotechnique**, v. 51, n. 3, p. 245-255, 2001.

CLAYTON, C. R. I.; PRIEST, J. A.; REES, E. V. L. The effects of hydrate cement on the stiffness of some sands. **Geotechnique**, v. 60, p. 435-445, 2010. doi:10.1680/geot.2010.60.6.435.

CLAYTON, C. R. I.; THERON, M.; BEST, A. I. The measurement of vertical shear-wave velocity using side-mounted bender elements in the triaxial apparatus. **Geotechnique**, v. 54, n.7, p. 495-498, 2010.

CLOUGH, R. W.; PENZIEN, J. **Dynamic of structures**. 2nd. e.d [s.l.] McGraw-Hill, 1993.

CONSOLI, N. C.; ROTTA, G. V.; PRIETTO, P. D. M. Influence of curing under stress on the triaxial response of cemented soils. **Géotechnique**, v. 50, n. 1, p. 99–105, 2000.

- CONSOLI, N. C.; ROTTA, G. V.; PRIETTO, P. D. M. Yielding–compressibility–strength relationship for an artificially cemented soil cured under stress. **Géotechnique**, v. 56, n. 1, p. 69–72, 2006. doi:10.1680/geot.2006.56.1.69.
- CONSOLI, N. C.; CASAGRANDE, M. D. T.; COOP, M. R. Performance of a fibre-reinforced sand at large shear strains. **Géotechnique**, v. 57, n. 9, p. 751–756, 2007. doi:10.1680/geot.2007.57.9.751.
- CONSOLI, N. C.; CASAGRANDE, M. D. T.; THOMÉ, A.; DALLA ROSA, F.; FAHEY, M. Effect of relative density on plate loading tests on fibre-reinforced sand. **Géotechnique**, v. 59, n. 5, p. 471–476, 2009a. doi:10.1680/geot.2007.00063.
- CONSOLI, N. C.; VIANA DA FONSECA, S.; CRUZ, R. C.; HEINECK, K. S. Fundamental Parameters for the Stiffness and Strength Control of Artificially Cemented Sand. **Journal of Geotechnical and Geoenvironmental Engineering**, v. 135, n. 9, p. 1347-1353, 2009b.
- CONSOLI, N. C.; LOPES JR., L. S.; PRIETTO, P. D. M.; FESTUGATO, L.; CRUZ, R. C. Variables controlling stiffness and strength of lime-stabilized soils. **Journal of Geotechnical and Geoenvironmental Engineering**, v. 137, n. 6, p. 628–632, 2011. doi:10.1061/(ASCE)GT.
- CONSOLI, N. C.; da FONSECA, A. V.; SILVA, S. R.; CRUZ, R. C.; FONINI, A. Parameters controlling stiffness and strength of artificially cemented soils. **Géotechnique**, v. 62, n. 2, p. 177-183, 2012a.
- CONSOLI, N. C.; CABERLON CRUZ, R.; CONSOLI, B. S.; MAGHOUS, S. Failure envelope of artificially cemented sand. **Geotechnique**, v. 62, n. 00, p. 1–5, 2012b.
- COOP, M. R.; ATKINSON, J. H. The mechanics of cemented carbonate sands. **Géotechnique**, v. 43, n. 1, P. 53-67, 1993.
- CRAIG, R. F. **Craig's soil mechanics**. [s.l.] Taylor & Francis Group, 2004.
- CUCCOVILLO, T.; COOP, M. R. Yielding and pre-failure deformation of structured sands. **Géotechnique**, n. 47, v. 3, p.491-508, 1997.
- DALLA ROSA, F. **Effect of curing stress state on the behaviour of an artificially cemented sand**. 2009. 191 p. Thesis (D.Sc.) – Civil Engineering Post-Graduation Program, Department of Civil Engineering, Federal University of Rio Grande do Sul, Porto Alegre, BR-RS, 2009. In Portuguese.
- DUNCAN, J. M.; AND CHANG, C.-Y. Nonlinear analysis of stress and strain soils. **J. of the Soil Mech. and Found. Division**, v. 96, n. SM5, 1970.
- DYVIK, R.; MADSHUS, C. Lab Measurements of Gmax using Bender Elements. **Proc. Advances in the Art of Testing Soils under Cyclic Conditions**, ASCE, 1985.
- FERNANDEZ, A. L.; SANTAMARINA, J. C. Effect of cementation on the small-strain parameters of sands. **Canadian Geotechnical Journal**, v. 38, n. 1, p. 191–199, 2001. doi:10.1139/t00-081.

FESTUGATO, L. **Análise do Comportamento Mecânico de um solo Micro-Reforçado com Fibras de Distintos Índices Aspecto**. 2008. 145 p. Master thesis (MSc) – Civil Engineering Post-Graduation Program, Department of Civil Engineering, Federal University of Rio Grande do Sul, Porto Alegre, BR-RS, 2008. In Portuguese.

FESTUGATO, F. **Comportamento de hidratação e Resposta Cisalhante Cíclica de Resíduos de Mineração Cimentado Reforçado com Fibras**. 2011. 221 p. Thesis (D.Sc.) – Civil Engineering Post-Graduation Program, Department of Civil Engineering, Federal University of Rio Grande do Sul, Porto Alegre, BR-RS, 2011. In Portuguese.

FESTUGATO, L.; MENGER, E.; BENEZRA, F.; KIPPER, E. A.; CONSOLI, N. C. Fibre-reinforced cemented soils compressive and tensile strength assessment as a function of filament length. **Geotextiles and Geomembranes**, v. 45, n. 1, p. 77-82, 2017.

FLOSS, M. F. **Parâmetros de controle de resistência e da rigidez de solos granulares artificialmente cimentados**. 2012. 183 p. Thesis (D.Sc.) – Civil Engineering Post-Graduation Program, Department of Civil Engineering, Federal University of Rio Grande do Sul, Porto Alegre, BR-RS, 2012. In Portuguese.

FONINI, A. **Comportamento Mecânico de uma Areia Cimentada: Análise Experimental e Micromecânica**. 2012. 201 p. Thesis (D.Sc.) – Civil Engineering Post-Graduation Program, Department of Civil Engineering, Federal University of Rio Grande do Sul, Porto Alegre, BR-RS, 2012. In Portuguese.

FONSECA, A. V.; FERREIRA, C.; FAHEY, M. A Framework Interpreting Bender Element Tests, Combining Time-Domain and Frequency-Domain Methods. **Geotechnical Testing Journal**, v. 32, n. 2, p 1-17, 2009.

FOPPA, D. **New Method for Calculating Bearing Capacity of Footings Resting on Soil-Cement Layers**. 2016. 229 p. Thesis (D.Sc.) – Civil Engineering Post-Graduation Program, Department of Civil Engineering, Federal University of Rio Grande do Sul, Porto Alegre, BR-RS, 2017. In Portuguese.

FRATTA, D.; SANTAMARINA, L. C. Wave propagation in Soils: Mult-Mode, Wide-Band Testing in a Waveguide Device. **Geotechnical Testing Journal**, v. 19, n. 2, p. 130-140, 1996.

GAJO, A.; FEDEL, A.; MONGIOVI, L. Experimental analysis of the effects of fluid-solid coupling on the velocity of elastic waves in saturated porous media. **Géotechnique**, v. 47, n. 5, p. 993-1008, 1997.

GASPARRE, A.; HIGHT, D. W.; COOP, M. R.; RJARDINE, R. J. The laboratory measurement and interpretation of the small-strain stiffness of stiff clays. **Géotechnique**, v. 64, n. 12, p. 942-953, 2014.

GOOGLE MAPS. **GOOGLE MAPS**. Available at: <
<https://www.google.com.br/maps/place/Os%C3%B3rio,+RS,+95520-000/@-29.8943374,-50.258841,14z/data=!3m1!4b1!4m5!3m4!1s0x95186607a0d8a30b:0x1f868499f78b9231!8m2!3d-29.8885619!4d-50.2698884?hl=en>>.
 Accessed on: 10th July 2017.

GORDON, M. A.; CLAYTON, C. R. I. Measurements of stiffness of soils using small strain triaxial testing and bender elements. **Proceedings of a conference on modern geophysics in engineering geology**, Geological Society Engineering Group Especial Publication, n. 12, p. 365-371, London, 1997.

GRANJA, J. L.; AZENHA, M.; SOUSA, C.; FERREITA, C. Comparison Between Different Experimental Techniques for Stiffness Monitoring of Cement Pastes. **Journal of Advanced Concrete Technology**, v. 12, p. 46-61, 2014.

GREENING, P. D.; NASH, D. F. T. Frequency domain determination of G_0 using bender elements. **Geotechnical Testing Journal**, v. 27, n. 3, p. 288-296, 2004.

HARDIN, B. O.; RICHART, F. E. Elastic wave velocities in granular soils. **Proc. ASCE**, v. 89, n. SM1, p. 33-65, 1963.

HEAD, K. H. **Manual of soil laboratory testing: Effective stress tests**. 2nd ed. West Sussex: John Wiley & Sons Ltd., 1998. 3v.

HEINECK, K. S. **Estudo do comportamento hidráulico e mecânico de materiais geotécnicos para barreiras horizontais impermeáveis**. 2002. 251 p. Thesis (D.Sc.) – Civil Engineering Post-Graduation Program, Department of Civil Engineering, Federal University of Rio Grande do Sul, Porto Alegre, BR-RS, 2002. In Portuguese.

HEINECK, K. S.; COOP, M. R.; CONSOLI, N. C. Effect of Microreinforcement of Soils from Very Small to Large Shear Strains. **Journal of Geotechnical and Geoenvironmental Engineering**, v. 131, n. 8, p. 1024-1033, 2005.

HUANG, J. T.; AIREY, D. W. Properties of Artificially Cemented Carbonate Sand. **J. Geotech. Geoenviron. Eng.**, v. 124, n. 6, p. 492-499, 1998.

ISHIHARA, K. **Soil behavior in earthquake geotechnics**. [s.l.] Clarendon Press - Oxford, 1996.

ISMAIL, M. A.; JOER, H. A.; SIM, W. H.; RANDOLPH, M. F. Effect of Cement Type on Shear Behavior of Cemented Calcareous Soil. **Journal of Geotechnical and Geoenvironmental Engineering**, Vol. 128, No. 6, p. 520-529, 2002.

JOVIČIĆ, V. The measurement and interpretation of small strain stiffness of soils. 1997. 181 p. Thesis (PhD) - Civil Engineering Department, City University, London, UK, 1997.

JOVIČIĆ, V.; COOP, M. R. Stiffness of coarse-grained soils at small strains. **Géotechnique**. n. 47, n. 3, p. 545-561, 1997.

JOVIČIĆ, V.; COOP, M. R.; SIMIĆ, M. Objective criteria for determining G_{max} from bender element. **Géotechnique**, v. 46, n. 2, p. 357-362, 1996.

KARASUDHI, P. **Foundations of solid mechanics: Solid Mechanics and its Applications**. Springer Science+Business Media, 1991. 3v.

LADE, P. V.; OVERTON, D. D. Cementation Effects in Frictional Materials. **Journal of Geotechnical Engineering**, v. 115, n. 10, p. 1373-1387, 1989.

LAMBE, T. W.; WHITMAN, R. V. **Soil mechanics, si version**. [s.l.] John Wiley & Sons, Inc., 1979.

LEE, J.-S.; SANTAMARINA, J. C. Bender Elements: Performance and Signal Interpretation. **Journal Of Geotechnical And Geoenvironmental Engineering**, v. 131, n. 9, p 1063-1070, 2005.

LEONG, E. C.; CAHYADI, J.; RAHARDJO, H. Measuring shear and compression wave velocities of soil using bender-extender elements. **Canadian Geotechnical Journal**, v. 46, p. 792-812, 2009.

LEONG, E. C.; YEO, S. H.; RAHARDJO, H. Measuring shear wave velocity using bender elements. **Geotechnical Testing Journal**, v. 28, n. 5, p. 488-498, 2005.

LO PRESTI, D. C. F.; JAMIOLKOWSKI, M.; PALLARA, O.; CAVALLARO, A.; PEDRON, S. Shear modulus and damping of soils. **Géotechnique**, v. 47, n. 3, p. 603-617.

LOPES JUNIOR, L. S. **Prevision Methodology of Mechanical Behaviour of Soils Treated with Lime**. 2001. 199 p. Thesis (D.Sc.) – Civil Engineering Post-Graduation Program, Department of Civil Engineering, Federal University of Rio Grande do Sul, Porto Alegre, BR-RS, 2001. In Portuguese.

MARQUES, S. F. V. **Comportamento de uma Areia Artificialmente Cimentada até Altas Tensões de Confinamento**. 2016. 238 p. Thesis (D.Sc.) – Civil Engineering Post-Graduation Program, Department of Civil Engineering, Federal University of Rio Grande do Sul, Porto Alegre, BR-RS, 2016. In Portuguese.

MARQUES, S. F. V.; CONSOLI, N. C.; SOUSA, J. A. E. Testing Cement Improved Residual Soil Layers. **Journal of Materials in Civil Engineering**, n. March, p. 121029065558009, 2012. doi:10.1061/(ASCE)MT.1943-5533.0000725.

MEHTA, P. K.; MONTEIRO, P. J. M. **Concrete: microstructure, properties, and materials**. 4th. ed. [s.l.] McGraw-Hill Education, 2014.

MITCHELL, J. K.; SOGA, K. **Fundamentals of soil behavior**. 3rd. ed. [s.l.] John Wiley & Sons, Inc., 2005.

MONTOYA, B. M.; GERHARD, R.; DEJONG, J. T.; WILSON, D. W.; WEIL, M. H.; MARTINEZ, B. C.; PEDERSON, L. Fabrication, Operation, and Health Monitoring of Bender Elements for Aggressive Environments. **Geotechnical Testing Journal**, v. 35, n. 5, p. 1-15, 2012.

MOHSIN, A. K. M. Automated Gmax Measurement to Explore Degradation of Artificially Cemented Carbonate Sand. Thesis (PhD) – The University of Sydney. 2008.

O'DONOVAN, J. **Micromechanics of Wave Propagation through Granular Material**. 2014. 401 p. Thesis (PhD) - Department of Civil & Environmental Engineering, Imperial College, London, UK, 2014.

O'DONOVAN, J.; IBRAIM, E.; O'SULLIVAN, C.; HAMLIN, S.; WOOD, D. M.; MARKETOS, G. Micromechanics of seismic wave propagation in granular materials. **Granular matter**, v. 56, p. 1-18, 2016.

O'DONOVAN, J.; O'SULLIVAN, C.; MARKETOS. Two-dimensional discrete element modelling of bender element tests on an idealised granular material. **Granular Matter**, v. 14, p. 733-747, 2012.

O'DONOVAN, J.; O'SULLIVAN, C.; MARKETOS, G.; MUIRWOOD, D. Analysis of bender element test interpretation using the discrete element method. **Granular Matter**, v. 14, p. 197-216, 2015.

OGINO, T.; KAWAGUCHI, T.; YAMASHITA, S.; KAWAJIRI, S. Measurement deviations for shear wave velocity of bender element test using time domain, cross-correlation, and frequency domain approaches. **Soils and Foundations**, v. 55, n. 2, p. 329-342, 2015.

OGINO, T.; MITACHI, T.; CHAN, K. H.; OIKAWA, H.; TSUSHIMA, M. A method for received waveform reconstruction based on bender element test using frequency-swept signal. **Soils and Foundations**, v. 48, n. 2, p. 287-295, 2008.

OGINO, T.; MITACHI, T.; OIKAWA, H.; TAKAHASHI, T.; TSUSHIMA, M. Frequency response characteristics of bender element test system identified by frequency-swept signal input-influence on accuracy of received waveform reconstruction. **Soils and Foundations**, v. 50, n. 5, p. 737-745, 2010.

PIEZO SYSTEMS, INC. **Piezo Systems: Piezoceramic, PZT, Piezoelectric TRansducers, Piezoelectric Actuators and Sensors, Piezoelectric Fans, Piezoelectric Amplifiers, Piezoelectric Engineering, Ultrasonic Transducers, and Energy Harvesters.** Available at <<http://www.piezo.com/index.html>>. Accessed on: 18th Jan. 2016.

PROCEQ. PROCEQ. Available at <<https://www.proceq.com>> . Accessed on: 23th Aug. 2016.

PROCEQ SA **Operating instructions: Pundit LAb / Pundit Lab⁺ Ultrasonic Instrument.** [s.l:s.n.], 2013. Manual.

RICHART JR., F. E.; WOODS, R. D.; HALL JR., J. R. **Vibrations of soils and foundations.** Englewood Cliffs, N.J.: Prentice-Hall, 1970, 414 p.

RIO, J. F. M. E. **Advances in Laboratory Geophysics Using Bender Elements.** 2006. 363 p. Thesis (PhD) - Civil Engineering Department, City University, London, UK, 2006.

RIO, J.; GREENING, P.; MEDINA, L. Influence of sample geometry on shear wave propagation using bender elements. **Deformation Characteristics of Geomaterials**, p. 963-967, 2003.

ROTTA, G. V.; CONSOLI, N. C.; PRIETTO, P. D. M.; COOP, M. R.; GRAHAM, J. Isotropic yielding in an artificially cemented soil cured under stress. **Géotechnique**, v. 53, n. 5, p. 493–501, 2003. doi:10.1680/geot.2003.53.5.493.

SALGADO, R. The Engineering of Foundations. **Journal of Chemical Information and Modeling**, v. 53, n. 9, p. 1689–1699, 2013. doi:10.1017/CBO9781107415324.004.

SÁNCHEZ-SALINERO, I.; ROESSET, J. M.; STOKOE, K.H. **Analytical studies of body wave propagation and attenuation**. Report GR86-15, the University of Texas at Austin, 1986.

SANTAMARINA, J. C.; KLEIN, J. C.; FAM, M. A. **Soils and waves: particulate materials behaviour, characterization and process monitoring**. [s.l.] John Wiley & Sons Ltd, 2001.

SANTAMARINA, J. C. Soil Behavior at the Microscale: Particle Forces. **Proc. Soil Behavior and Soft Ground Construction**, ASCE, 2001.

SENTHILMURUGAN, T.; ILAMPARUTHI, K. Study on Compaction Characteristics and Strength Through Ultrasonic Method GSP 130 Advances in Pavement Engineering, 2005.

SHARMA; FAHEY, Degradation of Stiffness of Cemented Calcareous Soil in Cyclic Triaxial Tests. **Journal of Geotechnical And Geoenvironmental Engineering**, v. 129, n. 7, p. 619-629, 2003.

SHIRLEY, D. J. An improved shear wave transducer. **J. Acoust. Soc. Am.**, v. 63, n. 5, p. 1643-1645, 1978.

SHIRLEY, D. J.; HAMPTON, L. D. Shear-wave measurement in laboratory sediments. **J. Acoust. Soc. Am.**, v. 63, n. 2, p. 607-613, 1978.

SILVA, J.; AZENHA, A., CORREIA, A. G.; FERREIRA, C. Continuous stiffness assessment of cement-stabilised soils from early age. **Géotechnique**, v. 63, n. 16, p. 1419-1432, 2013.

SILVANI, C. **Artificially Cemented Soil Tested in a Cubical Cell: Isotropy at Small Strain and at Failure**. 2017. 194 p. Thesis (D.Sc.) – Civil Engineering Post-Graduation Program, Department of Civil Engineering, Federal University of Rio Grande do Sul, Porto Alegre, BR-RS, 2017. In Portuguese.

SPINELLI, L. F. **Comportamento de fundações superficiais em solos cimentados**. 1999. 133 f. Master thesis (MSc) – Civil Engineering Post-Graduation Program, Department of Civil Engineering, Federal University of Rio Grande do Sul, Porto Alegre, BR-RS, 1999. In Portuguese.

TEKTRONIX. **TDS1000- and TDS2000-Series Digital Storage Oscilloscope**. [s.l.s.n.], 2002. User Manual.

TIMOSHENKO, S. P.; GOODIER, J. N. **Theory of elasticity**. 3rd ed. [s.l.] McGraw-Hill Kogakusha, Ltd., 1970.

VIANA DA FONSECA, A.; FERREIRA, C.; FAHEY, M. A framework interpreting bender element tests, combining time-domain and frequency-domain methods. **Geotechnical Testing Journal**, v. 32, n. 2, p. 91-107, 2009.

VIGGIANI, G.; ATKINSON, J. H. Stiffness of fine-grained soil at very small strains. **Géotechnique**, v. 45, n. 2, p. 249-265, 1995a.

VIGGIANI, G.; ATKINSON, J. H. Interpretation of bender element tests. **Géotechnique**, v. 5, n. 1, p. 149-154, 1995b.

VIGGIANI, G.; ATKINSON, J. H. Interpretation of bender element tests (discussion). **Géotechnique**, v. 47, n. 4, p. 873-877, 1997.

WANG, Y. H.; LO, K. F.; YAN, W. M.; DONG, X. B. Measurement biases in the bender element test. **Journal of Geotechnical and Geoenvironmental Engineering**, v. 133, n. 5, p. 564-574, 2007.

WHITLOW, R. **Basic soil mechanics**. Fourth Edi ed. [s.l.] Pearson Education Limited, 2001.

YAMASHITA, S.; KAWAGUCHI, T.; NAKATA, Y.; MIKAMI, T.; FUJIWARA, T.; SHIBUYA, S. Interpretation of international parallel test on the measurement of G_{max} using bender elements. **Soils and foundations**, v. 49, n. 4, p. 631-650, 2009.

APPENDICES

APPENDIX A - BE EQUIPMENT

INTRODUCTION

Two pairs of operational bender elements (one for bench and another for triaxial tests) were fabricated. This section aims to describe the entire BE system in detail, including BE fabrication, analogical amplification, signal acquisition and processing, and the design of each element used. The entire system was designed to be as simple as possible, with the main goal of accomplishing an operational and user-friendly system.

The first section presents the entire BE system, from wave generation, wave transmission and reception, amplification, visual inspection and acquisition, to data processing using Matlab[®] software. Then, the second section presents a detailed step-by-step BE fabrication. The third section presents the final version of the signal amplifier device, and a justification for its design. It is important to point out that the amplifier was developed specifically for BE use, and it was designed to prevent the introduction of noise as much as possible. The final section presents all the parts fabricated for BE system operation.

APPENDIX A.1 - BE SYSTEM

A scheme of the entire BE system developed for the present study is presented in Figure A.1. The system is composed by a function generator, BE transmitter and receiver, signal amplifier (powered by two 12 V batteries), and an oscilloscope. The shape (square or sine), mode (pulse or continuous), frequency and amplitude of the input signal were defined by the function generator, sent to the BE transmitter through a shielded BNC cable. Due to electrical excitation, the coated piezoceramic is expected to vibrate in a movement similar to cantilever bending (Rio, 2006). Because BE have to be embedded into the soil, the very small mechanical movements, 10^{-5} in terms of strains (DYVIK; MADSHUS, 1985), generate waves, mainly shear-waves, that propagate perpendicularly to BE movement. These waves travel through the soil and reach the piezoceramic embedded in the opposite side of the soil specimen, inducing the BE receiver to move as well. This mechanical movement generates an electrical signal that was amplified 500x before being observed on the oscilloscope screen. The electrical input signal (from the function generator) was also displayed on the oscilloscope. When all the scales on the oscilloscope were adjusted, the screen was recorded on a flash drive and then transferred to a computer for data analysis.

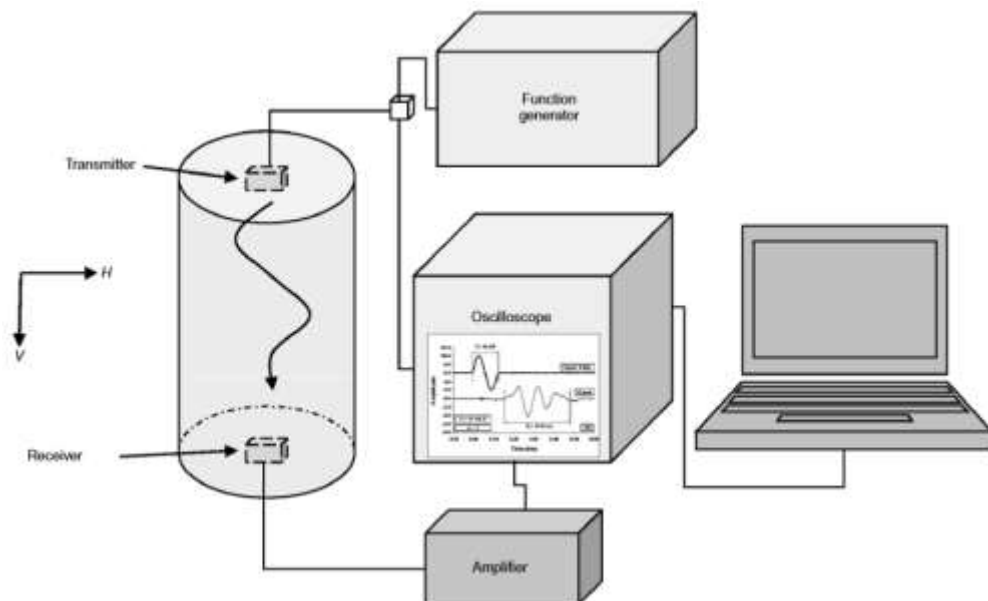


Figure A.1: Scheme of the BE system components and assembling (ALVARADO; COOP, 2007 *apud* ALVARADO; COOP, 2012)

There are three possible ways to mount the BE: a) floating, b) permanent, or c) modular (Figure A.2). The mounting of choice directly affects piezoceramics mechanical anchoring (MONTTOYA *et al.*, 2012). The modular alternative was selected for the present study (Figure A.3). Apart from facilitating piezoceramic repairing or replacement whenever necessary, it also provides better anchoring to the piezoceramic during bending.

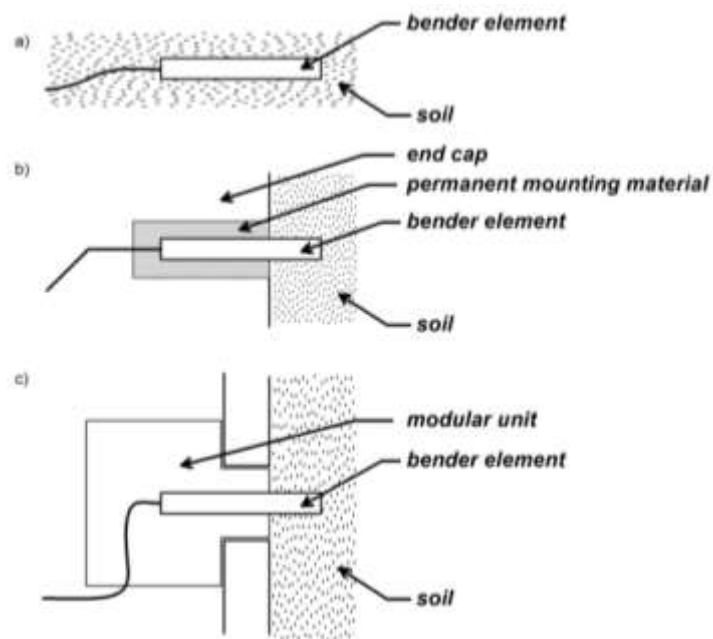


Figure A.2: BE mounting alternatives – (a) floating; (b) permanent; (c) modular (MONTTOYA *et al.*, 2012)

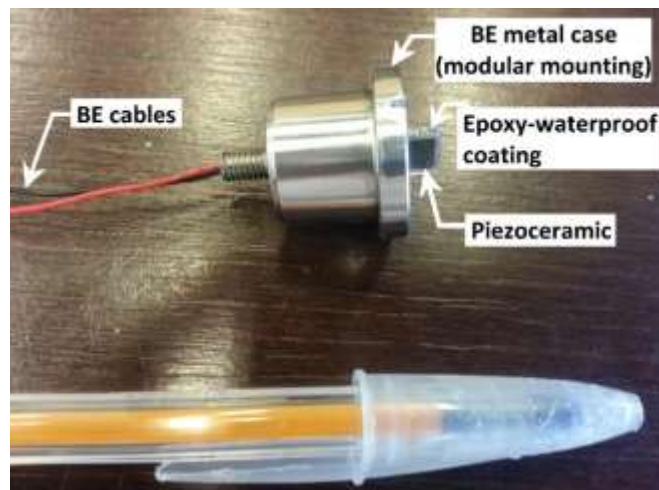


Figure A.3: Modular BE fabricated for the present work

The metal cases used in all BE pairs were basically the same. A slight change was made only in the metal case used in the triaxial transmitter BE. Two grooves were made outside the metal case to accommodate two o-rings (Figure A.4) to isolate the electrical cables. As the top cap was made of acrylic, it was considered too fragile to receive the grooves for the o-rings. In contrast, for the triaxial BE receiver, the grooves were made on the internal surface of the metal pedestal.



Figure A.4: BE triaxial transmitter before being encapsulated with o-rings positioned into grooves made on the metal case

A BE system representation as an electrical circuit is presented in Figure A.5. In this scheme, a drain line (“ R_{drain} ”) is represented. Based on Montoya *et al.* (2012), the drain line was added to the BE receiver to ground the noise. As the BE metal case was in direct contact with the specimen (and sometimes with pore fluid), the metal case was the beginning of the drain line (for more details, see A.1.3). The BE receiver was also connected to a 3-way XLR connector, rather than a 2-way BNC connector. Two of the ways were used for the BE received signal, while the remaining way was used for the drain line. Thus, the amplifier could be directly connected to the BE receiver through a XLR port.

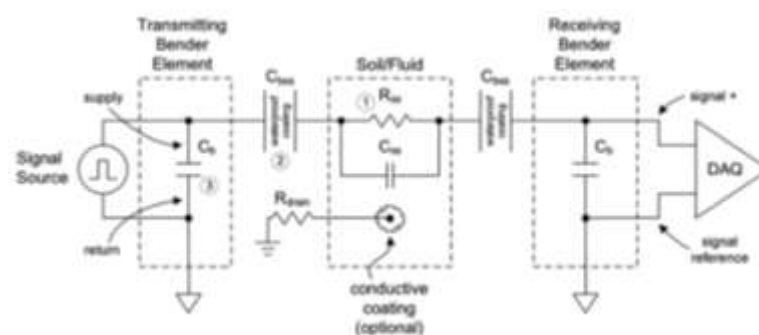


Figure A.5: BE system representation as an electrical circuit
(MONTAYA *et al.*, 2012)

The final BE system setup used in triaxial tests is presented in Figure A.6. This figure illustrates all BE components, except for the two batteries that feed the signal amplifier.

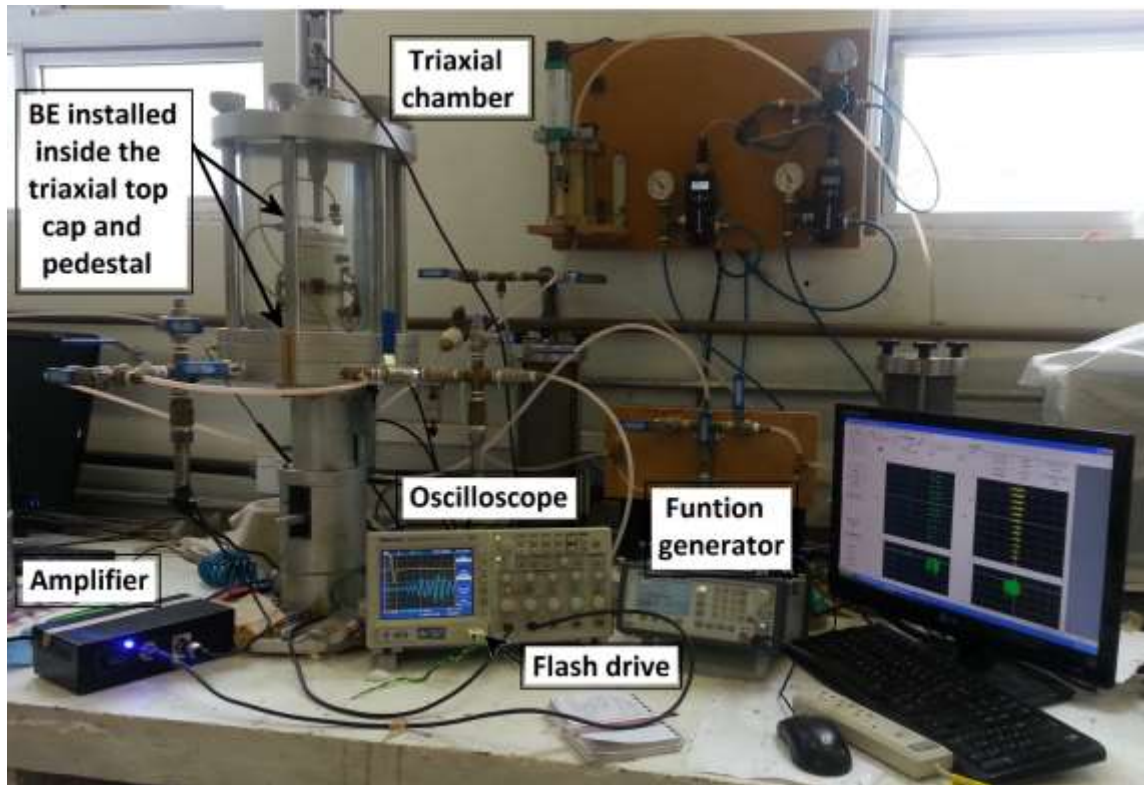


Figure A.6: BE system set up for triaxial tests

A.1.1 Wave generation - Function generator

A Direct Digital Synthesizer (DDS) Sweep Function Generator – Model 4045 manufactured by BK PRECISION® (Figure A.7) was used. The function generator is able to generate sine, square, triangle, and arbitrary waveforms, which can be generated using continuous, triggered, gate, burst, trigger source operating modes. Although this device is also capable of generating waves with a sweep characteristic (shape, time, and trigger), this function was not used in the present work. Whenever required, sweep was conducted manually. The most relevant specifications of the function generator are presented in Chart A.1.

The device was used to generate the electrical input signals sent by the BE transmitter. Only square and sine waveforms, and continuous and burst operating modes were used. The burst option was preferred to the trigger option due to its simple parameters setting. Although the offset option was available, it was never used, as it would not produce realistic BE movement.

Usually, 20 V peak-to-peak (p-p) were applied, and the frequency sweep was manually adjusted between 1 and 35 kHz.



Figure A.7: BK PRECISION® function generator used to create the electrical input signals sent by the BE transmitter

Chart A.1: Function generator main specifications

Frequency characteristics	0.01 Hz to 20 MHz
Waveform length	2 – 1,000 points
Vertical resolution	12 bits
Amplitude range	20 mV* – 20 V* p-p into 50 ohms
Amplitude accuracy	$\pm 2\% \pm 20$ mV of the programmed output from 1.01 V – 10 V
Output impedance	50 ohms

*Real values are presented (different from the values presented in the equipment manual)

(source: BK PRECISION®, 2014)

A.1.2 Wave transmission and reception – BE transducers

Mechanical movement is generated when a voltage is applied to the transmitter piezoceramic. As the piezoceramic moves, it pushes and pulls surrounding soil particles. Sine pulses are generated when cycles involving the piezoceramic moving back, forward and returning to its rest position are completed. Then, transversal waves (s-waves) are propagated through the soil until they reach the receiver piezoceramic located on the opposite side of the specimen, moving the receiver piezoceramic. The mechanical movement generates an electrical signal, which needs to be amplified because of signal attenuation and energy loss.

In our first attempt, BE transmitters were built with parallel-to-series connections, as recommended by the literature (Figure 2.16). However, due to limitations regarding BE fabrication (see A.2.2) the parallel-to-series BE connections did not present adequate performance in all cases, and had to be replaced by series-to-series BE connections. In three attempts to produce quality parallel-to-series BE connections, only one performed successfully, and was used in the triaxial tests. Therefore, the two BE transducers used in the bench tests presented series-to-series connections. The drain line was added to the receiver for both bench and triaxial BE pairs.

To maintain standardization among all the BE modules, BE cables had to be as small as possible to fit inside the already existing passage holes of the triaxial apparatus. These tiny holes were designed to prevent possible pressure leaks. Therefore, computer mouse cables were soldered to the piezoceramics and then connected to a shielded cable, whose twisted shield was used as a drain line in the case of receiver transducers (Figure A.8).

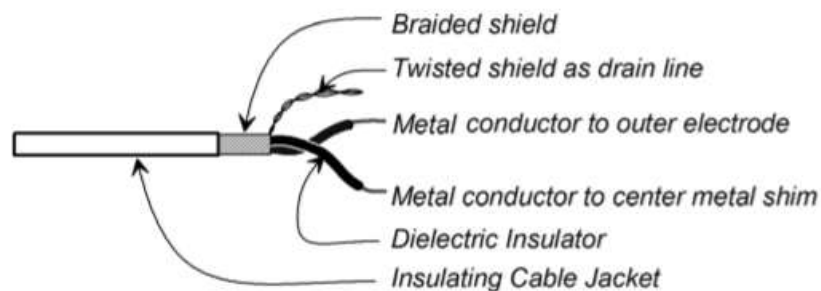


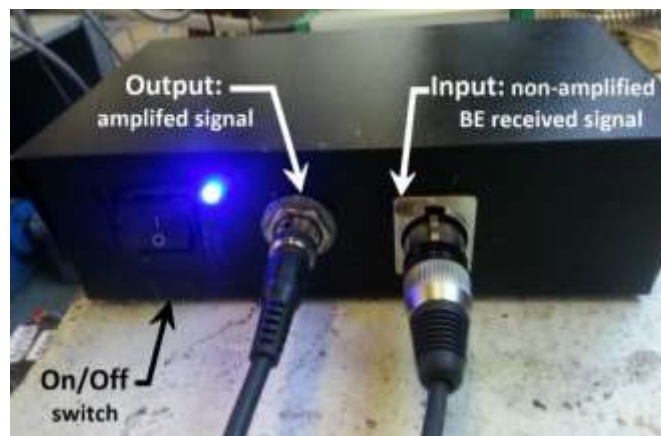
Figure A.8: Shielded cable scheme used for the BE receiver
(based on: MONTROYA *et al.*, 2012)

A.1.3 Wave amplification – Signal amplifier

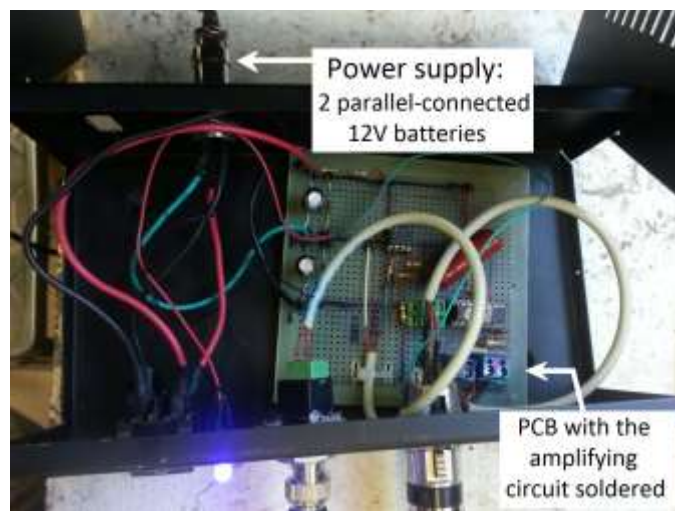
Because the received signal was too small for the oscilloscope vertical sensitivity, and also because it was an alternating signal, a signal amplifier had to be specially designed and fabricated (Figure A.9). The final design needed to be able to capture very small signals, and result in big gains at the end of the amplification process. Thus, amplification was separated into two gain steps. In the first step, a very sensitive integer circuit (INA116) was used, which provided a gain of 50x. It was followed by the second step, in which a regular operational amplifier (op-amp) chip was employed, providing an extra gain of 10x, resulting in a final gain of 500x. The first gain step was designed to allow changes in gain by simply changing the

resistor (with no need of soldering). Although higher amplifications can be obtained with this design, it is important to be aware that the higher the gains, the higher the working frequencies ranges that are affected by signal attenuation. The detailed description of the amplification design is presented in A.3.

The entire circuit was soldered to a universal printed circuit board (PCB), which was conditioned inside a metal box, which worked as a Faraday cage, helping filter high frequency noise. This metal box was connected to a real ground, which was obtained by connecting two 12 V batteries (power supply) in parallel connection, and using their centre as the ground. Silicon was added to the edges of the PCB to create a gap between the parts soldered to the circuit board and the metal box, and prevent contact between them.



(a)



(b)

Figure A.9: Fabricated signal amplifier – (a) front view (closed); (b) top view with the amplifying circuit exposed

Figure A.9 – (a) shows the XLR cable connected to the amplifier. This cable was responsible for delivering the signal to the amplifier (considered as the input signal), which was previously captured by the BE receiver. The drain line (connected to the BE metal case) was connected to the XLR connector, which was then connected to the guard ports of the integer circuit (IC) INA116. Those ports were grounded on the centre of the two batteries. After total amplification (500x), the signal left the system through a BNC cable connected to the oscilloscope. The system has an on/off switch and a blue led light to indicate when the system was on. Figure A.9 – (b) illustrates the open box with the circuit inside. A MIKE connector with 3 ways can be seen at the back, to which the power supply cable is connected. The amplifier is supplied by two 12 V batteries in a parallel-connection.

A.1.4 Signal acquisition – Oscilloscope

After amplified, the BE received signal (channel 2) was visualised on the oscilloscope screen. The electrical signal input (channel 1) was also seen using the “trigger” option, which enabled freezing the signals on the screen. When horizontal and vertical scales (channels 1 and 2) were adjusted, the data on the oscilloscope screen were saved in a flash drive in a “.csv” (comma separated values) format. The data were saved as raw as possible, as it will be discussed further in the text.

The oscilloscope device used in the present research was a TDS 2014B Four Channel Digital Storage Oscilloscope manufactured by Tektronix® (Figure A.10). Each of the 4 channels can acquire 1×10^9 samples/second for frequencies up to 100 MHz. It has a USB port in the front-panel that allows data acquisition. The advanced pulse trigger offers 3 trigger types: edge, video, and pulse width. The edge trigger type (rising) was selected. Trigger level was defined in respect to channel 1 (source), which was connected to the function generator and, therefore, exhibited BE electrical input. The auto (rather than the normal) mode option, as well as the direct current (DC) coupling (present in the trigger menu) were also selected.

The oscilloscope provides 3 types of data acquisition: sample mode, peak detected mode, and average mode. The average mode is very helpful to remove random noise and, because of that, it was the acquisition mode chosen for all tests. Regardless the oscilloscope sampling capacity, a sampling rate had to be selected during data acquisition among the available options (4, 16, 64, and 128 points). The higher the sampling rate, the smoother and less noisy the signal. However, depending on the signal frequency, higher sampling rates may not detect the signal

at all, or can cause a time-delay. Therefore, the minimum sampling rate (4) was chosen whenever possible. However, in some conditions, a lot of noise was present and a higher sampling rate was necessary to enable data interpretation at real time. Thus, the adequacy of the input frequency had to be defined at the moment of acquisition, i.e., whether further tests with different frequencies were required or not.

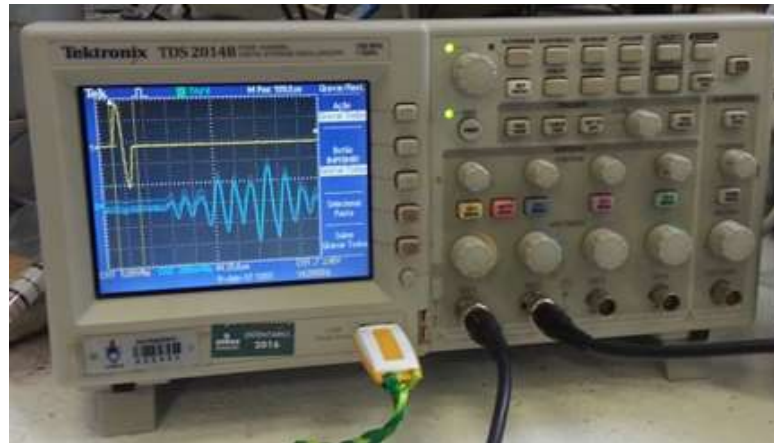


Figure A.10: Tektronix® oscilloscope used for observing and acquiring BE input and the amplified output signals

Chart A.2: Oscilloscope specifications

Input impedance (DC coupled)	1.10 ⁶ ohms ±2% in parallel with 20 pF ±3 pF
Input coupling	DC, AC, and GND
Vertical scale range	2 mV/div - 5 V/div at input BNC
Vertical resolution	8 bits (except when set to 2 mV/div)
Horiz. sample rate range	1.10 ⁹ Sample/second
Horiz. record length	2,500 samples for each channel
Horiz. scale range	5 ns/div – 50 s/div

(source: Tektronix®, 2002)

Regarding the effect of the oscilloscope resolution on data accuracy, Clayton (2011, p. 25) emphasizes the limits previously stated by Yamashita *et al.* (2009): “[...] the sampling time interval should be less than 1/100th of the travel time between transmitter and receiver. Voltage resolution should be better than 1/100th of the amplitude of the of the received signal”. As the

smallest wave travelling time measured in the present study was $62.90 \mu\text{s}$, $1/100^{\text{th}}$ of this value was 6.29×10^{-7} seconds and, therefore, higher than the sampling time interval (1×10^{-9} s). Voltage resolution is a more complicated matter. The amplified received signal could be only a few mV; assuming it was 3 mV, $1/100^{\text{th}}$ of this value would be 0.03 mV. When 2 mV/div (smallest vertical scale range) is used, the manual does not clearly state what the vertical resolution should be. Thus, if 5 mV/div is used, the stated resolution is 8 bits, resulting in a resolution better than the $1/100^{\text{th}}$ of the received vertical range. Based on these results, the oscilloscope used in the present study was adequate for BE data analysis.

In respect to each individual channel, all settings were always the same for both channels 1 and 2. Vertical coupling was a DC type, bandwidth limit (20 MHz) was turned on, and the waveform was never inverted, as each BE pair was calibrated so that sent and received peaks were aligned.

A.1.5 Data processing

After saved in a flash driver, all data were transferred to a computer. Data opening and “processing” was performed with Matlab[®] script. The script, specially written for this study, is fully presented and described in Appendix B. Although the script was designed to be simple and user-friendly, it contains some limitations concerning data processing and handling. The main limitations refer to the fact that the script can only adequately process single sine pulses, the analysis is entirely in the time-domain, and a maximum of 8 different frequencies can be processed at each time. Data presentation was based on Viana da Fonseca, Ferreira, and Fahey (2009). Output signals from different input frequencies were stacked, while all input signals were grouped at the top of the graph, as previously presented in Figure 2.25. There is one difference between the graph presented by the authors and the representation chosen for the present study. Instead of aligning the input signals at the beginning of the pulses, all input signals were aligned based on their peaks. Therefore, measurements in the present study were conducted using the time-domain and the peak-to-peak alternative to determine the first-wave arrival time.

When using the Matlab[®] script, a directory matching the data files directory had to be initially selected, and the file path introduced inside the script. After that, the system was fed by answering the prompts that appeared on the command window. Depending on the answers, the script was automatically directed to relevant questions; e.g., when testing BE in direct contact, no question was asked regarding time of cure or the distance between transducers; however,

when a cemented specimen was tested, several questions were asked. After feeding the script, all files in the inserted interval were opened. As each file was opened, a Microsoft[®] Excel spreadsheet was created to summarise all tested data. For each input frequency, a different sheet (tag) was used to write data and details regarding individual tests. Moreover, an individual sheet summarised all times and voltages from channels 1 and 2 for each and all tests. At the end, a graph with the plotted data was generated and opened in the Matlab[®] environment, and the length of the “imdistline” could be manually moved until a suitable position indicating the first-peak arrival was chosen. After that, the figure could be saved in a Matlab[®] format (“:fig”), allowing further manipulation, or in regular image format, preferably TIFF (“:tif”).

APPENDIX A.2 - BE FABRICATION

The fabrication of the BE used in the present study, except for the machined parts, was conducted at LEGG-UFRGS. In the following items, a detailed description of how to produce the BE device is presented.

A.2.1 Piezoceramic

A piezoceramic plate was purchased from Piezo Systems[®] (Figure A.11). The following description is based on the information available in their website (PIEZO SYSTEMS, 2016). The code T220-A4-503X stands for unmounted (T), 2 piezo-layers (2) with a total thickness of 0.51mm or 0.020” (20) piezoceramic. “A4” stands for the piezoceramic material (PSI-5A4E), defined as an “[...] industry type 5A (Navy Type II) piezoceramic. This vacuum sputtered nickel electrodes produce extremely low current leakage and low magnetic permeability. 5A has a wide temperature range and is most insensitive to temperature”. The lack of a code between “A4” and “503X” means that the centre shim is made of brass. The size of the piezoceramic plate is designated by “503”, which indicates that the plate dimensions are 31.8 mm wide x 63.5 mm long. The “X” indicates that the piezoceramic x-poled for series operation; in other words, no part of the metal shim is exposed. See A.2.2 for details on how to produce y-poled for parallel operation.

Chart A.3 presents the most relevant piezoceramic specifications. Using the stated values, capacitance, rated voltage (V_p), free deflection, and block force can be calculated for a piece of piezoceramic with specific dimensions, and in a free (not embedded) condition. The equations for calculations are available at the manufacturer website. As the free condition cannot be used in BE tests, calculations were not relevant for the present study, but were used to perform a security check to verify whether the voltage (and consecutive force) applied would cause any damage to the piezoceramic piece used for BE fabrication. The check showed that the voltage (20V p-p) applied did not cause any damage on the piezoceramic pieces. As a matter of fact, the voltage used was much lower than the calculated limit for the free condition.



Figure A.11: Piezoceramic plate packaging

Chart A.3: Piezoceramic specifications

d_{31} (strain produces / electric field applied)	-190×10^{-12} metre/Volt
g_{31} (open circuit electric field produced / stress applied)	-11.6×10^{-3} Volt-metre/Newton
E_p – polarising field	$> 2 \times 10^6$ Volt/metre
E_c – initial depolarising field	$\sim 5 \times 10^5$ Volt/metre
Density	7,800 kg/metre³
Y_3^E – elastic modulus	5.2×10^{10} Newton/metre ²

(source: PIEZO SYSTEMS, 2016)

A.2.2 Piezoceramics wiring

The size of the piezoceramic plate was the largest available in the market, and permitted to be cut in several BE-sized pieces, representing the best cost-benefit option. Plate width (31.8 mm) was divided in 4 bands of 7.95 mm wide, while the length of the sheet was cut in 7 pieces of 9.07 mm. This process resulted in 28 pieces of piezoceramic for BE fabrication (Figure A.12).

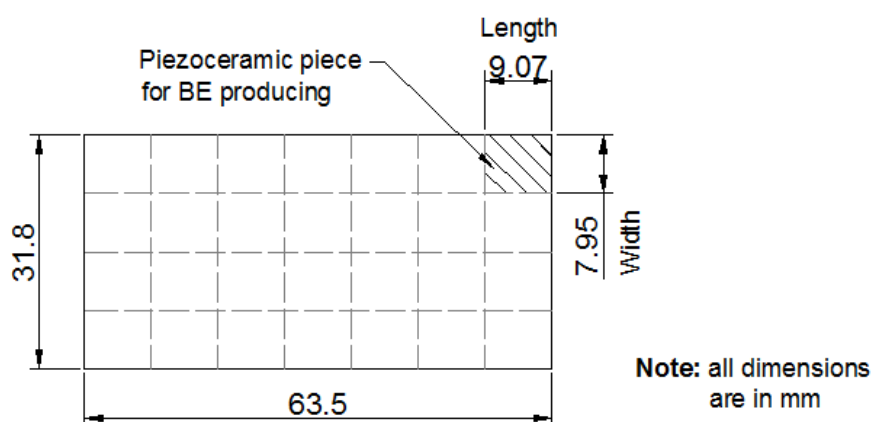


Figure A.12: Piezoceramic plate cut into 28 BE-sized pieces

The piezoceramic sectioning process was conducted on a clean, flat surface to avoid damaging the material. As the material is quite fragile, piezoceramic handling and marking had to be conducted very carefully. First, the 7.95 mm bands were lightly marked using a soft pencil. After that, a sharp thin blade was used to cut the band with the assistance of a flexible plastic ruler (Figure A.13 – a). The cutting movement was conducted as many times as necessary. Care had to be taken with the force applied on the ruler, as not to break the piezoceramic. After forming a groove on the top side, a crack line started to form on the back side (Figure A.13 – b). At this moment, the plate was turned and the cutting process was carefully repeated on the back side along the crack line. This light cutting movement was repeated until the band was completely separated from the plate.

Once a band was cut off, marks of approximately 9.07 mm were made on the band with the same soft pencil (Figure A.14 – a). The cutting process was the same as described before to achieve each individual BE-sized piezoceramic piece (Figure A.14 – b). Because of the size of the band and the difficulty to hold it in place during cutting, extra care was employed.

After being separated, sandpaper was carefully used to remove any irregularities from the edges (Figure A.15 – a). A coarser sandpaper was initially used, followed by a finer sandpaper for a smooth finishing. For parallel connection, the metal shim was exposed in one of the edges by carefully sanding off the top surface with the coarser sandpaper. As the piezoceramic piece was small, and to facilitate the process, a tiny piece of sandpaper band was glued to a small piece of wood (Figure A.15 – b), such as a clothes peg, so that just a small portion of the piezoceramic

edge was exposed. The pieces of sandpaper were replaced whenever necessary. The piezoceramic edge was sanded until a golden colour (the metal shim) was observed (Figure A.15 – c). The sanding process was very carefully conducted until all the remaining ceramic layer was removed (Figure A.15 – d). When ready, each piece was wiped with a clean piece of cloth imbued in isopropyl alcohol.



(a)



(b)

Figure A.13: Piezoceramic band cutting – (a) top side with a light groove; (b) crack line on the back side of the plate after using the blade several times



(a)



(b)

Figure A.14: A 7.95-mm piezoceramic band – (a) piece marking; (b) 2 BE-sized pieces already cut

Figure A.16 presents BE wiring scheme. Series operation elements (x-poled) were used for all BE receivers by simply soldering 2 wires, one on each side of the piezoceramic piece. When subjected to a voltage, series elements tend to have piezo-layers with polarisation vectors pointing to opposite directions. Because parallel operation (y-poled) requires only half of the voltage to produce the same motion of series-elements (PIEZO SYSTEMS, 2016), an attempt was made to fabricate parallel connections to be used as transmitters. Parallel elements were obtained by soldering 3 wires: 2 wires, one to each side of the piezoceramic piece, and 1 to the shim. The 2 outer surfaces were connected to the same voltage, while the metal shim was connected to the opposite voltage. Therefore, both polarisation vectors points to the same direction.

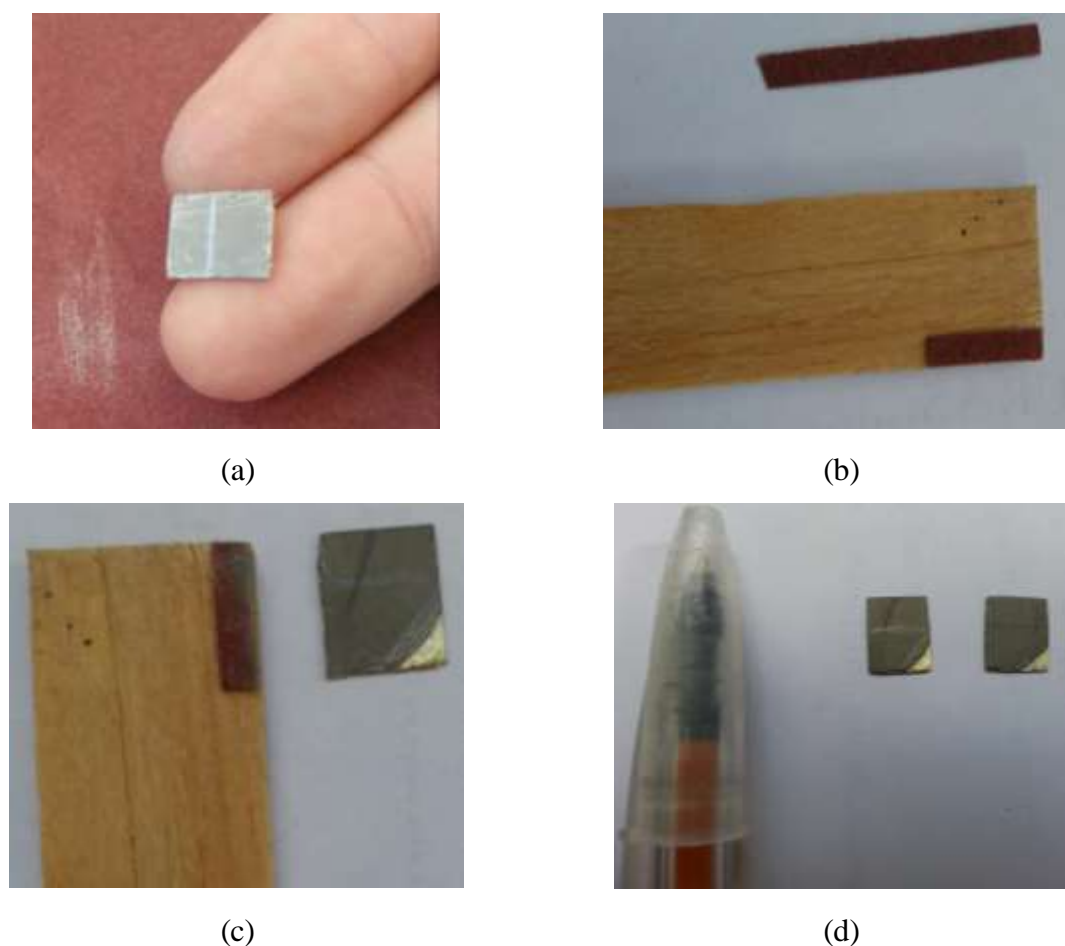


Figure A.15: BE-sized piezoceramic piece preparation for parallel wiring – (a) sanding the rough edges; (b) piece of sandpaper glued to a piece of wood used for sanding off the first ceramic layer; (c) exposed metal shim; (d) final look of BE-sized piezoceramic pieces with the metal shim exposed

The tip of the wire was exposed, dipped into soldering paste (excess paste was removed), and a small amount of molten soldering tin was used to cover the tip (Figure A.17 – a). After that, the piezoceramic piece and the previously prepared wire were fixed to a clean, flat surface with adhesive tape (Figure A.17 – b). The wire was fixed in such a way that its edges was on the top of surface of the piece or the exposed metal shim, depending on the type of connection. In parallel connections, wiring started by soldering the wire to the metal shim (Figure A.17 – c).

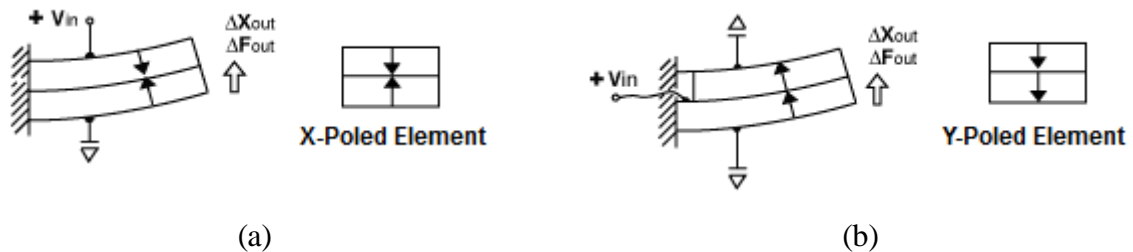


Figure A.16: Piezoceramic wiring scheme – (a) x-poled element for series operation (2 wires); (b) y-poled element for parallel operation (3 wires)

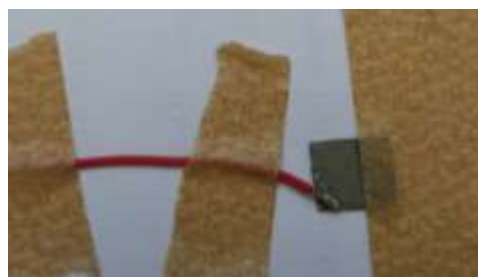
(PIEZO SYSTEMS, 2016)

Soldering quality was inspected by lightly trying to move the soldered wire; if the union was poorly conducted, the wire could be easily separated from the piezoceramic. That was the most common problem encountered while soldering the wires to the piezoceramic surfaces, which frequently led to resoldering in another position, as the soldering heat damaged the surface in contact with the wire. Once soldering was mechanically inspected, continuity was tested with a multimeter device (continuity function) by positioning one of its terminals on the tip of the wire free of soldering, and the other on the piezoceramic surface. In the case of wires soldered to the surface, different spots all over the surface were tested to ensure that continuity existed. When connected to the metal shim, check was only conducted on one spot. After all checks were completed, the area around the soldering was cleaned with isopropyl alcohol, and covered with super glue (Superbonder®) with the tip of a needle (Figure A.17 – e). The use of super glue had two purposes: first, to increase the mechanical strength of the soldered wire; and second, to insulate the soldered area. Because the wire dielectric insulator usually melted during the soldering process, super glue was also added on the top of those exposed regions. After the super glue had dried, a new wire was soldered to the piezoceramic piece (Figure A.17 – f).

When 3 wires were used, the first wire was soldered to the metal shim, the second on the surface in the same side (as presented in Figure A.17), and then the third on the opposite side. However, when using 2 wires, the opposite electrode side was wired immediately after the first. Colour code for the wires is recommended, so that each colour is soldered to an electrode surface or the metal shim.



(a)



(b)



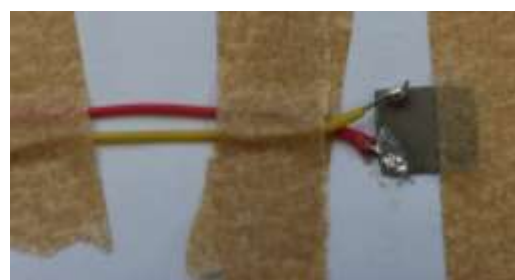
(c)



(d)



(e)



(f)

Figure A.17: Wiring a parallel connection element – (a) wire tips covered with solder; (b) piezoceramic piece and wire fixed to a clean, flat surface; (c) wire soldered to the metal shim; (d) continuity test; (e) covering the soldered parts with super glue using a needle; (f) next wire (yellow) in position to be soldered

As previously mentioned, BE transmitters using parallel connections were not very successful. Possibly, the reason for that was the fact that the piezoceramic piece had to be sanded to expose the shim and permit the extra connection, resulting in the poor performance observed in most parallel connected elements, with 2 out of 3 elements failing. Therefore, this step requires further consideration.

A.2.3 Piezoceramic encapsulating

To ensure that the piezoceramic piece stayed in place inside the metal case, a piece of insulating cable jacket of 3-4 mm was used (Figure A.18 – a). A small cut was made on one side with a blade (Figure A.18 – b). Then, the piece of cable jacket was passed along the cables until the cut was fixed to the piezoceramic (Figure A.18 – c, d). Then the cables were passed through the metal case until the piezoceramic was accommodated inside the metal case, so that the piece of cable jacket around the piezoceramic held it firmly in place.



(a)



(b)



(c)



(d)

Figure A.18: Accommodating the piezoceramic inside the metal case – (a) piece of insulating cable jacket side-by-side the metal case; (b) the piece of cable jacket being cut on one side; (c) cables passed through the cable jacket; (d) cable jacket fixed to the piezoceramic

To prevent the encapsulating resin to stick to the walls of the mould, a de-moulding agent had to be used. Among the several de-moulding agents tested (different types of oil), white washable glue proved to be the most effective. Apart from being cheap and easily accessible, it effectively prevented the epoxy resin to stick to the mould after BE encapsulating. It was applied with a soft paint brush (Figure A.19) on the surfaces of the mould in contact with the metal case, and on the surfaces that separated the two parts composing the mould. Two to three layers of glue were applied to form a thin coat. Before a new layer was applied, it was necessary to wait for the previous layer to dry completely.

Once the glue had dried, the metal case was fixed to the bottom part of the mould with 3 screws (Figure A.20 – c). Before tightening, the slot on the side of the metal case was aligned with the surface of the mould (red arrow in Figure A.20 – a). The piezoceramic was carefully moved with the help of a needle and a pair of tweezers until a small gap (about 1 mm) was created between the piezoceramic and the mould (Figure A.20 – b). The piezoceramic was carefully placed parallel to the surface of the mould for uniform epoxy-coverage.

Piezoceramic encapsulating demanded a low viscosity resin to be applied with a cannula. As the common type of epoxy resin was too viscous, a special low viscosity epoxy resin (Redelease®) was used. After cure, the resin became a rigid, impermeable, durable layer of epoxy. Both BE pairs (bench and triaxial) presented a very good performance after encapsulating, even when subjected to high pressures (triaxial).



Figure A.19: De-moulding agent (white glue) being applied on the bottom part of the metal mould for BE encapsulating

The resin and hardener were mixed together in the proportions established by the manufacturer (1:0.5 of the mass of the resin to the hardener, respectively). After thoroughly mixing both elements together on a metal tray, the mixture was left aside for about 10 minutes to permit that any air bubbles trapped inside were released. When ready, a syringe was filled with the mixture, which was carefully deposited around and under the piezoceramic, filling the gap between the piezoceramic and the mould and inside the metal case completely (Figure A.21 – a).

Before closing the mould, the needle was placed inside the metal case through the back hole where cables left the case from. The mould was closed and tightened with the 2 big screws on the top part (Figure A.21 – b). Then, the small screw on the side of the top part of the mould was also tightened, holding the metal case firmly in place. After that, the mould was rotated 90°, with the metal case in an upright position, and resin was slowly injected inside the assembly until excess resin could be seen at the opening where the needle was introduced. While carefully removing the needle, more resin was added to fill the space previously occupied by the needle (Figure A.21 – c). The assembly was left in the same position for 24 h before de-moulding.



(a)



(b)



(c)

Figure A.20: Metal case with piezoceramic positioned in the bottom part of the mould – (a) metal case groove alignment (red arrow); (b) gap between the piezoceramic and mould; (c) 3 small screws holding the metal case in place

During de-moulding, the 2 big screws were simultaneously untightened first (Figure A.22 – a). As this can be a very difficult process, because resin usually covered the screw threads, the mould had to be placed in a vice. After that, the small screw holding the metal case to the top part of the mould was also untightened. The mould was then opened by introducing the Allen key into the indentation on the back of the mould (Figure A.22 – b), using as a lever to push the two parts open (Figure A.22 – c).



(a)



(b)



(c)

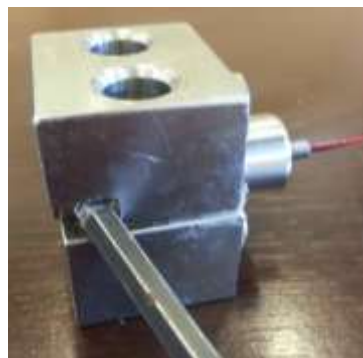
Figure A.21: Resin-encapsulating process – (a) mould indentation being filled with resin; (b) closing the mould; (c) metal case upright position that should be left for 24 h

The remaining 3 small screws positioned on the bottom part of the mould were then removed (Figure A.22 – d). Removing the BE from the mould could be tricky. The advice is to hold the mould firmly, and lightly knock it off the metal case with a small hammer. After removing the BE module, the mould was washed in warm water to remove the glue (Figure A.22 – e) and any remaining epoxy-resin adhered to the mould. To reach maximum strength and

impermeability, the BE was stored for 5 days to allow for chemical reactions to be completed. Finally, any glue residue or excess resin was removed and the BE module was ready to be further processed (Figure A.22 – f).



(a)



(b)



(c)



(d)



(e)



(f)

Figure A.22: De-moulding process – (a) untightening the 2 big screws; (b) opening the mould by creating a lever mechanism; (c) opened mould; (d) untightening the remaining 3 screws; (e) glue layer after opening the mould; (f) appearance of encapsulated BE

A.2.4 Final assembling

After the cure period, each BE module was prepared to be placed in its respective pedestal or top cap. All BE to be used as receptors had a third wire soldered to the threaded part of their metal cases, which was covered with a heat shrinkable plastic lining (Figure A.23). After that, the whole extent of the cables was also covered with a heat shrinkable lining.



Figure A.23: BE receiver (series connection) with a third wire soldered to the threaded part of the metal case (drain line)

The triaxial BE pair, to be inserted in the top cap and pedestal, required long wires that needed to be soldered to the cables with the BNC and XLR connectors after they left the chamber. Therefore, thin well insulated wires with no junctions were required to be used inside the triaxial chamber. To reinforce water insulation, 2 to 3 layers of liquid rubber were deposited around cables. The insulation of the cables inside the top cap and pedestal was obtained with the use of 2 o-rings on each element. Moreover, special hydraulic connectors were used to isolate cables inside the top cap and pedestal, and when those cables exited the triaxial chamber.

The final appearance of the BE fixed inside the nylon bench pedestal is presented in Figure A.24. The bench BE had short cables, so that the connection to the shielded cable was hidden inside the nylon pedestal. Shielded cables were about 500 mm long with a BNC and XLR connector soldered on the opposite side. Silicon was used to ensure that BE did not move inside the pedestal and to isolate the cables from any contact with water.



Figure A.24: Bench BE modules positioned in their nylon pedestal

APPENDIX A.3 - SIGNAL AMPLIFIER CIRCUIT DESIGN

Figure A.25 presents the entire electronic scheme of the fabricated signal amplifier, which can be divided into 4 main parts: power supply; input and output amplifier connectors; and each of the two gain steps.

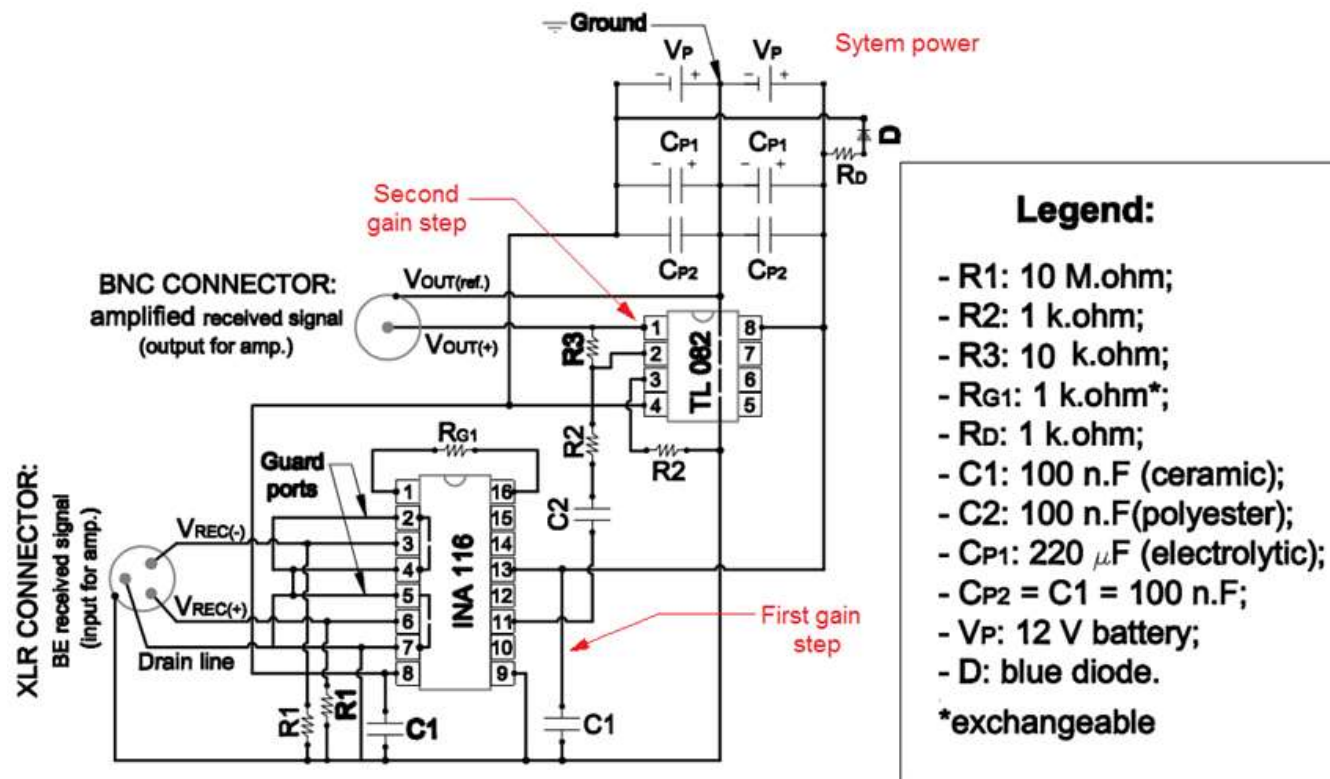


Figure A.25: Electronic scheme for the BE received signal amplifier

A.3.1 Amplifier power supply

The two gain steps, or amplification chips, require a symmetrical direct current (DC) voltage source. A few attempts were made to establish the best power supply alternative to the system. Initially, a voltage divider (two equal resistors connected in parallel) was used to provide a symmetrical power source to the circuit because the two different DC power supplies were non-symmetrical. The first attempt used a switched-mode power supply (SMPS), commonly used to charge mobile phones. This alternative introduced noise, interfering with the amplifier output. Then in the second attempt, a precision variable voltage power supply DC converter, typically used in laboratory bench tests, was tested. Although its performance was superior than the previous attempt, noise was still present as it is an AC-to-DC converter.

The best alternative for the circuit was to use 12 V batteries. The main drawback was the fact that the batteries require recharging. However, as energy system consumption was very low, recharging was not frequently required. Using 2 batteries connected in parallel eliminated the need of a voltage divider in the system. Moreover, batteries are natural DC sources, which means that no extra noise or AC components is normally introduced when they are used as power source.

The two 12 V batteries used as the amplifier power supply are presented in Figure A.26. They were connected to 3 wires: 1 brown wire connected to the negative pole of one battery; 1 blue wire connected to the positive pole of the other battery; and 1 green-yellow wire connected to the remaining negative and positive poles of the two batteries, creating a real ground that was used for the entire circuit. Those cables entered the amplifier circuit through a 3-way MIKE connector, attached to the amplifier metal box. The two MIKE pins delivering the positive and negative voltage were connected to the on/off switch. This is a 4-pin switch, allowing 2 wires to arrive (positive and negative supply), and 2 to leave the switch, which were then connected to the circuit board. When pushing this switch, both lines had their system opened or closed simultaneously. The third MIKE pin (connected to the real ground) was directly soldered to the circuit board (Figure A.27).



Figure A.26: Two parallel-connected 12 V batteries. The brown cable is connected to the negative pole of the circuit, the blue cable to the positive, and the green-yellow cable connected to remaining poles of the batteries, creating a real ground

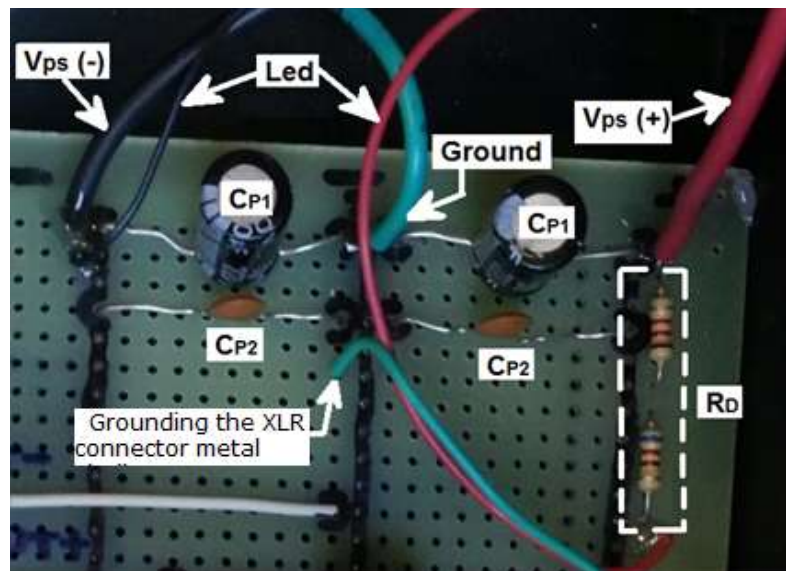


Figure A.27: Power supply elements soldered to the circuit board

Figure A.27 presents the power supply system entrance. The red wire represents the positive pole, while the black wire represents the negative pole, and the green wire represents the real ground. The two-thin red and black wires were connected to the blue led (diode) positioned on the amplifier front panel. As the available voltage to the circuit was 24 V, the current reaching

the led was limited by adding a series-resistor (R_D). Then, when the on/off switch closed the system, the blue led was lit. Two pairs of capacitors were added at the point that the power supply entered the system. They worked as a filter, and the set formed by the pairs of ceramic and electrolytic capacitors were used to block higher and lower frequencies signals that could be delivered to the system

The INA116 (responsible for the first gain step) datasheet recommends that a Faraday shield is built around the IC and the input connection to eliminate stray fields. Although an individual Faraday shield was not built, the entire system was placed inside a metal box where the amplifier was conditioned. Moreover, this metal box was grounded to the real ground created between the two parallel-connected batteries.

A.3.2 Input and output amplifier connectors

An XLR connector was used because 3 ways to deliver the signal (pins 1 and 2) and the drain line (pin 3) were required. Therefore, a female XLR connector (Figure A.28 – a) was used at the entrance of the amplifier circuit. The XLR connector metal shell was directly soldered to the ground, as previously indicated in Figure A.27. After total gain was obtained, the amplified signal (amplifier output) left the system through a regular BNC cable, whose centre pin delivered the amplified signal, while the outside part was the signal reference (Figure A.28 – b).

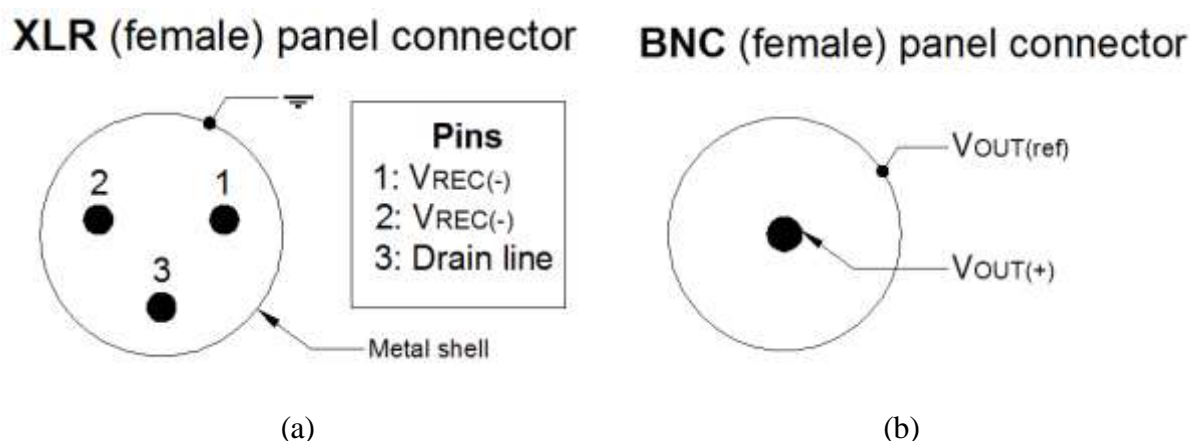


Figure A.28: Connector pins diagram – (a) XLR panel connector receiving the amplifier input; (b) BNC connector delivering the amplifier output

A.3.3 First gain step

In the present study, the IC INA116 responsible for the first gain step type was the 16-pin plastic DIP (dual in-line packages). This is an instrumentation amplifier, whose specifications are presented in Chart A.4. INA116 is equivalent to 3 op-amp, which allows gains from 1 to 1,000 times by simply exchanging one resistor (R_{G1}). The very low input bias current is very effective to prevent additional errors; and the input bias ground maximum value (± 25 fA) is usually associated to high temperatures (85°C). Additionally, the guard ports on both inputs can be helpful in maintaining low input bias when connecting the shield of the input cable to guard ports.

Chart A.4: IC INA116 specifications

Input bias current	± 3 fA (typical) to ± 25 fA (max)
Offset voltage	2 mV (max)
Common-mode rejection	86 dB (Gain of 100x)
Input over-voltage protection	± 40 V
Frequency response – Bandwidth 3dB	70 kHz (Gain of 100x)
Output voltage positive	$(V_{p(+)} - 1)$ V
Output voltage negative	$(V_{p(-)} + 0.2)$ V
Power supply	± 4.5 to ± 18 V

(source: BURR-BROWN®, 1994)

Although the input bias current is very low for this IC, a return path is necessary for proper operation (BURR-BROWN®, 1994). The alternative was to add resistors with high resistive capacity in parallel to each input and ground (Figure A.29 – a). The case presented in the datasheet illustrates a ceramic transducer (very similar to BE) with a 100 M.ohms resistor. Because resistors as higher as the example are difficult find nowadays, a smaller resistor ($R_1=10$ M.ohms) was tested on the protoboard, producing goo results. Therefore, in order to provide an input bias current return path, 10 M.ohms resistors (R_1) were connected in parallel with each input and ground (Figure A.30).

Despite the fact that batteries were used as power supply, 2 ceramic capacitors ($C_1=100$ nF) were used as decoupling capacitors, which should prevent noise from entering the system (Figure A.30). Those capacitors were connected in parallel with (and as close as possible to)

the power supply pins and the real ground, as illustrated by C1 in Figure A.29 – (b) (BURR-BROWN®, 1994).

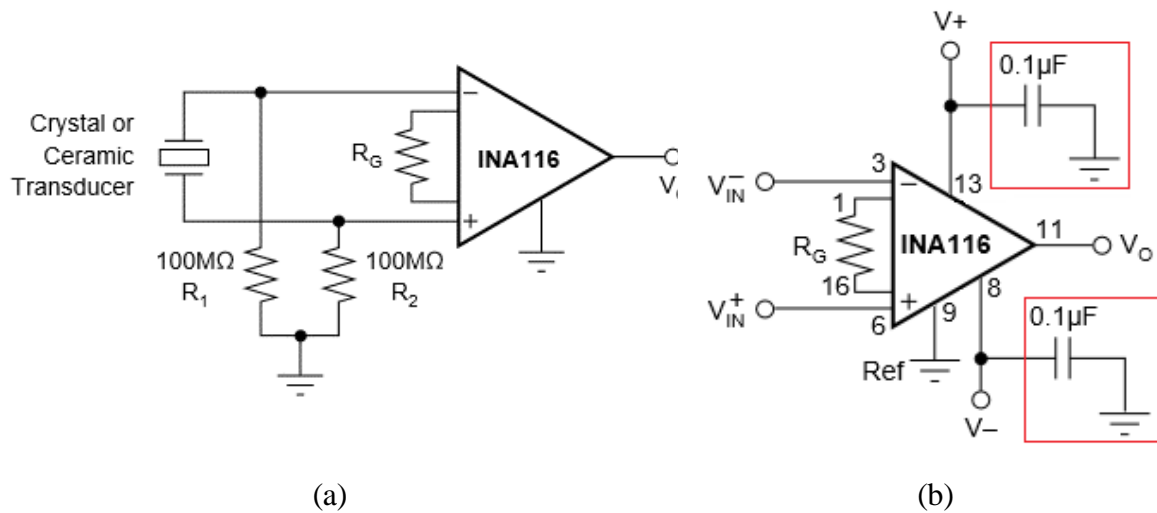


Figure A.29: Datasheet suggestions – (a) input bias current return path with a high resistor; (b) addition of decoupling capacitors in order to block noise
(based on: BURR-BROWN®, 1994)

An 18-pin IC DIP hole round socket was used to accommodate the IC INA116. According to the datasheet (BURR-BROWN®, 1994), sockets contribute with additional gain errors when reaching gains of 100x or greater. However, as the chosen gain was 50x, this gain was affected by socket use. Nonetheless, to reduce leakage, amplifier input requires “grounding” along all the way between the source signal and the input amplifier, which can be achieved by connecting the shield to the guard ports.

As mentioned before, the input signal entered the amplifier circuit through an XLR connector; the wires were then connected to the board using two 2-wire interface modules (Figure A.30). Two entrances were used for the input signal, while the other two were used by the drain line that was divided in half. Before reaching the INA116 ports, R1 resistors provided the input current path. After that, the signal was amplified, and its gain was dependant on the exchangeable resistor (R_{G1}) connected to another 2-wires interface modules. The amplified signal left the IC through the pin 11 in respect to the reference pin 9.

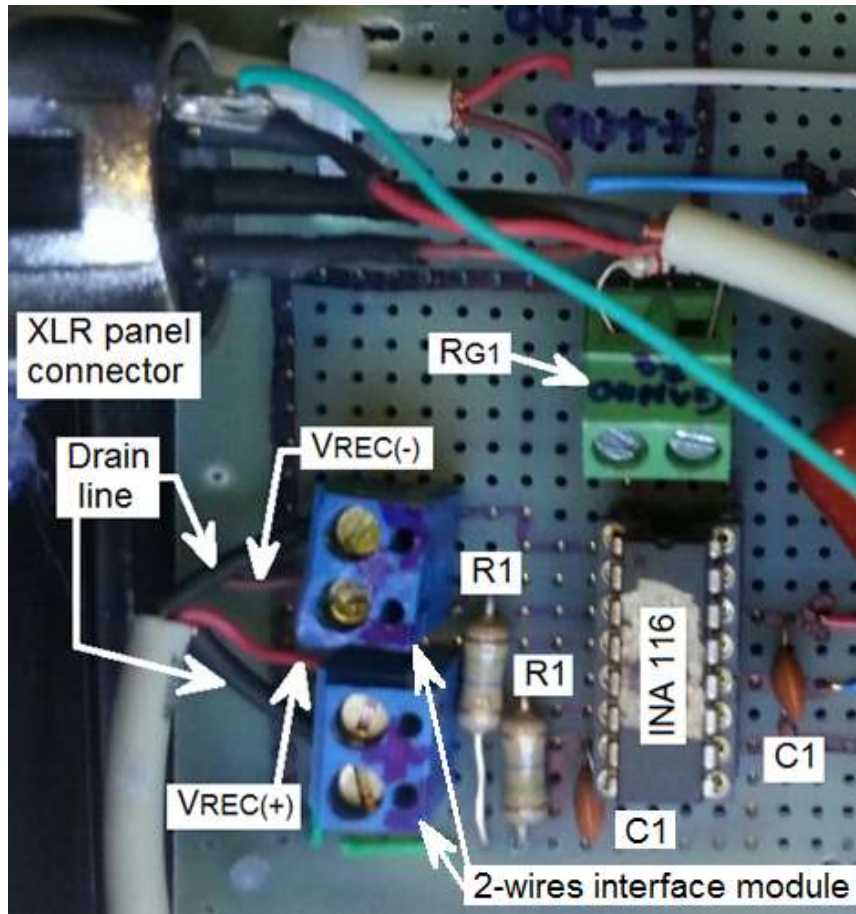


Figure A.30: BE input signal entrance and first gain step soldered elements

A.3.4 Second gain step

After the first amplification, the signal passed through a series connected polyester capacitor ($C_2=100$ nF), which worked to uncouple any DC component that may have been added to the signal (Figure A.31). This uncoupling process before the second gain stage is extremely important because the DC component would also be amplified in case it reached the amplifier. Depending on the magnitude of the DC component and the chosen gain, the output line may be saturated.

The second gain step used a simple op-amp: the dual operational TL082 amplifier. However, only part of the dual amplifier was used. An IC DIP hole round socket with 8 pins was also used to accommodate the op-amp. As op-amp are regularly used in basic electronic, the specifications of the TL082 are going to be omitted. Although the use of the inverter input results in an inversion of the output signal, this input (rather than the non-inverter) accomplishes more stable results.

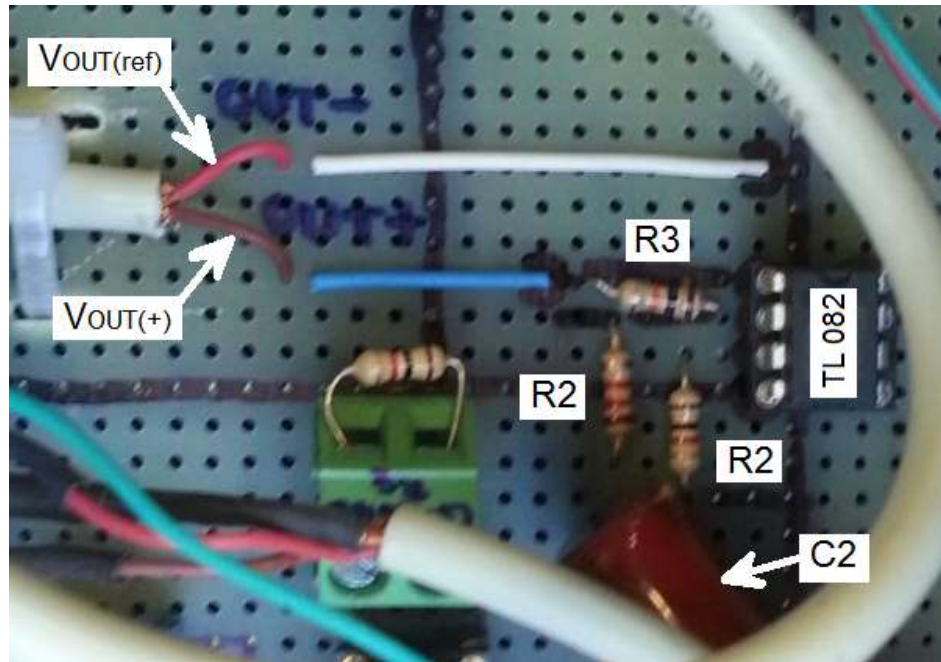


Figure A.31: BE second gain step soldered elements

The gain was determined by the ratio between R3 (10 k.ohm) and the R2 (1 k.ohm) connected to the inverter input. The other R2 resistor connected to the non-inverter input had the objective to reduce the additional offset voltage (that might result in error). This resistor should be equivalent to the 2 parallel-connected resistors (R2 and R3) associated to the inverter input. As these 2 resistors provided the same voltage drop as the R2 connected to the non-inverter input, a bias compensation occurred, preventing any extra offset voltage.

At the end of the second gain step, the signal was amplified 500x, which was enough to reach the vertical resolution of the oscilloscope. The amplified signal was entirely delivered in a single exit, “V_{OUT(+)}”, and used the ground as signal reference “V_{OUT(ref)}” (Figure A.31). After that, both wires were connected to the BNC connectors (Figure A.28 – b) and, then, to the oscilloscope, allowing to be compared with the theoretical BE driven signal.

APPENDIX A.4 - MACHINED PARTS

This item regards all machined elements involved in BE fabrication and housing, or used during tests and calibration. Pictures of the final appearance of all parts are going to be presented in this item, while detailed plans are presented in Appendix C. All machined parts were manufactured by specialists.

A.4.1 BE mould

The BE mould used to encapsulate the piezoceramic is composed by two parts: the bottom (on left side of the figure) and top part (right side of the figure) (Figure A.32). Stainless steel was used to fabricate a durable and non-porous mould, with two 2 big screws to hold the two parts together. While the top part has through holes for the screws, the bottom part has the threads.



Figure A.32: Bi-parted BE encapsulating mould

A.4.2 BE metal case

The BE metal case is presented in Figure A.33. As the triaxial BE pair would be subjected to water under high pressures, they were also fabricated in stainless steel to be durable and waterproof. The threaded part of the case had no practical use during this study, and may be removed for future studies.



Figure A.33: BE metal case

A.4.3 Metal BE templates

A pair of metal templates (Figure A.34) were fabricated to imitate BE geometry. The initial idea was to compact specimens with one template at the bottom of the mould, after which the other template would be pushed into the top of the specimen. However, practical limitations demonstrated that the time required to remove the template from the specimen was too long and the idea was eventually abandoned.



Figure A.34: Pair of metal templates

A.4.4 Bench pedestal

Bench pedestals (Figure A.35) were used to house the BE transmitter and receiver. Pedestals were made from a nylon bar 800 mm long with 50 mm in diameter. Pieces 100 mm long were cut, and holes were made to house the BE module. An oblique lateral passage hole was made for the BE cables (Figure A.35 – a). Moreover, a small cavity on the top of the pedestal (red arrow in Figure A.35 – b) was added to assist in the removal of the BE by inserting a thin metal wire (paper clip).

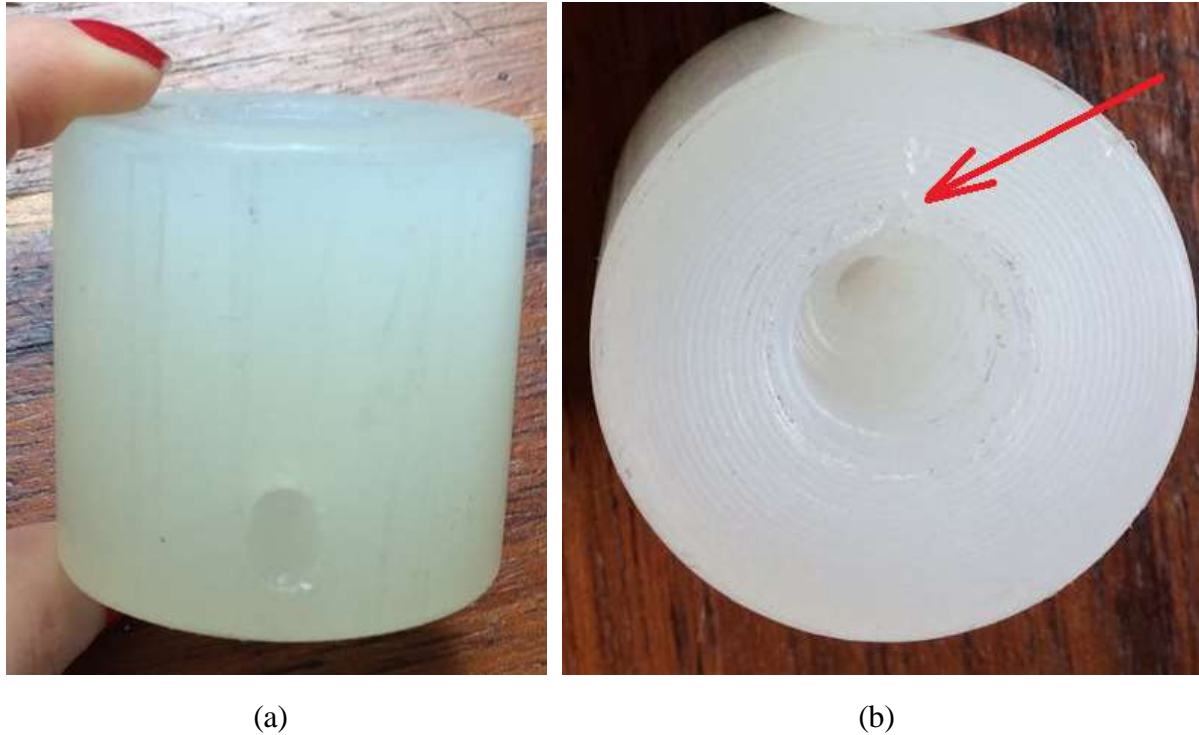


Figure A.35: Bench pedestal – (a) oblique view showing the passage hole for BE cables; (b) top view showing the cavity used for pulling out the BE module

A.4.5 Triaxial top cap and pedestal

To install a BE pair inside the triaxial chamber, a new top cap and pedestal had to be designed. The pedestal (Figure A.36 – a) was made in stainless steel, while the top cap was fabricated in acrylic (Figure A.36 – b) to be as light as possible, in conformance with ASTM D7181 (ASTM, 2011).

The top cap and pedestal have only one water drainage line. The holes for the drainage lines and BE cables were designed to be sealed by NPT threads. Moreover, BE cables sealing was obtained using a pair of o-rings in each element. As discussed before, because of the fragile nature of the acrylic top cap, grooves were made in the BE metal case and, therefore, exclusively in the case of the triaxial BE transducer. The grooves were made in the internal surface of the metal pedestal where the BE would be housed. The pedestal had four through holes used for fixation to the triaxial chamber with 4 screws. The top cap was connected to the triaxial chamber through its drainage line and BE cables.

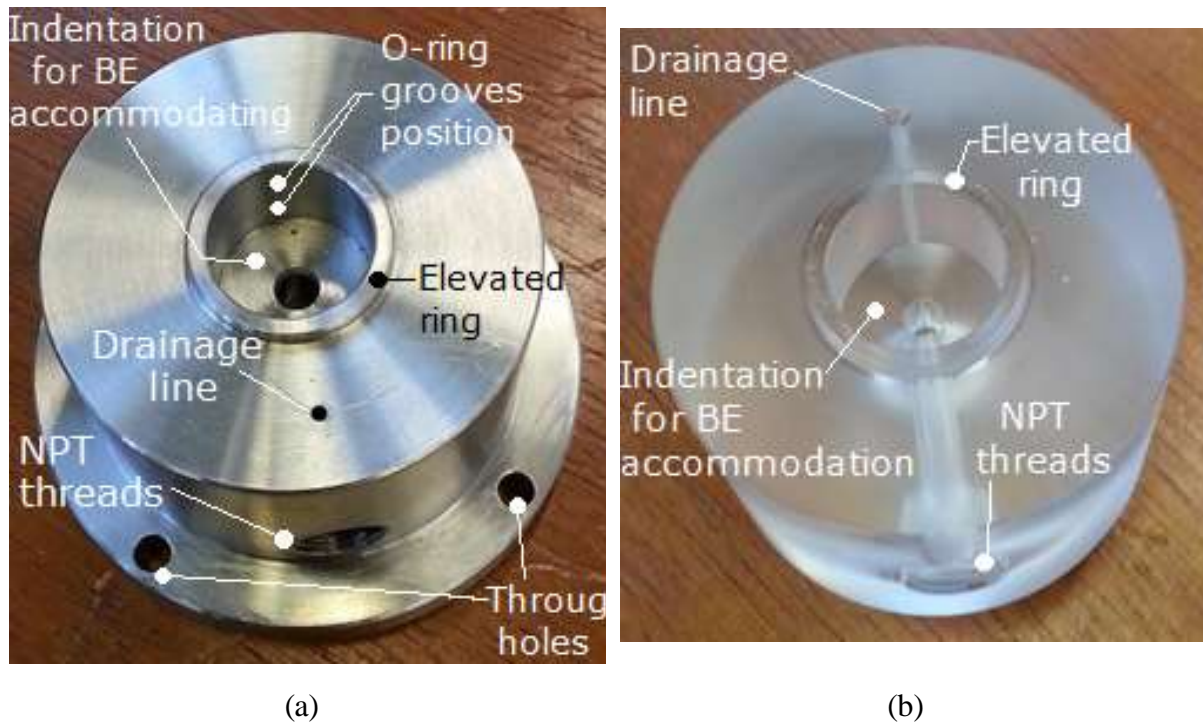


Figure A.36: Machined triaxial parts with BE openings – (a) stainless steel pedestal; (b) acrylic top cap

Elevated rings were machined around the BE module entrance to permit the porous disk seating. As both parts were fabricated before the porous disks, their elevated rings were slightly higher than the porous disks and had to be reduced to a compatible height. Moreover, because the elevated rings were reduced, the floor of the top cap cavity also had to be lowered, and a piece of the threaded portion of the metal case had to be removed to fully accommodate the BE module inside the top cap.

A.4.6 Porous disks

A pair of porous disks were specially fabricated in order to be accommodated around the BE triaxial pair (Figure A.37). A pair of 50 mm round x 3 mm thick rings made of sintered copper was initially acquired. Then the central hole (to accommodate BE) was carefully drilled its centre. A smooth surface was required in order to not damage the rubber membrane.



Figure A.37: Porous disk accommodated on the triaxial pedestal

A.4.7 Calibration rods

Two calibration rods were fabricated to evaluate signal quality and the effects of the coupling paste used to cement BE to the soil (Figure 3.24). Briefly, one rod was fabricated with two slots in opposite sides to introduce the BE module, while the other rod has circular cavities on both faces as well. They were made from the same nylon dowel used for bench pedestals with approximately 90 mm high.

APPENDIX B – MATLAB® SCRIPT

```

% Opens and plots files from a format '.csv' saved straight from an
%oscilloscope.%
%-----%
%-----%
%Initial comments:%
% I. The path to the directory containing the data to be processed must be
%inserted manually by changing the path contained into the variable 'dir';%
% II. The current folder of Desktop Environmental needs to be changed in
% order to match the directory path, or at least, the root directory;%
% III. The label of received signals must be manually inserted, go to item
% 4.3.4 and re-write each frequency inside the 'annotation' commands.%
%-----%
% 1. Providing initial information regarding specimen and test conditions %
%The user is required to answer prompts which will feed the script with
%essential data%

prompt=('\\n What is the initial folder to be opened?\\n Only the last 3
numbers are required, e.g. 001 or 102.\\n');
N1=input(prompt);
prompt=('What is the final folder to be opened?\\n Only the last 3 numbers
are required, e.g. 001 or 102.\\n');
N2=input(prompt);

prompt=('What is the shape of the input wave?\\n (Sine=1; Square=2) -
Please, provide number 1 or 2.\\n');
if input(prompt)==1
    shape_wave=char('SN');
else shape_wave=char('SQ');
end;
prompt=('Which kind is the wave? Continuous or pulse(s)? \\n (Cont.=0;
Pulse(s)=1) - Please, provide number 0 or 1.\\n');
if input(prompt)==0
    input_pulses=char('0C');
else prompt=('How many pulses had been sent? \\n (1 pulse= 1; 3 pulses= 3;5
pulses= 5)\\n');
    input_pulses=sprintf('%ldP',input(prompt));
end;
prompt=('Please, provide information about the tested material. \\nType one
of the following numerical option for the tested material: \\n- Osorio sand
(0); \\n- Calibration cylinder (1); and \\n- None/direct contact (2).\\n');
input_a=input(prompt);
if input_a==0
    prompt=('Provide \\eta/C_{iv} as two integer numbers\\n(e.g. if
\\eta/C_{iv}=39.01, then the input should be "39").\\n');
    neta_civ=input(prompt);
    prompt=('Provide the density as the following numerical input: \\n-
Loose (1); \\n- Dense (2); and \\n- Medium (3).\\n');
    input_b=input(prompt);
    if input_b==1
        density=('LO');
    elseif input_b==2
        density=('DE');
    else density=('ME');
    end;
    tested_mat=sprintf('OS%02d%2s', neta_civ, density);
elseif input_a==1
    prompt=('Please, specify which calibration cylinder was used: \\nthe one
with circular bore (1) or the one with slots (2).\\n');
    if input(prompt)==1
        tested_mat=('NY00CB');

```

```

        else tested_mat=('NY00SL');
        end;
else ultras_rho_kgperm3=0;
    ultras_length_m=0;
    delta_t_ultras=1;
    tested_rho_kgperm3=0;
    tested_length_m=0;
    real_neta_civ=0;
    prompt=('Please, specify whether the signal was amplified (1) or not
(2).\n');
    if input(prompt)==1
        tested_mat=('NN00AM');
    else tested_mat=('NN00NA');
    end;
end;
prompt=('Please, provide the tests data in a format "ddmmyy". \n');
tests_data=sprintf('%06d', input(prompt));
prompt=('Please, provide the respective curing day. If there is no cure,
input should be zero.\n');
curing_day=sprintf('%02dD', input(prompt));
summary_file=strcat(shape_wave, input_pulses, '_', tested_mat, '_',
tests_data, '_', curing_day);

prompt=('Please, provide acquisition mode:\n- Sample mode (SAMP);\n- Peak
detect mode (PEAK); and\n- Average mode (AVER).\n');
acq_mode=input(prompt, 's');
prompt=('Please, provide number of points during data acquisition.\n');
number_acq=sprintf('%02d', input(prompt));
prompt=('Please, specify if the electrical coupling (oscilloscope)\n was
current or alternate current ("CC" or "CA").\n');
elect_coup=input(prompt, 's');
prompt=('Please, provide the amplification gain (e.g. 100, 500...).\n');
amp_gain=input(prompt);

if input_a==2
    tested_length_m=0;
else prompt=('Please, provide the natural specific mass of the specimen in
kg/m^3.\n');
    tested_rho_kgperm3=input(prompt);
    prompt=('Please, provide the distance between the tips of BEs, in
centimenters.\n');
    tested_length_m=(input(prompt))/100;
    prompt=('Is there any ultrasound measurement for the same material?
\nPlease, press "1" for yes, and "2" for no. \n');
    if input(prompt)==2
        ultras_length_m=0;
    else prompt=('What was the measured time obtained by ultrasound (in
micro.sec)?\n');
        delta_t_ultras=input(prompt);
        prompt=('What was the distance between ultrasound transducers (in
cm)?\n');
        ultras_length_m=(input(prompt))/100;
        if input_a==1
            ultras_rho_kgperm3=tested_rho_kgperm3;
            real_neta_civ=0;
        else prompt=('Whats was the natural specific mass of the specimen
tested by ultrasound (in kg/m^3)?\n');
            ultras_rho_kgperm3=input(prompt);
            prompt=('For calculation purposes, whats was the real
\eta/C_{iv} for the specimen tested by BEs? \n');
            real_neta_civ=input(prompt);

```

```

        end;
    end;
end;

shear_mod_ultras=ultras_rho_kgperm3*((ultras_length_m/(delta_t_ultras/(10^6
)))^2);
delta_t_corr=(sqrt(tested_rho_kgperm3*(tested_length_m^2)/shear_mod_ultras
)*10^6;
shear_mod_Consoli2012=((17.504*10^9)*((real_neta_civ)^-0.99));
delta_t_Consoli2012=(sqrt((tested_rho_kgperm3)*(tested_length_m^2)/shear_mo
d_Consoli2012))*10^6;
shear_mod_Consoli2009=((10.086*10^9)*((real_neta_civ)^-0.79));
delta_t_Consoli2009=(sqrt((tested_rho_kgperm3)*(tested_length_m^2)/shear_mo
d_Consoli2009))*10^6;
%
%
% 2. Titles and information regarding Microsoft® excel spreadsheet that
will be
%generated%

title_l1={'RAW DATA', '', '', 'MANIPULATED DATA', '', 'FFT', '', '', '', ...
'', 'DATA SUMMARY', '', '', '', 'INFORMATION SUMMARY'};
title_l2={'Time', 'CH1 - Voltage', 'CH2 - Voltage', 'Time', ...
'CH2 - Cor. Volt.', 'FFT Freq. - CH1', 'Magn. FFT - CH1', ...
'FFT Freq. - CH2', 'Magn. FFT - CH2'};
sum_colland2={'Time', 'dt (\mus)'; '', 't_{max,peak} (\mus)'; '', ...
't_{min,peak} (\mus)'; '', '\Deltat_{ultras.} (\mus)'; 'Voltage', ...
'V_{max} (V)'; 'CH1', 'V_{min} (V)'; 'Voltage', 'V_{max} (V)'; ...
'CH2', 'V_{min} (V)'};
info_sum_coll={'Tested material'; 'Tests data'; 'Curing day'; ...
'Shape of wave'; 'Input pulses'; 'Input freq. (kHz)'; ...
'Acquisition mode'; 'Number os points - acquis.'; ...
'Electrical coupling'; 'Gain (x)'; 'Vert. scale (CH2)'};

letters1=['A'; 'B'; 'C'; 'D'; 'E'; 'F'; 'G'; 'H'; 'I'; 'J'; 'K'; ...
'L'; 'M'; 'N'; 'O'; 'P'; 'Q'; 'R'; 'S'; 'T'; 'U'; 'V'; 'W'; ...
'X'; 'Y'; 'Z'];
%
%
% 3. Opening '.csv' files and writing a spreadsheet (Microsoft® excel) with
different sheets%
    %Remembering: the user is required to provide the folder path (which
    %could be in a flash drive).%

for nn=1:(N2-N1+1);
    step0=nn;
    step1=N1+nn-1;
    dir= strcat('D:\BE Data\BE bench tests\CP4 - BE1\Day
01\SN1P', (sprintf('ALL0%03d', step1)), '/');
    % 3.1 - Opening channel 1 (oscilloscope): input or sent signal (ss)%
    name_file=sprintf('F0%03dCH1.csv', step1);
    local_data= strcat(dir,name_file);
    channel1=dlmread(local_data, ',', 0, 3);    % Vector of channel 1
                                                %including time,
amplitude,
                                                %and one empty column.%
    t= (channel1(:, 1)-channel1(1))*10^6;    % Returns time vector
(t)

```

```

                                                                    %in micro.s.%
dt=t(2)-t(1);
sent_signal= channel1(:,2);                                     % Returns the amplitude
                                                                    %vector of the sent

signal

                                                                    % (ss) in volts.%
max_ss= max(sent_signal);                                     %Max. amplitude of ss.%
min_ss= min(sent_signal);                                     %Min. amplitude of ss.%
totalamp_ss= abs(max_ss - min_ss);
ss= sent_signal;
position_max0_ss=find(sent_signal==max_ss,1,'first');
position_min0_ss=find(sent_signal==min_ss,1,'first');
position_max2_ss=find(sent_signal==max_ss,1,'last');
position_min2_ss=find(sent_signal==min_ss,1,'last');
position_max_ss=round((position_max0_ss+position_max2_ss)/2);
position_min_ss=round((position_min0_ss+position_min2_ss)/2);

t_max_ss=t(position_max_ss,1); %Respective time to max.
t_min_ss=t(position_min_ss,1); %and min. ampl. of ss.%
freq_ss=round((1/((t_min_ss-t_max_ss)*2)/(10^6)))/10^3 %Freq. in
kHz.%

t_peak_displac=t_max_ss-250;
time_reset_peak=t-t_peak_displac;
%-----%
% 3.2 - Opening channel 2 (oscilloscope): received signal(rs)%
name_file=sprintf('F0%03dCH2.csv', step1);
local_data= strcat(dir,name_file);
channel2=dlmread(local_data, ',', 0, 3);
received_signal= channel2(:,2);                               % Returns the amplitude
                                                                    %vector of the rec.

signal

                                                                    % (rs) in volts.%

max_rs= max(received_signal);
min_rs= min(received_signal);
totalamp_rs= abs(max_rs - min_rs);
%-----%
% 3.2.1 - Verification of a good scale for presenting the rs %
ratio_signals=round(totalamp_ss/totalamp_rs);
first100= received_signal(1:100,1);
vertical_offset=mean(first100); % Reduces floatation of

signal;%
rs_zero_offset= received_signal-vertical_offset;
rs_amp_corrected= (received_signal-vertical_offset)*ratio_signals;
%-----%
% 3.3 - Writing titles on a spreadsheet for each individual frequency
% in the respective sheet.%
title_l3= {'(\mus)', '(V)', '(V)', '(\mus)', ...
           (strcat('(', sprintf('%3d',ratio_signals), '*V'))),
' (kHz)', ...
           '-', '(kHz)', '-'};
xlswrite(summary_file, title_l1, sprintf('%03dkHz', freq_ss),
'A1:O1');
xlswrite(summary_file, title_l2, sprintf('%03dkHz', freq_ss),
'A2:I2');
xlswrite(summary_file, title_l3, sprintf('%03dkHz', freq_ss),
'A3:I3');
xlswrite(summary_file, sum_colland2, sprintf('%03dkHz', freq_ss),
'K2:L9');
xlswrite(summary_file, info_sum_coll, sprintf('%03dkHz', freq_ss),
'O2:O12');
%-----%

```

```

% 3.4 - Writing data for individual frequency on the respective sheet%
col_data= [t, ss, rs_zero_offset, time_reset_peak,
rs_amp_corrected];
xlswrite(summary_file, col_data, sprintf('%03dkHz', freq_ss),
'A4:E2504');
col_data_sum=[dt; t_max_ss; t_min_ss; delta_t_corr; max_ss; min_ss;
max_rs; min_rs];
xlswrite(summary_file, col_data_sum, sprintf('%03dkHz', freq_ss),
'M2:M9');
col_info_sum=vertcat(sprintf('%6s', tested_mat), sprintf('%6s',
tests_data), sprintf('%6s', curing_day), sprintf('%6s', shape_wave),
sprintf('%6s', input_pulses), sprintf('%6s', freq_ss), sprintf('%6s',
acq_mode), sprintf('%6s', number_acq), sprintf('%6s', elect_coup),
sprintf('%6s', amp_gain));
xlswrite(summary_file, col_info_sum, sprintf('%03dkHz', freq_ss),
'P2:P11');
xlswrite(summary_file, ratio_signals, sprintf('%03dkHz', freq_ss),
'P12:P12');
%-----%
% 3.5 - Writing data for individual frequency on the summary sheet%
% 3.5.1 - Placing data in successive pack of columns%
start_col=3*nn-2;
final_col=start_col+2;
flag1=1;
if (start_col<=104) && (final_col<=104)
    if (start_col<=78) && (final_col<=78)
        if (start_col<=52) && (final_col<=52)
            if (start_col>26) && (final_col>26)
                start_coll=start_col-26;
                final_coll=final_col-26;
                ex_interv=sprintf('%2s4:%2s2504', strcat('A',
letters1(start_coll)), strcat('A', letters1(final_coll)));
                ex_titles=sprintf('%2s1:%2s3', strcat('A',
letters1(start_coll)), strcat('A', letters1(final_coll)));
                interv_edge=strcat('A', letters1(final_coll));
            elseif (start_col<=26) && (final_col>26)
                final_coll=final_col-26;
                ex_interv=sprintf('%1s4:%2s2504',
letters1(start_col), strcat('A', letters1(final_coll)));
                ex_titles=sprintf('%1s1:%2s3', letters1(start_col),
strcat('A', letters1(final_coll)));
                interv_edge=strcat('A', letters1(final_coll));
            else ex_interv=sprintf('%1s4:%1s2504',
letters1(start_col), letters1(final_col));
                ex_titles=sprintf('%1s1:%1s3', letters1(start_col),
letters1(final_col));
                interv_edge=letters1(final_col);
                flag1=0;
            end;
        elseif (start_col<=52) && (final_col>52)
            start_coll=start_col-26;
            final_coll=final_col-52;
            ex_interv=sprintf('%2s4:%2s2504', strcat('A',
letters1(start_coll)), strcat('B', letters1(final_coll)));
            ex_titles=sprintf('%2s1:%2s3', strcat('A',
letters1(start_coll)), strcat('B', letters1(final_coll)));
            interv_edge=strcat('B', letters1(final_coll));
        else (start_col>52) && (final_col>52)
            start_coll=start_col-52;
            final_coll=final_col-52;

```



```

        ex_interv=sprintf('%2s4:%2s2504', strcat('B',
letters1(start_coll)), strcat('B', letters1(final_coll)));
        ex_titles=sprintf('%2s1:%2s3', strcat('B',
letters1(start_coll)), strcat('B', letters1(final_coll)));
        interv_edge=strcat('B', letters1(final_coll));
    end;
elseif (start_col<=78) && (final_col>78)
    start_coll=start_col-52;
    final_coll=final_col-78;
    ex_interv=sprintf('%2s4:%2s2504', strcat('B',
letters1(start_coll)), strcat('C', letters1(final_coll)));
    ex_titles=sprintf('%2s1:%2s3', strcat('B',
letters1(start_coll)), strcat('C', letters1(final_coll)));
    interv_edge=strcat('C', letters1(final_coll));
else (start_col>78) && (final_col>78)
    start_coll=start_col-78;
    final_coll=final_col-78;
    ex_interv=sprintf('%2s4:%2s2504', strcat('C',
letters1(start_coll)), strcat('C', letters1(final_coll)));
    ex_titles=sprintf('%2s1:%2s3', strcat('C',
letters1(start_coll)), strcat('C', letters1(final_coll)));
    interv_edge=strcat('C', letters1(final_coll));
end;
elseif (start_col<=104) && (final_col>104)
    start_coll=start_col-78;
    final_coll=final_col-104;
    ex_interv=sprintf('%2s4:%2s2504', strcat('C',
letters1(start_coll)), strcat('D', letters1(final_coll)));
    ex_titles=sprintf('%2s1:%2s3', strcat('C',
letters1(start_coll)), strcat('D', letters1(final_coll)));
    interv_edge=strcat('D', letters1(final_coll));
else (start_col>104) && (final_col>104)
    start_coll=start_col-104;
    final_coll=final_col-104;
    ex_interv=sprintf('%2s4:%2s2504', strcat('D',
letters1(start_coll)), strcat('D', letters1(final_coll)));
    ex_titles=sprintf('%2s1:%2s3', strcat('D',
letters1(start_coll)), strcat('D', letters1(final_coll)));
    interv_edge=strcat('D', letters1(final_coll));
end;

%-----%
% 3.5.2 - Writing data on the "Summary data" sheet%
sum_data=[time_reset_peak,ss, rs_amp_corrected];
sum_titles={sprintf('%11s', (sprintf('%3dkHz',freq_ss))),
sprintf('%11s', ''), sprintf('%11s', '');...
    sprintf('%11s', 'Time'), sprintf('%11s', 'Volt. - CH1'),
sprintf('%11s', 'Volt. - CH2');...
    sprintf('%11s', '(Amus)'), sprintf('%11s', '(V)'),
sprintf('%11s', (strcat('(', (sprintf('%3d',ratio_signals)), '*V')))};
xlswrite(summary_file, sum_data, 'summary_data', ex_interv);
xlswrite(summary_file, sum_titles, 'summary_data', ex_titles);
%-----%
% 3.6 - Writing data corresponding to the resonance response%
% 3.6.1 - Placing data%
start_col2=nn+1;
if start_col2<=104
    if start_col2<=78
        if start_col2<=52
            if start_col2>26
                start_col2=start_col2-26;

```

```

        col_data2=sprintf('%2s1:%2s4', strcat('A',
letters1(start_col2)), strcat('A', letters1(start_col2)));
        elseif start_col2<=26
            col_data2=sprintf('%2s1:%2s4',
letters1(start_col2), letters1(start_col2));
        end;
        elseif start_col2>52
            start_col2=start_col2-27;
            col_data2=sprintf('%2s1:%2s4', strcat('B',
letters1(start_col2)), strcat('B', letters1(start_col2)));
        end;
        elseif start_col2>78
            start_col2=start_col2-27;
            col_data2=sprintf('%2s1:%2s4', strcat('C',
letters1(start_col2)), strcat('C', letters1(start_col2)));
        end;
        elseif start_col2>104
            start_col2=start_col2-27;
            col_data2=sprintf('%2s1:%2s4', strcat('D',
letters1(start_col2)), strcat('D', letters1(start_col2)));
        end;
    %-----%
    % 3.6.2 - Writing data on the "Resonance resp" sheet%
    col_title={'Freq. (kHz)'; 'V_{max} (V)'; 'V_{min} (V)'; '\Delta V
(V)'};
    resonance_resp=[freq_ss; max_rs; min_rs; totalamp_rs];
    xlswrite(summary_file, col_title, 'resonance_resp', 'A1:A4');
    xlswrite(summary_file, resonance_resp, 'resonance_resp',
col_data2);
    %-----%
end;
%-----%
% 4. Plotting signals %
% 4.1 - Reading spreadsheet%
if flag1==0
    sum_sheet=xlsread(summary_file, 'summary_data',
sprintf('A4:%1s2503',interv_edge));
else sum_sheet=xlsread(summary_file, 'summary_data',
sprintf('A4:%2s2503',interv_edge));
end;
%-----%
% 4.2 - Preparing data for plotting%
X1=sum_sheet((4:2403), 1);
Y1=(sum_sheet((4:2403), 2))*1.5;
Y2=(sum_sheet((4:2403), 3))-30;
X2=sum_sheet((4:2403), 4);
Y3=(sum_sheet((4:2403), 5))*1.5;
Y4=(sum_sheet((4:2403), 6))-50;
X3=sum_sheet((4:2403), 7);
Y5=(sum_sheet((4:2403), 8))*1.5;
Y6=(sum_sheet((4:2403), 9))-70;
X4=sum_sheet((4:2403), 10);
Y7=(sum_sheet((4:2403), 11))*1.5;
Y8=(sum_sheet((4:2403), 12))-90;
X5=sum_sheet((4:2403), 13);
Y9=(sum_sheet((4:2403), 14))*1.5;
Y10=(sum_sheet((4:2403), 15))-110;
X6=sum_sheet((4:2403), 16);
Y11=(sum_sheet((4:2403), 17))*1.5;
Y12=(sum_sheet((4:2403), 18))-130;
X7=sum_sheet((4:2403), 19);

```

```

Y13=(sum_sheet((4:2403), 20))*1.5;
Y14=(sum_sheet((4:2403), 21))-150;
X8=sum_sheet((4:2403), 22);
Y15=(sum_sheet((4:2403), 23))*1.5;
Y16=(sum_sheet((4:2403), 24))-170;
%-----%
% 4.3 - Plotting data%
figure (2);
    h(1)=plot(X1, Y2, '-k', 'LineWidth',2);
    hold on;
        h(2)=plot(X2, Y4, '-k', 'LineWidth',2);
        h(3)=plot(X3, Y6, '-k', 'LineWidth',2);
        h(4)=plot(X4, Y8, '-k', 'LineWidth',2);
        h(5)=plot(X5, Y10, '-k', 'LineWidth',2);
        h(6)=plot(X6, Y12, '-k', 'LineWidth',2);
        h(7)=plot(X7, Y14, '-k', 'LineWidth',2);
        h(8)=plot(X8, Y16, '-k', 'LineWidth',2);

        h(9)=plot(X1, Y1, '-.k', 'LineWidth',1);
        h(10)=plot(X2, Y3, '--', 'Color', [0.5 0.5 0.5], 'LineWidth',1.2);
        h(11)=plot(X3, Y5, ':k', 'LineWidth',1);
        h(12)=plot(X4, Y7, '-', 'Color', [0.5 0.5 0.5], 'LineWidth',1.2);
        h(13)=plot(X5, Y9, '--k', 'LineWidth',1);
        h(14)=plot(X6, Y11, ':', 'Color', [0.5 0.5 0.5], 'LineWidth',1.2);
        h(15)=plot(X7, Y13, '-k', 'LineWidth',1);
        h(16)=plot(X8, Y15, '-', 'Color', [0.5 0.5 0.5], 'LineWidth',1.2);
%-----%
% 4.3.1 - Plotting predictions an UPV measurements%
peak0=[250 40; 250 -180];
peak_ultras= [(272.085+delta_t_corr) 40; (272.085+delta_t_corr) -
180];
peak_Consoli2012= [(272.085+delta_t_Consoli2012) 40;
(272.085+delta_t_Consoli2012) -180]
peak_Consoli2009= [(272.085+delta_t_Consoli2009) 40;
(272.085+delta_t_Consoli2009) -180]
first_peak_arrival=[300 40; 300 -180];
h(17)=plot((peak0(:,1)), (peak0(:,2)), '-k', 'LineWidth',1);
h(20)=plot((first_peak_arrival(:,1)), (first_peak_arrival(:,2)),
':b', 'LineWidth',2);
h(21)= plot((peak_Consoli2009(:,1)), (peak_Consoli2009(:,2)), '-
.m', 'LineWidth',1.3);
%-----%
% 4.3.2 - Plotting the legend box%
if input_a==0
    h(18)=plot((peak_ultras(:,1)), (peak_ultras(:,2)), '--r',
'LineWidth',2);
    h(19)=plot((peak_Consoli2012(:,1)), (peak_Consoli2012(:,2)), '-
-k', 'LineWidth',1.5);
    legend0=legend([h(1) h(17) h(18) h(19) h(21) h(20)], 'Received
signals', 't_{0,peak}', '\Deltat_{ultras}', 'Consoli \itet \ital. (2012)',
'Consoli \itet \ital. (2009)', 'First-peak arrival', 'Location',
'NorthEast', 'FontSize', 6);
elseif input_a==1
    h(18)=plot((peak_ultras(:,1)), (peak_ultras(:,2)), '--r',
'LineWidth',2);
    legend0=legend([h(1) h(17) h(18) h(21) h(20)], 'Received
signals', 't_{0,peak}', '\Deltat_{ultras}', 'Consoli \itet \ital.
(2009)', 'First-peak arrival', 'Location', 'NorthEast', 'FontSize', 6);
else legend0=legend([h(1) h(17)], 'Received signals', 't_{0,peak}',
'Location', 'NorthEast', 'FontSize', 6);
end;

```

```

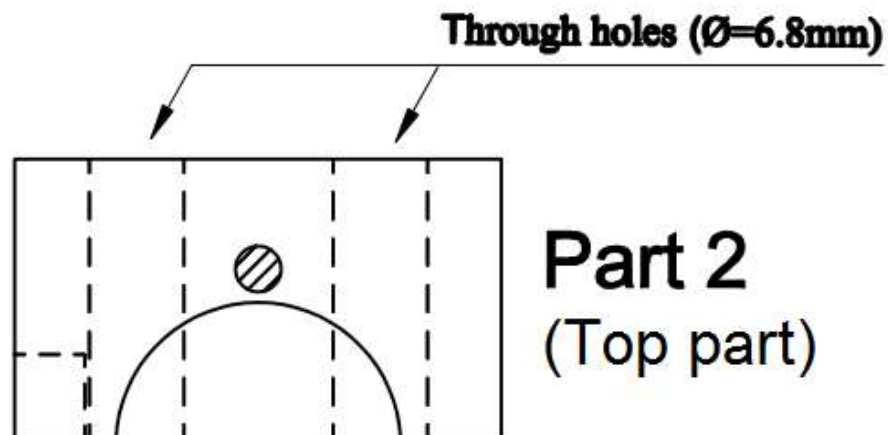
%-----%
% 4.3.3. - Limiting and specifying axes%
hx=xlabel('Time (micro.s)', 'FontWeight', 'bold');
hy=ylabel('Amplitude (arbitrary V scale)', 'FontWeight', 'bold');
set(gcf, 'position', [.13 0.1 1 .8])
set(gca, 'Yticklabel', [])
ylim([-180 40]);
xlim([100 1000]);
%-----%
% 4.3.4 - Labelling received signals%
% Note: the label of each frequency must be changed manually%
annotation('textbox', [0.135 0.75 0.008 0.005], 'String', '1kHz',
'FitBoxToText', 'on', 'FontSize', 8, 'EdgeColor', 'white');
annotation('textbox', [0.135 0.67 0.008 0.005], 'String', '5kHz',
'FitBoxToText', 'on', 'FontSize', 8, 'EdgeColor', 'white');
annotation('textbox', [0.135 0.59 0.008 0.005], 'String', '10kHz',
'FitBoxToText', 'on', 'FontSize', 8, 'EdgeColor', 'white');
annotation('textbox', [0.135 0.51 0.008 0.005], 'String', '15kHz',
'FitBoxToText', 'on', 'FontSize', 8, 'EdgeColor', 'white');
annotation('textbox', [0.135 0.43 0.008 0.005], 'String', '20kHz',
'FitBoxToText', 'on', 'FontSize', 8, 'EdgeColor', 'white');
annotation('textbox', [0.135 0.35 0.008 0.005], 'String', '25kHz',
'FitBoxToText', 'on', 'FontSize', 8, 'EdgeColor', 'white');
annotation('textbox', [0.135 0.27 0.008 0.005], 'String', '30kHz',
'FitBoxToText', 'on', 'FontSize', 8, 'EdgeColor', 'white');
annotation('textbox', [0.135 0.19 0.008 0.005], 'String', '35kHz',
'FitBoxToText', 'on', 'FontSize', 8, 'EdgeColor', 'white');
annotation('textarrow', [0.53 0.48], [0.88 0.84], 'String', 'Sent
signals', 'FontSize', 8);
%-----%
% 4.3.5 - Adding dimension line
hx = imdistline(gca);
api = iptgetapi(h);
fcn = makeConstrainToRectFcn('imline',
get(gca, 'XLim'), get(gca, 'YLim'));
%-----%
hold off;
%-----%
% 5. Saving figure
freq_ss0=sum_sheet(1, 1);
name= strcat(summary_file, '--', (sprintf('%3d',freq_ss0)), 'to',
(sprintf('%3d',freq_ss)), 'kHz');
saveas (figure(1), name, 'jpg');
%-----%

```

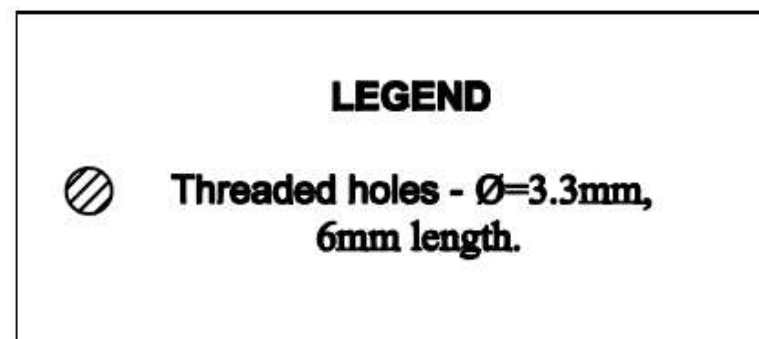
APPENDIX C – MACHINED PARTS

APPENDIX C.1 – BE mould

Front view



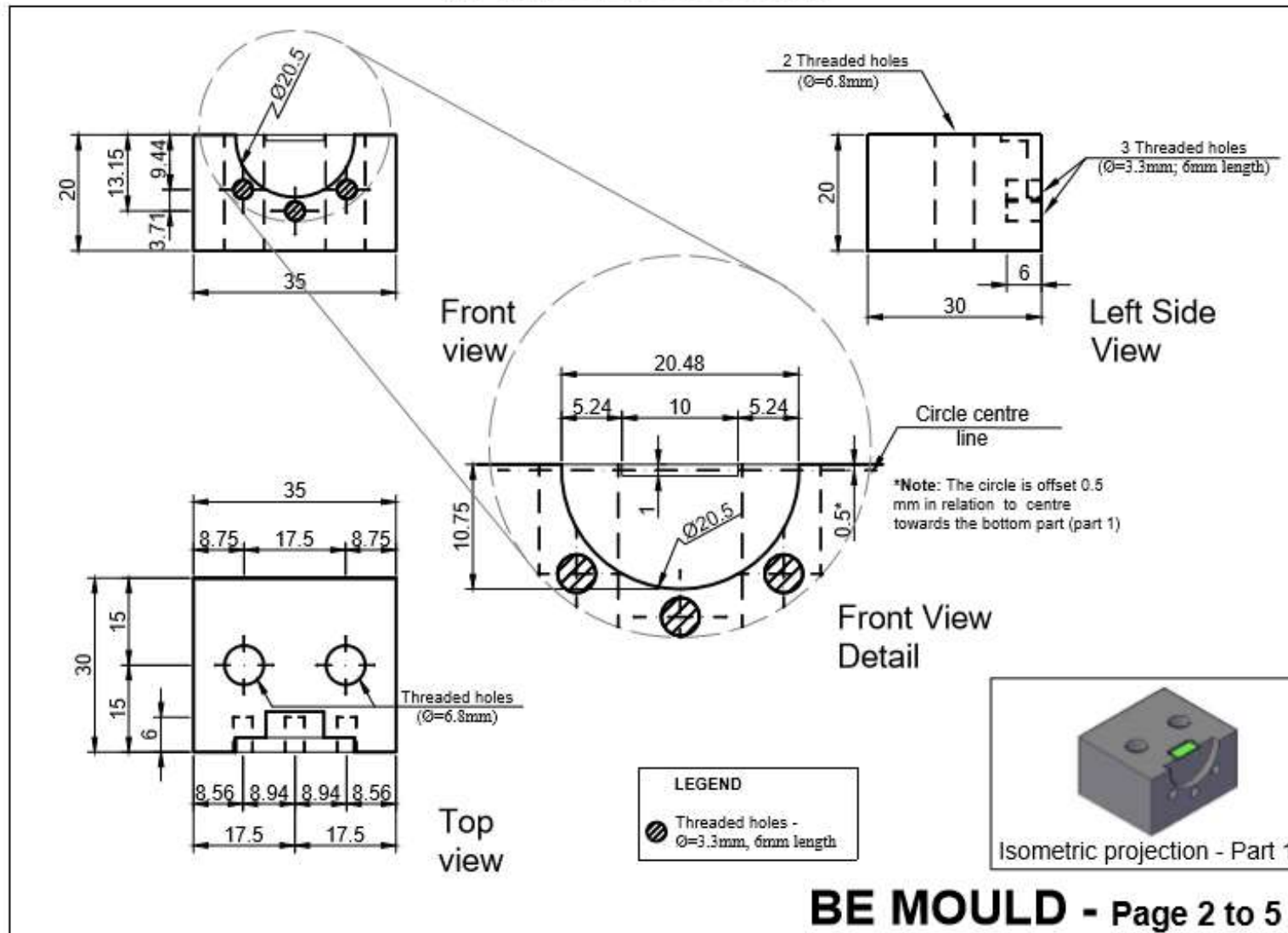
Threaded holes ($\varnothing=6.8\text{mm}$)
must coincide with through holes (part 2)



BE MOULD
Page 1 to 5

Mould - part 1

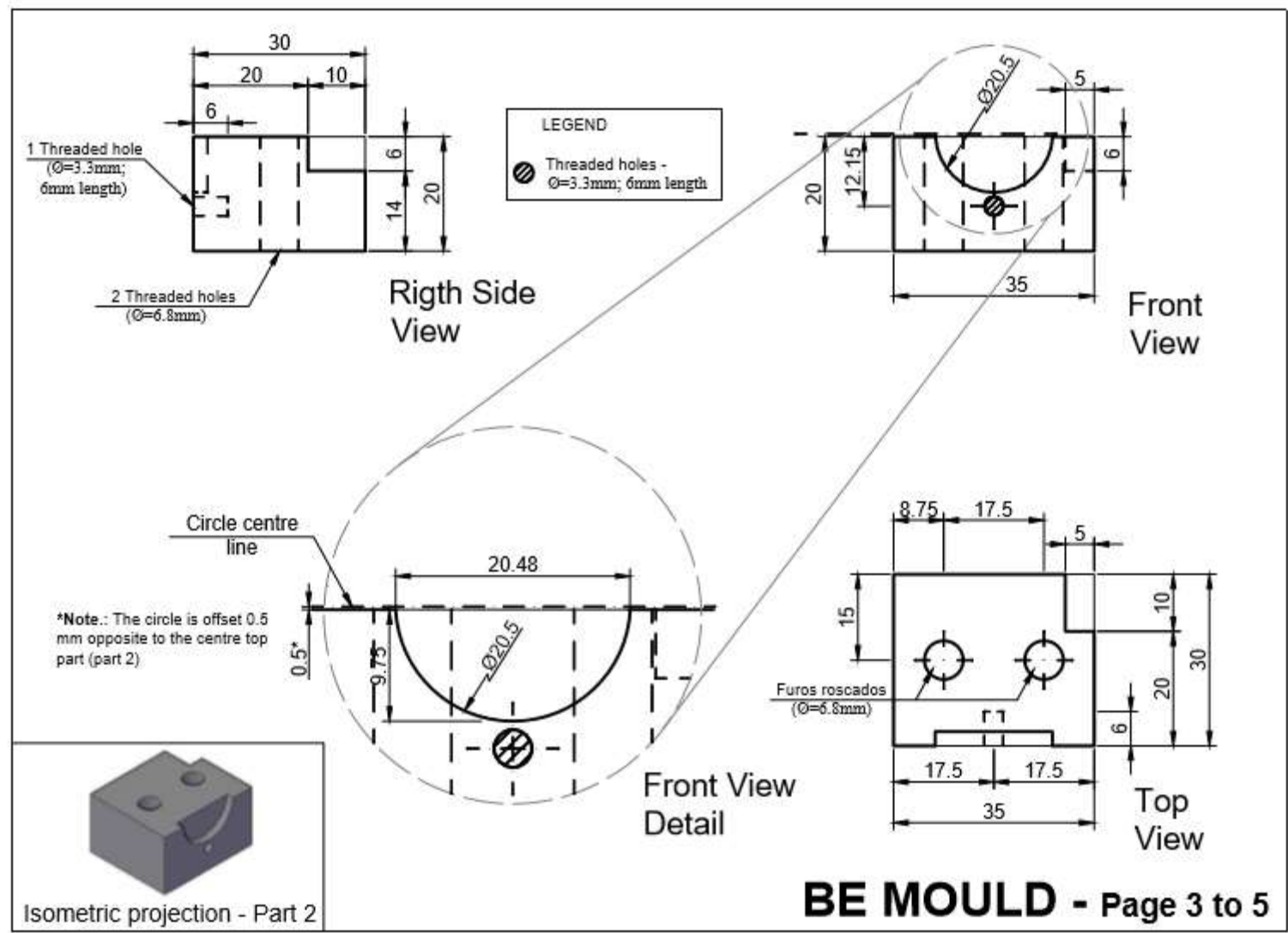
(all dimensions are in mm)



BE MOULD - Page 2 to 5

Mould - part 2

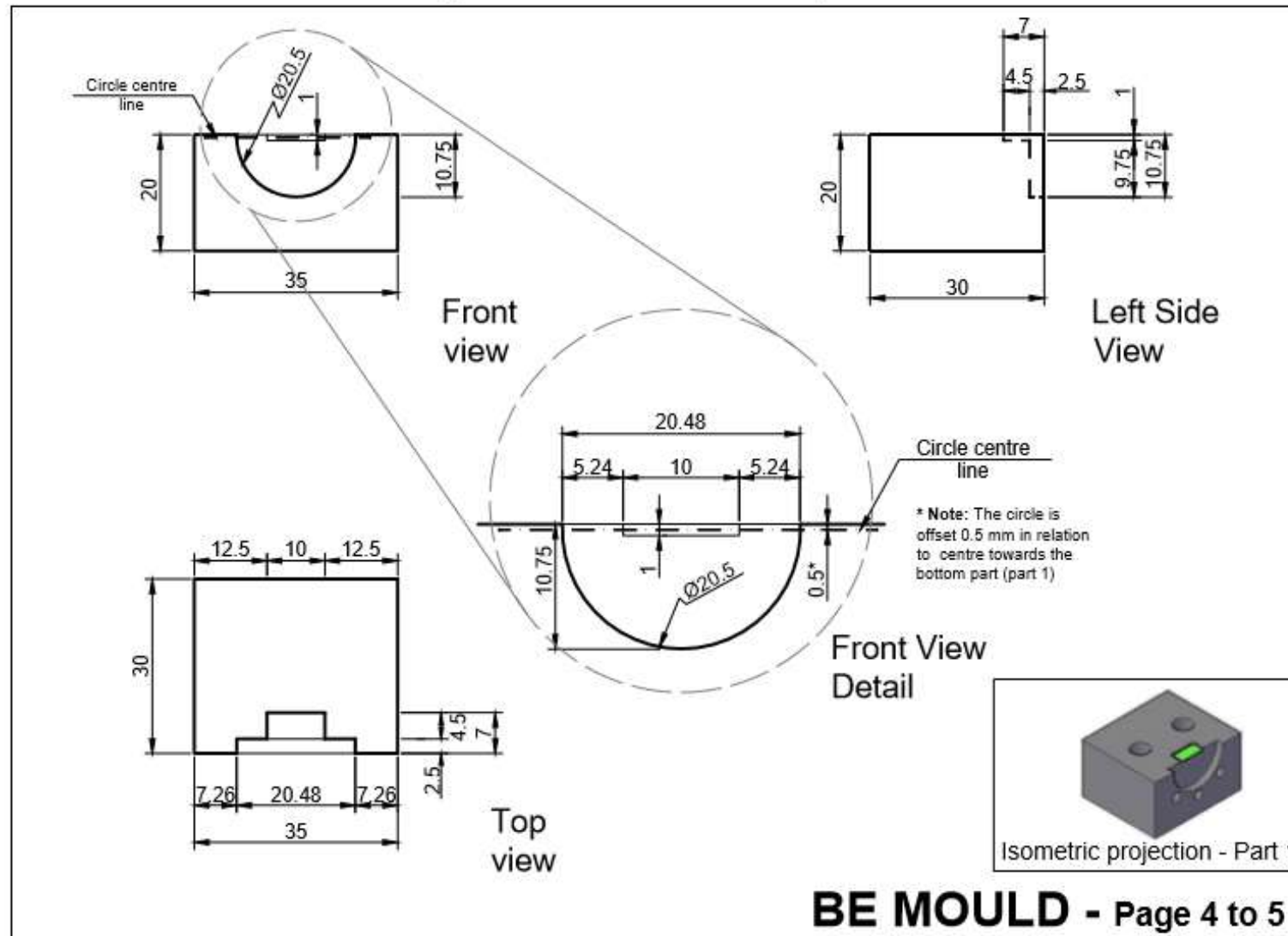
(all dimensions are in mm)



BE MOULD - Page 3 to 5

Mould - part 1

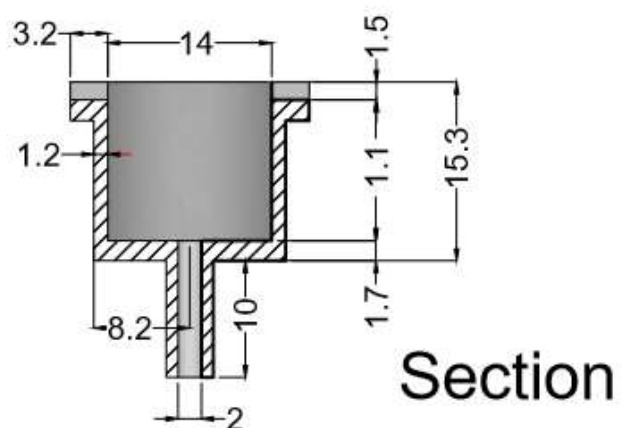
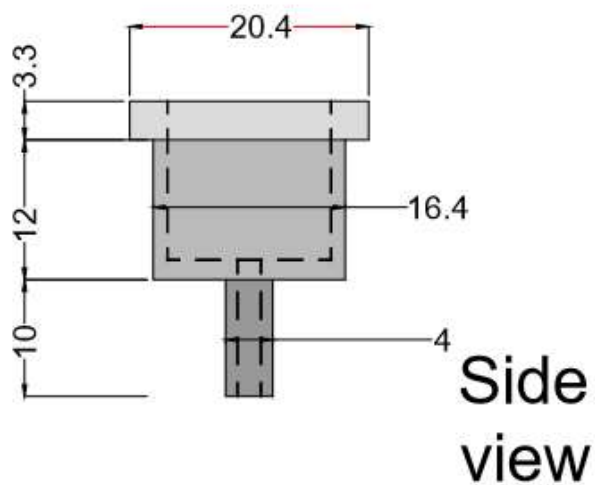
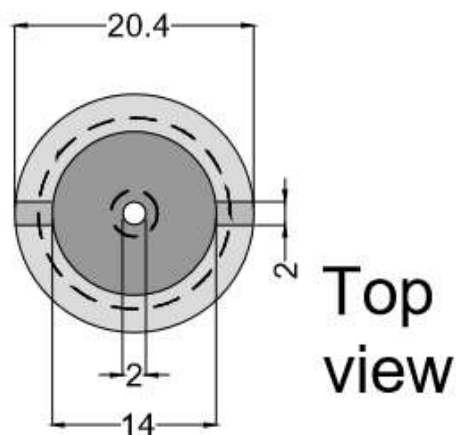
(all dimensions are in mm)



BE MOULD - Page 4 to 5

APPENDIX C.2 – BE metal sockets

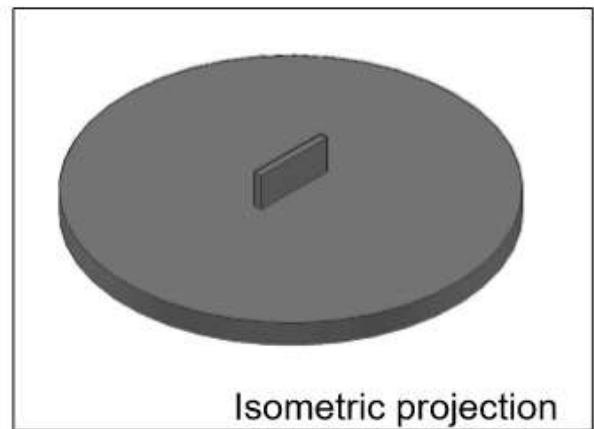
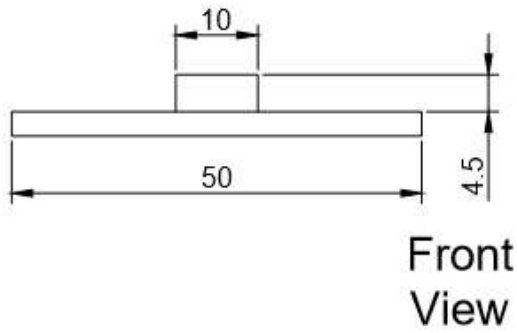
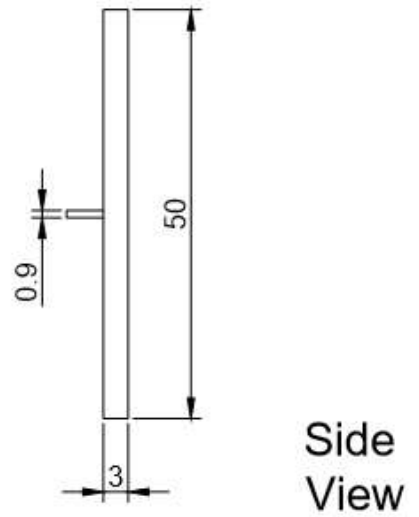
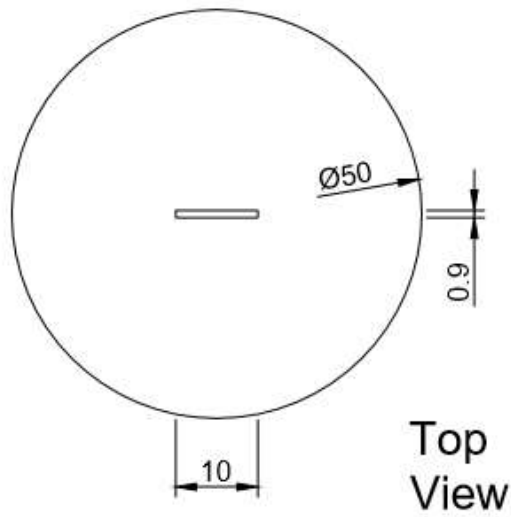
(all dimensions are in mm)



**BE METAL
SOCKETS**

Page 1 to 1

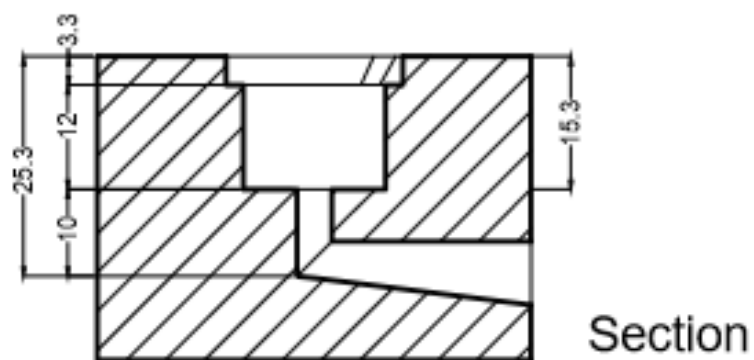
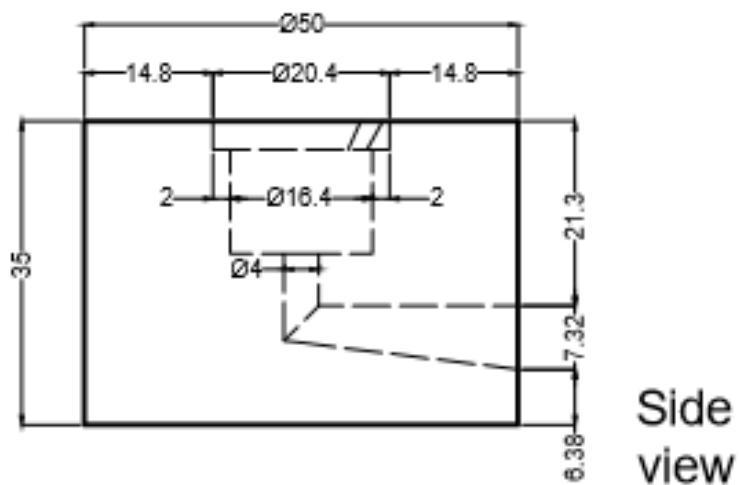
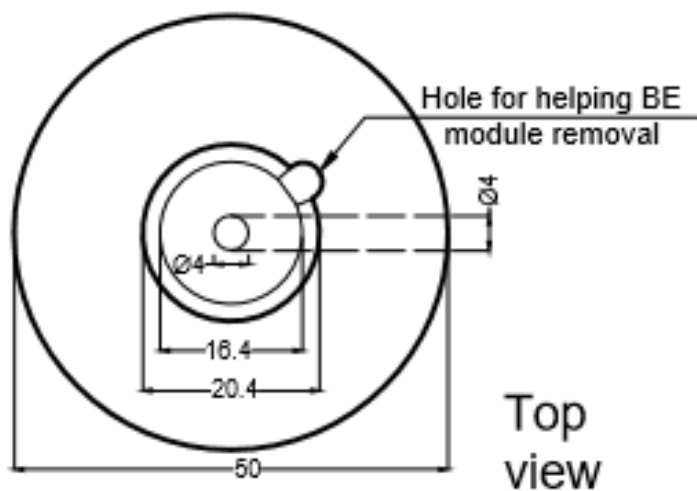
APPENDIX C.3 – Metal BE templates



METAL BE TEMPLATES - Page 1 to 1

APPENDIX C.4 – Bench pedestal

(all dimensions are in mm)

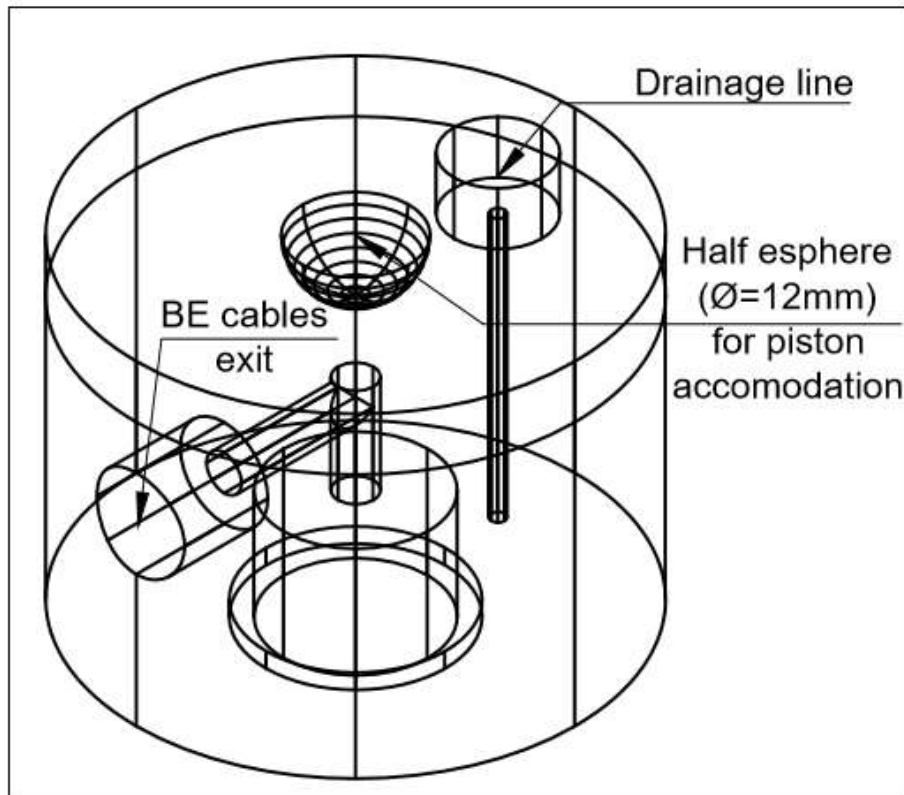


BENCH
PEDESTAL
Page 1 to 1

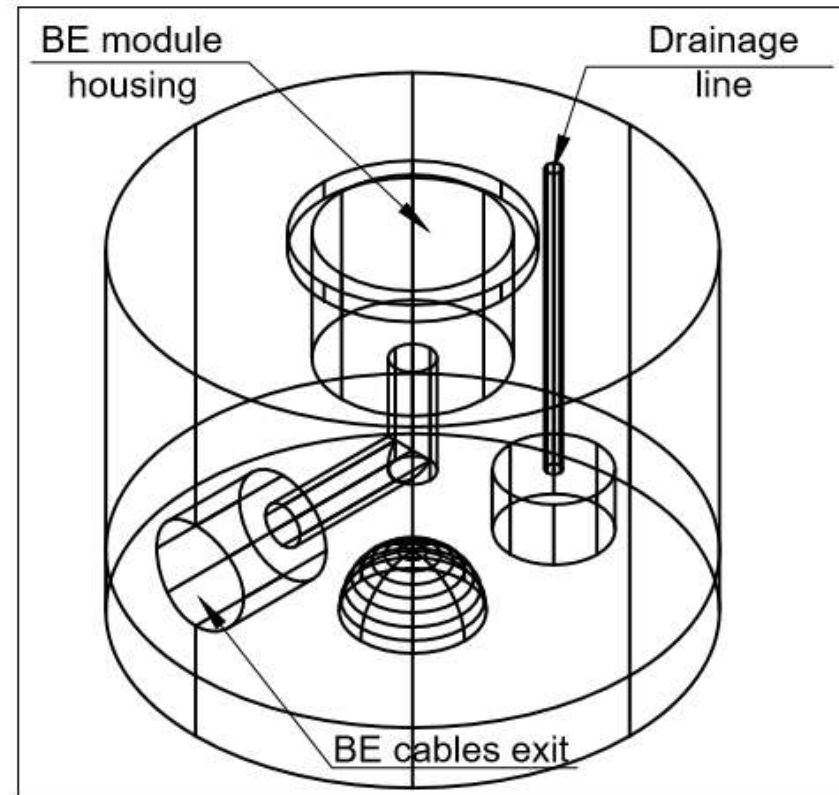
APPENDIX C.5 – Triaxial top cap and pedestal

Isometric projection - Top cap (triaxial) Acrylic

Top view - highlighting BE cables exit

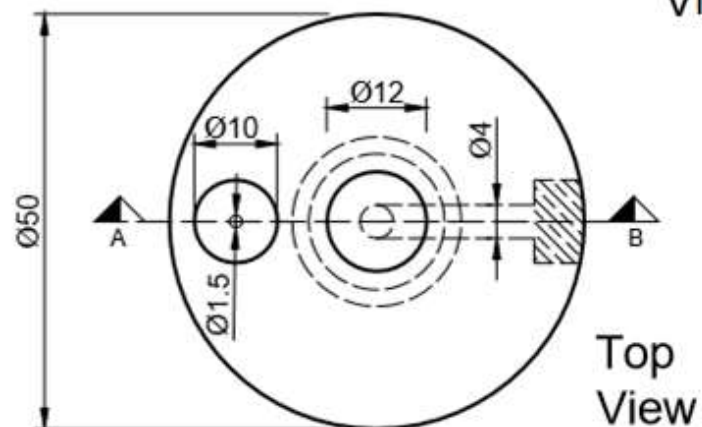
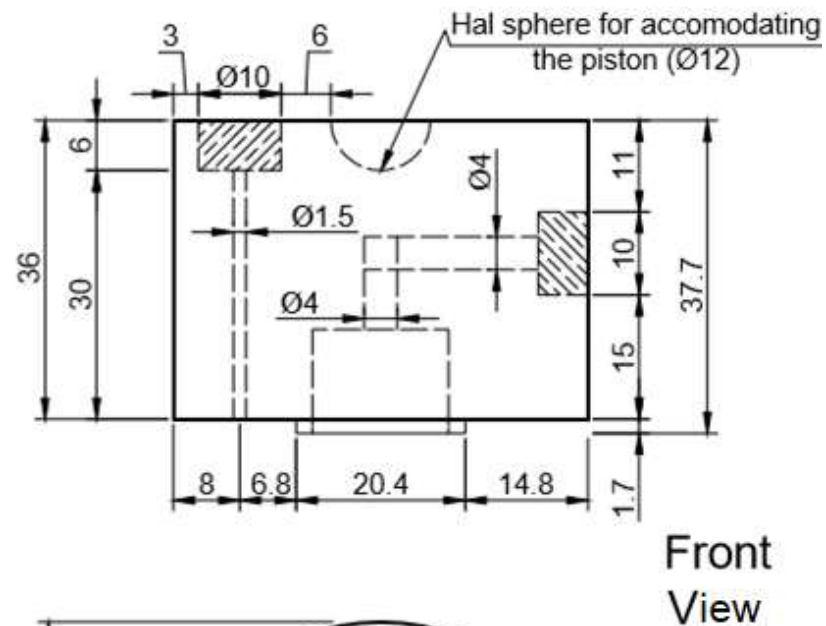
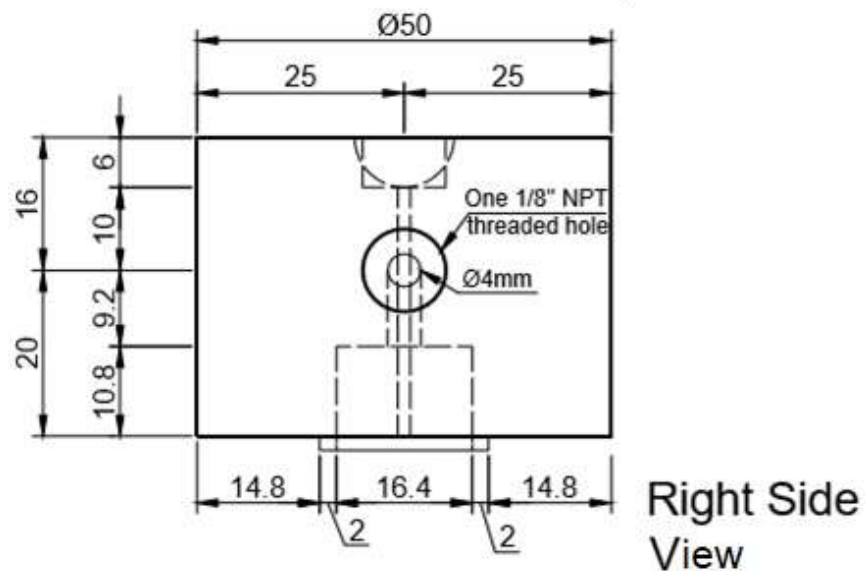


Bottom view



TOP CAP (TRIAxIAL) - Page 1 to 3

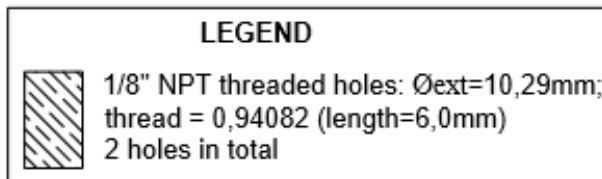
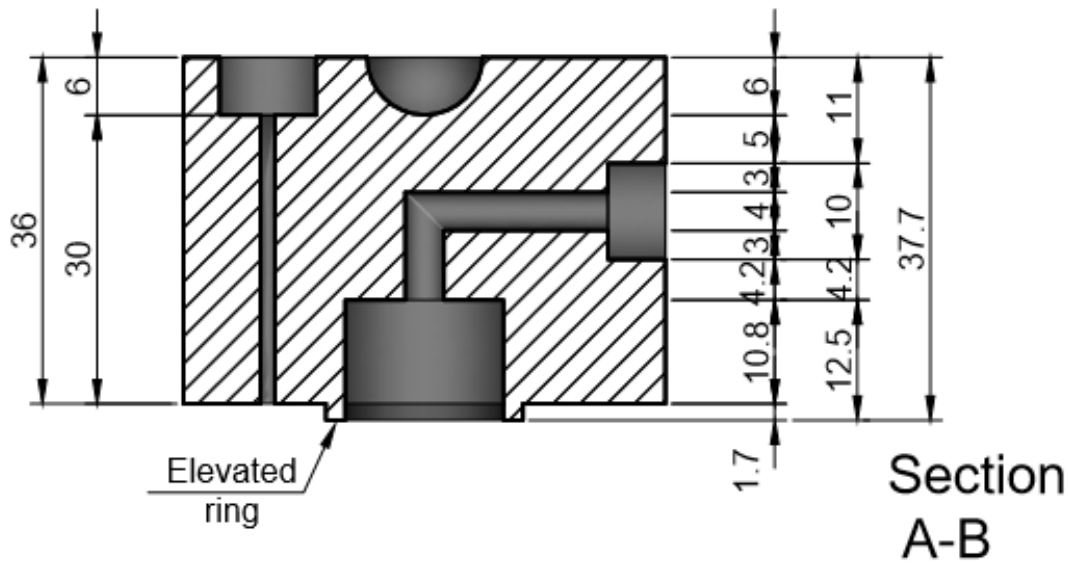
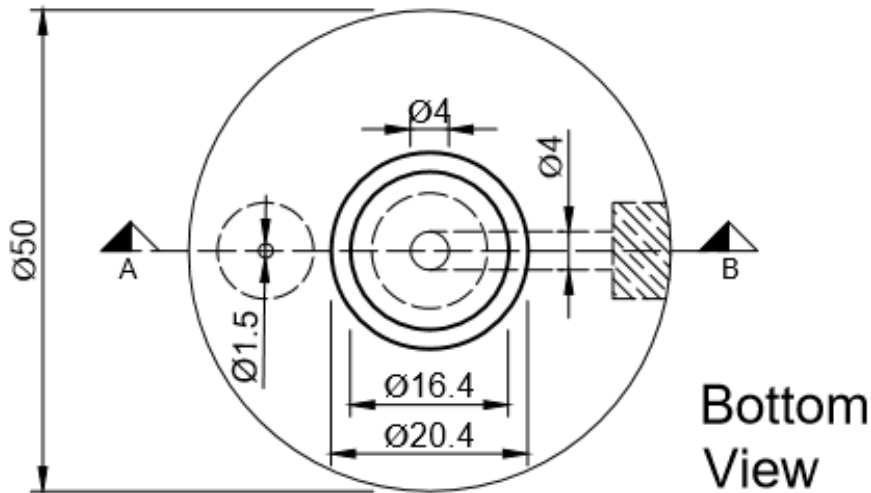
(all dimensions are in mm)



LEGEND	
	1/8" NPT threaded holes: Øext=10,29mm; thread = 0,94082 (length=6,0mm) 2 holes in total

TOP CAP (TRIAXIAL) - Page 2 to 3

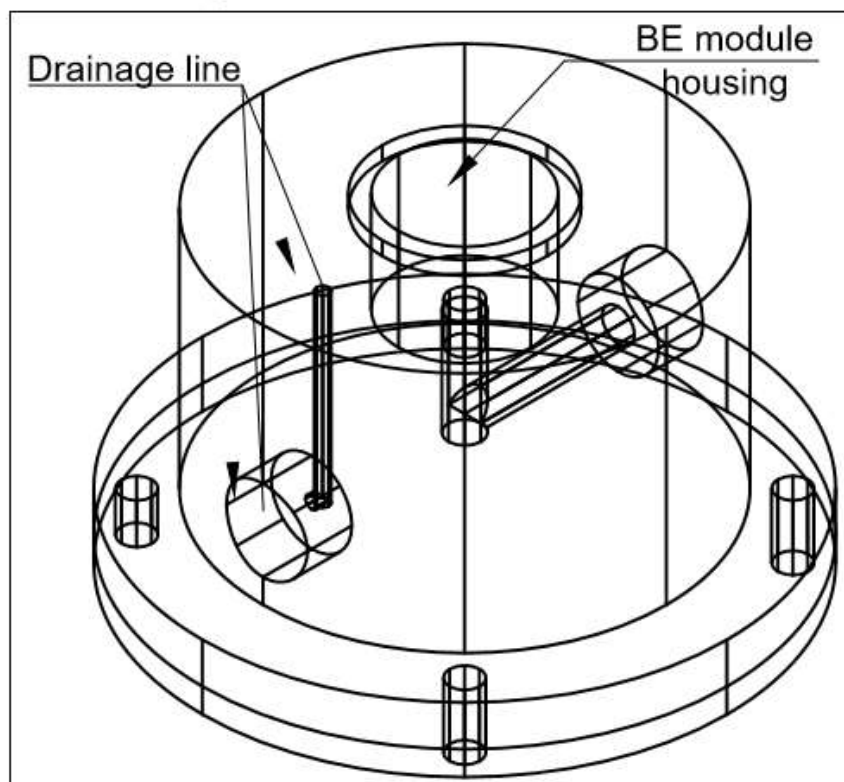
(all dimensions are in mm)



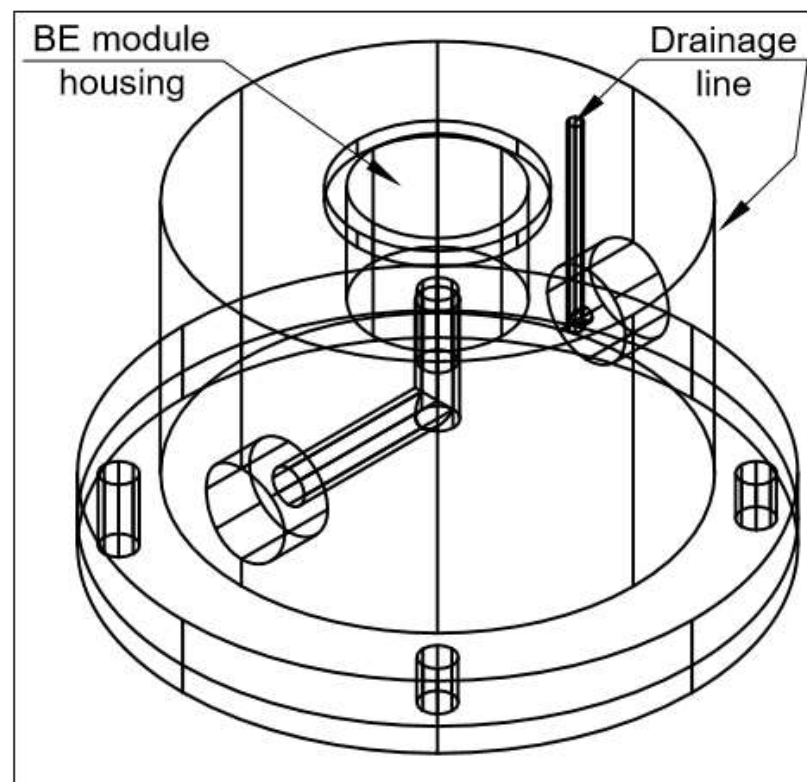
TOP CAP (TRIAxIAL)
Page 2 to 3

Isometric projection - Pedestal (triaxial) Stainless steel

Right side view

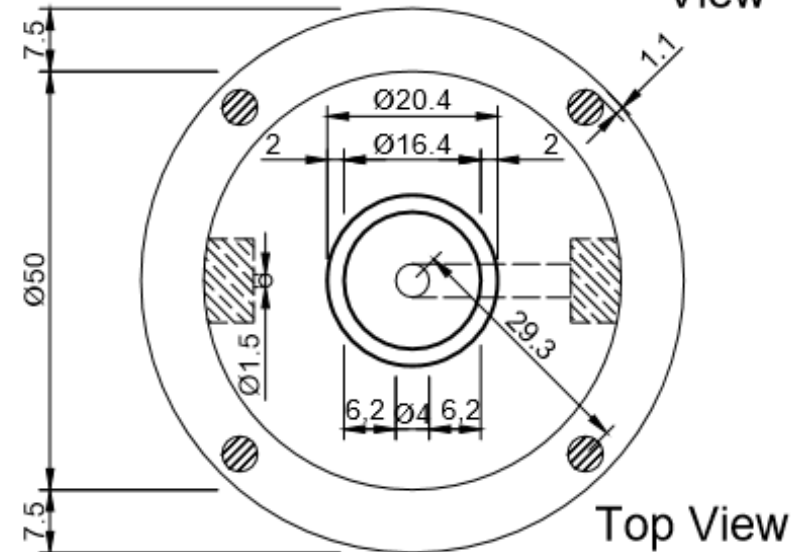
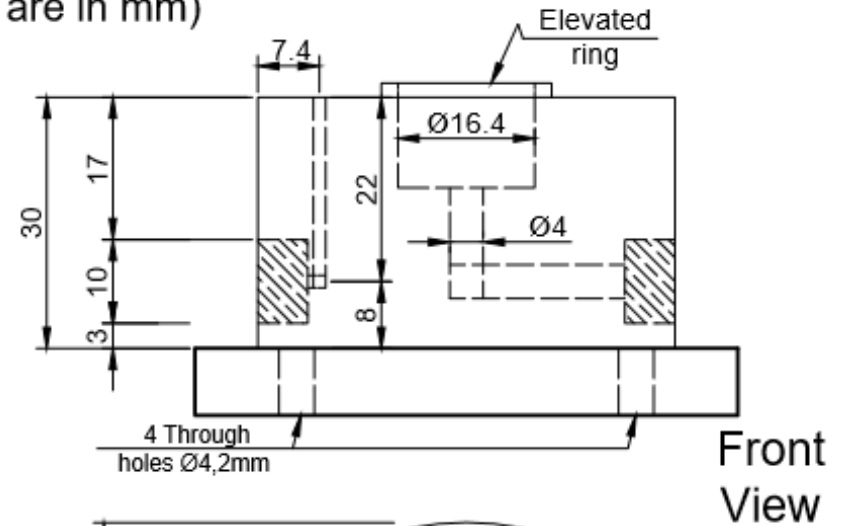
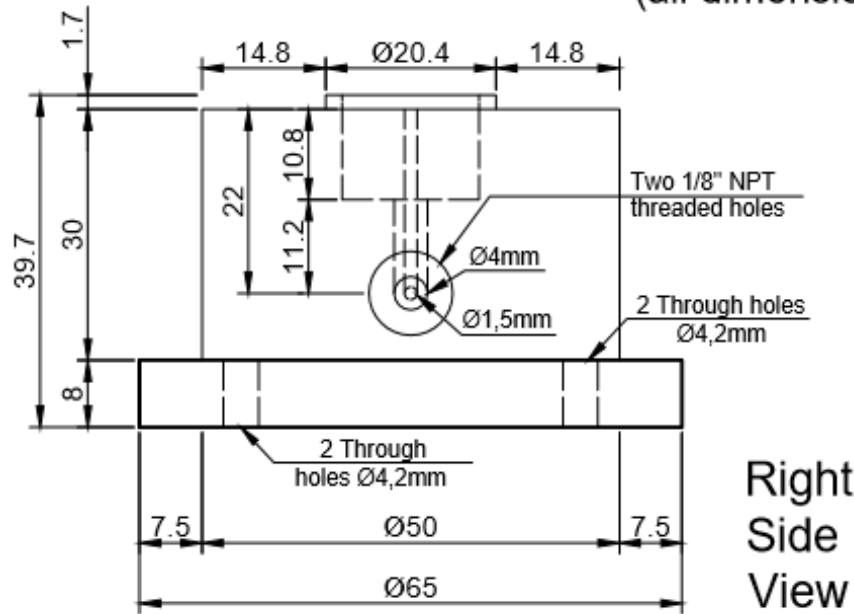




Left side view



PEDESTAL (TRIAxIAL) - Page 1 to 2

(all dimensions are in mm)

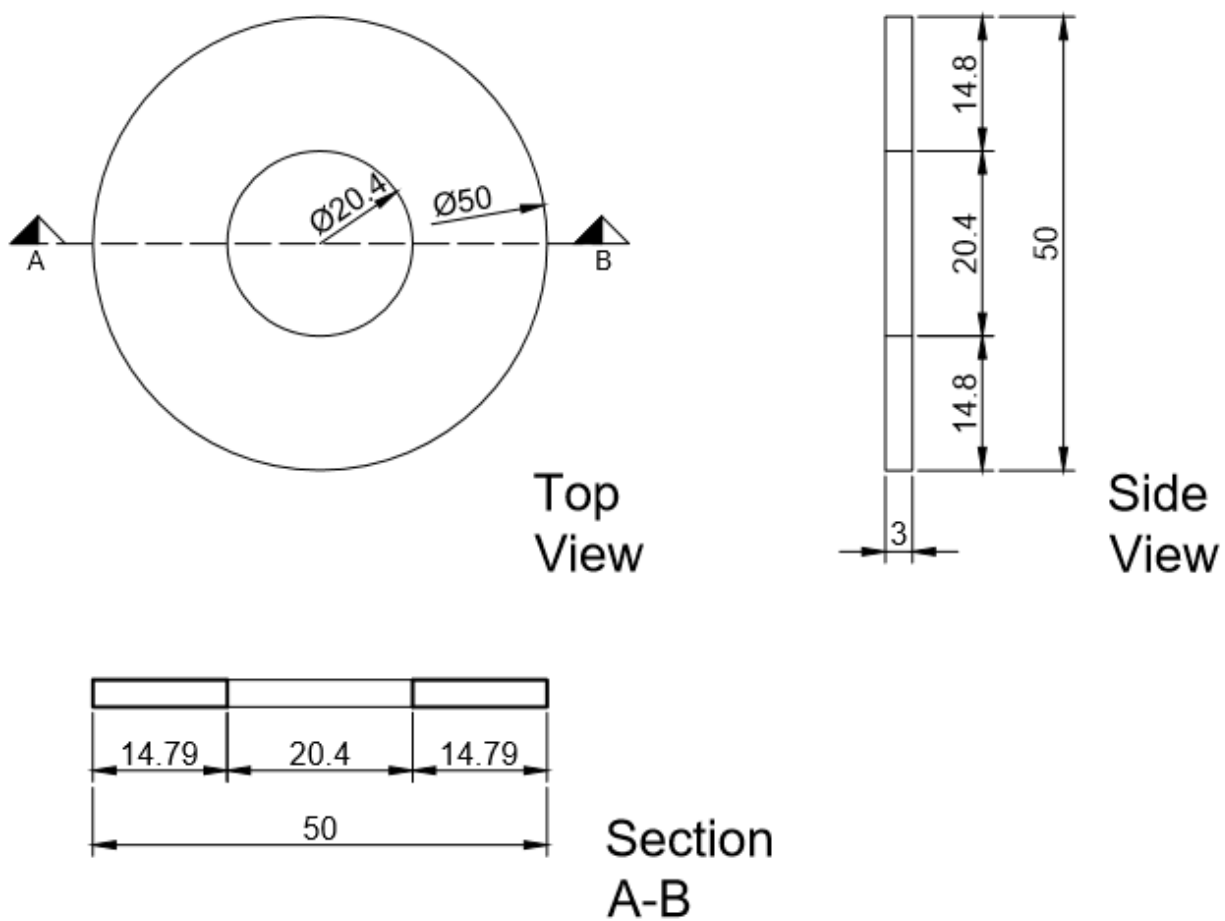


LEGEND	
	Through holes: Ø=4,2mm; 4 holes in total
	1/8" NPT threaded holes: Ø _{ext} =10,29mm; thread = 0,94082 (length=6,0mm) 2 holes in total

PEDESTAL (TRIAXIAL) - Page 2 to 2

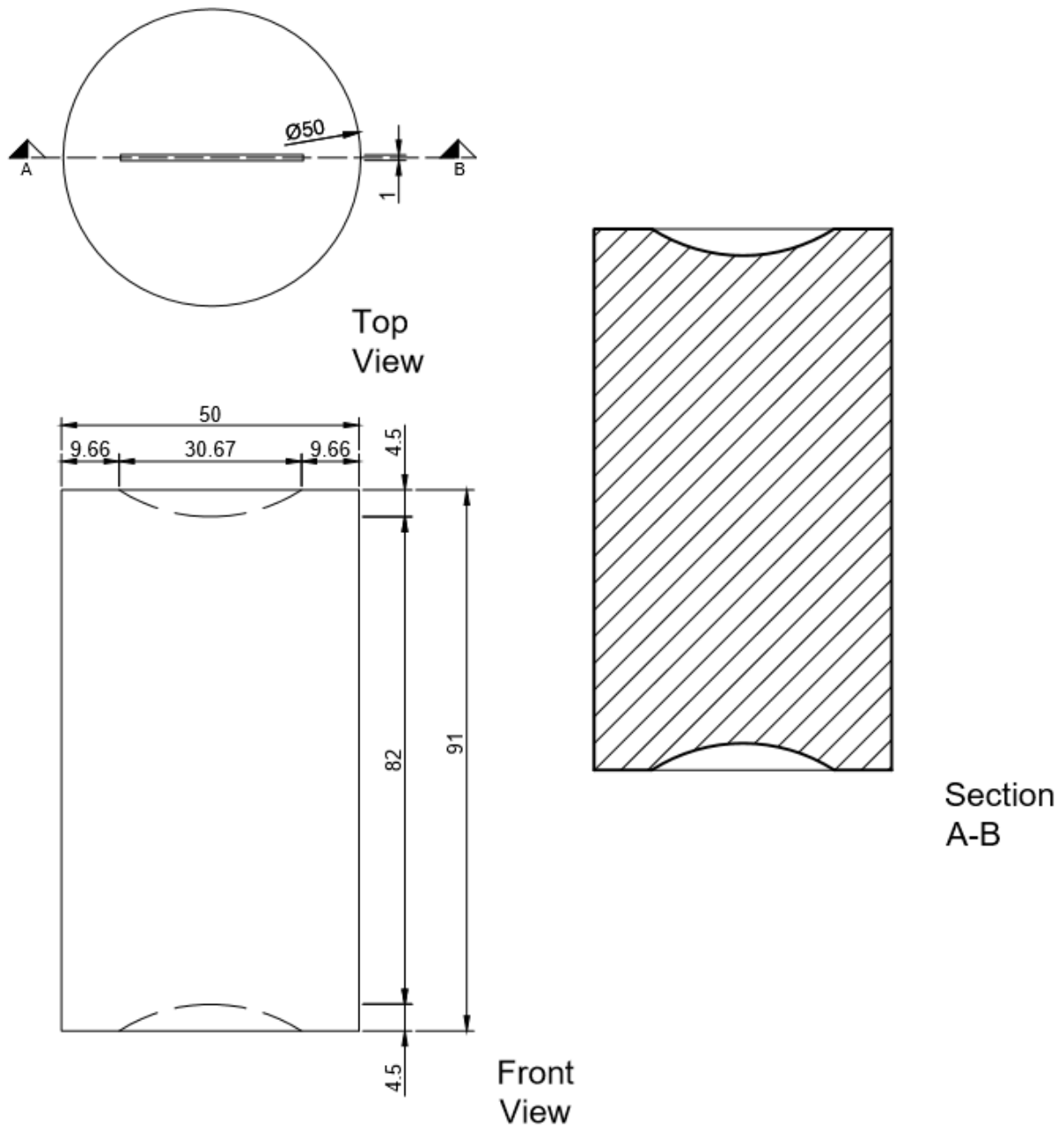
APPENDIX C.6 – Porous disks

(all dimensions are in mm)

**POROUS DISKS - Page 1 to 1**

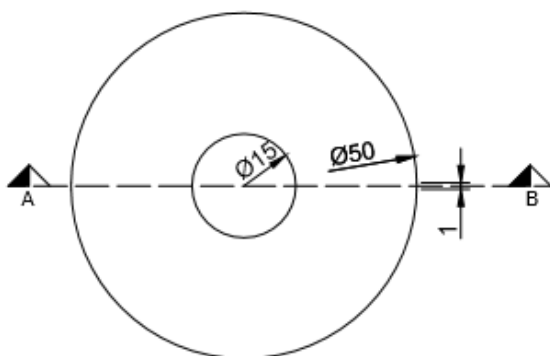
APPENDIX C.7 – Calibration rods

(all dimensions are in mm)

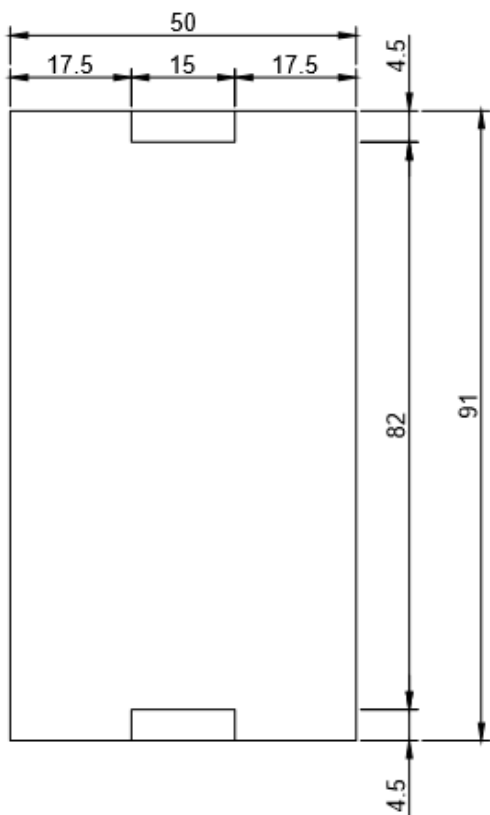


SLOTTED CALIBRATION CYLINDER - Page 1 to 1

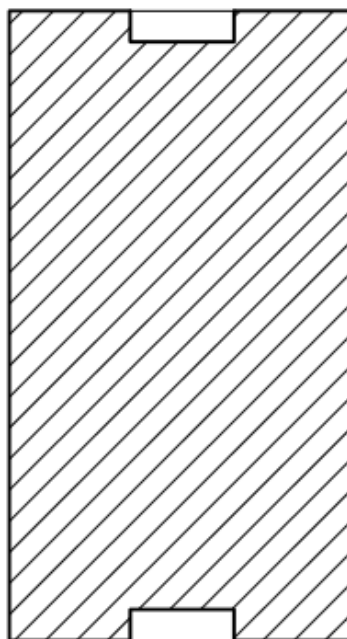
(all dimensions are in mm)



Top
View



Front
View

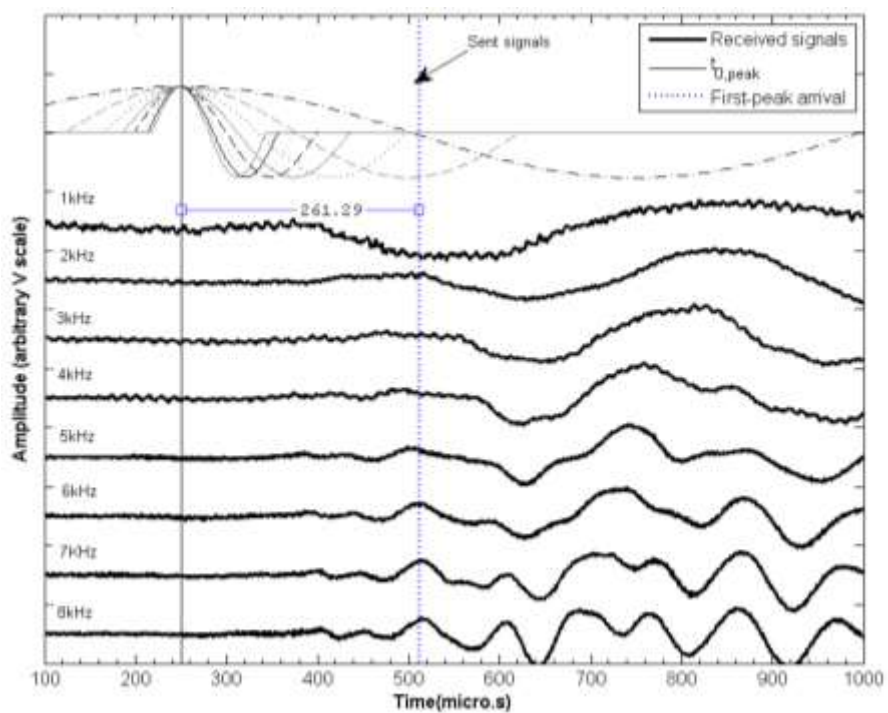


Section
A-B

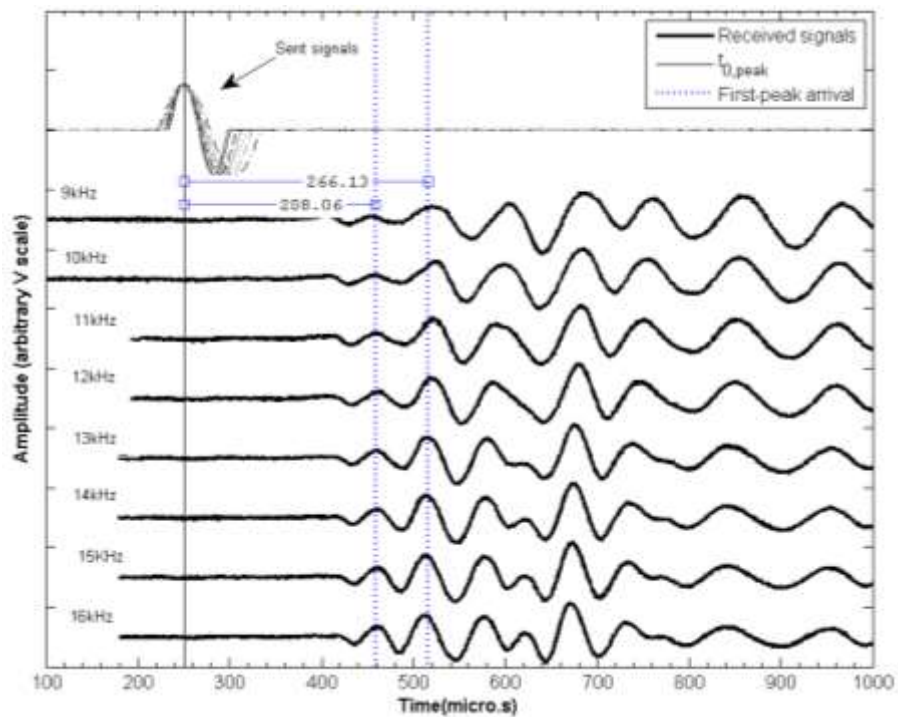
CALIBRATION CYLINDER WITH CIRCULAR CAVITIES - Page 1 to 1

APPENDIX D – SPECIMEN TRX_0.00_15.4 AFTER CONSOLIDATION

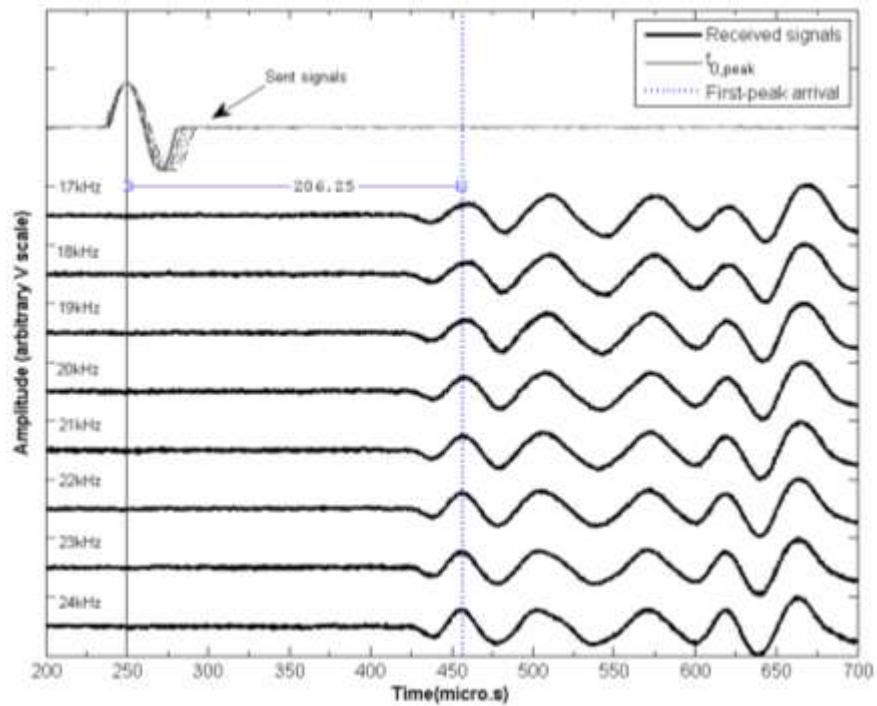
- Input: single sine pulses from 1 kHz and 8 kHz



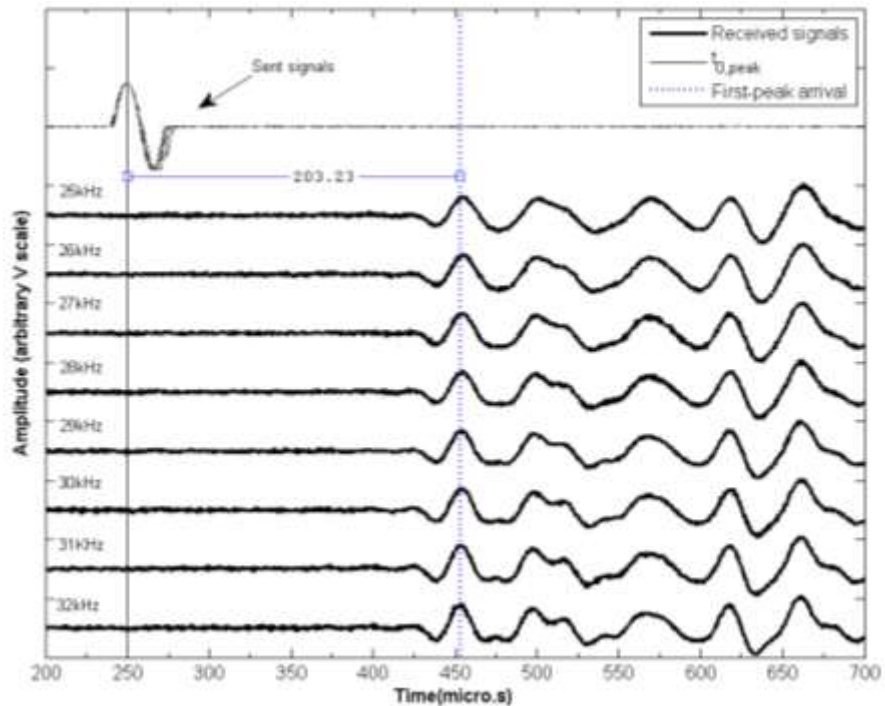
- Input: single sine pulses from 9 kHz to 16 kHz



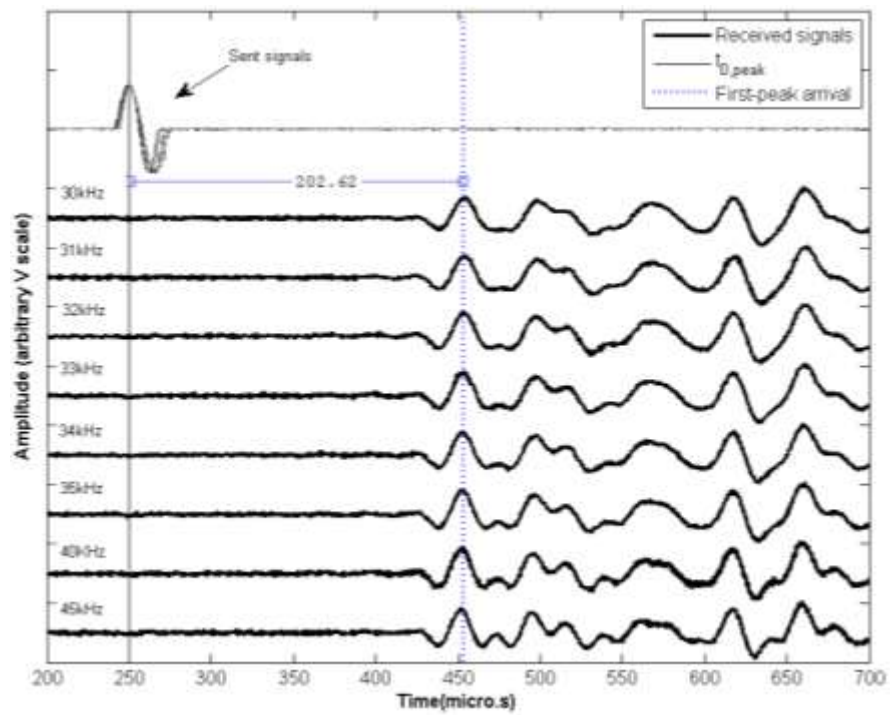
- Input: single sine pulses from 17 kHz to 24 kHz



- Input: single sine pulses from 25 kHz to 32 kHz



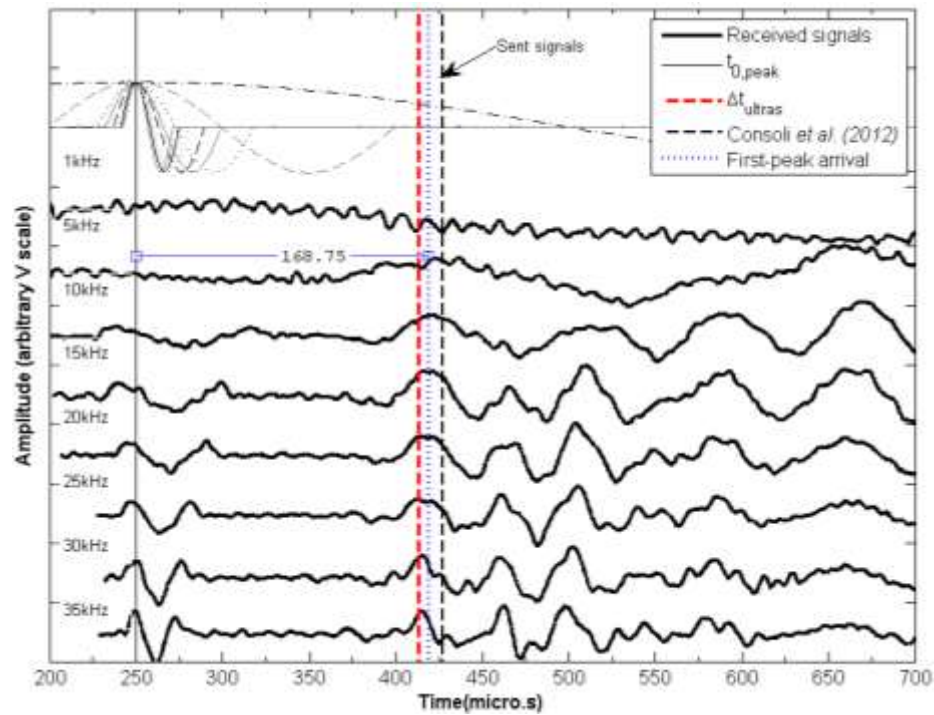
- Input: single sine pulses from 30 kHz to 45 kHz



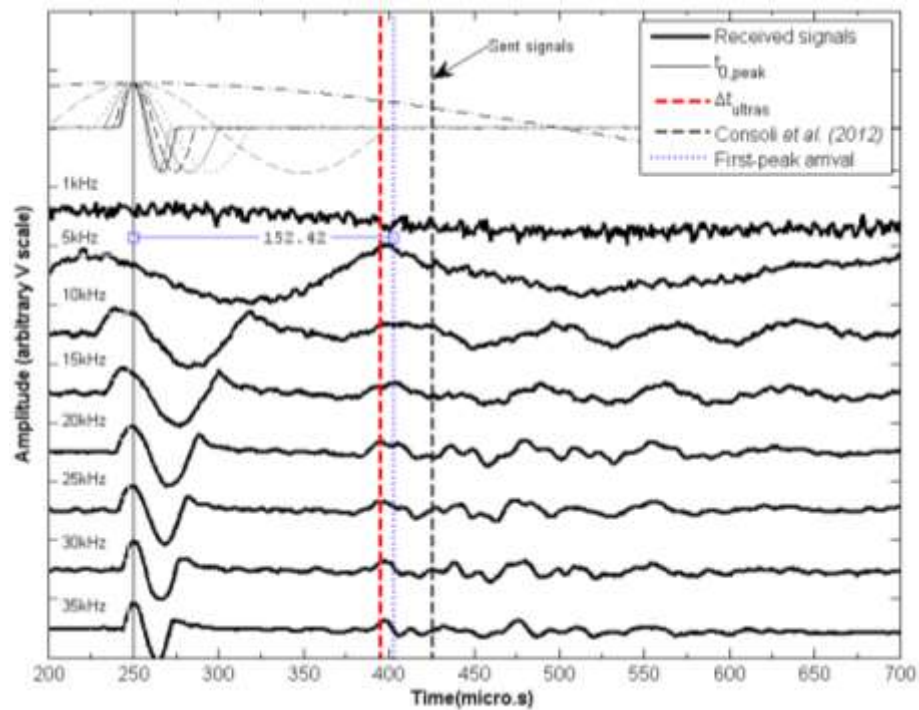
APPENDIX E –DAILY BE BENCH TESTS

APPENDIX E.1 – Specimen BEN_31.9_15.4

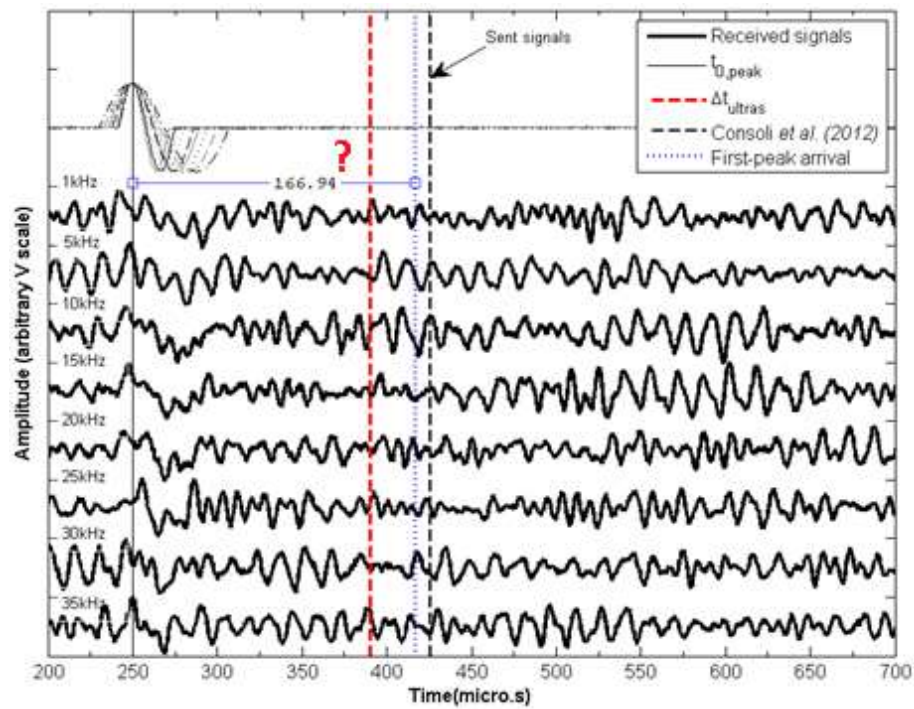
- Day 02 of cure



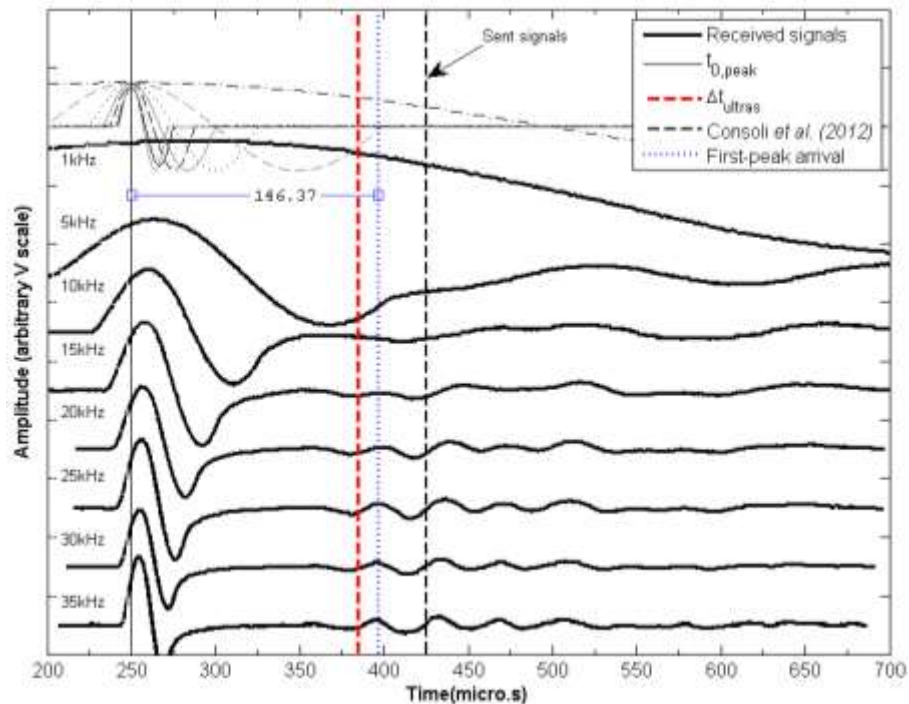
- Day 03 of cure



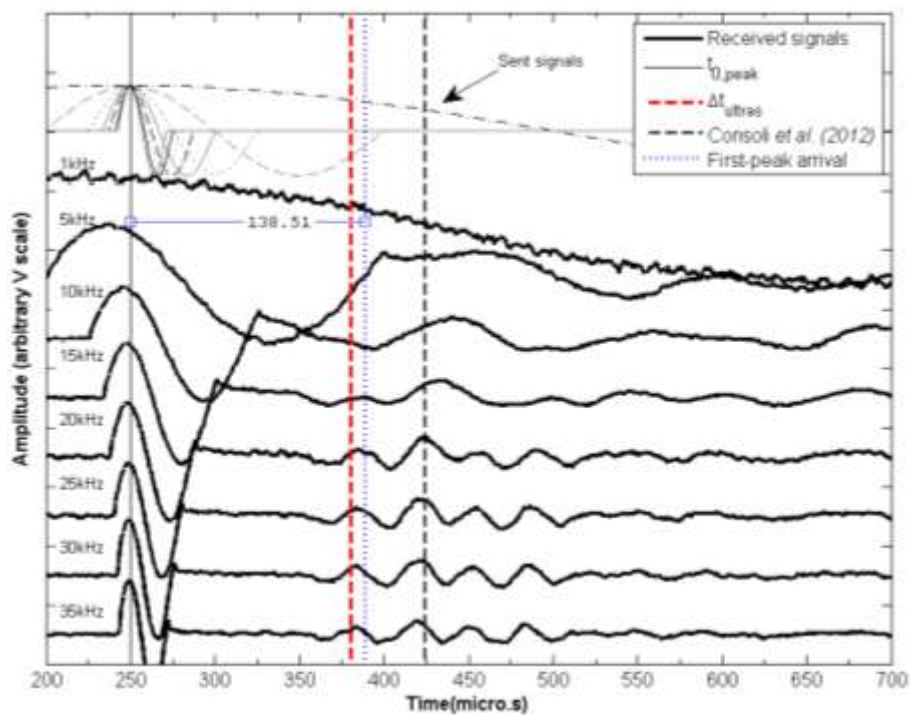
- Day 04 of cure



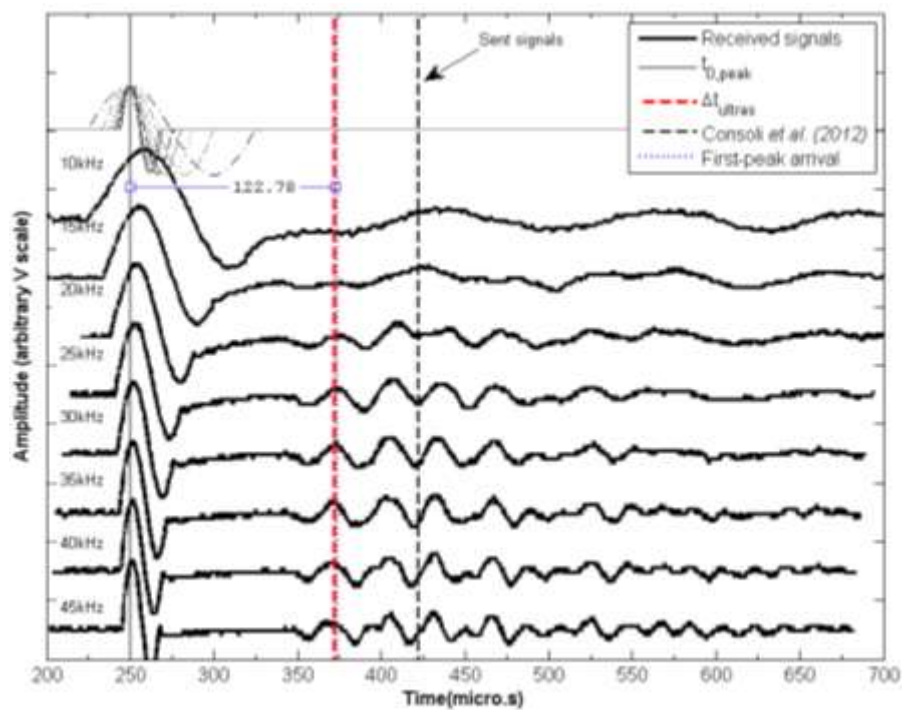
- Day 05 of cure



- Day 07 of cure

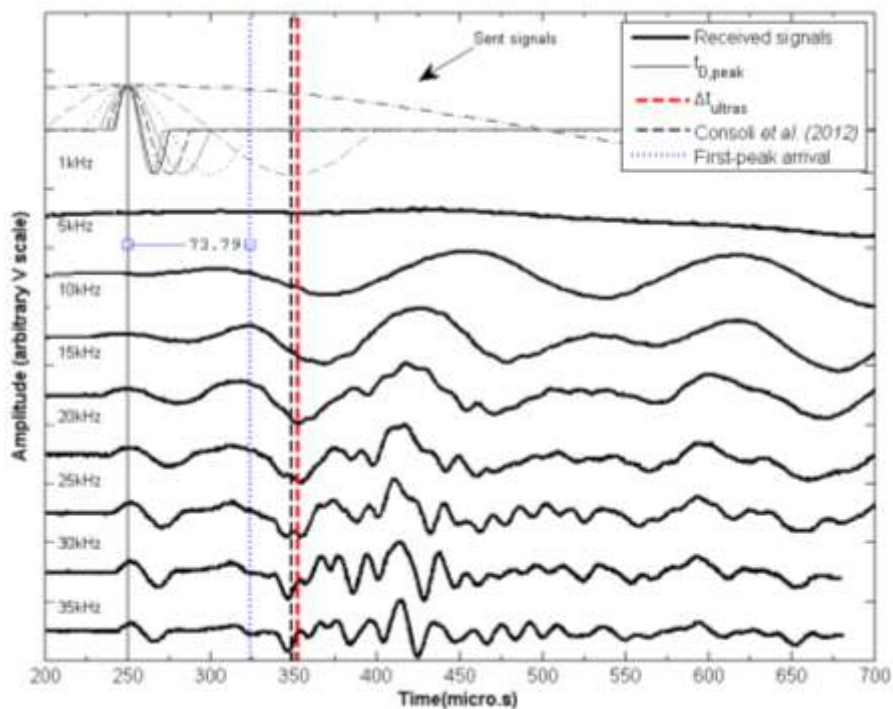


- Day 14 of cure

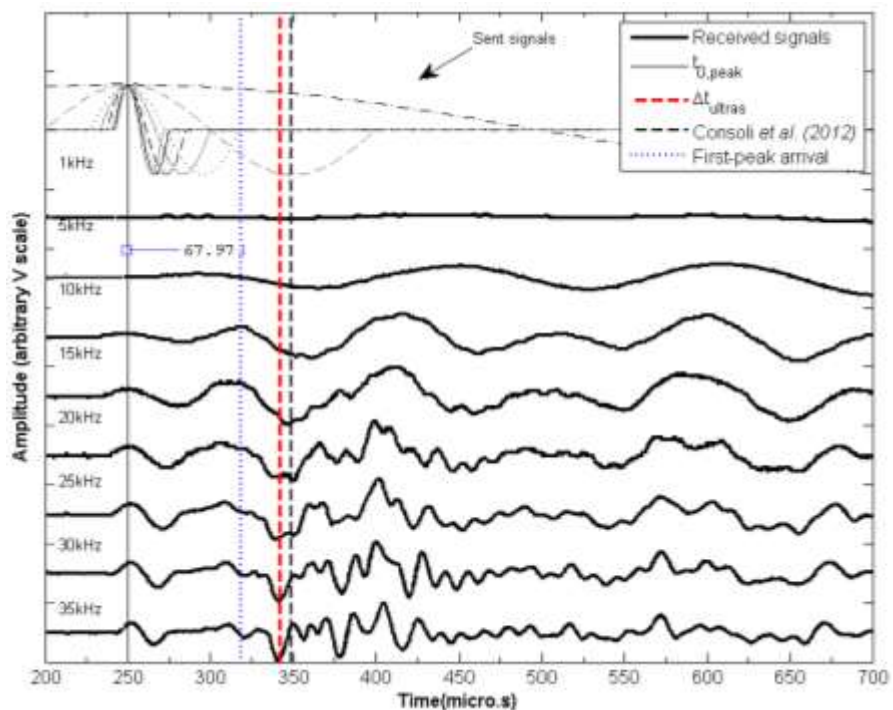


APPENDIX E.2 – Specimen BEN_8.64_15.4

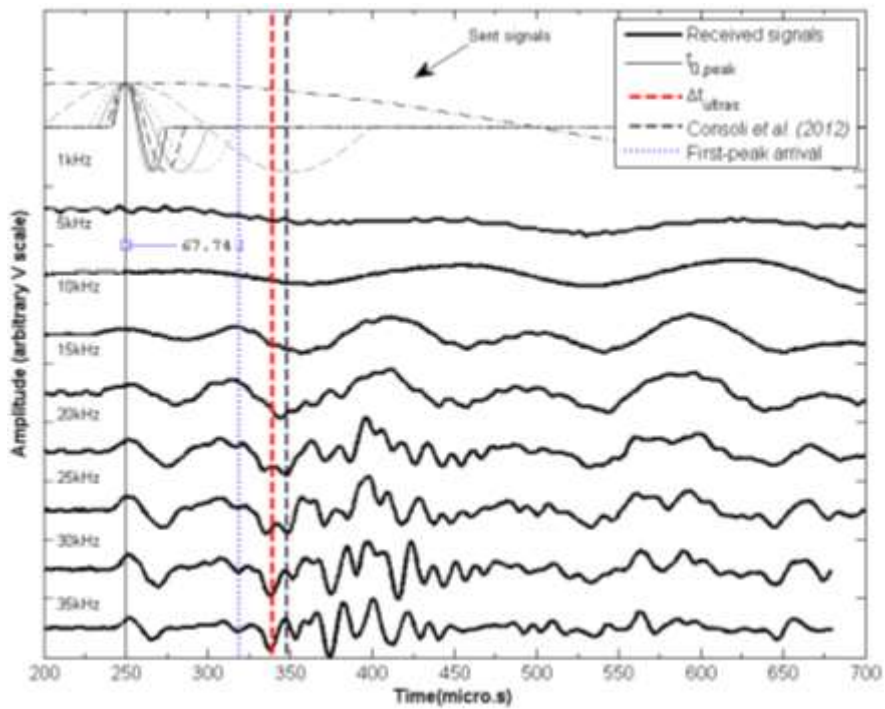
- Day 02 of cure



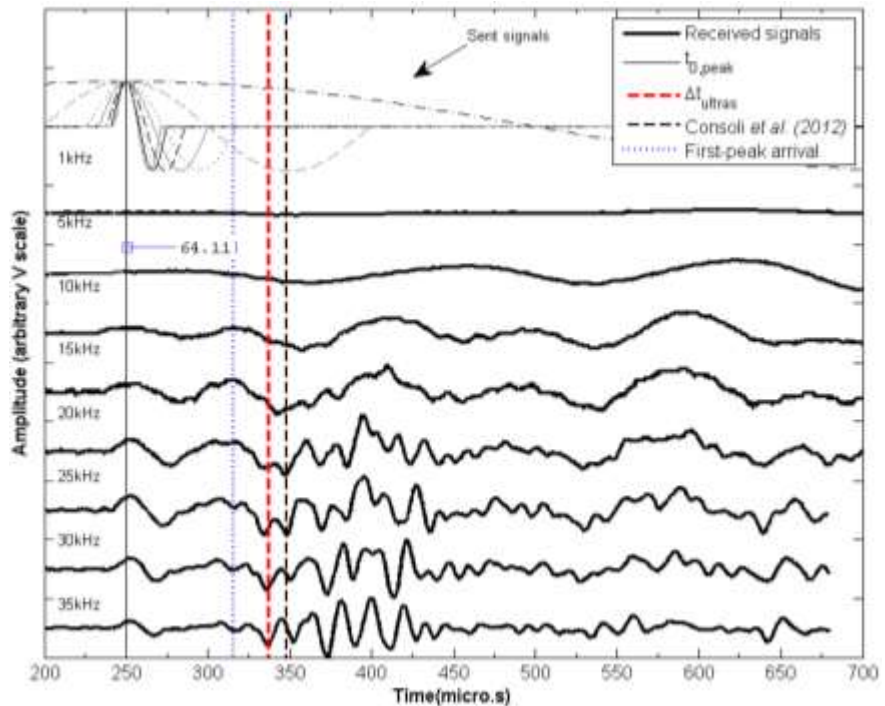
- Day 03 of cure



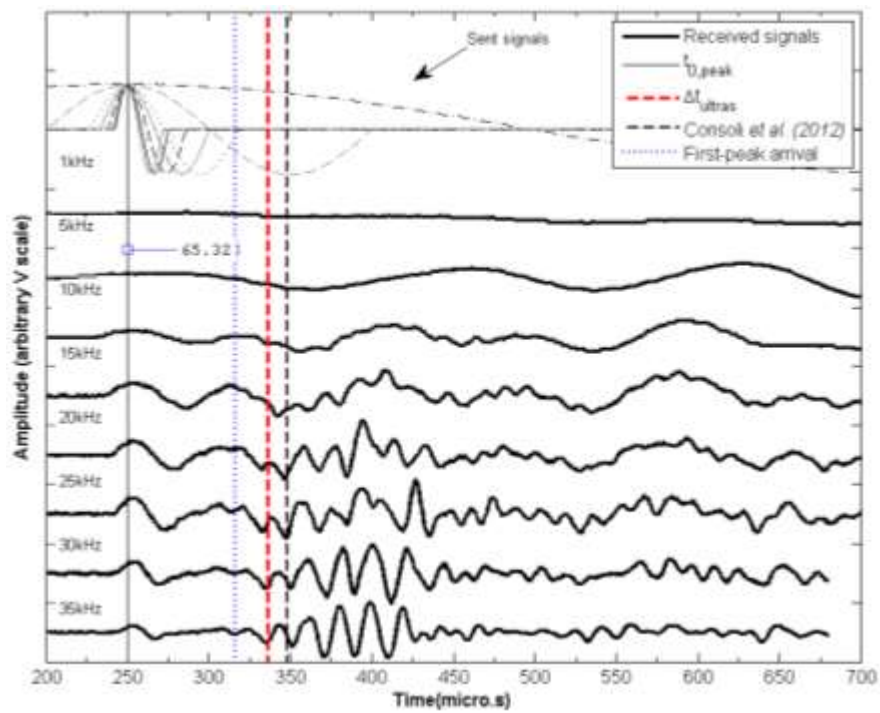
- Day 04 of cure



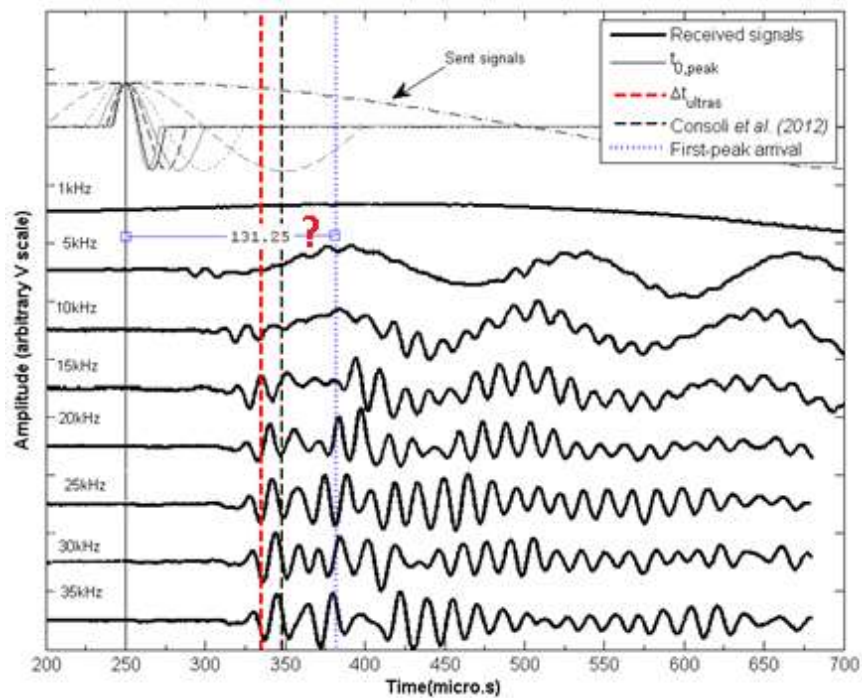
- Day 05 of cure



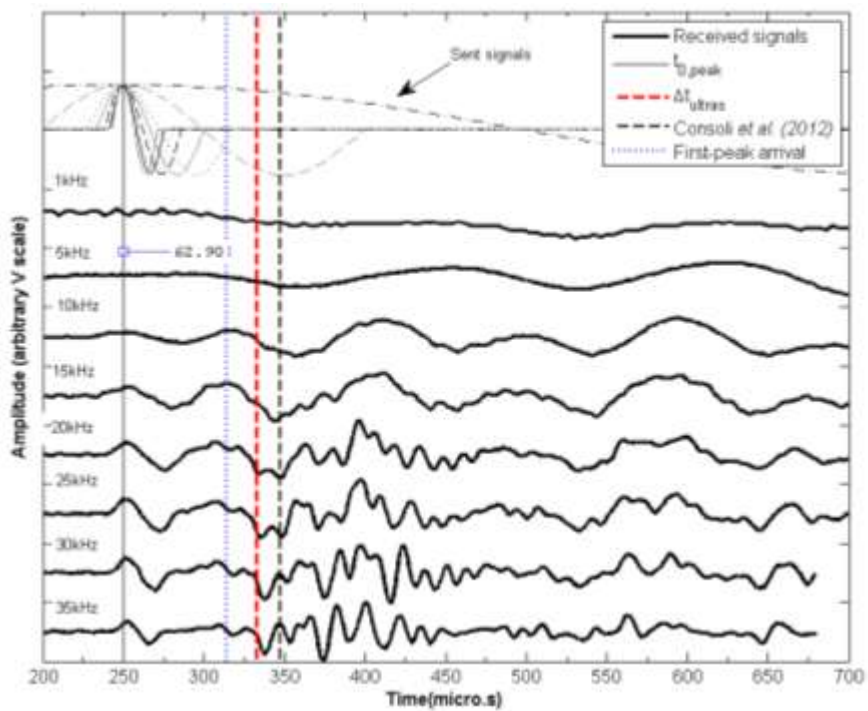
- Day 06 of cure



- Day 07 of cure

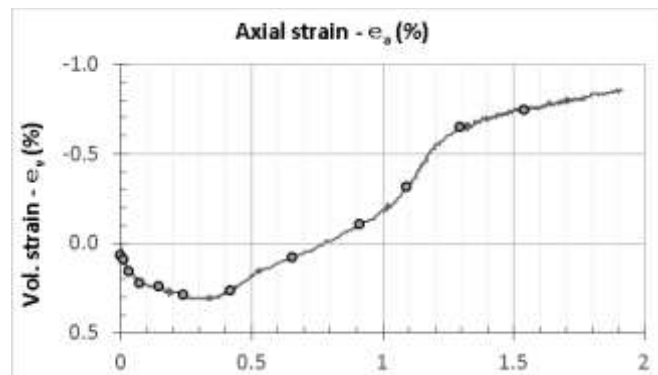
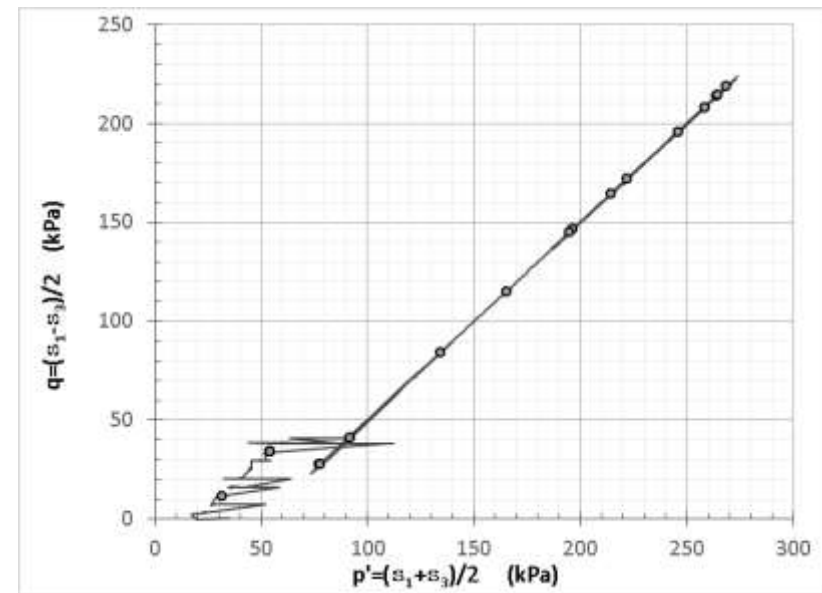
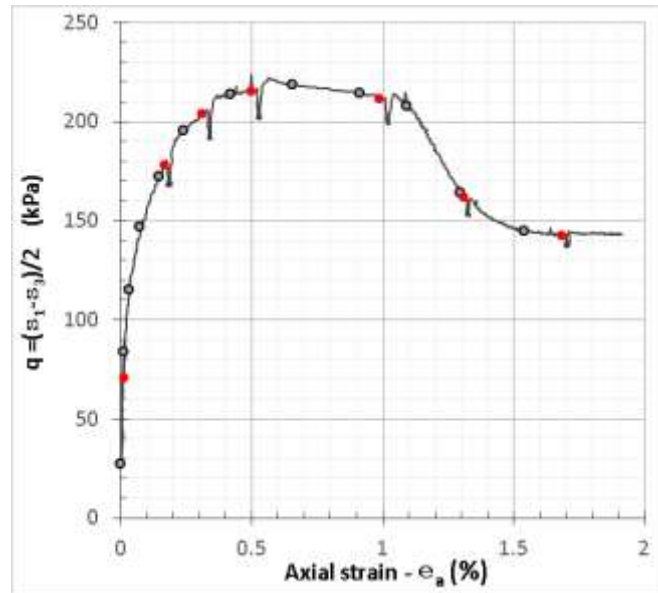


- Day 14 of cure



APPENDIX F – TRIAXIAL TESTS

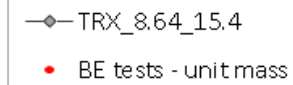
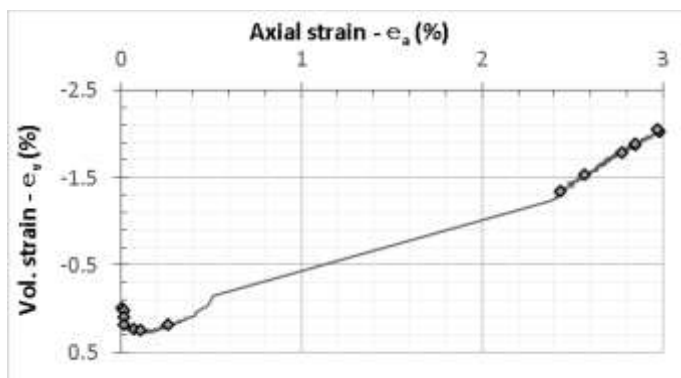
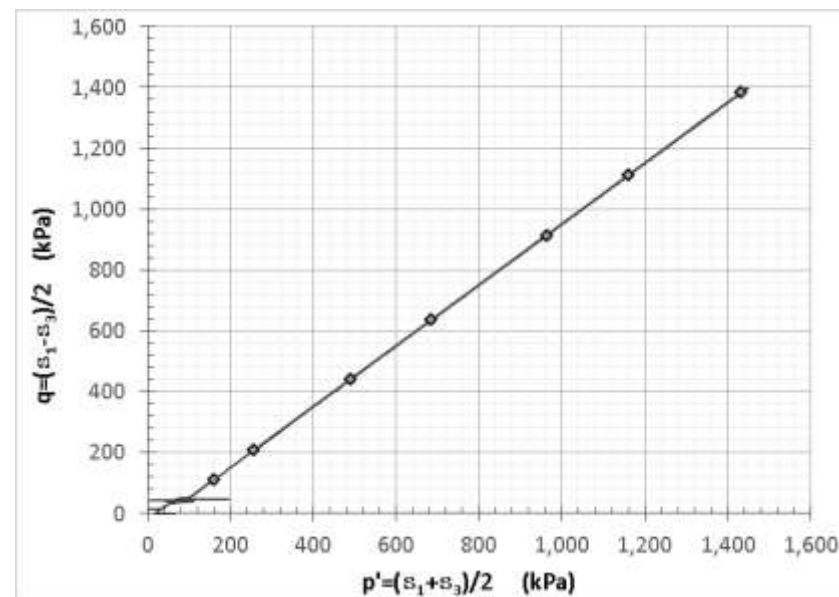
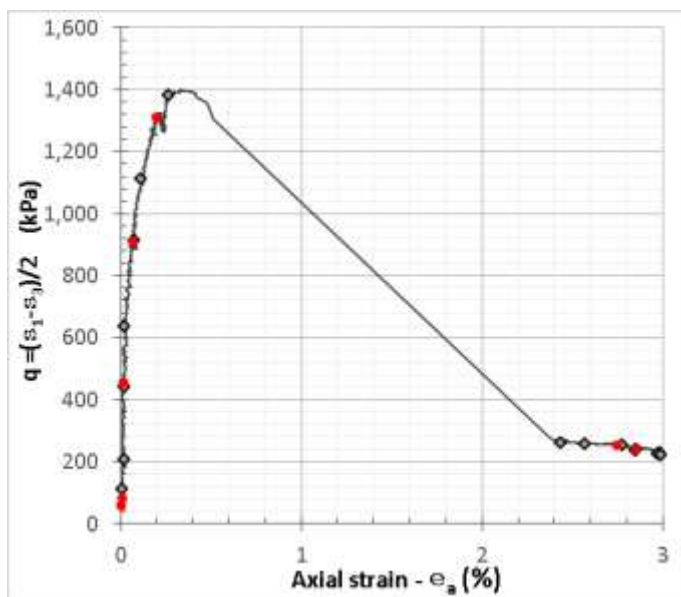
APPENDIX F.1 - Specimen TRX_31.9_15.4



—○— TRX_31.9_15.4
 • BE tests - unit mass

Note: Red dots represent the moment BE tests were conducted. Saturated unit mass was calculated using data related to these points.

APPENDIX F.2 - Specimen TRX_8.64_15.4

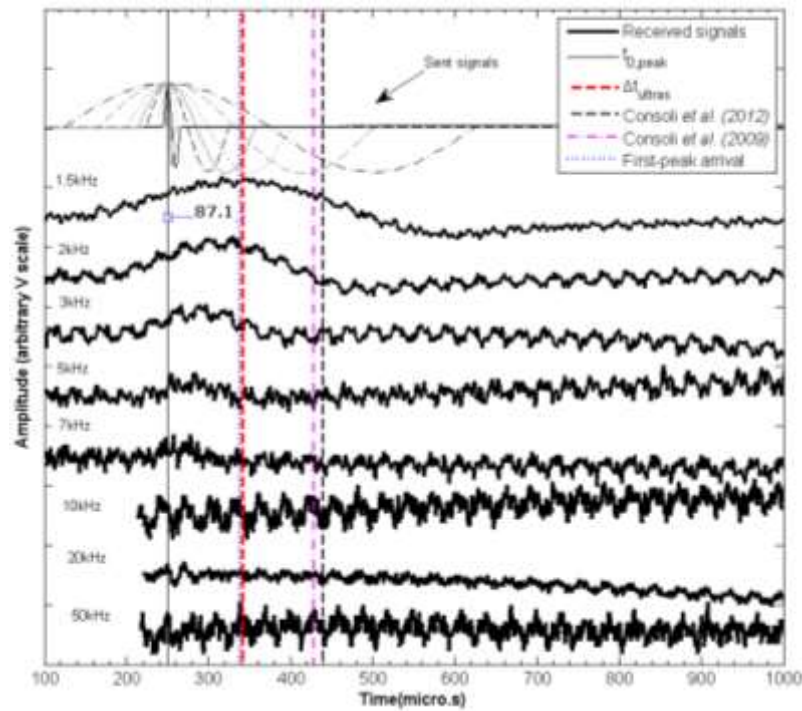


Red dots represent the moment BE tests were conducted. Saturated unit mass was calculated using data related to these points.

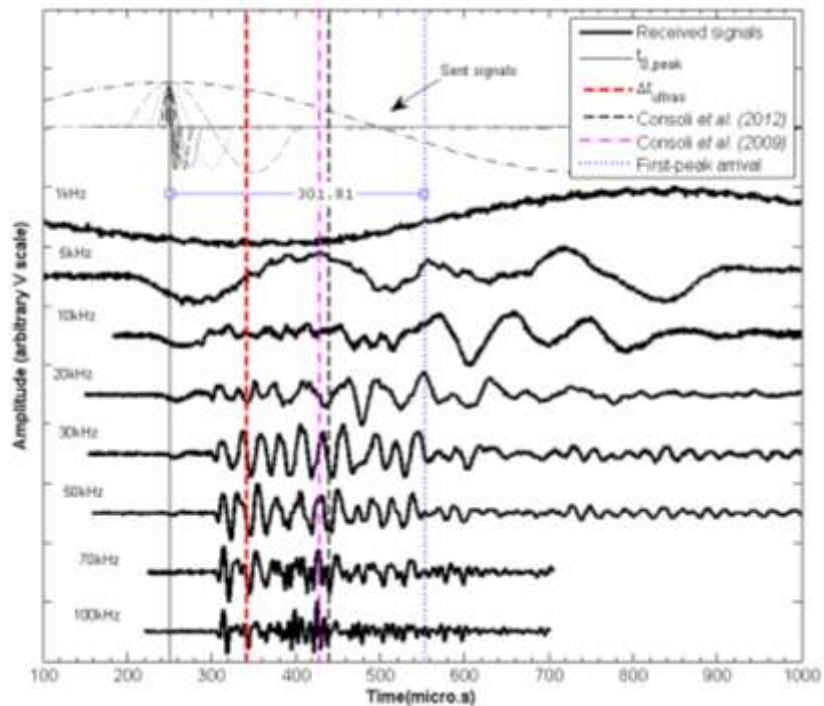
APPENDIX G – BE TRIAXIAL TESTS

APPENDIX G.1 – Specimen TRX_31.9_15.4

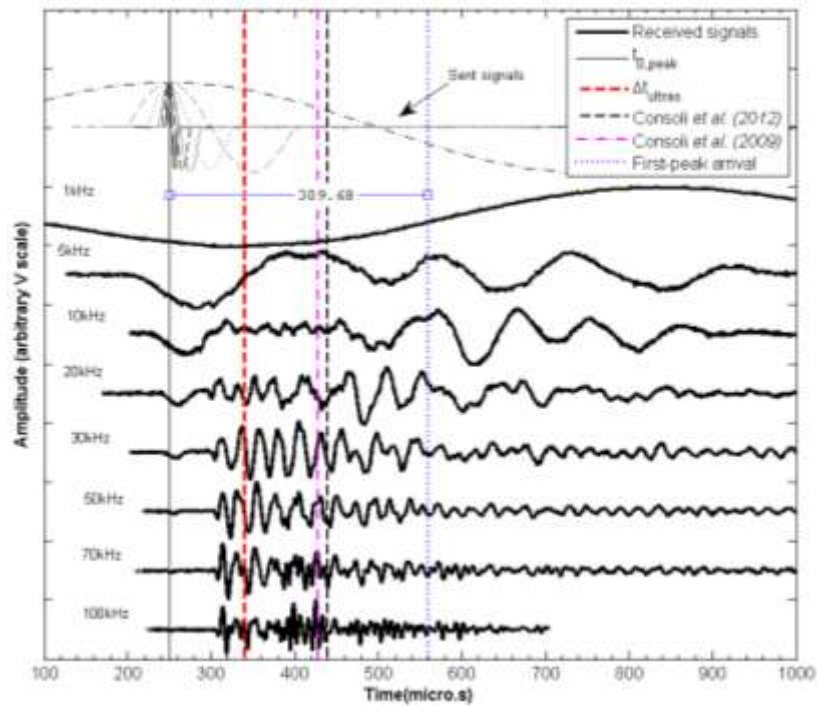
- Measurement 0 – Before shearing



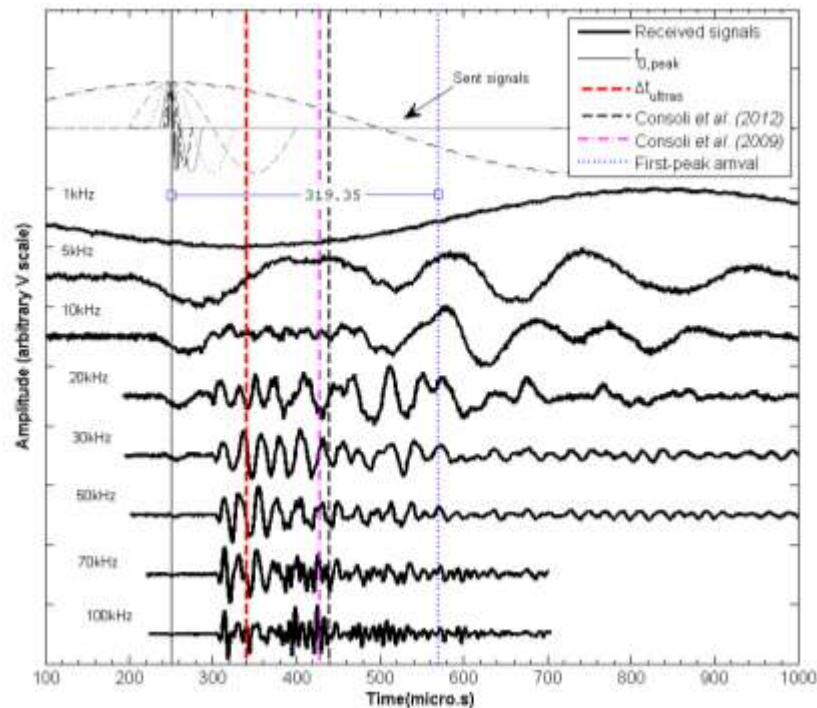
- Measurement II – During shearing: before the maximum peak



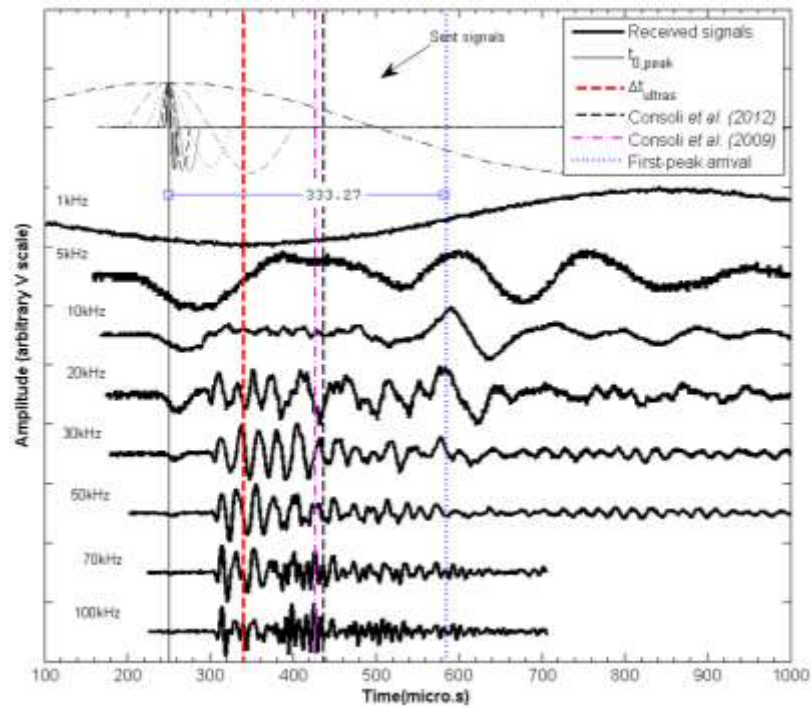
- Measurement III – During shearing: before the maximum peak



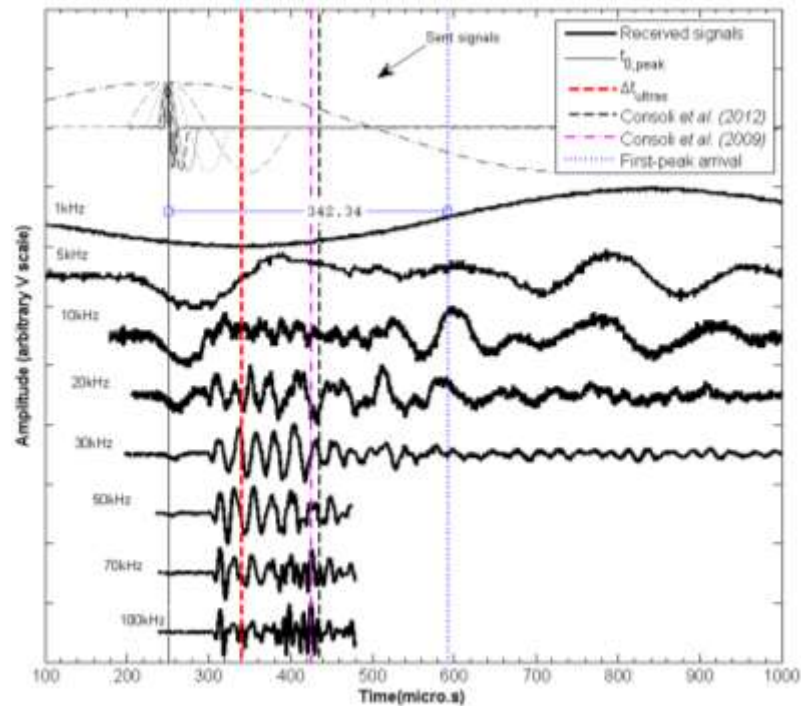
- Measurement IV – During shearing: before the maximum peak



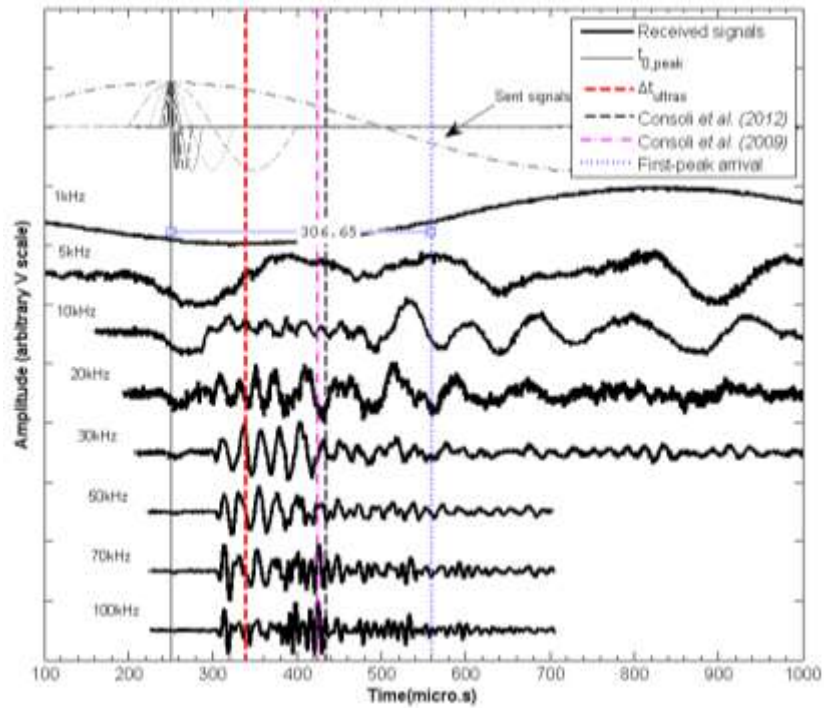
- Measurement V – During shearing: right before the maximum peak



- Measurement VI – During shearing: after the maximum peak

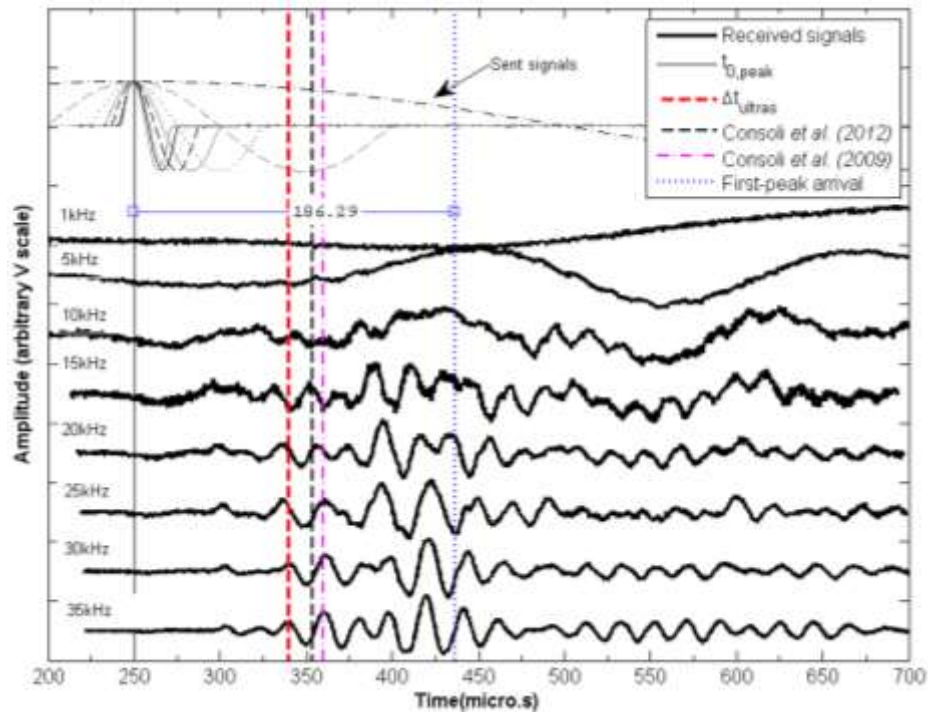


- Measurement VII – During shearing: after the maximum peak

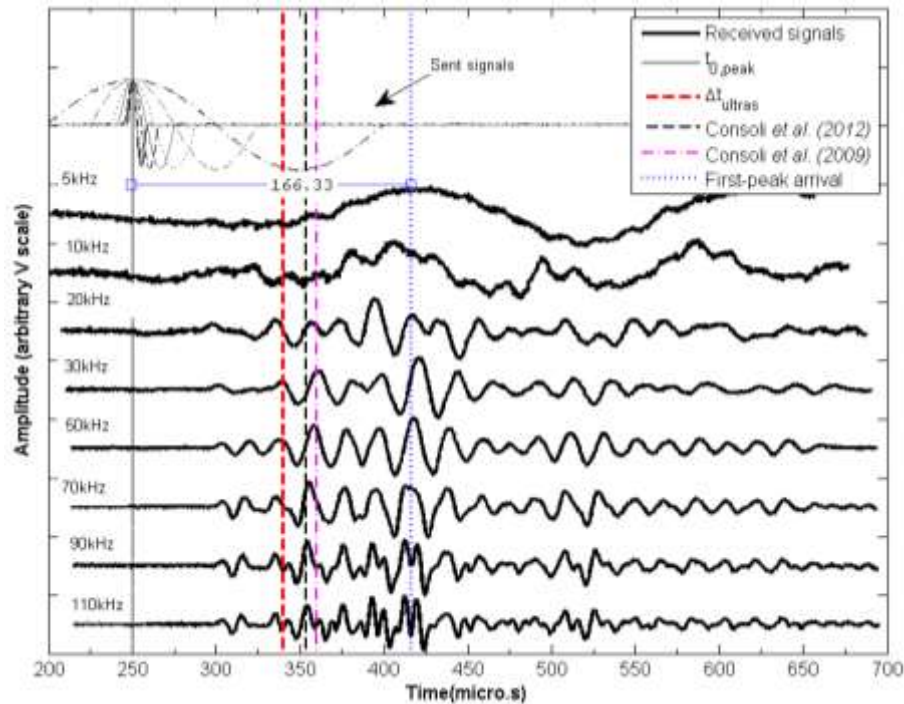


APPENDIX G.2 – Specimen TRX_8.64_15.4

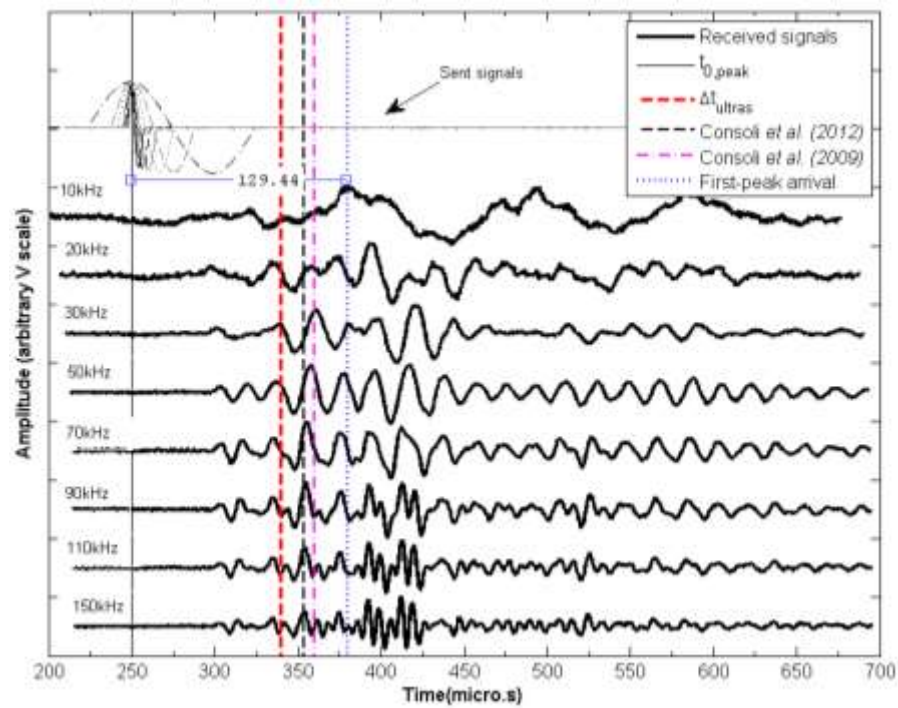
- Measurement 0 – Before shearing



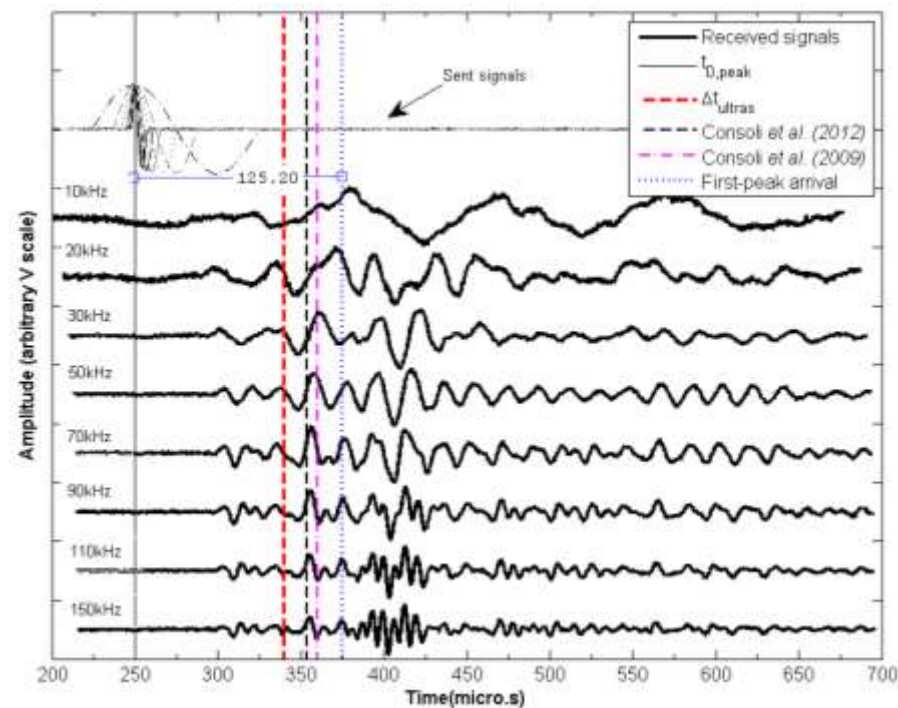
- Measurement I – During shearing: before the maximum peak



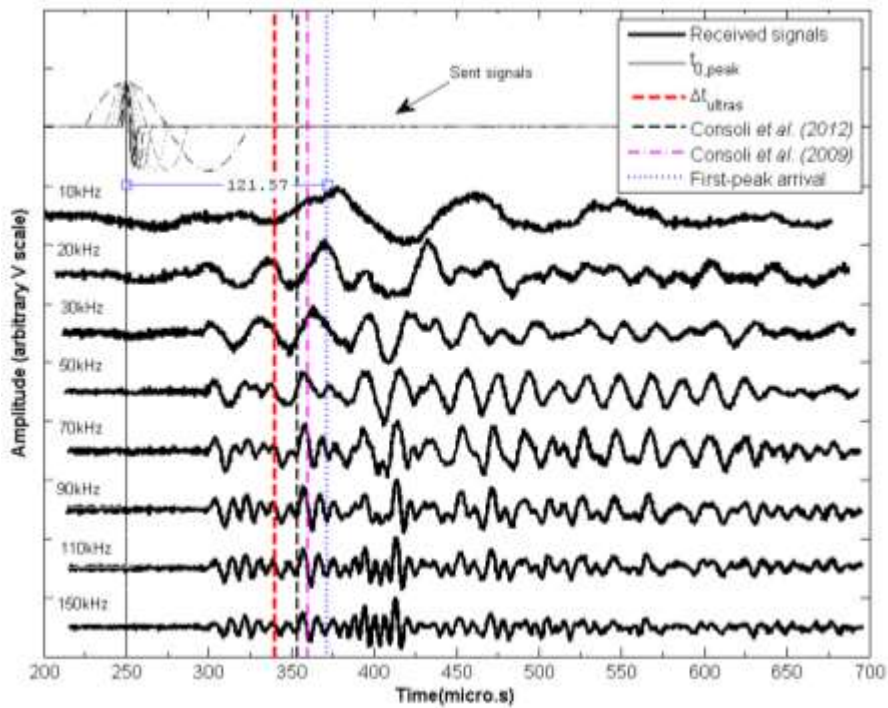
- Measurement II – During shearing: before the maximum peak



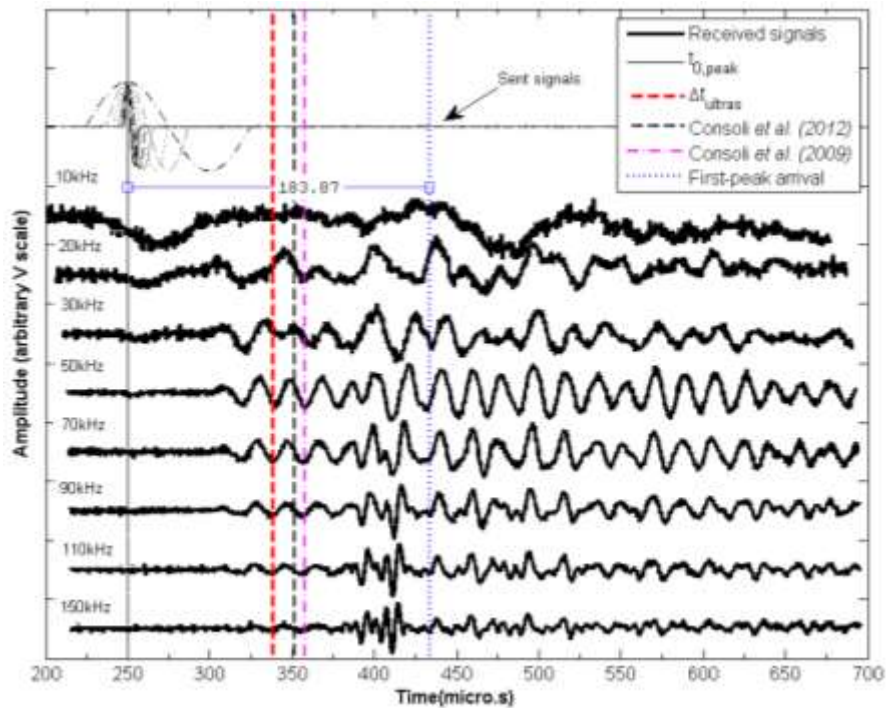
- Measurement III – During shearing: before the maximum peak



- Measurement IV – During shearing: right before the maximum peak



- Measurement V – During shearing: after the maximum peak



- Measurement VI – During shearing: after the maximum peak

